Acta Polytechnica

Editorial Board:

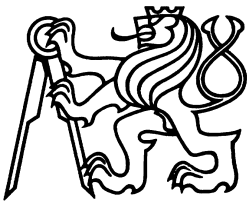

Title of journal: Acta Polytechnica. **Volume:** 62. **Number:** 2.
Periodicity: Bimonthly; 6 issues per year. **Date of issue:** April 30, 2022.
Published by: Czech Technical University in Prague,
Jugoslávských partyzánů 1580/3, 160 00 Praha 6 – Dejvice, Czech Republic.
IČO: 68407700.

Editorial Office: CTU — Central Library,
Technická 6, 160 80 Praha 6, Czech Republic.
acta@cvut.cz

Acta Polytechnica is available at http://ojs.cvut.cz/ojs/index.php/ap
Each article is assigned a digital object identifier https://doi.org/10.14311/AP.2022.62.⟨*4-digit article page number*⟩

ISSN 1805–2363 (online) MK ČR E 4923

Dear Reader

The Acta Polytechnica journal that you have just opened is a scientific journal published by the Czech Technical University in Prague. This journal first appeared in 1961 under the name "Proceedings of the Czech Technical University". The main purpose of the journal was to support publication of the results of scientific and research activities at the Czech technical universities. Five years later, in 1966, the name of the journal was changed to Acta Polytechnica, and it started appearing quarterly. The main title Acta Polytechnica is accompanied by the subtitle Journal of Advanced Engineering, which expresses the scope of the journal more precisely. Acta Polytechnica covers a wide spectrum of engineering topics in civil engineering, mechanical engineering, electrical engineering, nuclear sciences and physical engineering, architecture, transportation science, biomedical engineering and computer science and engineering. The scope of the journal is not limited to the realm of engineering. We also publish articles from the area of natural sciences, in particular physics and mathematics.

Acta Polytechnica is now being published in an enlarged format. Our aim is to be a high-quality multi-disciplinary journal publishing the results of basic research and also applied research. We place emphasis on the quality of all published papers. The journal should also serve as a bridge between basic research in natural sciences and applied research in all technical disciplines.

We invite researchers to submit high-quality original papers. The conditions of the submission process are explained in detail on: `http://ojs.cvut.cz/ojs/index.php/ap`. All papers will be reviewed, and accepted papers are published in English.

We hope that you will find our journal interesting, and that it will serve as a valuable source of scientific information.

Editorial Board

Contents

IMPROVEMENT OF SPECTRUM SENSING PERFORMANCE IN COGNITIVE RADIO USING MODIFIED HYBRID SENSING METHOD

Hadeel S. Abed*, Hikmat N. Abdullah

Al-Nahrain University, College of Information Engineering, Department of Information and Communication Engineering, Jadriah, 10001 Baghdad, Iraq

* corresponding author: hadeel_sami@coie.nahrainuniv.edu.iq

Abstract. Cognitive radio (CR) is a wireless technology for increasing the bandwidth usage. Spectrum sensing (SS) is the first step in CR. There are three basic techniques in SS, energy detection (ED), matched filter (MF), and cyclostationary detection (CFD). These techniques have many challenges in performance detection (P_d) and computational complexity (CC). In this paper, we propose a hybrid sensing method that consists of MF and CFD to exploit their merits and overcome their challenges. The proposed method aims to improve P_d and reduce CC. When MF hasn't had enough information about PU, it switches to CFD with a reduction of CC in both MF and CFD. The proposed method is simulated under fading with cooperative and non-cooperative scenarios, measured using P_d and CC ratio C_{ratio}, and evaluated by comparing it with traditional and hybrid methods in the literature. The simulation results show that the proposed method outperforms other methods in P_d and C_{ratio}. For example, at E_b/N_o equal to 0 dB under the Rayleigh fading channel, the P_d in the proposed method increased by 38 %, 28 %, 28 %, and 18 % as compared with the modified hybrid method, traditional hybrid method, traditional CFD method, and traditional MF method in the literature, respectively.

Keywords: Cognitive radio, spectrum sensing, matched filter, cyclostationary, energy detection, hybrid sensing method.

1. Introduction

Due to the large number and diversity of wireless devices and applications, the emergence of new applications, and the continuous demand for higher data rates, the Radio Frequency (RF) spectrum is becoming increasingly crowded [1, 2]. Cognitive radio (CR) has been proposed as a promising technique that provides a solution to the spectrum scarcity problem by dynamically exploiting the unused part of the spectrum band [3, 4]. A cognitive radio was defined as a radio or system that senses, and is aware of its operational environment and can dynamically adjust its radio operating parameters accordingly [5]. Cognitive radio is a wireless technology that provides the ability to share the spectrum while avoiding any imposed harmful interference to the PU [6]. The CR aims to exploit the natural resources efficiently, including frequency, time, etc. [7]. Spectrum sensing is the first step to implementing a CR system. The basic component of spectrum sensing is a primary user (PU) signal or license band, and a secondary user (SU) or cognitive user (CU) that senses the PU band to detect the activity of PU and can use its spectrum when the PU is absent [8]. The SU must not interfere in any way with the PU to succeed the cognitive radio networks [9]. Spectrum sensing techniques can be classified into two scenarios, non-cooperative and cooperative. Three basic techniques are used for spectrum sensing, these are energy detection ED, matched filter MF, and cyclostationary feature detection CFD. The ED spectrum sensing technique is more used as compared to others due to its simplicity and minimal computational complexity. However, at low signal-to-noise ratio (SNR) values, and bad channel conditions, the ED cannot differentiate between the PU signal and the noise. The matched filter (MF) maximizes the received SNR in communication systems, so it can be considered as the best detector [10]. MF has a challenge that it must know the information about the PU signal properties, i.e., packet format, pulse shaping, and the type of modulation. If the CR has incomplete information about the PU signal, then the MF cannot be used as an optimum detector. A cyclostationary detector can be used as a sub-optimal detector. CFD can distinguish between the PU signal and the noise. It has a good performance in low SNR conditions because of its noise rejection characteristic [11]. However, a cyclostationary detector has a high computational complexity since it has a long sensing time, which is not favourable in some situations [12]. To improve the performance detection, CSS (cooperative spectrum sensing) is applied. CSS could overcome fading and shadow in wireless channels. There are two basic structures of CSS, centralised and distributed [13, 14]. In CSS, SUs sense the spectrum separately and transmit their local decisions to a fusion centre (FC). By applying some fusion logic scheme, FC is responsible for the overall decision [11]. The decision fusion rules can be either hard or soft. In a hard fusion rule, every

SU makes the local binary decision independently of the activity of PU, while in the soft fusion rule, the SUs send their sensing information to the fusion centre without making local decisions. The decision is made at FC by using one of the combining rules [15–17]. The rest of the paper is organized as follows: Section 2 presents the literature review of the related works. Section 3 displays the theoretical background of spectrum sensing techniques. Section 4 explains the procedures of the proposed hybrid method. Section 5 shows the computational complexity of the proposed method. Section 6 illustrates the simulation results and discussions, and finally, the conclusions of the paper are drawn.

2. Related works

Several works related to the spectrum sensing technique are proposed to improve its performance. In [11] traditional hybrid method based on energy and cyclostationary detectors, the cooperative scenario is proposed to improve the detection performance without taking into consideration the computational complexity. In this method, the PU signal is first scanned by ED to detect whether the PU is present or not. If ED is not certain about the detection of PU, then the PU signal is sensed by a cyclostationary detector. In [12], the reduction of the computational complexity in CFD is done by choosing optimum parameters. In [18], the hybrid method consists of two parallel paths of detectors. The first path is created from two sequential detector stages; in the first phase, ED is used to identify the PU signal existence where the signal has not been detected. Maximum–Minimum Eigenvalue (MME) is used as a second stage to detect the PU signal presence. In [19], the hybrid method is done by artificial neural networks (ANN). In [20], the hybrid method consists of five types of detectors, each one having its special functions to detect the spectrum whether it is free or occupied. In [21], the hybrid sensing method is proposed based on ED and cyclostationary detector with a reduced computational complexity and an improved detection performance. In [22], the idea of the proposed method is similar to [12], it reduced the computational complexity with a good performance, its process is based on the optimal parameter selection strategy for choosing detection parameters of the cyclic frequency and lag. To improve the performance of spectrum sensing techniques and solve its complexity problem, we proposed a hybrid spectrum sensing method based on matched filter and cyclostationary feature detection. This method improves the performance detection of the matched filter when it does not have sufficient information about a PU signal or at very low SNR values, and reduces the computational complexity of the cyclostationary process with an excellent performance detection. The proposed method is measured using the probability of detection (P_d) and computational complexity ratio under the Rayleigh multipath fading channel with cooperative and non-cooperative scenarios, and evaluated by comparing it with traditional sensing techniques (cyclostationary and MF), the traditional hybrid method in reference [11] and improved hybrid method in reference [21].

3. Spectrum sensing techniques

There are three basic techniques used for spectrum sensing, which are energy detection, matched filter, and cyclostationary feature detection. Each technique is explained in the following sections.

3.1. Energy detector

Energy detection (ED) is the simplest sensing technique that does not require any knowledge about the PU signal to operate. It performs the detection by comparing the accumulated energy of the received signal with a predefined threshold. The threshold depends only on the noise power [1]. The received samples at the CU receiver are shown in the following Equation [23]:

$$y(n) = H_\theta x(n) + Noi(n), \tag{1}$$

where $y(n)$ is the received sensed signal by the CU, $x(n)$ is the PU signal, $Noi(n)$ is the Additive White Gaussian Noise (AWGN) and H is the gain of the channel, and θ is the activity pointer and has one of two values as shown in Equation (2),

$$\theta = \begin{cases} 0 & \text{for } H_0 \text{ hypothesis} \\ 1 & \text{for } H_1 \text{ hypothesis.} \end{cases} \tag{2}$$

When PU is present, it is represented by hypothesis H_1, while when the PU is absent, it is represented by hypothesis H_0. The probabilities of false alarm and detection are measured by comparing the energy computed from the sensed signal on observation window W with a pre-defined threshold λ. The accumulated energy En_j can be written as shown in Equation (3).

$$En_j = \frac{1}{N} \sum_{n=1}^{N} |y(n)|^2, \tag{3}$$

where N is the total number of sensed samples $N = WF_s$, where F_s is the frequency sampling. The probabilities of false alarm P_f and detection P_d are shown in Equations (4) and (5), respectively:

$$P_f = pr(En_j > \lambda \mid H_0), \tag{4}$$

$$P_d = pr(En_j > \lambda \mid H_1). \tag{5}$$

Numerically, the threshold value can be computed for a constant P_f value, which is shown in the following Equation (6) [24].

$$\lambda = (Q^{-1}(P_f) + \sqrt{N})2\sqrt{N}(N)^2 \tag{6}$$

3.2. Cyclostationary feature detection

Cyclostationary feature detection is a spectrum sensing technique for detecting the PU signals by exploiting the cyclostationary features of the received signals, these features are the periodicity, number of signals, their modulation type, symbol rate, and presence of interferer [25]. This method is achieved by the autocorrelation process. The autocorrelation can be computed by multiplying the received signal $y(n)$ with its delay version. The sum of autocorrelation is compared with a pre-defined threshold to detect the activity of the PU signal. If the summation is larger than the threshold, it means that the PU is present, otherwise, it is absent [11, 26]. This technique can distinguish between the signal and the noise, so it has a better performance as compared to ED. However, it has a high computational complexity, since it consumes a long sensing time. A signal is called a cyclostationary if its autocorrelation is a periodic function of time t with a given period. This type of cyclostationary detector is called a 2^{nd} order cyclostationary detector [25]. A discrete cyclic autocorrelation function of a discrete-time signal $y(n)$ with a fixed lag l is defined in Equation (7) [21].

$$R_{yy}^{\alpha}(l) = \lim_{N\to\infty} \frac{1}{N} \sum_{n=0}^{N-1} y[n]y^*[n+l]e^{-j2\pi\alpha n\Delta n}, \quad (7)$$

where N is the number of samples of a signal $y[n]$ and Δn is the sampling interval. By applying the discrete Fourier transform to $R_{yy}^{\alpha}(l)$, the cyclic spectrum (CS) is given as [21]:

$$S_{yy}^{\alpha}(f) = \sum_{l=-\infty}^{\infty} R_{yy}^{\alpha}(l)e^{-j2\pi fl\Delta l}. \quad (8)$$

The detection of the PU signal is achieved by sensing the (cyclic frequency) of its cyclic spectrum or cyclic autocorrelation function (CAF). If the CAF is larger than the pre-defend threshold, the signal is present, otherwise, the signal is absent [25].

3.3. Matched filter

The matched filter is a coherent detection technique. This technique requires prior information about the PU signals at SU. Assuming that the PU transmitter sends a pilot stream simultaneously with the data, the SU receives the signal and the pilot stream. Matched filter detection is performed by projecting the received signal in the direction of the pilot [1]. The test statistic can be written as:

$$T_{MFD} = \sum_{N} y(n)x_p^*(n), \quad (9)$$

where x_p represents the PU signal, y represents the SU received signal. The test statistics, T_{MFD}, are then compared with a pre-defined threshold to detect the activity of PU, as shown in the following Equation (10).

$$\begin{cases} \text{If } T_{MFD} \geq \lambda, \text{ PU signal present} \\ \text{If } T_{MFD} < \lambda, \text{ PU signal absent} \end{cases} \quad (10)$$

4. The proposed method

In this method, the design is based on the matched filter and cyclostationary techniques with an improvement in detection performance and reduction in computational complexity in both of them. The process of this method is that the matched filter receives the PU signal and senses the half number of samples by selecting one and skipping another to reduce the computational complexity in the convolution process between the incoming received signal (PU signal) and its impulse response, which is stored in the matched filter of the spectrum sensing technique. When the detector does not have a better knowledge about the PU or when the received signal is distorted due to the channel effect, it switches to the cyclostationary technique to overcome the degradation of performance detection. In the cyclostationary stage, it also senses the PU signal by using the half number of samples by sensing one and skipping one to reduce the computational complexity in the autocorrelation process. So, in this proposed method, we gain a high-performance detection with a reduction in computational complexity. Figure 1 shows the flowchart that explains the procedures of the proposed method. Figure 2 shows the proposed system model using the centralised cooperative network. According to [11] and [21], the probability of detection of the proposed method can be written as:

$$P_{d,proposedi} = 1 - (1 - P_{d,MFi})(1 - P_{d,cycoi}) \quad i = 1, 2, \ldots k, \quad (11)$$

where k is the number of SUs in the cooperative scenario, $P_{d,proposedi}$ is the probability of detection of the proposed method, $P_{d,MFi}$ is the probability of detection in matched filter stage, and $P_{d,cycoi}$ is the probability of detection in cyclostationary stage.

5. Computational complexity of the proposed method

In this section, we compute the computational complexity in two stages (MF and CFD). Since the MF is based on the convolution process between the received and previous information of the PU signal, the computational complexity in the convolution process based on the frequency domain equals to a multiplication between two signals and we need to compute the frequency domain transformation of both the received PU signal and its impulse, then, we need to compute the multiplication between them. The computational complexity of FFT for N samples is $o(Nlog_2N)$ according to [21], while for multiplying two signals, each

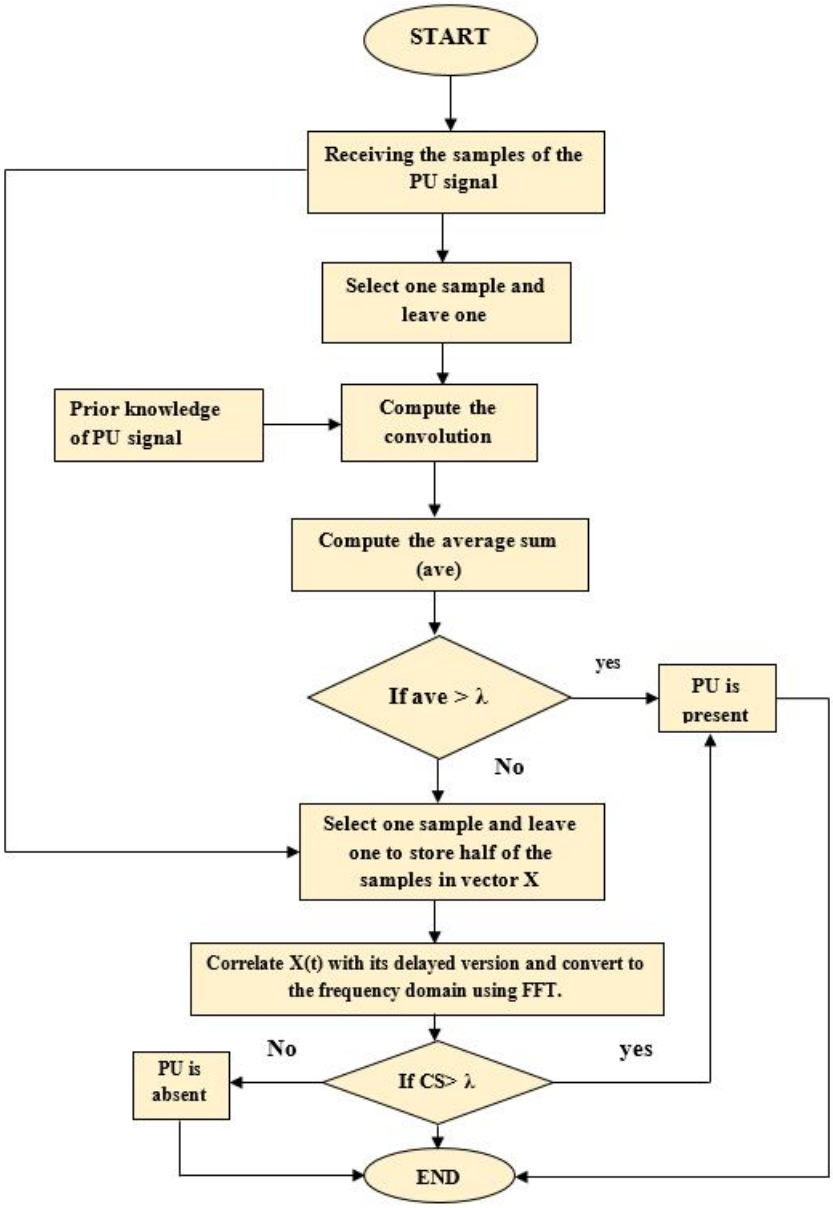

FIGURE 1. Procedures of the proposed method.

with N samples, it is $o(N)$. So, the computational complexity of a traditional MF becomes:

$$C_{conFFT} = 2o(Nlog_2N) + o(N), \tag{12}$$

where N is the number of samples. In the proposed method, we select a half of the samples by choosing one and skipping one, so the Equation (12) becomes:

$$C_{conpropoFFT} = 2o\left(\frac{N}{2}\log_2\frac{N}{2}\right) + o\left(\frac{N}{2}\right). \tag{13}$$

In the second stage, the cyclostationary process is based on the autocorrelation process and its computational complexity is [22, 27]:

$$\begin{aligned} C_{auto} &= No.\ of\ real\ multiplications \\ &\quad +\ No.\ of\ real\ additions \\ C_{auto} &= 4N + 4N - 2 \end{aligned} \tag{14}$$

The complexity of a traditional cyclostationary process is written as shown below:

$$C_{cycl} = 4N + 4N - 2 + o(Nlog_2N). \tag{15}$$

Since, in the proposed method, only a half of the samples was chosen for the cyclostationary process by selecting one and skipping one, the Equation (15) reduces to:

$$\begin{aligned} C_{cyclproposed} &= 2N + 2N - 2 + o\left(\frac{N}{2}log\frac{N}{2}\right) \\ &= 4N - 2 + o\left(\frac{N}{2}log\frac{N}{2}\right) \end{aligned} \tag{16}$$

The total computational complexity of the proposed method is the addition of Equations (13) and (16), as shown in Equation (17).

$$C_{Totalproposed} = 4N - 2 + 3o\left(\frac{N}{2}log_2\frac{N}{2}\right) + o\left(\frac{N}{2}\right) \tag{17}$$

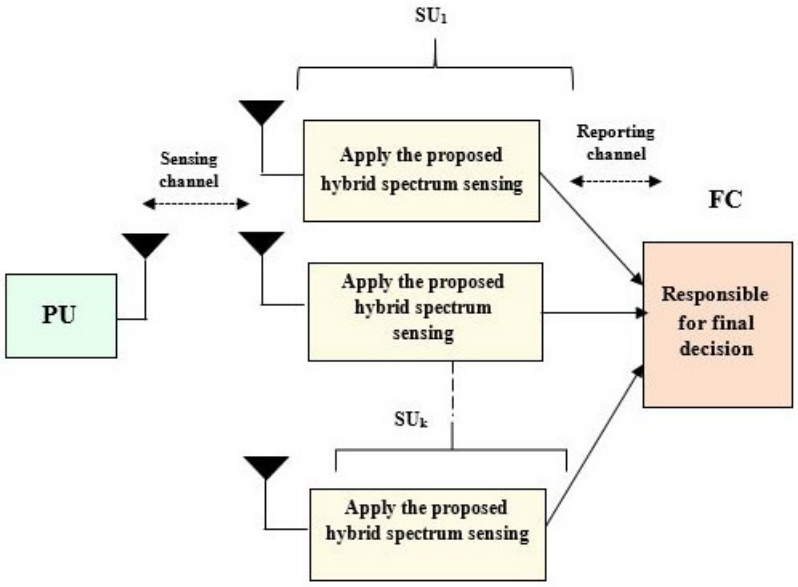

Figure 2. The proposed system model using the centralised cooperative network.

Method	Computational complexity
Proposed method	$C_{Totalproposed} = 4N - 2 + 3o\left(\frac{N}{2} log_2 \frac{N}{2}\right) + o\left(\frac{N}{2}\right)$
Hybrid method in [21]	$C_{hybrid} = 2N + 2N - 2 + O\left(Nlog_2(N)\right)$
Traditional hybrid [11]	$C_{hybridtradi} = 4N + 4N - 2 + O\left(Nlog_2(N)\right)$
Traditional Cyclostationary [21]	$C_{cycl} = 4N + 4N - 2 + o\left(Nlog_2 N\right)$
Traditional MF	$C_{conFFT} = 2o\left(Nlog_2 N\right) + o(N)$

Table 1. Comparison of computational complexity.

The computational complexity ratio is defined as the ratio of computational complexity in the proposed method to the maximum computational complexity (in the traditional Cyclostiationary method).

$$C_{ratio} = \frac{C_{Totalproposed}}{C_{cycl}} \tag{18}$$

Table 1 displays the summary of the computational complexity of the proposed method, the traditional hybrid method in [11], the hybrid method in [21], traditional cyclostationary, and traditional MF. It can be noted that the complexity of the traditional hybrid method is the same as the one of the traditional cyclostationary method.

6. Simulation results and discussion

This section shows the simulation results of the proposed method in both the cooperative and the non-cooperative scenarios. The performance is tested under AWGN and Rayleigh multipath fading channels. The results have been achieved using MATLAB 2018 on Windows 10. The performance results of the proposed method are measured using the probability of detection and computational complexity ratio and evaluated by comparing it with: hybrid methods in references [11] and [21], and with traditional methods (cyclostationary feature detection (CFD) and matched filter method MF). The simulation parameters used are presented in Table 2. The multipath fading used is "ITU indoor channel model (A)" with the specification shown in Table 3 [28].

Parameters	Values
PU signal	QPSK
Carrier frequency F_c	200 Hz
Sampling frequency F_s	4000 Hz
P_f	0.001

Table 2. Simulation results.

Figure 3 shows the performance curves of P_d vs E_b/N_o for traditional sensing methods (energy detection, cyclostationary, and matched filter) in AWGN using the non-cooperative scenario.

It can be seen from this figure that the matched filter has a better performance as compared to the energy detection and cyclostationary methods, especially at a low value of E_b/N_o, since it has a good knowledge of the PU signal. For example, at E_b/N_o equal to 0 dB, the probability of detection in the matched filter is increased by 36 % and 91 % as compared to cyclo-

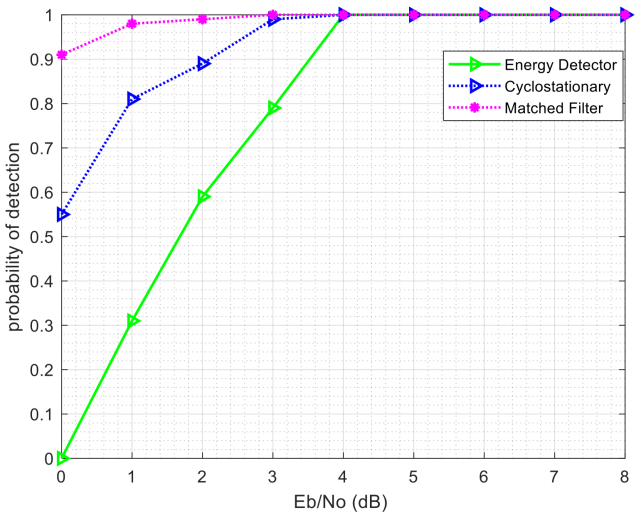

FIGURE 3. Performance comparison between traditional sensing techniques under AWGN and non-cooperative scenarios.

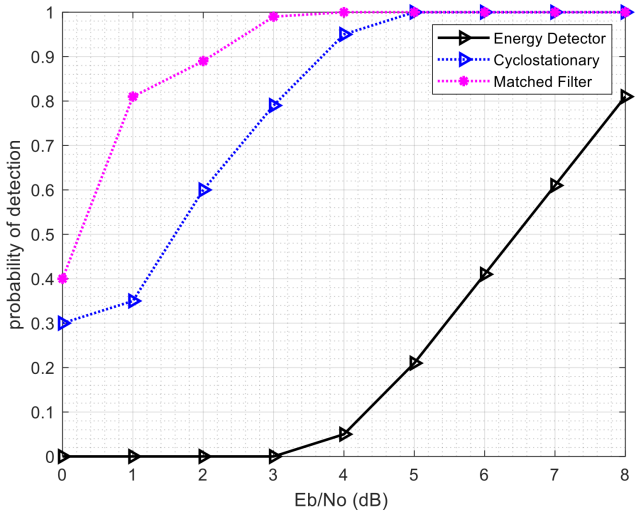

FIGURE 4. Performance comparison between traditional sensing techniques under Rayleigh fading and non-cooperative scenarios.

Tap	Relative delay [ns]	Average power [dB]	Doppler spectrum
1	0	0	flat
2	50	-3.0	flat
3	110	-10.0	flat
4	170	-18.0	flat
5	290	-26.0	flat
6	310	-32.0	flat

TABLE 3. Multipath fading properties of ITU indoor channel model (A).

stationary and energy detection, respectively. But the performance of matched filter becomes very bad when the knowledge of PU signal becomes poor and the cyclostationary technique becomes the best technique in the detection performance. The calculation of percentage improvement in this and all bellow results are as shown below:

$$percentage = (high\ value - low\ value) * 100\,\%.$$

When comparing two curves at the same E_b/N_o or N, we take the values from the curves and make sure that one curve has a value lower than the other, which is computed as shown in the above formula.

Figure 4 presents the same performance as in Figure 3, but in Rayleigh multipath fading, it can be noted that all techniques have the same detection performance as compared with Figure 3, but with a degradation in the probability of detection due to multipath fading, and the matched filter also outperforms other technique in the case of a good knowledge of PU.

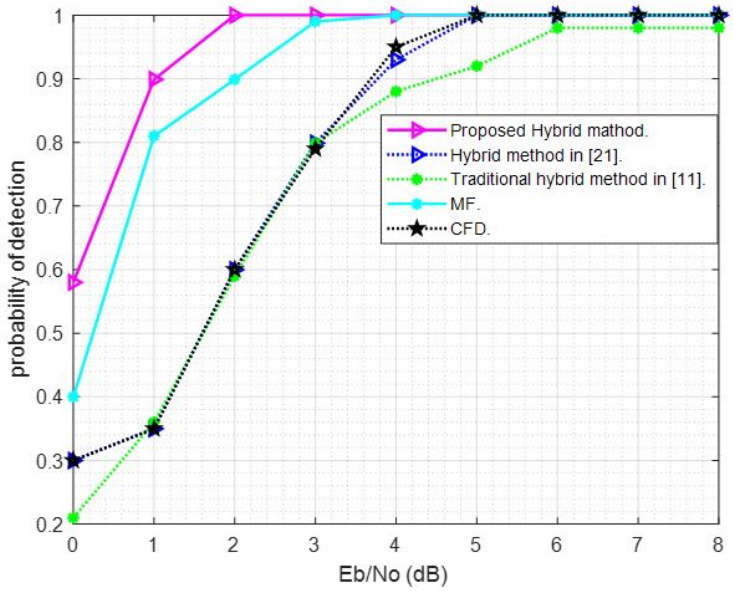

Figure 5. P_d versus E_b/N_o of proposed sensing methods under Rayleigh fading and non-cooperative scenario.

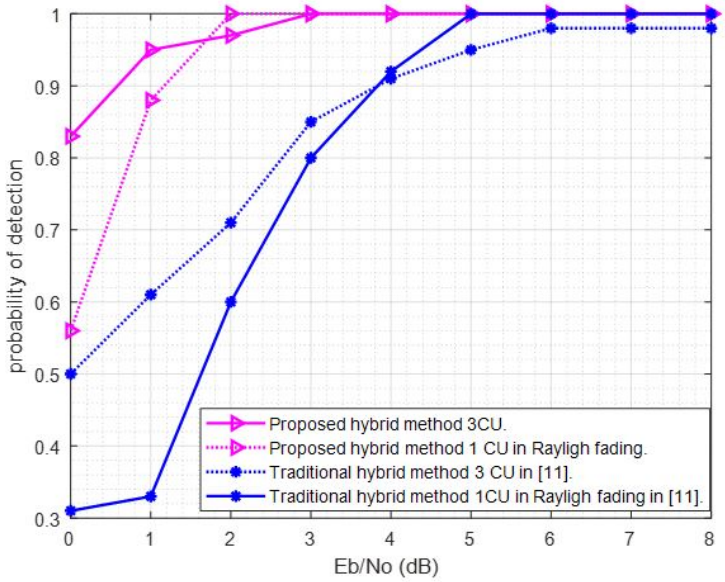

Figure 6. Performance comparison between the cooperative and non-cooperative scenarios in the proposed and traditional methods.

Figure 5 illustrates P_d vs E_b/N_o of the proposed method in the non-cooperative scenario under Rayleigh multipath fading as compared with hybrid methods in [11] and [21] and traditional methods (cyclostationary feature detection (CFD), and matched filter detection). It can be observed that the probability of detection of the proposed method outperforms the other methods especially at low E_b/N_o values, since the matched filter gives an excellent performance detection when it has the best knowledge about the PU signal. When it has a poor knowledge, it switches to the cyclostationary technique, which is a blind technique (does not need information about the PU signal) and gives a very good performance detection especially at low values of E_b/N_o. So, the overall detection performance of the proposed method gives an excellent detection performance with a low computational complexity. For example, at E_b/N_o equal to 0 dB, the proposed method achieves an increase in detection probability of 38 %, 28 %, 28 %, and 18 % as compared with the traditional hybrid method in [11], the hybrid method in [21], traditional CFD method, and traditional MF method, respectively.

Figure 6 displays the performance curves of the average P_d vs E_b/N_o of the proposed method in cooperative and non-cooperative scenarios as compared to the traditional hybrid method in [11]. In the cooperative scenario, we assumed 3 CUs do the sensing and one of them is suffering from multipath fading. It can be noted that the detection performance of the

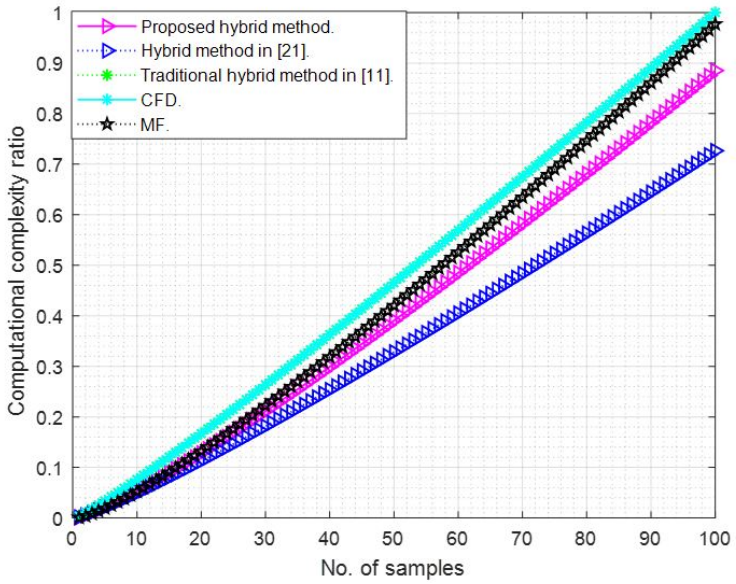

FIGURE 7. Computational complexity ratio versus the number of samples.

Method	Performance detection	Computational complexity
Proposed method	Excellent	Moderate
Hybrid method in [21]	Good	Low
Traditional hybrid method in [11]	Good	High
CFD	Good	High
MF	Very good (in best PU information)	Moderate
ED	Low	Low

TABLE 4. Summary of performance measurement.

cooperative scenario has a larger improvement than non-cooperative in both methods, since the effect of fading is reduced. For instance, at E_b/N_o equal to 0 dB in the proposed method, the performance detection is increased by 26 % as compared with a single CU in multipath fading and increased by 20 % as compared with the traditional hybrid also with a single CU in multipath fading. In all cases, the proposed method has a better performance than the traditional hybrid method.

Figure 7 shows the computational complexity ratio versus the number of samples. It can be seen that the proposed method has a lower computational complexity than the hybrid method in [11], traditional cyclostationary method, and MF, since it computes the convolution process in the MF stage or autocorrelation process in CFD with a half of the samples, and it is slightly greater than the hybrid method in [21], since this method uses an ED in the first stage. However, the proposed method outperforms the hybrid method in [21] and others in the probability of detection. For example, at N equal to 100, the computational complexity ratio in the proposed method decreased by 14 %, 14 %, and 12 % as compared to CFD, traditional hybrid in [11], and MF, respectively. So, we conclude that the proposed method has an excellent probability of detection and a very good reduction in computational complexity. Table 4 summarizes the performance of the proposed method, hybrid methods in [11] and [21], and traditional methods (ED, cyclostationary, and MF). This table shows that at very low SNR values, the proposed method is a perfect choice for spectrum sensing in terms of detection performance and computational complexity and for a very good channel environment, the ED become the best choice, but since in most cases, the channel environment is bad, the proposed method is more appropriate than others.

7. CONCLUSIONS

In this paper, we proposed a modified hybrid sensing method to overcome the problems of the traditional spectrum sensing technique. The proposed method is based on a combination of MF and CFD to improve the detection performance and reduce the computational complexity. The proposed method is simulated using MATLAB under Rayleigh multipath fading with two scenarios: cooperative and non-cooperative, measured using P_d and C_{ratio},and evaluated by a comparison with traditional and hybrid sensing methods in the literature. The simulation results show that the proposed method outperforms other methods in

the literature in terms of probability of detection and computational complexity in both channels. In future work, this method can be tested under other types of fading channels.

List of symbols

$y(n)$ Received sensed signal by the CU
$x(n)$ PU signal
$Noi(n)$ Additive White Gaussian Noise
H The gain of the channel
θ Activity pointer
H_1 Hypothesis when the PU is present
H_0 Hypothesis when the PU is absent
W Observation window
λ Pre-defined threshold
En_j Accumulated energy
N Number of sensed samples
F_s Sampling frequency
P_f Probability of false alarm
P_d Probability of detection
$R^{\alpha}_{yy}(l)$ The discrete cyclic autocorrelation function
Δn Sampling interval
$S^{\alpha}_{yy}(f)$ Cyclic spectrum
xp Previous information of PU signal
T_{MFD} The test statistic of MF
$P_{d,proposedi}$ Probability of detection of the proposed method
$P_{d,MFi}$ Probability of detection of MF stage
$P_{d,cycoi}$ Probability of detection of CFD stage
k Number of SU
C_{conFFT} The computational complexity of traditional MF
C_{cycl} The computational complexity of traditional CFD
$C_{Totalproposed}$ The computational complexity of the proposed method
C_{ratio} The ratio of computational complexity
E_b/N_o Signal to noise ratio per bit

List of abbreviations

CR Cognitive Radio
SS Spectrum Sensing
ED Energy Detection
MF Matched Filter
CFD Cyclostationary Feature Detection
CC Computational Complexity
RF Radio Frequency
PU Primary User
SU Secondary User
CU Cognitive User
SNR Signal to Noise Ratio
CSS Cooperative Spectrum Sensing
FC Fusion Center
SUs Secondary Users
MME Maximum–Minimum Eigenvalue
ANN Artificial Neural Networks
CAF Cyclic Autocorrelation Function
CS Cyclic Spectrum
FFT Fast Fourier Transform
ITU International Telecommunication Union
AWGN Additive White Gaussian Noise

References

[1] F. Salahdine. Spectrum sensing techniques for cognitive radio networks, 2017. Cornell University Library [internet] [2021-11-05], https://doi.org/10.48550/arXiv.1710.02668.

[2] M. E. Bayrakdar, A. Çalhan. Performance analysis of sensing based spectrum handoff process for channel bonding mechanism in wireless cognitive networks. In *2017 25th Signal Processing and Communications Applications Conference (SIU)*. Turkey, Antalya, 2017. https://doi.org/10.1109/SIU.2017.7960157.

[3] A. Mukherjee, S. Choudhury, P. Goswami, et al. A novel approach of power allocation for secondary users in cognitive radio networks. *Computers & Electrical Engineering* **75**:1–8, 2018. https://doi.org/10.1016/j.compeleceng.2018.03.006.

[4] M. Cicioğlu, M. E. Bayrakdar, A. Çalhan. Performance analysis of MAC technique developed for wireless cognitive radio networks. In *2018 26th Signal Processing and Communications Applications Conference (SIU)*. Turkey, Izmir, 2018. https://doi.org/10.1109/SIU.2018.8404747.

[5] S. Althunibat. *Towards energy efficient cooperative spectrum sensing in cognitive radio networks*. Ph.D. thesis, University of Trento, Italy, 2014. http://eprints-phd.biblio.unitn.it/1335/.

[6] E. Katis. Resource management of energy-aware cognitive radio networks and cloud-based infrastructures, 2015. Cornell University Library [internet] [2021-11-05], https://doi.org/10.48550/arXiv.1505.00906.

[7] M. Matinmikko (editor), M. Höyhtyä, M. Mustonen, et al. Cognitive radio: An intelligent wireless communication system. Tech. rep., 2008. Report no. VTT-R-02219-08, http://www.vtt.fi/inf/julkaisut/muut/2008/CHESS_Research_Report.pdf.

[8] A. Mukherjee, S. Maiti, A. Datta. Spectrum sensing for cognitive radio using blind source separation and hidden markov model. In *2014 Fourth International Conference on Advanced Computing & Communication Technologies*, pp. 409–414. 2014. https://doi.org/10.1109/ACCT.2014.63.

[9] M. E. Bayrakdar, A. Çalhan. Optimization of ant colony for next generation wireless cognitive networks. *Journal of Polytechnic* **24**(3):779–784, 2021. https://doi.org/10.2339/politeknik.635065.

[10] M. S. Falih, H. N. Abdullah. DWT based energy detection spectrum sensing method for cognitive radio system. *Iraqi Journal of Information and Communications Technology* **3**(3):1–11, 2020. https://doi.org/10.31987/ijict.3.3.99.

[11] K. Yadav, S. D. Roy, S. Kundu. Hybrid cooperative spectrum sensing with cyclostationary detection for cognitive radio networks. In *2016 IEEE Annual India Conference (INDICON)*, pp. 1–6. 2016. https://doi.org/10.1109/INDICON.2016.7839118.

[12] H. Arezumand, H. Sadeghi. A low-complexity cyclostationary-based detection method for cooperative spectrum sensing in cognitive radio networks. *International journal of information and communication technology* **3**(3):1–10, 2011. https://elmnet.ir/article/605357-22041/A-Low-Complexity-Cyclostationary-Based-Detection-Method-for-Cooperative-Spectrum-Sensing-in-Cognitive-Radio-Networks.

[13] P. Bachan, S. K. Ghosh, S. K. Saraswat. Comparative error rate analysis of cooperative spectrum sensing in non-fading and fading environments. In *2015 Communication, Control and Intelligent Systems (CCIS)*, pp. 124–127. 2015. https://doi.org/10.1109/CCIntelS.2015.7437891.

[14] P. Bachan, S. K. Ghosh, S. R. Trankatwar. Parametric optimization of improved sensing scheme in multi-antenna cognitive radio network over erroneous channel. In A. Khanna, D. Gupta, Z. Pólkowski, et al. (eds.), *Data Analytics and Management*, vol. 54, pp. 533–541. 2021. https://doi.org/10.1007/978-981-15-8335-3_41.

[15] H. N. Abdullah, N. S. Baker, M. T. S. Al-Kaltakchi. Proposed two-stage detection rules for improving throughput in cognitive radio networks. *Iraqi journal of computers, communications, control & system engineering (IJCCCE)* **19**(4):1–11, 2019. https://doi.org/10.33103/uot.ijccce.19.4.1.

[16] A. Mukherjee, P. Goswami, A. Datta. HML-Based smart positioning of fusion center for cooperative communication in cognitive radio networks. *IEEE Communications Letters* **20**(11):2261–2263, 2016. https://doi.org/10.1109/LCOMM.2016.2602266.

[17] S. K. Ghosh, S. R. Trankatwar, P. Bachan. Optimal voting rule and minimization of total error rate in cooperative spectrum sensing for cognitive radio networks. *Journal of Telecommunications and Information Technology* **1**:43–50, 2021. https://doi.org/10.26636/jtit.2021.144420.

[18] A. R. Mohamed, A. A. A. El-Banna, H. A. Mansour. Multi-path hybrid spectrum sensing in cognitive radio. *Arabian Journal for Science and Engineering* **46**:9377–9384, 2021. https://doi.org/10.1007/s13369-020-05281-0.

[19] A. Nasser, M. Chaitou, A. Mansour, et al. A deep neural network model for hybrid spectrum sensing in cognitive radio. *Wireless Personal Communications* **118**:281–299, 2021. https://doi.org/10.1007/s11277-020-08013-7.

[20] A. S. Khobragade, R. D. Raut. Hybrid spectrum sensing method for cognitive radio. *International Journal of Electrical and Computer Engineering (IJECE)* **7**(5):2683–2695, 2017. https://doi.org/10.11591/ijece.v7i5.pp2683-2695.

[21] H. N. Abdullah, Z. O. Dawood, A. E. Abdelkareem, H. S. Abed. Complexity reduction of cyclostationary sensing technique using improved hybrid sensing method. *Acta Polytechnica* **60**(4):279–287, 2020. https://doi.org/10.14311/AP.2020.60.0279.

[22] D. Shen, D. He, W.-h. Li, Y.-p. Lin. An improved cyclostationary feature detection based on the selection of optimal parameter in cognitive radios. *Journal of Shanghai Jiaotong University (Science)* **17**(1):1–7, 2012. https://doi.org/10.1007/s12204-012-1222-z.

[23] M. Emara, H. S. Ali, S. E. A. Khamis, F. E. A. El-Samie. Spectrum sensing optimization and performance enhancement of cognitive radio networks. *Wireless Personal Communications* **86**:925–941, 2016. https://doi.org/10.1007/s11277-015-2962-5.

[24] S. Atapattu. *Analysis of energy detection in cognitive radio networks*. Ph.D. thesis, University of Alberta, Canada, 2013. http://www.ece.ualberta.ca/~chintha/pdf/thesis/phd_saman.pdf.

[25] W. Adigwe, O. R. Okonkwo. A review of cyclostationary feature detection based spectrum sensing technique in cognitive radio networks. *E3 Journal of Scientific Research* **4**(3):041–047, 2016. https://doi.org/10.18685/EJSR(4)3_EJSR-16-010.

[26] I. G. Anyim. *Wideband Cyclostationary Spectrum Sensing with Receiver Constraints and Optimization*. Ph.D. thesis, University of Portsmouth, United Kingdom, 2018.

[27] S. Narieda. Low complexity cyclic autocorrelation function computation for spectrum sensing. *IEICE Communications Express* **6**(6):387–392, 2017. https://doi.org/10.1587/comex.2016XBL0211.

[28] M. Pätzold. *Mobile Fading Channels*. John Wiley & Sons, Ltd, 2002. https://doi.org/10.1002/0470847808.fmatter.

ZNO-ZEOLITE NANOCOMPOSITE APPLICATION FOR PHOTOCATALYTIC DEGRADATION OF PROCION RED AND ITS ADSORPTION ISOTHERM

Tuty Emilia Agustina[a,*], Rianyza Gayatri[b], David Bahrin[a], Rosdiana Moeksin[a], Gustini[c]

[a] *Universitas Sriwijaya, Faculty of Engineering, Chemical Engineering Department, Jl. Raya Palembang – Prabumulih Km 32 Indralaya 30662, South Sumatera, Indonesia*

[b] *Universitas Sriwijaya, Environmental Technology, Master Program of Chemical Engineering, Jl. Srijaya Negara, Bukit Besar, Palembang 30139, South Sumatera, Indonesia*

[c] *Universitas Sriwijaya, Faculty of Engineering, Mechanical Engineering Department, Jl. Raya Palembang – Prabumulih Km 32 Indralaya 30662, South Sumatera, Indonesia*

[*] corresponding author: tuty_agustina@unsri.ac.id

Abstract. In this paper, the photocatalytic degradation of procion red dye, one of the most frequently used dyes in the textile industry, was studied. The objective of the research is to study the ZnO-Zeolite nanocomposite application to degrade procion red dye by using different irradiation sources. The adsorption isotherm was also investigated. The ZnO-Zeolite nanocomposite was prepared by a sol-gel process. Photodegradation test was applied under the sunlight irradiation, ultraviolet (UV) lamp, and in a darkroom. The dye degradation was also examined by the synthetic zeolite and ZnO for a comparison. Another objective of this study is to analyse the appropriate adsorption isotherm to describe the degradation process of procion red dye by using ZnO-Zeolite nanocomposite. The adsorption ability of the nanocomposite was described by Langmuir and Freundlich isotherms. The adsorption of the nanocomposite was reported to depend on the degradation time. The highest photodegradation result of 98.24 % was achieved by irradiating 50 mg/l of procion red dye under the sunlight for 120 minutes. The result showed that the Langmuir adsorption isotherm was the appropriate adsorption equation for the degradation process of procion red dye by using ZnO-Zeolite nanocomposite with R^2 value of 0.995.

Keywords: Nanocomposite, ZnO, zeolite, adsorption isotherm, photocatalytic degradation, procion red.

1. Introduction

The growing textile industry, in addition to producing commercial products, also produces byproducts in the form of dye wastewater. Procion red is one of most often used synthetic dye that is hard to decompose and is present in the wastewater. One of the most important aspects of water treatment technology is the process to remove the organic compounds in the wastewater [1]. Based on previous research, there are several conventional methods used to degrade textile dye wastewater. However, the photodegradation process and the use of photocatalyst is the best and most suitable method for wastewater treatment.

The photocatalytic oxidation process combines UV irradiation with a catalyst; TiO_2, CdS, ZnO [2]. The photocatalytic reaction produces hydroxyl radicals as an oxidator to break down the pollutant gradually in a stepwise process [3]. ZnO is the most suitable and is often used as a photocatatalyst [4]. In photocatalytic applications, semiconductor ZnO is cheaper than the other nanosized metal oxides and ZnO is also better due to its environmental stability. The adsorption capacity of the photocatalyst is still weak, and the combination of photocatalyst and adsorbents will solve this problem [5].

This combination is carried out in order to maximize the dye pollutants' contact with photocatalysts [6]. The adsorbent used also does not need to be regenerated because the photocatalyst will immediately degrade the pollutants that have been absorbed in the adsorbent in situ so that the adsorbent is not easily saturated.

Zeolite has good adsorption properties and has a large surface, so it is used as an adsorbent and helps the adsorption-catalytic process [7]. The activation of zeolite aims to increase its purity [8]. However, synthetic zeolite, which has physical properties is much better than natural zeolite; the pore size of the synthetic zeolite is uniform, and it maximizes the adsorption results. This is the basis for selecting the synthetic zeolite adsorbents to be combined with the ZnO photocatalysts.

The zeolite adsorbent also has a good adsorption ability. The adsorption capacity can be determined by the adsorption isotherm equation, generally by the Freundlich or Langmuir equation [9]. Among the several adsorption isotherms, the equations proposed

by Freundlich and Langmuir are most frequently used and are very useful for a mathematical description of adsorption from aqueous solutions [10].

Therefore, this study will use the photodegradation process as a method of removal of red procion textile colour substances using composites consisting of photocatalyst ZnO and synthetic zeolite adsorbent.

In this study, the sol-gel process is used for the formation of ZnO-Zeolite nanocomposites, the process will produce metal oxides using alcohol or water [11]. Based on several researches that have been carried out, the ZnO-Zeolite nanocomposite was applied for the photodegradation process of procion red dye, and the effect of the irradiation source in the photodegradation process should also be seen.

Therefore, in this study, the determination of the adsorption isotherm that is suitable for the degradation process of the procion red dye by using ZnO-Zeolite nanocomposites was also considered, to study the adsorption mechanism and the interaction between the adsorbent and the absorbed substance, and to determine the maximum adsorption capacity [12].

2. Materials and methods

Zinc acetate, zinc oxide, ethanol, NaOH, and HCl were obtained from Sigma Aldrich and synthetic procion red powder dye was obtained from dyestuff store (Fajar Setia, Jakarta). Commercial synthetic zeolite of A-Type ($Na_2O.Al_2O_3.2SiO_2.4.5H_2O$) was purchased from PT. Phy edumedia, East Java.

Synthetic zeolites with a 400 mesh size have been activated by heating in oven at 110 °C for 2 hours, then washed with 0.4 M HCl for 60 minutes, and finally, washed with distilled water. The synthetic zeolite was dried in an oven at 110 °C for 2 hours [13].

2.1. Synthesys and characterisation of ZnO-Zeolite nanocomposite

ZnO-synthesis zeolite nanocomposite is produced by sol-gel method, as referred to in [13]. The reason for using the precursor weight of Zinc acetate and zeolite 2:1 is because the ratio produces the highest degradation of colour substances, as it was discovered in previous research [14] which has also compared the influence of ZnO and zeolite photocatalyst ratios and the 2:1 weight ratio is the best ratio.

Zinc acetate as precursor is added with active synthetic zeolite in the precursor and synthetic zeolite ratio of 2:1, then dissolved in 80 ml of 99 % ethanol. The precursor and zeolite mixture was heated in a reflux flask to 76 °C for 2 hours. Then, 225 ml of 2 M NaOH was added to the solution and stirred for 60 minutes. The mixture was stood for 12 hours and then it was filtered. Next, the precipitate obtained was heated at 60 °C for 24 hours and then stored in a desiccator to keep it dry [13]. The ZnO-Zeolite nanocomposites were analysed by SEM-EDX, BET, and XRD.

2.2. ZnO-Zeolite nanocomposite application for photocatalytic degradation

ZnO-Zeolite nanocomposite have been tested for the degradation of 50 mg/l of procion red dye. Dye photodegradation was applied in three ways, by using sunlight, ultraviolet (UV) lamp and dark conditions. The use of only zeolite and only ZnO was also tested for the photodegradation process. Before the degradation process, the maximum wavelength of procion red solution was measured. A 100 mg of ZnO-Zeolite nanocomposite, mixed with 25 ml of 50 mg/l procion red, was stirred and placed directly under the sun. Experiments using sunlight were carried out at noon between 11.00 am–1.00 pm. The light intensity at that time was measured by a luxmeter.

Samples were tested in several time variations from 5–120 minutes; first, they were filtered and then the colour degradation was analysed. The experiments were also carried out with ultraviolet light irradiation [14] by using UV lamp (Evaco 254 nm) and in dark conditions. The experiments in dark conditions were carried out without turning on the UV lamp and closing the reactor using a black plastic coated box.

The final dye's absorbance and dye's concentration were measured by using a UV-Vis spectrophotometer. The maximum wavelength of procion red solution is 470 nm. The degradation percentage of procion dye and the adsorption percentage formulas are shown in Equations (1) and (2).

$$Degradation\ Percentage = \frac{A_0 - A_1}{A_0} \times 100\,\% \quad (1)$$

Equation (1) explains how to find the dye degradation percentage, A_0 is the value of the initial absorbance of the dye and A_1 is the value of the final absorbance.

$$Adsorption\ Percentage = \frac{C_0 - C_1}{C_0} \times 100\,\% \quad (2)$$

Equation (2) shows the adsorption percentage calculation, C_0 is the value of the initial concentration of the dye and C_1 is the value of the final concentration.

2.3. Determination of ZnO-Zeolite nanocomposite adsorption isotherm type

The adsorption process in dark conditions with ZnO-Zeolite nanocomposite provides data on the photodegradation results of procion red dye in the form of adsorption values and the final concentration of the dye. The data analysis weas performed by determining the final content of the procion red dye after the adsorption process.

Calculations of the Langmuir and Freundlich equations are carried out to determine the pattern or type of adsorption isotherm suitable for the absorption process of procion red dye by ZnO-Zeolite nanocomposites. The calculation results of each type will be plotted on the graph, and the most suitable ZnO-Zeolite nanocomposite adsorption isotherm will be

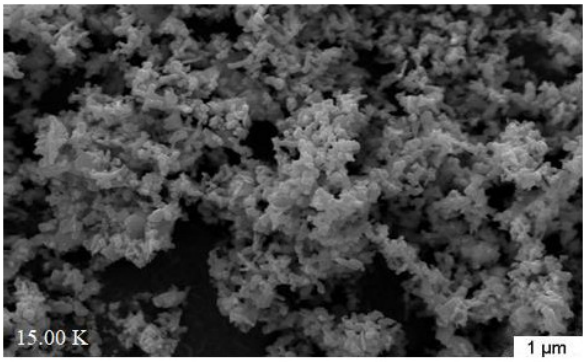

Figure 1. SEM image of ZnO.

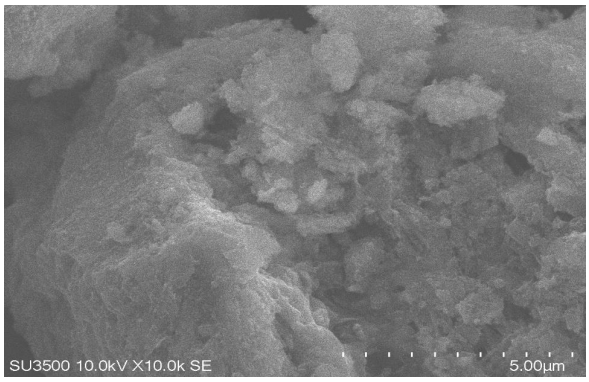

Figure 2. SEM image of Activated Synthetic Zeolite.

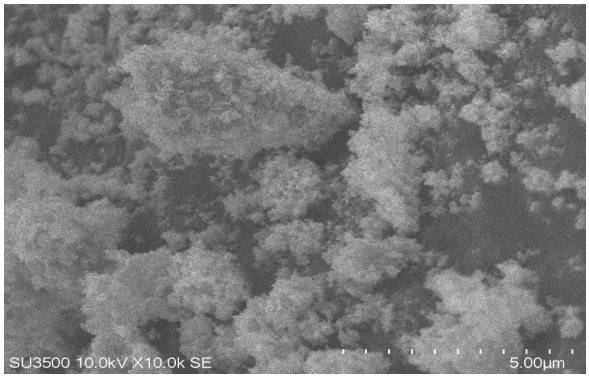

Figure 3. SEM image of ZnO-Zeolite nanocomposite.

determined. A good linearization of the line on the graph and the coefficient of determination $R^2 \geq 0.9$ (close to 1) are parameters for determining the corresponding adsorption isotherm equation to describe the degradation process of procion red dye using the ZnO-Zeolite nanocomposite.

The Langmuir isotherm model in Equation (3) assumes that a single particle will be adsorbed by each site and a monolayer on the surface of adsorbent will be formed by the adsorbate,

$$\frac{C_e}{q_e} = \frac{1}{a.b} + \frac{1}{a} C_e. \tag{3}$$

The Freundlich isotherm in Equation (4) explains the adsorption on heterogeneous surfaces and microporous adsorbent [2].

$$\ln q_e = \ln K_f + \frac{1}{n} \ln C_e \tag{4}$$

3. Results and discussion

3.1. ZnO-Zeolite nanocomposite characters

Figure 1 shows the SEM image of ZnO with a magnification of 15 000. The image shows a uniform distribution of the particle shape. Figure 2 presents the SEM image of activated synthetic zeolite with a magnification of 10 000. The active synthetic zeolite has a smoother structure and has a more regular shape and size than before the activation process. The EDX results of ZnO-Zeolite nanocomposites showed that ZnO and zeolite components are present in the ZnO-Zeolite nanocomposite with a Zn content of 56.13 % and an oxygen content of 22.42 % weight percent. The other components are carbon content of 12.61 %, aluminium of 2.75 % and silica of 6.09 % weight percent [13]. The silica and aluminium contents indicate the presence of zeolite in the nanocomposites. SEM image result of the nanocomposite, with a magnification of 10 000, is showed in Figure 3. The nanocomposite particle distribution and particle size look smooth and uniform.

Based on a previous study, the surface area of the nanocomposite that consists of ZnO and synthetic zeolite also has a significant impact on the photodegradation process. The results of BET characterisation showed that the surface area of the activated synthetic zeolite was 47.192 m^2/g, for ZnO, it was 19.192 m^2/g, and for ZnO-Zeolite nanocomposite, it was 95.981 m^2/g. The ZnO-Zeolite nanocomposite has the highest surface area. These BET results have also been discussed in previous research by [13].

The XRD of ZnO-Zeolite nanocomposite confirmed and proved that the nanocomposite consisted of zinc oxide (ZnO) and synthetic zeolite components as shown in Figure 4. The XRD pattern of the nanocomposite shows the diffraction peaks at 2θ of 31.43°, 34.51°, 36.37°, and 54.99° that are identical to hexagonal ZnO peaks [15]. The other peaks found at 2θ= 10.01°, 22.12°, 26.11°, and 29.98°, represent the presence of synthetic zeolite [16], [13].

3.2. The photodegradation results of procion red

Overall, the highest dye photodegradation was achieved by using the ZnO-Zeolite nanocomposite for the longest time period of 12 minutes. Research by [17] showed similar results where ZnO photocatalysts with natural zeolites were the most effective and resulted in the highest degradation of dyes. The percentage rate of dye removal increases by increasing the time up to 120 minutes, because the nanocomposite has a high photocatalytic activity and produces more hydroxyl radicals to degrade the dye, moreover, the

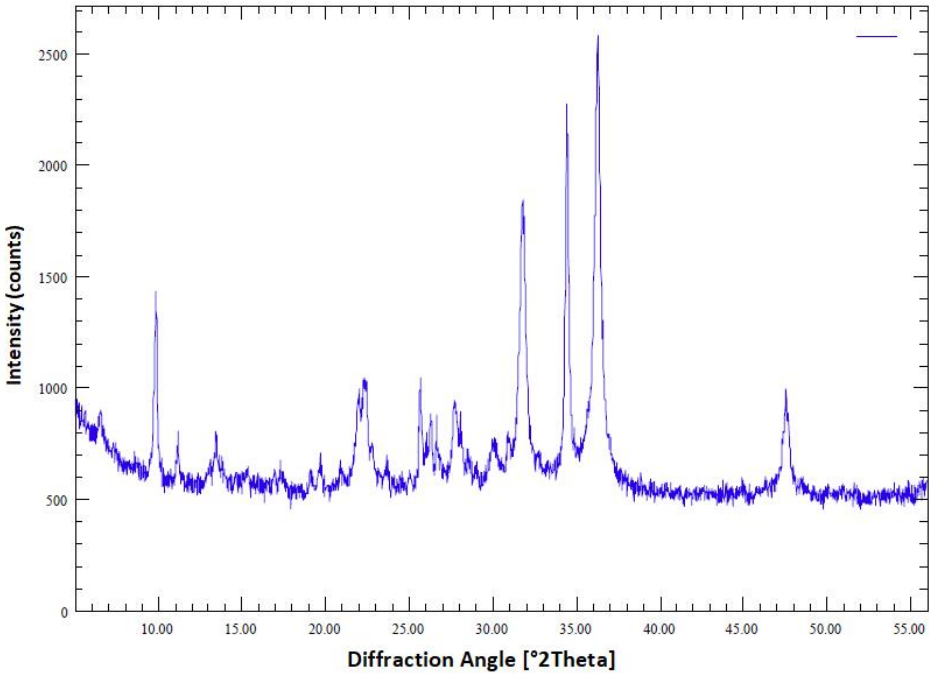

FIGURE 4. XRD of ZnO-Zeolite nanocomposite.

ZnO photocatalysts will directly degrade pollutants on the surface of the zeolite adsorbent.

The photodegradation process was applied by using three different materials in different irradiation conditions. Figures 5–7 below shows a graph comparing the decrease in the procion red dye concentration by using nanocomposite of ZnO-Zeolite, ZnO, and synthetic zeolite under three different exposure conditions, the sunlight, UV light, and in dark conditions.

The results of the photodegradation using nanocomposite and ZnO under the sunlight showed the highest photodegradation percentage of procion red as compared to the photodegradation application under the UV light and dark conditions. As shown in Figure 5, the procion red dye showed the highest degradation rate by using nanocomposites under the sunlight.

During 5 minutes of degradation by using nanocomposites, the concentration of procion red dye under sunlight has decreased by 24.5 %, by 18 % under the UV lamps, and in the dark conditions, the concentration decreased by 17 %. During 15, 25 and 30 minutes of degradation, it was seen that the degradation of procion red under the UV light was higher than that of sunlight, this was due to the intensity of sunlight that was changing over the time, due to this, it was possible that the sun's intensity was decreasing or lower so the removal of colour substances also decreased.

After degrading under the sunlight for 30 minutes, the percentage of degradation was 70 % and had reached 91 % at 60 minutes of degradation. Degradation under the sunlight for 120 minutes resulted in the highest percentage of degradation of procion red, 98.24 %, meanwhile, in the case of the UV lamp, the degradation percentage was 90.42 %. The lowest degradation percentage of only 28.56 % was obtained in the dark conditions. As can be seen in the Figure 5, the degradation of procion red in the dark conditions by using ZnO-Zeolite nanocomposite showed no significant increase after 60 minutes, indicating the possibility that the zeolite adsorbent could have become saturated over time.

Degradation by using only ZnO also showed a similar result. Based on Figure 6, it can be noticed that the highest decrease in procion red concentration was obtained with radiation from the sunlight. However, for 20, 25, and 30 minutes, the UV lamp degradation shows higher results than under the sunlight, this is also due to the intensity of sunlight, which is not constant changes over time and at that time, the intensity of sunlight was low, thus reducing the degradation process. For 120 minutes, the percent degradation of procion red under the sun has reached 97.65 %, for UV lamp, it reached 80.64 %, and in the dark conditions it was still low, only 35.57 %.

ZnO-Zeolite nanocomposite and ZnO can decompose procion red dye using either a direct exposure to the sunlight or by using the UV lamp. This is because the ZnO-Zeolite nanocomposite and ZnO only, work based on the photocatalytic mechanism. These results are also reported from the research conducted by [18], which states that the differences in light sources also have an impact on the photocatalytic process. The photocatalytic process occurs under ultraviolet light (UV lamp) and the sun as the light source.

The sunlight can produce the highest percentage of degradation because the intensity of the light produced is very high. The sun's intensity is much greater than the UV rays. Energy from the sunlight produces the highest percentage not because it is better than

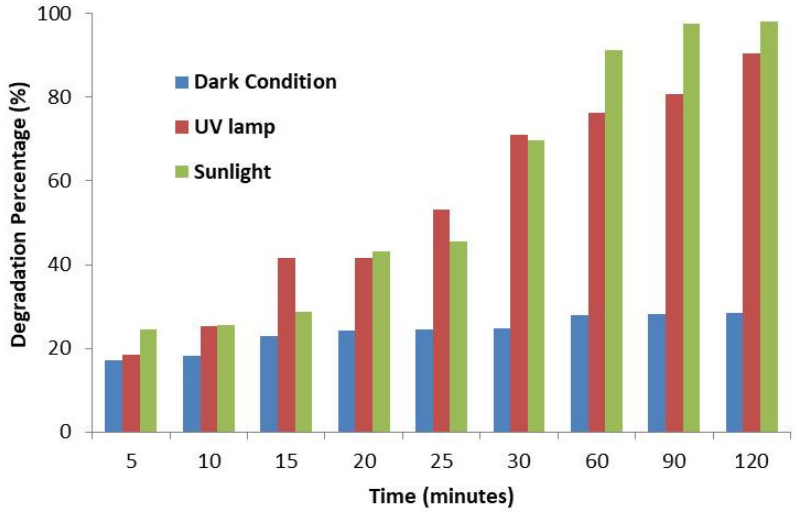

Figure 5. Effect of irradiation sources on degradation percentage of 50 mg/l procion red by using ZnO-Zeolite nanocomposite.

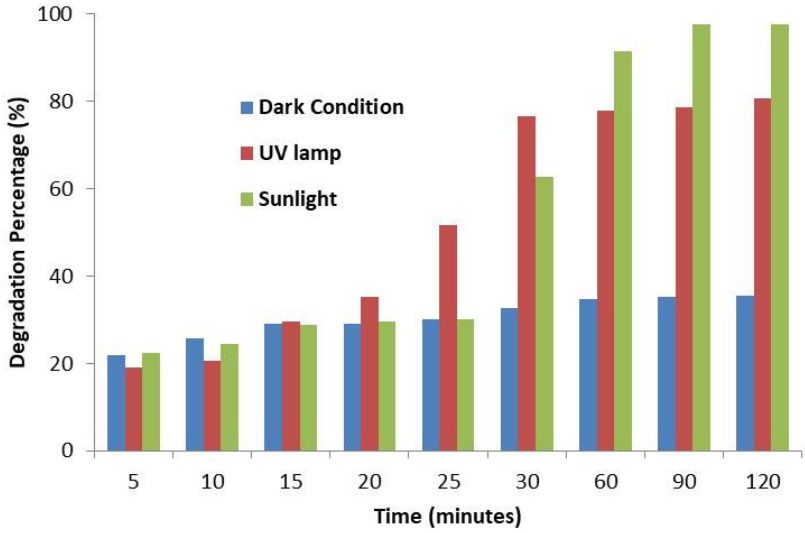

Figure 6. Effect of irradiation sources on degradation percentage of 50 mg/l procion red by using only ZnO.

the UV light, but because the energy from the sunlight is much higher than from the UV light installed in the reactor. The wavelength of sunlight is polychromatic, the sunlight has a wide range of wavelengths from ultraviolet light to infrared light, while the UV light is monochromatic, meaning that the range of wavelengths is narrower.

The photocatalytic process is yields better results using sunlight as a light source as compared to UV lamps. This is due to the fact that the sunlight has more energy than ultraviolet light, meaning a higher electron excitation takes place [18]. The sunlight has a greater light intensity than the UV light. The sunlight also has a wider wavelength, resulting in the highest reduction in dye concentration [17].

Research by [2] also reached similar results, namely that the percentage of dye degradation in the sunlight was higher than for the ultraviolet light, or the conditions without any light. The greater the sunlight intensity, the easier the photocatalytic process runs, so the percentage of dye degradation will be higher as well. The sunlight causes an even greater rate of decomposition of the dye. Electrons can be excited to a higher energy level due to the energy emitted by light both by sunlight and UV rays [19].

In this study, photodegradation was carried out between 11.00 am–1.00 pm, during hot conditions, or when the measurement results of light intensity by the luxmeter are very high. In that time frame, the highest light intensity measurement results were obtained, around or more than 100 000 lux. The results have shown that the highest average light intensity is at 12.00 am–1.00 pm. The large number of active photocatalysts exposed to visible light enhances the formation of hydroxyl radicals for the photodegradation process [20].

The photodegradation mechanism of sunlight and UV rays is different, the percentage degradation of

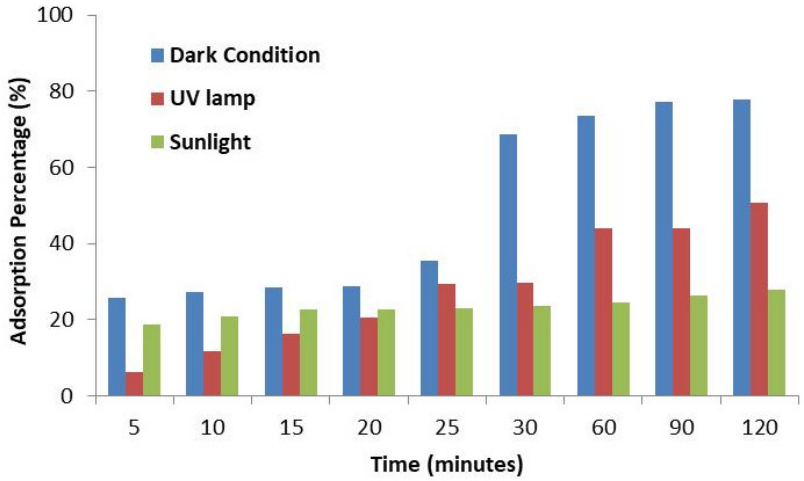

FIGURE 7. Effect of irradiation on adsorption percentage of 50 mg/l procion red by using synthetic zeolite.

the sun is higher than that of UV light. The sunlight provides a lot of visible light irradiation and its photodegradation uses the ultraviolet light mechanism and the visible light mechanism, whereas the UV light only uses the ultraviolet light mechanism [21]. Photon energy from the UV light makes the percentage of degradation increase, this is also due to the excitation of electrons and the formation of hydroxyl radicals.

The results of degradation in dark condition are not significant, because in dark conditions, there are no photons that can activate the ZnO or ZnO-Zeolite nanocomposite, so there were no hydroxyl radicals formed which are strong oxidizers for the photodegradation process of procion red. When it is dark, the degradation process happens only due to the entrapment process carried out by zeolite particles.

In dark conditions, there is no light that will help the ZnO photocatalysts to produce hydroxyl radicals that can degrade dyes, so the photocatalytic process does not run optimally, this is the reason why the degradation results of using nanocomposite and ZnO in the dark conditions are so unsatisfying. The ZnO-Zeolite nanocomposite can still degrade procion red dye even in dark conditions due to the dye adsorption process carried out by synthetic zeolite, but the results are still not optimal because they are not assisted by the ZnO photocatalytic process.

In the ZnO-Zeolite nanocomposite degradation, the ZnO photocatalyst plays a more important role as well, because in terms of its sustainability, the catalyst can be used continuously, and its sustainability is more guaranteed than that of the adsorbent. When using zeolite adsorbent, after the dye is absorbed, the adsorbate can become saturated and can no longer serve as an adsorbent. A longer degradation time will result in the zeolite getting saturated and the semiconductor photocatalyst ZnO itself then becomes responsible for the degradation of the dye.

Figure 7 shows the effect of irradiation on the adsorption percentage of procion red dye by using only synthetic zeolite. The adsorption of procion red showed that the highest yield was obtained in dark conditions. Meanwhile, the percentage of dye removal by using UV lamp and under the sunlight were 29.73 % and 23.74 %, respectively.

After 120 minutes, the adsorption in dark conditions reached an adsorption percentage of 78 %, 50.64 % for the UV lamp, and 27.91 % for the sun. After 90 minutes, the percent adsorption by synthetic zeolite did not increase anymore, this was due to the adsorption process of procion dye was only made by synthetic zeolite adsorbent, so which could have become saturated.

The adsorption percentage by using the synthetic zeolite under the sunlight and the UV light is lower than in the dark conditions because the adsorption process of procion red dye, unlike in the case of ZnO and nanocomposites, works based on the photocatalytic method that requires the light. The dye concentration decreasing was due to the adsorption process of the dye by the synthetic zeolite. The adsorption percentage by using the synthetic zeolite is quite low due to the fact that the adsorption process is only made by the zeolite adsorbent, for which the adsorption process occurs only at the surface. Meaning the larger the surface area of the zeolite is, the more dye is adsorbed [22].

The ZnO-Zeolite nanocomposite gave the highest photodegradation percentage as compared to using ZnO and synthetic zeolite, this is because they not only use the dye adsorption process by synthetic zeolite, but are also aided by the ZnO semiconductor presence in the ZnO-Zeolite nanocomposite. The effect of zeolite is also increased under the sunlight or UV light.

3.3. Types of adsorption isotherm for degradation of ZnO-Zeolite nanocomposite

The adsorption process carried out in dark conditions by using ZnO-Zeolite nanocomposite provided data

	C_e [mg/l]	q_e	$\ln q_e$	$\ln C_e$	C_e/q_e
50	33.56	4.11	1.41	3.51	8.18
100	81.31	4.67	1.54	4.44	18.21
150	128.12	5.47	1.69	4.91	24.77
200	176.53	5.87	1.77	5.24	32.14
250	227.25	5.69	1.73	5.47	41.69

Table 1. Calculation of the values of q_e, C_e/q_e, $\ln q_e$, and $\ln C_e$ for Freundlich and Langmuir Isotherms.

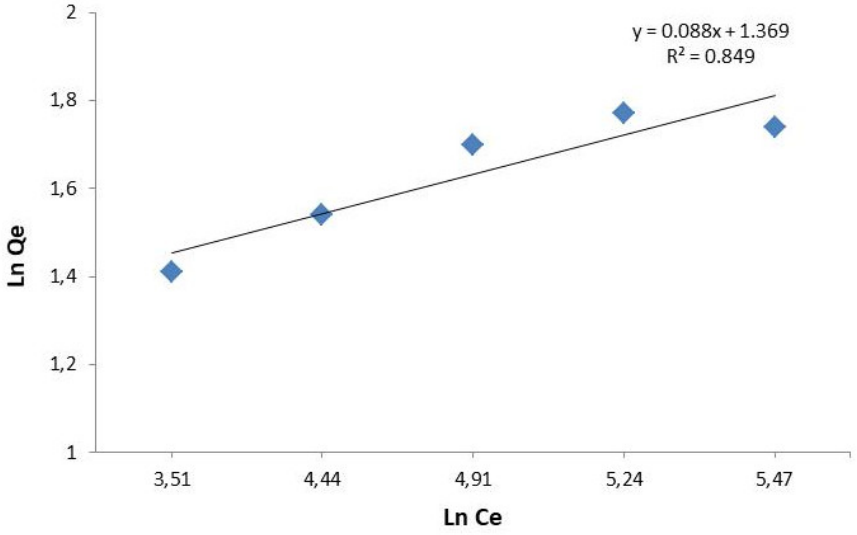

Figure 8. Freundlich Isotherm Graph.

on the degradation results of the procion red dye in the form of the adsorption value and the final concentration of the dye. Experiments in dark conditions were carried out without turning on the UV lamp and closing the reactor using a black plastic coated box.

The interaction between the adsorbent and the adsorbate was described in several types of adsorption isotherms. This adsorption isotherm will show the maximum capacity of the adsorbent [23]. The results were then analysed using the adsorption isotherm equation. The suitable type of adsorption isotherm for the adsorption process of procion red dye by ZnO-Zeolite nanocomposite was determined using the Langmuir and Freundlich equations. These equations are very well known and applicable [23].

In wastewater treatment, Freundlich and Langmuir isotherm equations are the most used. The calculation results of each type were plotted on the graph and the most suitable ZnO-Zeolite nanocomposite adsorption isotherm was be confirmed. The adsorption process of the adsorbent against the adsorbate and the maximum capacity of the adsorbent can be specified by determining the appropriate type of adsorption [24].

The adsorption process of ZnO-Zeolite nanocomposite was applied by varying the dye concentration during the degradation time of 60 minutes. The value of procion red dye concentration was set to 50, 100, 150, 200, and 250 mg/l.

The values of q_e, C_e/q_e, $\ln q_e$ and $\ln C_e$ were calculated to be included in the Langmuir and Freundlich isotherm equations and are presented in Table 1. The q_e value is obtained from the following Equation (5):

$$q_e = \frac{(C_0 - C_e) \times V}{W}. \tag{5}$$

Plotting the values for C_e/q_e and C_e will yield the Langmuir equation and plotting $\ln q_e$ versus $\ln C_e$ will yield the Freundlich equation.

3.4. Freundlich isotherm

A good linearization graph and the value of the coefficient of determination $R^2 \geq 0.9$ (close to 1) show the corresponding adsorption isotherm equation. Figure 8 demonstrates the relationship between $\ln q_e$ and $\ln C_e$ in the Freundlich isotherm equation. Based on the graph, an equation in the form of a linear equation $y = 0.088x + 1.369$ and the value of $R^2 = 0.849$ were obtained. The linear equation of the Freundlich isotherm graph fulfils Equation (6) and gives a constant K_f value of 3.933, a value of $1/n$ of 0.088 and an n value of 11.403.

$$\ln q_e = \ln K_f + \frac{1}{n} \ln C_e. \tag{6}$$

K and $1/n$ are Freundlich constants indicating the rate of adsorption and heterogeneity factors. Freundlich described a heterogeneous adsorption system.

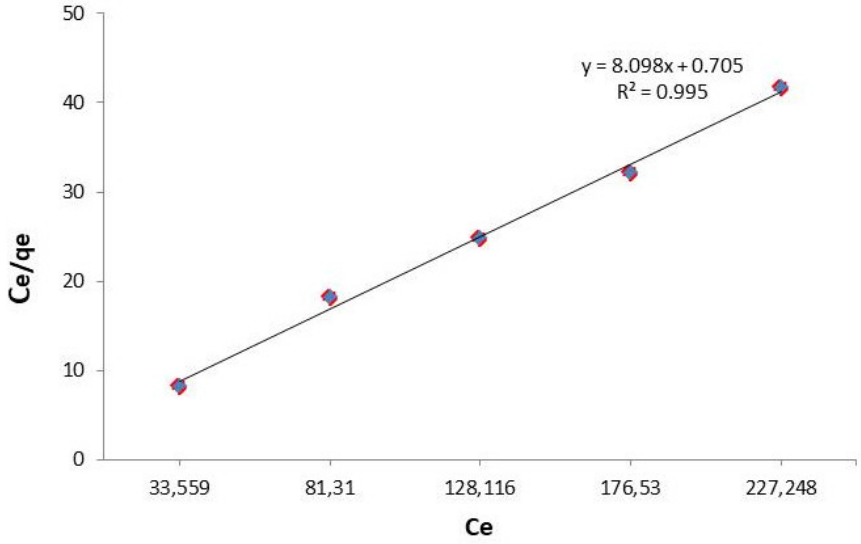

FIGURE 9. Langmuir Isotherm Graph.

The value of K_f (mg/g) also indicates the power or the maximum adsorption capacity of the material. The value of $1/n > 1$ explains that the saturation of the adsorbent is not achieved; on the contrary, when $1/n < 1$, the adsorbent has been saturated by the adsorbate molecules, this happens more in the adsorption system [24].

Isoterm Langmuir	Isoterm Freundlich
$R^2 = 0.995$	$R^2 = 0.849$
$b = 11.488\,\mathrm{L/mg}$	$n = 11.403$
$a = 0.124\,\mathrm{mg/g}$	$K_f = 3.933\,\mathrm{mg/g}$

TABLE 2. Adsorption Isotherm Parameters.

3.5. LANGMUIR ISOTHERM

The Langmuir isotherm equation is illustrated in Figure 9, which shows the C_e/q_e and C_e relationship curves for the Langmuir isotherm. The Langmuir graph produces the linear equation of $y = 8.098x + 0.705$ an $R^2 = 0.995$.

$$\frac{C_e}{q_e} = \frac{1}{a.b} + \frac{1}{a}C_e. \tag{7}$$

The linear equation of the Langmuir isotherm graph follows the Equation (7) and gives a constant value of b of 11.488 l/mg and a of 0.124 mg/g. The value of b is the Langmuir equilibrium constant or constant (l/mg) and the value of a is the maximum concentration value in the solid phase (mg/g), which can also indicate the maximum adsorption capacity of the material.

Table 2 shows the adsorption isotherm parameters for both types of adsorption isotherms. Based on the Langmuir and Freundlich graphs, the adsorption isotherm equation that is suitable for the process of degradation of the procion red dye with ZnO-Zeolite nanocomposites is the Langmuir adsorption equation with an R^2 value of 0.995, while the Freundlich isotherm equation does not meet the requirements, because the coefficient of determination R^2 is 0.849.

This is also similar to [2] research, where the dye adsorption isotherm pattern carried out by the ZnO-Zeolite composite follows the Langmuir isotherm, and from the graph, it can be seen that it produces a coefficient of determination R^2 that is close to 1 (0.94) as compared to the isotherm. Freundlich does not comply because the value of $R^2 = 0.1$. The research of [24] also conducted a similar study and obtained the highest correlation coefficient (R^2) value found in the Langmuir isotherm, this indicates that the adsorption of liquid waste follows a Langmuir isotherm approach.

This shows that the adsorption of procion red dye by using ZnO-Zeolite nanocomposite is more appropriate and in accordance with the Langmuir adsorption isotherm type, as evidenced by the value of the correlation coefficient (R^2) which is closer to 1 as compared to the Freundlich isotherm type, so it can be assumed that the adsorbed dye or adsorbates are adsorbed in a single form (monolayer) and the adsorption process of procion red dye by using ZnO-Zeolite nanocomposite is a homogeneous one. However, Freundlich isotherm type describes a multilayer adsorption process and involves more physical interactions [3].

4. CONCLUSIONS

Photodegradation application by using ZnO-Zeolite nanocomposite produced a higher decomposition percentage of the procion red dye under the sunlight as compared to UV light and in the dark condition. The highest degradation percentage was 98.24 % by irradiation under the sunlight for 120 minutes. The photodegradation process of procion red dye using the ZnO-Zeolite nanocomposite followed the Langmuir

adsorption isotherm pattern with the linear equation $y = 8.098x + 0.705$, the coefficient of determination $R^2 = 0.995$, Langmuir constant value b of 11.488 l/mg, and a maximum adsorption capacity a of 0.124 mg/g.

List of symbols

C_e Equilibrium concentration [mg/l]
C_o Concentration of initial pollutants [mg/l]
q_m The adsorption capacity at maximum
q_e Amount of adsorbate at equilibrium [mg/g]
V Volume of sample [l]
W Adsorbent weight [g]
a Maximum adsorption capacity [mg/g]
b Langmuir constant
K_f, n Freundlich's empirical constant

Acknowledgements

The authors would like to express their gratitude to all parties involved in this research. The authors would also like to thank the Waste Treatment Technology Laboratory of Chemical Engineering Department Universitas Sriwijaya, Integrated Research Laboratory of Postgraduate Universitas Sriwijaya, and Laboratory of Environmental Research Center (PPLH) Universitas Sriwijaya, for the laboratory support.

References

[1] P. Zawadzki, E. Kudlek, M. Dudziak. Kinetics of the photocatalytic decomposition of bisphenol a on modified photocatalysts. *Journal of Ecological Engineering* **19**(4):260–268, 2018. https://doi.org/10.12911/22998993/89651.

[2] P. Zawadzki, E. Kudlek, M. Dudziak. Titanium(IV) oxide modified with activated carbon and ultrasounds for caffeine photodegradation: Adsorption isotherm and kinetics study. *Journal of Ecological Engineering* **21**(8):137–145, 2020. https://doi.org/10.12911/22998993/126985.

[3] M. Ahda, S. Sutarno, E. S. Kunarti. Sintesis silika MCM-41 dan uji kapasitas adsorpsi terhadap metilen biru. *Pharmaciana* **3**(1), 2013. https://doi.org/10.12928/pharmaciana.v3i1.414.

[4] M. T. Adiwibowo, M. Ibadurrohman, Slamet. Synthesis of ZnO nanoparticles and their nanofluid stability in the presence of a palm oil-based primary alkyl sulphate surfactant for detergent application. *International Journal of Technology* **9**(2):307–316, 2018. https://doi.org/10.14716/ijtech.v9i2.1065.

[5] D. A. Wismayanti, N. P. Diantariani, S. R. Santi. Pembuatan komposit ZnO-arang aktif sebagai fotokatalis untuk mendegradasi zat warna metilen biru. *Jurnal Kimia (Journal of Chemistry)* **9**(1):109–116, 2015. https://doi.org/10.24843/JCHEM.2015.v09.i01.p18.

[6] S. Naimah, S. Ardhanie A., B. Jati, et al. Degradasi zat warna pada limbah cair industri tekstil dengan metode fotokatalitik menggunakan nanokomposit TiO_2 – Zeolit. *Jurnal Kimia dan Kemasan* **36**(2):225–236, 2014. https://doi.org/10.24817/jkk.v36i2.1889.

[7] M. O. Ruliza, T. E. Agustina, R. Mohadi. Impregnation of activated carbon-TiO_2 composite and its application in photodegradation of procion red synthetic dye in aqueous medium. *IOP Conference Series: Earth and Environmental Science* **105**:012024, 2018. https://doi.org/10.1088/1755-1315/105/1/012024.

[8] D. A. Wulandari, N. Nasruddin, E. Djubaedah. Selectivity of water adsorbent characteristic on natural zeolite in cooling application. *Journal of Advanced Research in Fluid Mechanics and Thermal Sciences* **55**(1):111–118, 2020.

[9] Jasmal, Sulfikar, Ramlawati. Kapasitas adsorpsi arang aktif ijuk pohon aren (arenga pinnata) terhadap Pb^{2+}. *Sainsmat : Jurnal Ilmiah Ilmu Pengetahuan Alam* **4**(1):57–66, 2015. https://doi.org/10.35580/sainsmat4112842015.

[10] A. Puszkarewicz, J. Kaleta. Adsorption of chromium (VI) on raw and modified Carpathian diatomite. *Journal of Ecological Engineering* **20**(7):11–17, 2019. https://doi.org/10.12911/22998993/108640.

[11] P. Laokul, V. Amornkitbamrung, S. Seraphin, S. Maensiri. Characterization and magnetic properties of nanocrystalline $CuFe_2O_4$, $NiFe_2O_4$, $ZnFe_2O_4$ powders prepared by the aloe vera extract solution. *Current Applied Physics* **11**(1):101–108, 2011. https://doi.org/10.1016/j.cap.2010.06.027.

[12] M. Murtihapsari, B. Mangallo, D. D. Handyani. Model isoterm Freundlich dan Langmuir oleh adsorben arang aktif bambu andong (G. Verticillata (Wild) Munro) dan bambu ater (G. Atter (Hassk) Kurz Ex Munro). *Jurnal Sains Natural* **2**(1):17–23, 2012. https://doi.org/10.31938/jsn.v2i1.31.

[13] R. Gayatri, T. E. Agustina, R. Moeksin, et al. Preparation and characterization of ZnO-Zeolite nanocomposite for photocatalytic degradation by ultraviolet light. *Journal of Ecological Engineering* **22**(2):178–186, 2021. https://doi.org/10.12911/22998993/131031.

[14] A. Salam, T. E. Agustina, R. Mohadi. Photocatalytic degradation of procion red synthetic dye using ZnO-Zeolite composites. *International Journal of Scientific & Technology Research* **7**(8):54–59, 2018.

[15] A. C. Mohan, B. Renjanadevi. Preparation of zinc oxide nanoparticles and its characterization using Scanning Electron Microscopy (SEM) and X-Ray Diffraction (XRD). *Procedia Technology* **24**:761–766, 2016. https://doi.org/10.1016/j.protcy.2016.05.078.

[16] E. Nyankson, J. K. Efavi, A. Yaya, et al. Synthesis and characterisation of zeolite-A and Zn-exchanged zeolite-A based on natural aluminosilicates and their potential applications. *Cogent Engineering* **5**(1):1440480, 2018. https://doi.org/10.1080/23311916.2018.1440480.

[17] T. E. Agustina, E. Melwita, D. Bahrin, et al. Synthesis of nano-photocatalyst ZnO-natural zeolite to degrade procion red. *International Journal of Technology* **11**(3):472–481, 2020. https://doi.org/10.14716/ijtech.v11i3.3800.

[18] A. Rahman, M. Nurjayadi, R. Wartilah, et al. Enhanced activity of TiO_2/natural zeolite composite for degradation of methyl orange under visible light irradiation. *International Journal of Technology* **9**(6):1159–1167, 2018. https://doi.org/10.14716/ijtech.v9i6.2368.

[19] R. Fraditasari, S. Wardhani, M. M. Khunur. Degradasi methyl orange menggunakan fotokatalis TiO_2-N : Kajian pengaruh sinar dan konsentrasi TiO_2-N. *Jurnal Ilmu Kimia Universitas Brawijaya* **1**(1):606–612, 2015.

[20] A. Charanpahari, S. S. Umare, S. P. Gokhale, et al. Enhanced photocatalytic activity of multi-doped TiO_2 for the degradation of methyl orange. *Applied Catalysis A: General* **443-444**:96–102, 2012. https://doi.org/10.1016/j.apcata.2012.07.032.

[21] D. Windy Dwiasi, T. Setyaningtyas. Fotodegradasi zat warna tartrazin limbah cair industri mie menggunakan fotokatalis TiO_2 - sinar matahari. *Molekul* **9**(1):56–62, 2014. https://doi.org/10.20884/1.jm.2014.9.1.150.

[22] I. Kustiningsih, D. K. Sari. Uji adsorbsi zeolit alam bayah dan pengaruh sinar ultraviolet terhadap degradasi limbah methylene blue. *Teknika: Jurnal Sains dan Teknologi* **13**(1):25–32, 2017.

[23] M. Ghosh, K. Manoli, X. Shen, et al. Solar photocatalytic degradation of caffeine with titanium dioxide and zinc oxide nanoparticles. *Journal of Photochemistry and Photobiology A: Chemistry* **377**:1–7, 2019. https://doi.org/10.1016/j.jphotochem.2019.03.029.

[24] D. Darmansyah, S. Ginting, L. Ardiana, H. Saputra. Mesopori MCM-41 sebagai adsorben: Kajian kinetika dan isotherm adsorpsi limbah cair tapioka. *Jurnal Rekayasa Kimia & Lingkungan* **11**(1):10–16, 2016. https://doi.org/10.23955/rkl.v11i1.4228.

EFFECT OF PIGMENTS ON BOND STRENGTH BETWEEN COLOURED CONCRETE AND STEEL REINFORCEMENT

Joseph J. Assaad*, Matthew Matta, Jad Saade

University of Balamand, Department of Civil and Environmental Engineering, Balamand, PO Box 100, Al Kourah, Lebanon

* corresponding author: joseph.assaad@balamand.edu.lb

Abstract. The effect of pigments on mechanical properties of coloured concrete intended for structural applications, including the bond stress-slip behaviour to embedded steel bars, is not well understood. Series of concrete mixtures containing different types and concentrations of iron oxide (red and grey colour), carbon black, and titanium dioxide (TiO_2) pigments are investigated in this study. Regardless of the colour, mixtures incorporating increased pigment additions exhibited higher compressive and splitting tensile strengths. This was attributed to the micro-filler effect that enhances the packing density of the cementitious matrix and leads to a denser microstructure. Also, the bond to steel bars increased with the pigment additions, revealing their beneficial role for improving the development of bond stresses in reinforced concrete members. The highest increase in bond strength was recorded for mixtures containing TiO_2, which was ascribed to formation of nucleus sites that promote hydration reactions and strengthen the interfacial concrete-steel transition zone. The experimental data were compared to design bond strengths proposed by ACI 318-19, European Code EC2, and CEB-FIP Model Code.

Keywords: Coloured concrete, iron oxide pigment, carbon black, titanium dioxide, durability, bond strength.

1. Introduction

Pigments including iron oxide (IO), carbon black (CB), and titanium dioxide (TiO_2) are finely ground particles for integral colouring of concrete and cementitious materials intended for architectural applications [1–3]. Often manufactured as per ASTM C979 [3] specification, the pigments are bound onto the surface of cement grains, thus altering the colour characteristics by absorbing certain wavelengths of the visible light and reflecting others. The IOs are synthetic colourants manufactured to display a variety of colours (i.e., red, grey, yellow, etc.), thus infusing the concrete with their shades [4, 5]. These pigments are stable in the high-alkaline Portland cement environment, conferring proper colour fastness to sunlight exposure and resistance to weathering effects. The CB is an economical black colourant with high tinting strength produced from petroleum and charring organic materials [1, 6]. Compared to IO, the CB generally disrupts the air-entrainment and increases the vulnerability of concrete to leaching when exposed to repeated wet/dry cycles [6]. The white-coloured TiO_2 mostly occurs in the natural rutile and anatase crystal forms [7, 8]; it is normally used with white cement and other pozzolanic materials (metakaolin) to brighten the cementitious mixture.

Earlier studies showed that the pigment characteristics (i.e., type, fineness, mineralogy, morphology, solubility, etc.), additions rates, and dispersion can drastically alter the fresh and hardened concrete properties [9–11]. For instance, it is accepted that pigments absorb part of the free mixing water because of a significantly higher surface area (vs. cement), thus requiring increased water demand and/or high-range water reducer (HRWR) to achieve a given workability [12–14]. Meng et al. [15] reported that the drop in fluidity due to TiO_2 can be controlled through HRWR and slag additions. If poorly dispersed, added pigments may agglomerate in the cement matrix, causing unreacted pockets or weak zones that decrease mechanical properties [15, 16]. Lopez et al. [17] suggested using the mortar phase, while others recommended the use of extended mixing time [18] or water-based colourants [19] to improve pigment dispersibility.

Despite their chemically inert nature, most studies showed that synthetic IO and CB pigments lead to increased strength and durability of cementitious materials. This is generally associated to a micro-filler effect that blocks the capillary pores and leads to a denser microstructure [9, 20, 21]. Yildizel et al. [22] found that yellow and black IOs lead to increased strength and resistance to water permeability. Mortars produced using red pigments exhibited relatively higher pore ratios, which detrimentally affected freeze/thaw resistance and durability. Assaad et al. [11] reported that strength and bond to existing substrates increased when red or yellow pigments are incorporated by up to 6 % of cement mass. The curtail in strength at high pigment rates (above 6 %) was related to improper hydration reactions resulting from the excessive amount of powders that are adsorbed onto the cement grains. Masadeh [23] found that

Physical properties	Specific gravity	Median particle size	Soundness	Blaine fineness	Lightness (L-value)
	3.15	26.5 µm	0.04 %	3150 cm^2/g	88.5
Chemical properties	CaO	SiO_2	Al_2O_3	Fe_2O_3	MgO
	68.5 %	21.8 %	4.15 %	0.27 %	1.18 %

TABLE 1. Physical and chemical properties of white cement.

CB incorporated up to 0.5 % of cement mass reduces the concrete chloride permeability and corrosion rates of inserted steel bars. Inoue et al. [24] noted that the CB treatment using aqueous solution of humic acids helps improving the dispersibility together with a reduced interaction with air-entraining surfactants and superior adhesion to the cement matrix (i.e., less leaching).

In addition to the micro-filler effect, numerous researchers found that TiO_2 can participate in the cement hydration process, at least as nucleation sites, to accelerate setting times and promote strength development [15, 16, 25, 26]. Chen et al. [27] showed that concrete durability and resistance to water infiltration significantly improved with 3 % TiO_2 additions, given the conversion of greater volume of calcium hydroxide (CH) crystals into C-S-H gels. Zhang et al. [28] reported that TiO_2 acts as a filler in empty spaces and crystallization centre of CH to refine the concrete microstructure including its resistance to chloride ion penetration. Folli et al. [29] speculated that the strength improvement might be related to alteration in packing density and nucleus orientation around the interfacial transition zones, rather than increased amounts of hydration products.

2. Context and paper objectives

The performance of coloured concrete in structural members, including the extent to which the use of pigments would alter the bond strengths to embedded steel bars, is not well understood. Generally, the transfer of stresses between the reinforcement and surrounding concrete is attributed to chemical adhesion and mechanical bearing arising from the concrete surface around the steel ribs [30, 31]. The parameters affecting the bond are broadly related to the reinforcement characteristics (i.e., yield strength of bar, size, geometry, epoxy coating, cover, position in cast member, etc.) and concrete constituents and properties (i.e., density, strength, workability, presence of fibres, mineral admixtures, etc.) [32]. The spliced or developed lengths are computed by relevant models proposed by various building codes; for example, ACI 318-19 [33] considers that the development length for deformed bars in tension members is inversely proportional to the square root of compressive strength, multiplied by specific factors to account for special considerations due to the reinforcement size, lightweight concrete, top bars, epoxy-coated bars, and contribution of confining transverse reinforcement. Yet, limited attempts have been made to assess the validity of existing models and design provisions in the case of coloured concrete.

This paper is a part of a comprehensive research project undertaken to assess the effect of pigments on durability and mechanical properties of coloured concrete mixtures. Two concrete series made with 350 and 450 kg/m^3 cement content and various concentrations of IO (red or grey colour), CB, and TiO_2 pigments are investigated. Tested properties included the compressive strength, splitting tensile strength, modulus of elasticity, and bond stress-slip behaviour to reinforcing steel bars. The experimental data were compared to design bond strengths proposed by relevant building codes including ACI 318-19 [33], European Code EC2 [34], and CEB-FIP Model Code [35]. Data reported herein can be of interest to civil engineers and architects seeking the use of pigments in coloured concrete intended for structural applications.

3. Experimental program

3.1. Materials

White-coloured Portland cement conforming to ASTM C150 Type I was used in this study. Its physical and chemical properties are listed in Table 1.

The gradations of siliceous sand and crushed limestone aggregate were within the ASTM C33 specifications. The specific gravity for the sand, fineness modulus, and absorption rate were 2.65, 3.1, and 0.75 %, respectively. Those values were 2.72, 6.4, and 1 %, respectively, for the coarse aggregate, while the nominal maximum particle size was 20 mm. Naphthalene-based HRWR was used; its specific gravity, solid content, and maximum dosage rate were 1.2, 40.5 %, and 3.5 % of cement mass, respectively.

Commercially available IO (i.e., red and grey colour), CB, and TiO_2 pigments were used. As shown in Figure 1, the red and grey coloured IOs had almost spherical shapes; their specific gravities were 4.64 and 4.8, respectively, while their Fe_2O_3 contents were 97.5 % and 98.8 %, respectively. The white-coloured TiO_2 is rutile-based manufactured by the chloride process; it also possesses round shape (Figure 1) with a specific gravity of 4.1. The CB is produced by combustion of aromatic petroleum oil feedstock and consists essentially of pure carbon (i.e., > 98 %); its specific gravity was 2.05.

The particle size gradation curves obtained by laser diffraction for the various pigments are plotted in

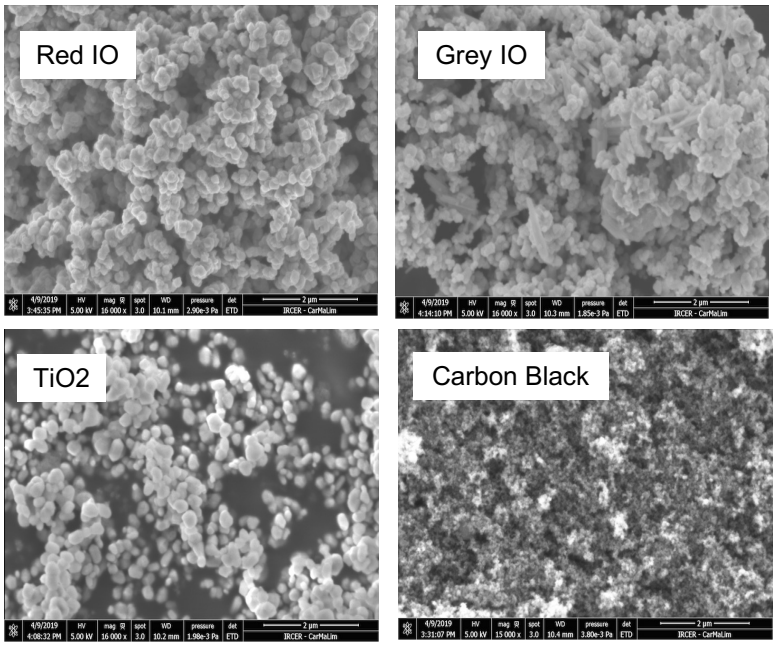

FIGURE 1. Morphology of various pigments used.

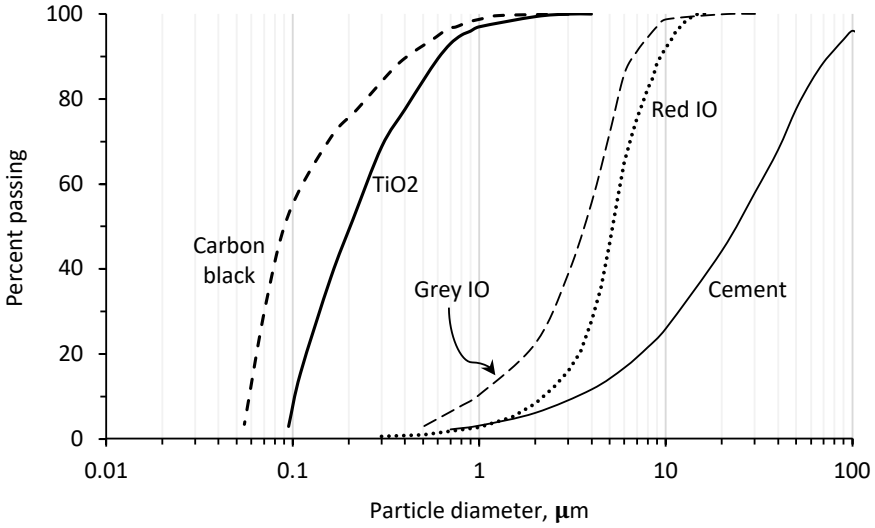

FIGURE 2. Particle size distribution curves for the cement and various pigments.

Figure 2. Generally speaking, the fineness of IO pigments is pretty close to each other; the median diameter (d_{50}) computed as the size for which 50 % of the material is finer for the grey and red IO is 4.1 and 5.3 µm, respectively. The TiO_2 and CB were remarkably finer, which shifted the gradation curves towards much smaller particle sizes. The resulting d_{50} dropped to 0.21 and 0.092 µm for the TiO_2 and CB, respectively.

Deformed steel bars complying to ASTM A615 No. 13 were used in this work to evaluate the effect of pigments on bond stress-slip properties of coloured concrete to embedded rebars. The bar nominal diameter (d_b), Young's modulus, and yield strength (f_y) were 12 mm, 205 GPa, and 520 MPa, respectively.

3.2. MIXTURE PROPORTIONS

Two control concrete mixtures containing 350 (or, 450) kg/m^3 cement with 0.5 (or, 0.42) water-to-cement ratio (w/c) were considered; the corresponding 28-days $f'c$ was 26.7 and 34.2 MPa, respectively. The fine and coarse aggregate contents in the lean concrete mixture were 830 and 1020 kg/m^3, respectively; while these were 790 and 925 kg/m^3 in the higher strength concrete mix. The resulting sand-to-total aggregate ratio was 0.45. The HRWR dosage was either 2.6 % or 2.35 % of cement mass, respectively, in order to secure a fixed workability corresponding to a slump of 210 ± 10 mm.

The IO, CB, and TiO_2 pigments were incorporated at three different concentrations varying from 1.5 % to 4.5 % of cement mass, at 1.5 % increment rates. The

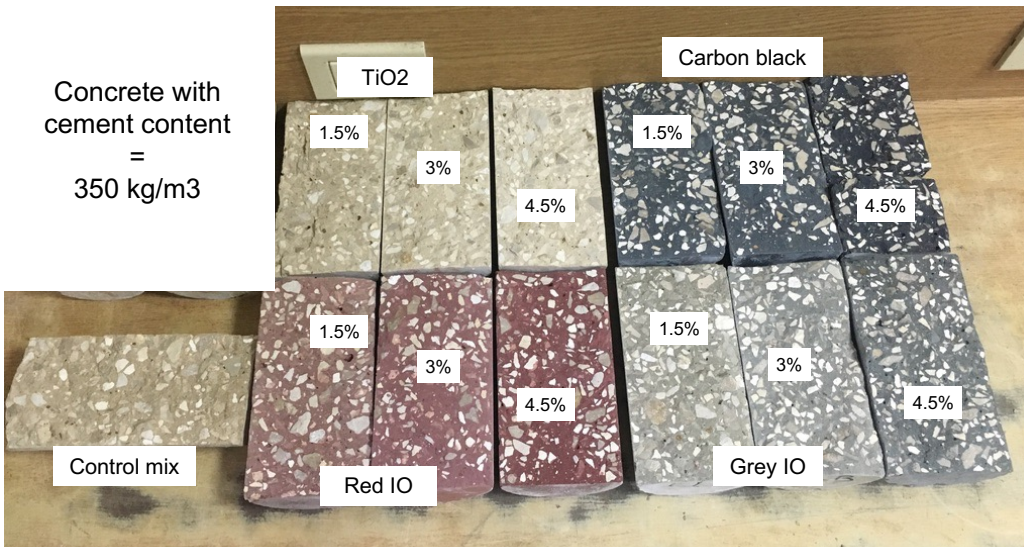

FIGURE 3. Photo of coloured cylinders after the splitting tensile test.

mixing sequence consisted on homogenizing the fine aggregate, coarse aggregate, and powder pigment for 3 minutes to ensure efficient dispersion of colourant materials. The cement, water, and HRWR were then sequentially introduced over 2 minutes. After 30 sec rest period, the mixing resumed for 2 more minutes. The ambient temperature and relative humidity (RH) remained within $23 \pm 3\,°C$ and $55 \pm 5\,\%$, respectively.

3.3. Testing procedures

3.3.1. Fresh and hardened properties

Right after mixing, the workability and air content were determined as per ASTM C143 and C231, respectively. The concrete was cast in 100×200 mm cylinders to determine the density, compressive strength ($f'c$), and splitting tensile strength (ft) as per ASTM C642, C39, and C496, respectively [36–38]. All specimens were demoulded after 24 hours, cured in water, and tested after 28 days. Averages of 3 values were considered. The modulus of elasticity (E) was determined through ultrasonic pulse velocity (UPV) measurements using 100×200 mm concrete cylinders, as per ASTM C597 [39]. The pulse velocity was computed as the ratio between the 200 mm length of the concrete specimen to the measured transit time. The E was computed using the conventional wave propagation equation in solid rocks, expressed as: $E, GPa = [(\rho \times UPV^2)/g]\,10^{-2}$, where g is gravity acceleration (9.81 m/s^2) and ρ is the concrete density (kg/m^3) [1, 31].

3.3.2. Colourimetry

The L, a, and b colour coordinates were determined following the Commission Internationale d'Eclairage (CIE) system using a portable colourimeter. The L-value reflects the colour lightness varying from 0 (black) to +100 (white), a-value represents the chromatic intense of magenta/red (+127) and green (–128), and b-value the chromatic intense of yellow (+127) and blue (–128) [19, 40]. The specimens were oven-dried for one day at $50 \pm 5\,°C$ prior to testing. The measurements were realized using the broken cylinders after the tensile splitting test, as shown in Figure 3. Special care was taken to position the colourimeter sensor in the mortar phase (not the aggregate particle); while an average of 6 measurements was considered. The colour deviation ($\Delta(E)$) due to pigment additions from the control mix was determined as:

$$\Delta(E) = \sqrt{(L_C - L)^2 + (a_C - a)^2 + (b_C - b)^2},$$

where $L_C = L_{Control}$, $a_C = a_{Control}$, $b_C = b_{Control}$.

3.3.3. Bond to steel reinforcement

The direct bond method was used to determine the bond stress-slip properties of concrete mixtures, in accordance with RILEM/CEB/FIB specification [41]. The bars were vertically centred in the 150 mm cubic moulds (Figure 4); the embedded length was 60 mm (5 d_b) and PVC bond breaker was inserted around the bar at the concrete surface to reduce the concentration of stresses during loading. After 24 hours from casting, the specimens were demoulded and covered with plastic bags to cure at 23 ± 3°C for 28 days. The direct bond test was realized using a universal testing machine, whereby the pullout load and slips of the steel bar relative to the concrete block are recorded [30, 42]. The tensile load was gradually applied until failure at a rate hovering 0.25 kN/sec.

4. Test results and discussion

4.1. HRWR demand

Table 2 summarizes the HRWR demand and colour coordinates for mixtures prepared with various pigment types and concentrations. In line with current literature [1, 4, 8], the demand for HRWR increased with pigment additions, given their higher fineness

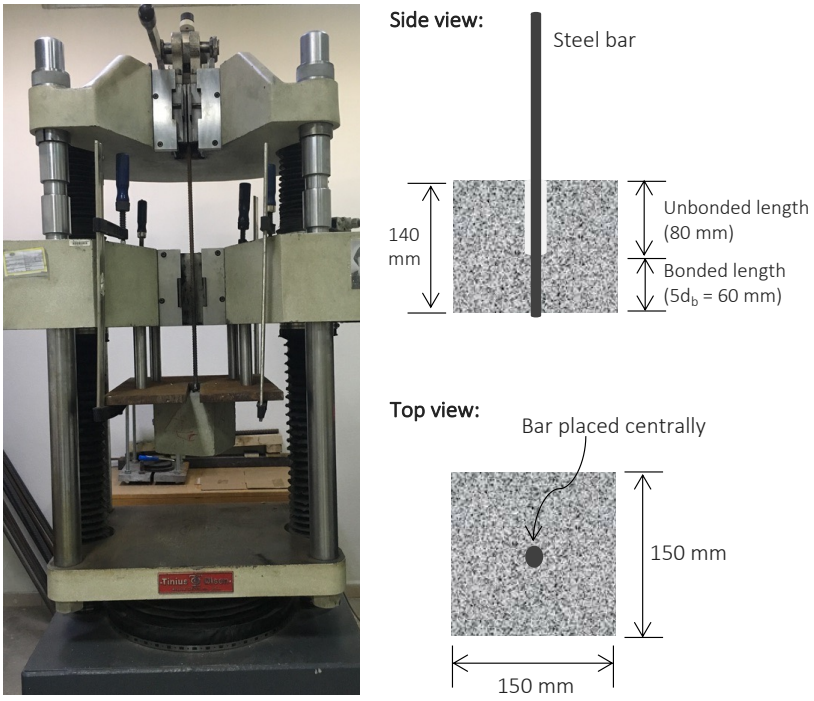

FIGURE 4. Photo of the experimental testing of bond stress-slip properties.

Mixture codification	HRWR [% of cement]	Slump [mm]	Air content [%]	Density $[kg/m]^3$	L	a	b	$\Delta(E)$
350-Control	2.6	205	2.8	2320	67.8	5.6	19.3	–
350-Red-1.5 %	2.6	205	n/a	2315	55.2	12.8	12.9	15.8
350-Red-3 %	2.9	200	2.7	2330	51.9	16.1	10.6	21.0
350-Red-4.5 %	3.2	200	2.9	2375	44.4	19.8	12	28.3
350-Grey-1.5 %	2.7	195	n/a	2330	61.9	2.2	12.4	9.6
350-Grey-3 %	2.9	205	3.1	2360	58.4	0.8	7.2	16.0
350-Grey-4.5 %	3.1	205	n/a	2350	49.4	-0.1	4.0	24.6
350-TiO2-1.5 %	2.7	210	n/a	2310	72.0	5.3	19.8	4.3
350-TiO2-3 %	3.0	210	3	2340	71.9	5.4	19.7	4.2
350-TiO2-4.5 %	3.1	195	2.9	2380	76.3	4.4	17.9	8.7
350-CBlack-1.5 %	2.9	190	n/a	2350	42.4	-0.2	-0.2	32.5
350-CBlack-3 %	3.5	195	3.2	2340	42.2	-0.5	-0.7	33.0
350-CBlack-4.5 %	3.6	205	3.4	2390	31.0	-0.05	-1.2	42.4
450-Control	2.4	205	3	2345	68.3	5.7	19.1	–
450-Red-3 %	2.5	210	3.1	2385	48.8	19.0	10.8	25.0
450-Grey-3 %	2.8	200	3	2385	56.2	0.58	6.9	17.9
450-TiO2-3 %	2.7	200	2.8	2405	77.1	5.1	19.1	8.9
450-CBlack-3 %	3.2	205	3.5	2415	41.9	-0.4	-0.8	33.6

The mix codification refers to cement content-Pigment type-Pigment dosage.
n/a refers to not tested.

TABLE 2. Effect of pigment types and concentrations on workability and colourimetry properties.

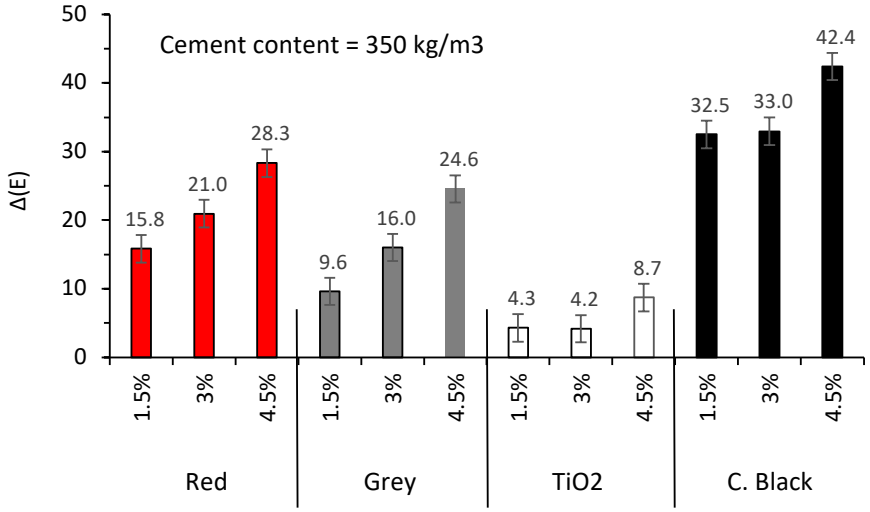

FIGURE 5. Effect of pigment type and concentration on $\Delta(E)$ variations for concrete prepared with 350 kg/m^3 cement.

that absorbs part of the mixing water and results in requirement of additional superplasticizing molecules to ensure the targeted slump of 210 ± 10 mm. For example, at a 3 % pigment rate, the HRWR dosage varied from 2.6 % for the 350-Control mix to 2.9 % and 2.85 % for the 350-Red-3 % and 350-Grey-3 % mixtures, respectively. The increase in HRWR was particularly pronounced for the CB pigment, given its extremely fine particles [13]. Hence, the HRWR reached 3.45 % and 3.6 % for the concrete containing 3 % or 4.5 % CB, respectively.

4.2. Colourimetry

As can be noticed in Table 2, the lightness of colour (L-value) increased from 67.75 for the 350-Control mix to 72 and 76.3 with the addition of 1.5 % and 4.5 % TiO_2, respectively, which can be attributed to the intrinsic white-coloured nature of this pigment [26, 29]. Yet, as expected, the L-value followed a decreasing trend when darker pigments were used; it dropped to 49.35, 44.35, and 31 for mixtures containing 4.5 % grey, red, and CB pigments, respectively. To the other end, the magenta chromatic intense (i.e., a-value) varied from 5.55 to 16.1 for the 350-Control and 350-Red-3 % mixtures, respectively, while in contrast, the highest b-value of 19.75 corresponded to the 350-TiO2-1.5 % mix. Concrete mixtures prepared with CB exhibited negative a and b values, reflecting the black colouring effects of such powders.

As shown in Figure 5, the mixtures containing the white-coloured TiO_2 pigments exhibited the lowest $\Delta(E)$ values, reflecting relatively limited variations with respect to the control mix. The incorporation of red or grey IO pigments gradually increased the $\Delta(E)$ values that varied from 9.6 to 28.3, while the CB-modified mixtures exhibited the highest $\Delta(E)$ that varied from 32.5 to 42.4. It should be noted that $\Delta(E)$ steadily increased with pigment additions (Figure 5), without showing a clear stabilization tendency that reflects colour saturation [11, 17]. This can be attributed to the relatively reduced cement volume (i.e., about 11 % of the overall concrete mix), thus requiring additional pigment powders to achieve colour saturation. Additionally, the beige-like colour of natural sand could have affected the pigment tinting strength, which reduced the tendency towards the colour saturation [10, 11].

4.3. Hardened properties

The effect of pigment type and concentration on the 28-days $f'c$ for concrete prepared with 350 kg/m^3 cement are summarized in Table 3, and plotted in Figure 6. Regardless of the colour, mixtures incorporating increased pigment additions exhibited higher strength values. For example, compared to the 26.7 MPa value obtained for the control mix, the $f'c$ increased to 29.7 and 34.9 MPa for the mixtures containing 1.5 % and 4.5 % red IO, respectively. Such values reached 30 and 34.2 MPa for the mixtures containing 1.5 % and 4.5 % grey IO, respectively. This could be associated to the micro-filler effect and enhanced packing density that lead to a denser microstructure capable of supporting higher loads. Yildizel et al. [22] reported that IO pigments are inert materials (i.e., do not react with water) that fill the interspaces and capillary pores in cementitious systems, leading to an improved resistance against permeability and attack of aggressive ions.

For the given concentration, the effect of CB on strength development is pretty similar or slightly higher than the IO pigments. Hence, the $f'c$ reached 35.1 MPa for the 350-CBlack-4.5 % mixture. Knowing the inert nature of such powders, the increase in strength can be physically related to the micro-filler effect that enhances packing density of the cementitious matrix.

The highest increase in $f'c$ was recorded for concrete mixtures prepared with TiO_2 additions; this

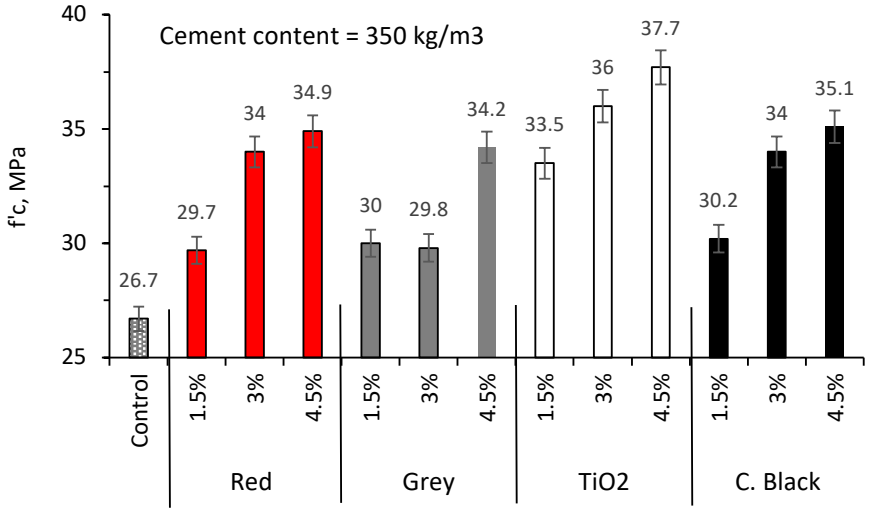

FIGURE 6. Effect of pigment types and concentrations on hardened properties and bond to steel bars.

Mixture codification	7-d $f'c$ [MPa]	28-d $f'c$ [MPa]	ft [MPa]	UPV [km/s]	E [GPa]	τ_u [MPa]	δ_u [mm]
350-Control	14.8	26.7	2.16	3.55	29.8	11.36	4.1
350-Red-1.5 %	17	29.7	2.28	3.58	30.2	11.94	5.3
350-Red-3 %	20.1	34	2.41	3.6	30.8	18.00	10.3
350-Red-4.5 %	19.8	34.9	3.06	3.62	31.7	17.78	10.5
350-Grey-1.5 %	17.2	30	n/a	3.5	29.1	n/a	n/a
350-Grey-3 %	20.2	29.8	2.86	3.62	31.5	12.74	4.9
350-Grey-4.5 %	20.6	34.2	3.36	3.58	30.7	14.05	6.1
350-TiO2-1.5 %	19.7	33.5	2.62	3.57	30.0	17.25	6.2
350-TiO2-3 %	19.6	36	2.7	3.66	32.0	n/a	n/a
350-TiO2-4.5 %	20.6	37.7	3.22	3.62	31.8	20.70	7.8
350-CBlack-1.5 %	19	30.2	2.87	3.6	31.0	15.34	4.4
350-CBlack-3 %	18.8	34	n/a	3.72	33.0	n/a	n/a
350-CBlack-4.5 %	20.5	35.1	3.28	3.8	35.2	17.89	5
450-Control	23.4	34.2	2.56	3.7	32.7	18.90	5.8
450-Red-3 %	27.3	38.9	3.76	3.8	35.1	23.41	11.5
450-Grey-3 %	25.8	42.3	n/a	3.83	35.7	19.78	6.3
450-TiO2-3 %	28.6	44.5	3.94	3.7	33.6	24.85	9.2
450-CBlack-3 %	27.6	41.6	3.85	3.9	37.4	21.96	7.2

n/a refers to not tested.

TABLE 3. Effect of pigment types and concentrations on workability and colourimetry properties.

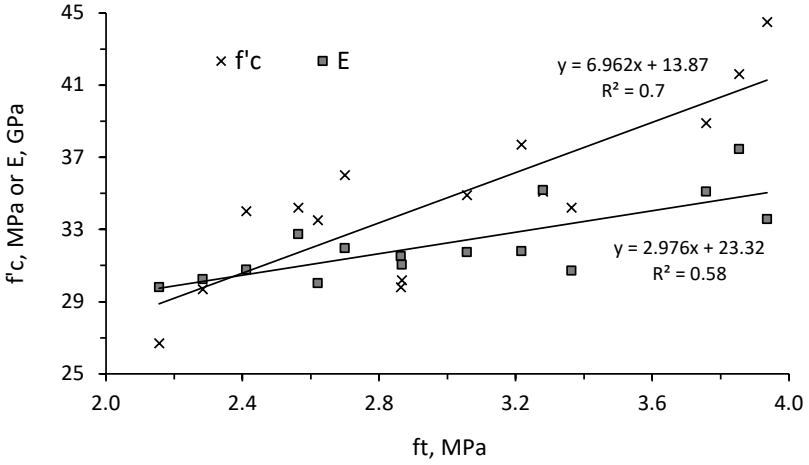

FIGURE 7. Relationships between ft with respect to $f'c$ and E responses for all tested concrete mixtures.

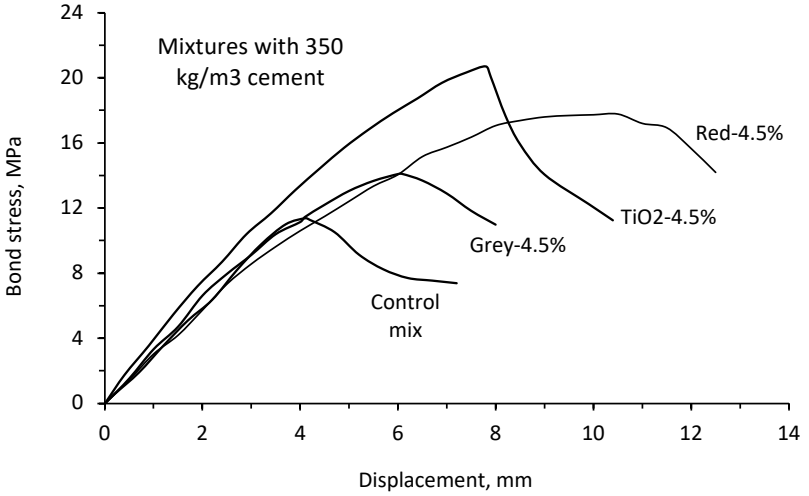

FIGURE 8. Typical bond stress vs. displacement curves for mixtures prepared with 350 kg/m^3 cement.

reached 33.5 and 37.7 MPa at 1.5 % and 4.5 % rates, respectively. Besides the micro-filler effect, the increase in strength may be ascribed to the formation of nucleation sites that promote hydration reactions and precipitate additional gels in the hardened matrix [16, 29]. The hydration products grow around the TiO_2 particles, causing the formation of secondary C-S-H in the capillary pores that reduces the porosity of the matrix. As shown in Table 3, the $f'c$ significantly increased from 34.2 MPa for the 450-Control mix to 44.5 MPa for the 450-TiO_2-3 % concrete, which can be associated to the micro-filler effect prompted with additional C-S-H hydrating compounds that could refine the concrete microstructure [27, 28].

The effect of pigment type and concentration on ft and E properties is quite similar to the one observed on $f'c$ responses. Hence, the strength increased with IO and CB pigments, while being particularly pronounced with the use of TiO_2 (Table 3). Moderate relationships with correlation coefficients (R^2) larger than 0.58 are obtained between the hardened properties for all tested concrete mixtures prepared with 350 and 450 kg/m^3 cement, as shown in Figure 7.

4.4. Bond stress-slip behavior

Table 3 summarizes the ultimate bond strength (τ_u) at failure and corresponding slip (δ_u) for all tested concrete mixtures. It is worth noting that the coefficient of variation (COV) for τ_u responses determined for selected mixtures varied from 9.6 % to 14.7 %, representing an acceptable repeatability. The steel bars did not reach their yielding state during pullout testing (i.e., the yielding load is 58.8 kN). A pullout mode of failure occurred for all tests, whereby the concrete crushed and sheared along the embedded steel region with no visible cracks on the external concrete specimens [30, 31].

Typical bond stress-slip (τ vs. δ) curves determined for the 350-Control mix and those incorporating different pigment types and concentrations are plotted in Figure 8. All curves are initially linear, which can be ascribed to the adhesive component of the bond and mechanical interlock that takes place between the

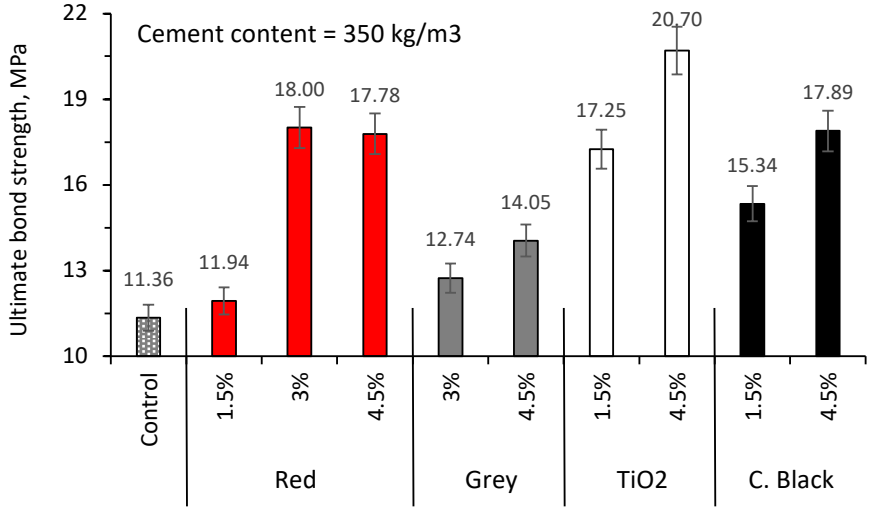

Figure 9. Effect of pigment type and concentration on τ_u for mixtures prepared with 350 kg/m^3 cement.

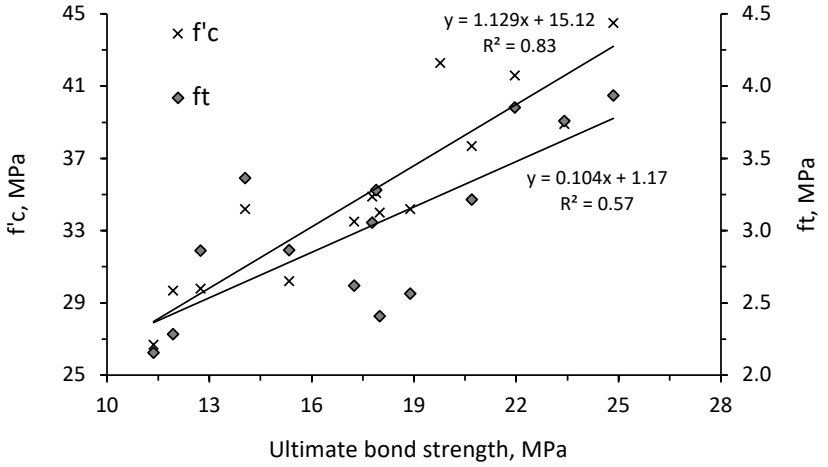

Figure 10. Relationships between τ_u with respect to $f'c$ and ft for all tested concrete mixtures.

embedded steel ribs and the surrounding concrete [32]. The 350-TiO2-4.5 % mixture exhibited the highest τ vs. δ responses, given the micro-filler effect and formation of secondary C-S-H hydrating compounds that strengthen the interfacial concrete-steel transition zone [26, 29]. Hence, compared to the 11.36 MPa value obtained from the control mix, τ_u reached 20.7 MPa for the 350-TiO2-4.5 % concrete. The increase in τ_u was also noticeable for mixtures prepared with IO pigments, albeit this remained comparatively lower than what was achieved with TiO_2 additions. Hence, τ_u reached 14.05 and 17.78 MPa for the 350-Grey-4.5 % and 350-Red-4.5 %, respectively. When the adhesive and interlock components fail, the concrete between the steel ribs breaks, causing excessive local slips at reduced bond stresses [42, 43]. Only the frictional bond component remains in the post-peak region of τ vs. δ curves, whereby the steel bars are dynamically pulled out from the concrete specimens.

Figure 9 summarizes the effect of the pigment type and concentration on τ_u responses determined for mixtures prepared with a 350 kg/m^3 cement content. Regardless of the pigment type, τ_u gradually increased with such additions, which practically reveals their beneficial role for improving the development and transfer of bond stresses in reinforced concrete members. The highest value of 20.7 MPa was recorded for the concrete containing the highest TiO_2 concentration of 4.5 %. This was followed by mixtures incorporating 3 % and 4.5 % red IO as well as those made using 4.5 % CB; the resulting τ_u hovered around 18 MPa. Just like the mechanical properties, the increase in τ_u due to inert IO or CB pigments can be attributed to the micro-filler effect that densifies the cementitious microstructure around the steel ribs, leading to an improved bond behaviour. Moderate relationships with R^2 of 0.57 and 0.83 are established between τ_u with respect to $f'c$ and ft for all tested concrete mixtures (Figure 10).

As shown in Figure 8, the increase in τ_u due to pigment additions is accompanied by an increase in the maximum slip that occurs at failure. For example, δ_u of 4.1 mm was registered for the 350-Control mix, while it reached 6.1 and 7.8 mm for the 350-Grey-

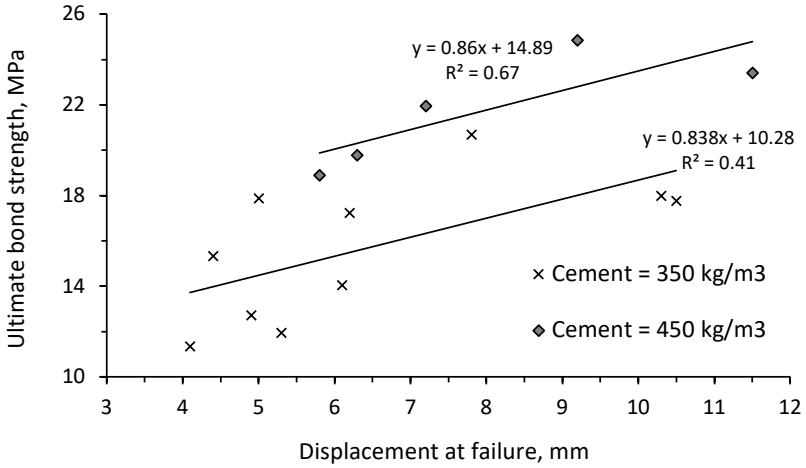

FIGURE 11. Relationships between τ_u and δ_u for mixtures prepared with 350 or 450 kg/m^3 cement.

4.5 % and 350-TiO2-4.5 %, respectively. In addition to the improved bond strength, this reflects that pigments confer higher ductility, which can be particularly relevant in high-strength concrete reinforced members [33, 43, 44]. Figure 11 plots the relationships between τ and δ for concrete mixtures prepared with 350 or 450 kg/m^3 cement. Clearly, mixtures exhibiting higher τ_u are characterized by increased displacements at failure.

5. Comparison with international bond models

In order to ensure compliance of bond properties of the coloured concrete to international design code models, the τ_u values determined experimentally are compared with the design bond strengths (τ_{max}) specified in CEB-FIP [35], ACI 318-19 [33], and European Code EC2 [34] models. The CEB-FIP (2010) considers that the stiffness of ascending τ vs. δ curves follows an exponential trend raised to a power of 0.4, until reaching τ_{max} equal to 2 or 2.5 $\sqrt{f'_c}$, depending on whether the concrete is confined or not. This can be expressed in Eqs. 1 and 2 as follows.

CEB-FIP for unconfined concrete:

$$\tau_{max} = 2\sqrt{f'_c} \tag{1}$$

CEB-FIP for confined concrete:

$$\tau_{max} = 2.5\sqrt{f'_c} \tag{2}$$

In ultimate state conditions, the ACI 318-19 [33] considers that τ_{max} can be calculated as:

$$\tau_{max} = \frac{10\sqrt{f'_c}\left(\frac{C_b+K_{tr}}{d_b}\right)}{4\times 9\,\Psi_t\,\Psi_e\,\Psi_s\,\lambda} \tag{3}$$

where C_b is the concrete cover and K_{tr} the transverse reinforcement index (note that the $(C_b+K_{tr})/d_b$ ratio is limited to 2.5). The Ψ_s, Ψ_e, Ψ_t, and λ factors refer to the bar-size, epoxy coated bars, bar location with respect to the upper surface, and lightweight concrete, respectively. In this study, Ψ_s is taken as 0.8 for bars No. 13, while Ψ_t, Ψ_e, and λ equal to 1.

The τ_{max} expression proposed by EC2 [34] for determining the ultimate bond stress is given as:

$$\tau_{max} = 2.25\,\eta_1\,\eta_2\,f_{ctd} \tag{4}$$

where η_1 is a coefficient reflecting the bond quality to the embedded steel (taken as 1.0) and η_2 is related to the bar diameter (taken as 1, given that d_b is less than 32 mm). The $f_{ctd} = \alpha_{ct}\,f_{ctk,0.05}/\gamma_c$ refers to concrete design tensile strength, where α_{ct} and γ_c refer to the long-term effects on tensile strength and partial safety factor, respectively (both taken as 1). The $f_{ctk,0.05}$ refers to the concrete characteristic axial tensile strength computed as $0.7\times 0.3\times f_{ck}^{(2/3)}$, where f_{ck} is the 28-days compressive strength concrete cylinder.

Table 4 summarizes the τ_{max} values computed using the different codes as well as the resulting experimental-to-design bond strength ratios (i.e., τ_u/τ_{max}). As shown in Figure 12, the τ_{max} values followed an increasing trend with pigment additions. On average, the experimental τ_u values are 3.35- and 4.85-times higher than the ACI 318-19 and EC2 equations (Table 4), respectively; this reveals the conservative nature of such models for predicting the bond strength between steel bars and coloured concrete structures. Yet, the τ_u/τ_{max} becomes pretty close or even lower than 1.0 when the CEB-FIP equations are used (i.e., Eqs. 1 and 2), reflecting the unconservative nature of such equations for assessing the bond strengths of coloured concrete.

6. Conclusions

This paper is part of an investigation that aims at investigating the impact of pigments on the structural properties of reinforced coloured concrete members. The findings of this paper reveal that such additions have a rather beneficial effect on the concrete bond

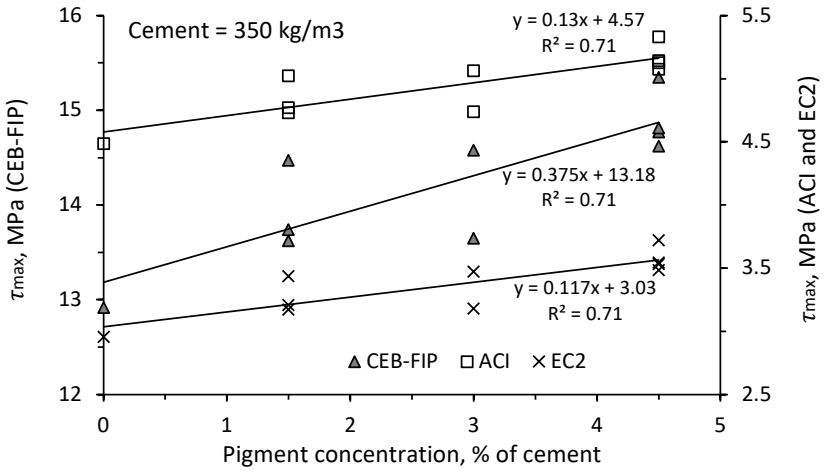

FIGURE 12. Relationships between pigment concentration and τ_{max} computed by different codes for mixtures prepared with 350 kg/m^3 cement.

Mixture codification	τ_{max} computed by different codes MPa				Experimental-to-design bond ratio (τ_u/τ_{max})			
	$2\sqrt{f'_c}$	$2.5\sqrt{f'_c}$	ACI 318	EC2	$2\sqrt{f'_c}$	$2.5\sqrt{f'_c}$	ACI 318	EC2
350-Control	10.3	12.9	4.5	3	1.1	0.88	2.53	3.84
350-Red-1.5 %	10.9	13.6	4.7	3.2	1.1	0.88	2.52	3.76
350-Red-3 %	11.7	14.6	5.1	3.5	1.54	1.23	3.56	5.19
350-Red-4.5 %	11.8	14.8	5.1	3.5	1.5	1.2	3.47	5.03
350-Grey-3 %	10.9	13.6	4.7	3.2	1.17	0.93	2.69	4.01
350-Grey-4.5 %	11.7	14.6	5.1	3.5	1.2	0.96	2.77	4.03
350-TiO2-1.5 %	11.6	14.5	5	3.4	1.49	1.19	3.43	5.02
350-TiO2-4.5 %	12.3	15.4	5.3	3.7	1.69	1.35	3.88	5.57
350-CBlack-1.5 %	11	13.7	4.8	3.2	1.4	1.12	3.22	4.78
350-CBlack-4.5 %	11.8	14.8	5.1	3.5	1.51	1.21	3.48	5.04
450-Control	11.7	14.6	5.1	3.5	1.62	1.29	3.72	5.42
450-Red-3 %	12.5	15.6	5.4	3.8	1.88	1.5	4.32	6.16
450-Grey-3 %	13	16.3	5.6	4	1.52	1.22	3.5	4.93
450-TiO2-3 %	13.3	16.7	5.8	4.2	1.86	1.49	4.29	5.98
450-CBlack-3 %	12.9	16.1	5.6	4	1.7	1.36	3.92	5.53
				Average =	1.45	1.16	3.35	4.85
				St. Deviation =	0.26	0.2	0.59	0.77

TABLE 4. Experimental-to-design bond strengths computed by different codes.

properties to embedded steel bars, which could practically be assuring to consultants and architects in the concrete building industry. Based on the foregoing, the following conclusions can be warranted:

- Mixtures containing TiO_2 exhibited the lowest $\Delta(E)$ values, reflecting relatively limited variations with respect to the control mix. The incorporation of gradually increased red or grey IO pigments led to an increased $\Delta(E)$, while the CB-modified mixtures exhibited the highest $\Delta(E)$ values.
- The steady $\Delta(E)$ increase with pigment additions was attributed to the relatively reduced cement volume and beige-like colour of natural sand, thus affecting the pigment tinting strength and reducing the tendency towards colour saturation.
- Regardless of the colour, mixtures incorporating increased pigment additions exhibited higher $f'c$ and ft responses. This was directly associated to the micro-filler effect and enhanced packing density that lead to denser microstructure. The IO and CB pigments are inert materials (i.e., do not react with water) that fill the interspaces and capillary pores in cementitious systems, leading to improved strength properties.
- The highest increase in strength was recorded for mixtures prepared with TiO_2 additions. Besides the micro-filler effect, the increase in strength was ascribed to the formation of nucleation sites that promote hydration reactions and reduce the porosity of the hardened matrix.
- Just like the $f'c$ and ft responses, τ_u gradually increased with such additions, which practically reveals their beneficial role for improving the development and transfer of bond stresses in reinforced concrete members. The highest increase was noticed for the concrete mixture containing TiO_2 additions, given the micro-filler effect and formation of additional hydrating gels that strengthen the interfacial concrete-steel transition zone.
- The increase in τ_u due to pigment additions was accompanied with an increase in the maximum slip that occurs at failure. This reflects that pigments confer higher ductility, which can be particularly relevant in high-strength concrete reinforced members.
- On average, the experimental τ_u values are 3.35- and 4.85-times higher than the ACI 318-19 and EC2 equations, respectively. Yet, the τ_u becomes pretty close to τ_{max} computed by the CEB-FIP equations, reflecting the unconservative nature of such equations to predict the bond strengths of coloured concrete mixtures.

Acknowledgements

The authors wish to acknowledge the support provided by Sodamco-Weber, Lebanon.

References

[1] P. Bartos. *Fresh concrete properties and test.* Elsevier, Amsterdam, 1992.

[2] L. Popelová. The symbolic-aesthetic dimension of industrial architecture as a method of classification and evaluation: the example of bridge structures in the Czech republic. *Acta Polytechnica* **47**(1):23–31, 2007. https://doi.org/10.14311/912.

[3] ASTM C979. Standard specification for pigments for integrally colored concrete. Annual book of ASTM standards. Farmington Hills, USA, 4(2), 2007.

[4] V. Hospodarova, J. Junak, N. Stevulova. Color pigments in concrete and their properties. *Pollack Periodica* **10**(3):143–151, 2015. https://doi.org/10.1556/606.2015.10.3.15.

[5] S. R. Naganna, H. A. Ibrahim, S. P. Yap, et al. Insights into the multifaceted applications of architectural concrete: A state-of-the-art review. *Arabian Journal for Science and Engineering* **46**:4213–4223, 2021. https://doi.org/10.1007/s13369-020-05033-0.

[6] Y.-M. Gao, H.-S. Shim, R. H. Hurt, et al. Effects of carbon on air entrainment in fly ash concrete: The role of soot and carbon black. *Energy Fuels* **11**(2):457–462, 1997. https://doi.org/10.1021/ef960113x.

[7] K. Loh, C. C. Gaylarde, M. A. Shirakawa. Photocatalytic activity of ZnO and TiO_2 'nanoparticles' for use in cement mixes. *Construction and Building Materials* **167**:853–859, 2018. https://doi.org/10.1016/j.conbuildmat.2018.02.103.

[8] S. S. Lucas, V. M. Ferreira, J. L. Barroso de Aguiar. Incorporation of titanium dioxide nanoparticles in mortars – Influence of microstructure in the hardened state properties and photocatalytic activity. *Cement and Concrete Research* **43**:112–120, 2013. https://doi.org/10.1016/j.cemconres.2012.09.007.

[9] H.-S. Jang, H.-S. Kang, S.-Y. So. Color expression characteristics and physical properties of colored mortar using ground granulated blast furnace slag and White Portland cement. *KSCE Journal of Civil Engineering* **18**(4):1125–1132, 2014. https://doi.org/10.1007/s12205-014-0452-z.

[10] R. Alves, P. Faria, A. Brás. *Brita Lavada* – An eco-efficient decorative mortar from Madeira Island. *Journal of Building Engineering* **24**:100756, 2019. https://doi.org/10.1016/j.jobe.2019.100756.

[11] J. J. Assaad, D. Nasr, S. Chwaifaty, T. Tawk. Parametric study on polymer-modified pigmented cementitious overlays for colored applications. *Journal of Building Engineering* **27**:101009, 2020. https://doi.org/10.1016/j.jobe.2019.101009.

[12] J. J. Assaad. Disposing waste latex paints in cement-based materials – effect on flow and rheological properties. *Journal of Building Engineering* **6**:75–85, 2016. https://doi.org/10.1016/j.jobe.2016.02.009.

[13] H.-S. Lee, J.-Y. Lee, M.-Y. Yu. Influence of inorganic pigments on the fluidity of cement mortars. *Cement and Concrete Research* **35**(4):703–710, 2005. https://doi.org/10.1016/j.cemconres.2004.06.010.

[14] A. Woods, J. Y. Lee, L. J. Struble. Effect of material parameters on color of cementitious pastes. *Journal of ASTM International* **4**(8):1–18, 2007. https://doi.org/10.1520/JAI100783.

[15] T. Meng, Y. Yu, X. Qian, et al. Effect of nano-TiO_2 on the mechanical properties of cement mortar. *Construction and Building Materials* **29**:241–245, 2012. https://doi.org/10.1016/j.conbuildmat.2011.10.047.

[16] A. Mohammed, N. T. K. Al-Saadi, J. Sanjayan. Inclusion of graphene oxide in cementitious composites: state-of-the-art review. *Australian Journal of Civil Engineering* **16**(2):81–95, 2018. https://doi.org/10.1080/14488353.2018.1450699.

[17] A. López, J. M. Tobes, G. Giaccio, R. Zerbino. Advantages of mortar-based design for coloured self-compacting concrete. *Cement and Concrete Composites* **31**(10):754–761, 2009. https://doi.org/10.1016/j.cemconcomp.2009.07.005.

[18] L. Hatami, M. Jamshidi. Application of SBR-included pre-milled colored paste as a new approach for coloring self-consolidating mortars (SCMs). *Cement and Concrete Composites* **65**:110–117, 2016. https://doi.org/10.1016/j.cemconcomp.2015.10.015.

[19] P. Weber, E. Imhof, B. Olhaut. Coloring pigments in concrete: Remedies for fluctuations in raw materials and concrete recipes. Tech. Report, Harold Scholz & Co GmbH, 2009.

[20] J. J. Assaad, M. Vachon. Valorizing the use of recycled fine aggregates in masonry cement production. *Construction and Building Materials* **310**:125263, 2021. https://doi.org/10.1016/j.conbuildmat.2021.125263.

[21] M. J. Positieri, P. Helene. Physicomechanical properties and durability of structural colored concrete. In *ACI Symposium Publication*, vol. 253, pp. 183–200. 2013. https://doi.org/10.14359/20175.

[22] S. A. Yıldızel, G. Kaplan, A. U. Öztürk. Cost optimization of mortars containing different pigments and their freeze-thaw resistance properties. *Advances in Materials Science and Engineering* **2016**:5346213, 2016. https://doi.org/10.1155/2016/5346213.

[23] S. Masadeh. The effect of added carbon black to concrete mix on corrosion of steel in concrete. *Journal of Minerals and Materials Characterization and Engineering* **3**(4):271–276, 2015. https://doi.org/10.4236/jmmce.2015.34029.

[24] D. Inoue, H. Sakurai, M. Wake, T. Ikeshima. Carbon black for coloring cement and method for coloring molded cement article. European patent, WO 01/046322, 10 p, 1999.

[25] J. Topič, Z. Prošek, K. Indrová, et al. Effect of pva modification on properties of cement composites. *Acta Polytechnica* **55**(1):64–75, 2015. https://doi.org/10.14311/AP.2015.55.0064.

[26] A. Nazari, S. Riahi. The effect of TiO_2 nanoparticles on water permeability and thermal and mechanical properties of high strength self-compacting concrete. *Materials Science and Engineering: A* **528**(2):756–763, 2010. https://doi.org/10.1016/j.msea.2010.09.074.

[27] J. Chen, S.-C. Kou, C.-S. Poon. Hydration and properties of nano-TiO_2 blended cement composites. *Cement and Concrete Composites* **34**(5):642–649, 2012. https://doi.org/10.1016/j.cemconcomp.2012.02.009.

[28] R. Zhang, X. Cheng, P. Hou, Z. Ye. Influences of nano-TiO_2 on the properties of cement-based materials: Hydration and drying shrinkage. *Construction and Building Materials* **81**:35–41, 2015. https://doi.org/10.1016/j.conbuildmat.2015.02.003.

[29] A. Folli, C. Pade, T. B. Hansen, et al. TiO_2 photocatalysis in cementitious systems: Insights into self-cleaning and depollution chemistry. *Cement and Concrete Research* **42**(3):539–548, 2012. https://doi.org/10.1016/j.cemconres.2011.12.001.

[30] M. Konrad, R. Chudoba. The influence of disorder in multifilament yarns on the bond performance in textile reinforced concrete. *Acta Polytechnica* **44**(5-6):186–193, 2004. https://doi.org/10.14311/654.

[31] J. J. Assaad, P. Matar, A. Gergess. Effect of quality of recycled aggregates on bond strength between concrete and embedded steel reinforcement. *Journal of Sustainable Cement-Based Materials* **9**(2):94–111, 2020. https://doi.org/10.1080/21650373.2019.1692315.

[32] ACI 408R-03. Bond and development of straight reinforcing bars in tension, 2003.

[33] ACI 318-19. Building code requirements for reinforced concrete, 2019.

[34] EN 1992-1-1. Eurocode 2: design of concrete structures – part 1-1: general rules and rules for buildings, 2004.

[35] FIB (International Federation for Structural Concrete). *Model Code for Concrete Structures*. Ernst & Sohn, Berlin, 2013.

[36] ASTM C642-13. Standard test method for density, absorption, and voids in hardened concrete. Annual book of ASTM standards. West Conshohocken, PA, 2013, USA.

[37] ASTM C39/C39 M-05. Standard test method for compressive strength of cylindrical concrete specimens. Annual book of ASTM standards. West Conshohocken, PA, 2005, USA.

[38] ASTM C496/C496 M-04. Standard test method for splitting tensile strength of cylindrical concrete specimens. Annual book of ASTM standards. West Conshohocken, PA, 2004, USA.

[39] ASTM C 597-16. Standard test method for pulse velocity through concrete. Annual book of ASTM standards. West Conshohocken, PA, 2016, USA.

[40] G. Teichmann. The use of colorimetric methods in the concrete industry. *Betonwerk Fertigteil-Technik* **11**:58–73, 1990.

[41] RILEM/CEB/FIB. Bond test for reinforcing steel: 2, pullout test. *Materials and Structures* **3**:175–178, 1970.

[42] J. Němeček, P. Padevět, Z. Bittnar. Effect of stirrups on behavior of normal and high strength concrete columns. *Acta Polytechnica* **44**(5-6):158–164, 2004. https://doi.org/10.14311/648.

[43] A. AlArab, B. Hamad, J. J. Assaad. Strength and durability of concrete containing ceramic waste powder and blast furnace slag. *Journal of Materials in Civil Engineering* **34**(1):04021392, 2022. https://doi.org/10.1061/(ASCE)MT.1943-5533.0004031.

[44] J. Machovec, P. Reiterman. Influence of aggressive environment on the tensile properties of textile reinforced concrete. *Acta Polytechnica* **58**(4):245–252, 2018. https://doi.org/10.14311/AP.2018.58.0245.

ANALYSIS OF OUTPUT VOLTAGE RIPPLE FOR DUAL RANDOMIZED PWM BUCK CONVERTER OPERATING IN CONTINUOUS AND DISCONTINUOUS CONDUCTION MODES

Aimad Boudouda[a,*], Nasserdine Boudjerda[b], Fares Nafa[a]

[a] *University M'hamed Bougara, Faculty of Technology, Laboratoire Ingénierie des Systèmes et Télécommunications (LIST) , Cité Frantz. Fanon, 35000, Boumerdes, Algeria*

[b] *University of Jijel, Laboratory of Renewable Energy (LER), Jijel, Algeria*

[*] corresponding author: a.boudouda@univ-boumerdes.dz

Abstract. Dual Randomized Pulse Width Modulation (DRPWM) is renowned for its better effectiveness than Simple Randomized Pulse Width Modulation (SRPWM) in reducing conducted Electro-Magnetic Interferences (EMI) in power converters. However, the introduction of low-frequency ripples into the output voltage by dual randomization has not yet been addressed; this effect is investigated in this paper for a buck converter operating in both the continuous conduction mode (CCM) and the discontinuous conduction mode (DCM). First, the modulating principle is presented. Then, a general analytical expression for power spectral density (PSD) of the input current is derived and validated for the proposed DRPWM scheme for both the CCM and DCM. A comparison of the PSDs of the input current for all RPWM schemes in both the CCM and DCM shows the PSD spreading effectiveness of the dual scheme as compared to simple schemes. Finally, the low-frequency output ripple is analysed using the PSD of output voltage. The results reveal that the output voltage ripple is affected by all the randomized schemes in both the CCM and the DCM. Also, the dual scheme (RCFM-RPPM) introduces the highest low-frequency voltage ripple, especially in the CCM and for low duty cycles. In DCM, the RPPM scheme gives the lowest voltage ripple, while the RCFM scheme gives the lowest voltage ripple in the CCM. The results are confirmed by both theory and simulations.

Keywords: Electro-magnetic interference (EMI), dual randomization, output voltage ripple, buck converter.

1. Introduction

Nowadays, much of the electrical energy is used through power converters, typically controlled by deterministic pulse width modulation (DPWM). This technique leads to conducted and radiated EMI to other surrounding electronic devices [1]. It is, therefore, necessary for power converters to perform the required electrical functionality while complying with international electromagnetic compatibility (EMC) standards by reducing conducted and radiated emissions [2]. For this purpose, a filtering technique can be used. However, the RPWM technique is one of the most efficient and cost-effective solutions: it allows spreading the power spectrum of input current and output voltage over a wide frequency range while significantly reducing its amplitude, which is a significant EMC benefit, requiring no additional hardware [3]. Several papers regarding this new technique have been published, principally, two simple RPWM schemes with a single randomized parameter are proposed; the scheme in which the switching period is randomized (Randomized Carrier Frequency Modulation: RCFM) and the scheme in which the period is kept constant and the pulse position is randomized (Randomized Pulse Position Modulation: RPPM), for both the DC-DC [3–10] and the DC-AC [8–11]. For a maximum spreading of the voltage spectrum, a combination of the two simple schemes (RCFM and RPPM) that we call (RCFM-RPPM) or the DRPWM scheme has also been proposed [8–11]. It has been reported, in [8], that this combined scheme gives the most spread spectrum of the input current in DC-DC converters operating in DCM. However, this effect has not yet been addressed in CCM. Despite the benefits of RPWM in spreading the spectrum and reducing EMI, this technique can introduce an undesirable continuous noise within the pass-band of the low-pass filter in DC-DC converters and induce low-frequency output voltage ripples, which require larger and expensive filters [4–6, 12–15]. Although detailed investigations of the effect of simple schemes (RCFM and RPPM) on the low-frequency output voltage ripples of DC-DC converters operating in CCM and DCM are given in [3, 7], the effect of (RCFM-RPPM) on the output voltage ripples at low-frequencies has not yet been investigated.

This paper aims to investigate the effect of the DRPWM scheme on both the input current and the output voltage ripples of a buck converter operating in CCM and DCM. At first, the modulating principle of DRPWM is presented. Then, a general analytical model of the PSD valid for input and output currents is derived in both CCM and DCM. Note that the simple schemes (RCFM and RPPM) are directly deduced as particular

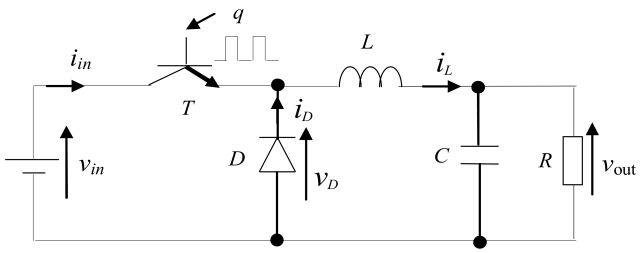

FIGURE 1. Buck converter.

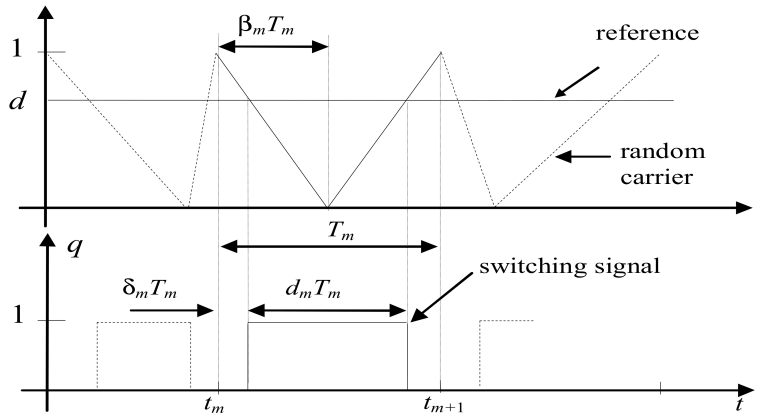

FIGURE 2. Modulating principle.

cases from the general model. The proposed analytical model is validated by a comparison to simulation results under MatLab-Simulink using the Welch estimation of the PSD, which gives satisfactory results [8, 10, 11]. A comparison between PSDs of the input current for the three schemes in both the CCM and the DCM is presented. The PSD of the output voltage ripple under each scheme is presented and compared in both conduction modes. Finally, simulation results confirm the theoretical evaluations.

2. RPWM technique in buck converter

2.1. Modulating principle

The converter under study is schematized in Figure 1; it requires one switching signal q. It can operate in CCM and DCM [3, 16–19].

For DPWM, the switching signal q is obtained by a comparison of a reference signal to a deterministic triangular carrier. In the case of RPWM, the reference signal is compared to a random triangular carrier.

The switching signal q is characterised by three parameters as shown in Figure 2: the switching cycle T, (the carrier period), the duty cycle d and the delay report δ. In DC-DC, the reference signal is fixed, which leads to a constant duty cycle d. In RPWM, these three parameters should be randomized in a combined or a separate way. In practice, d is deduced from a deterministic reference signal giving the control of the output voltage v_{out}. Thus, only the switching period T and the delay report δ can be randomized.

From Figure 2, the delay report δ_m of the switching signal q can be expressed as follows:

$$\delta_m = \beta_m(1-d) \tag{1}$$

Note The use of parameter β rather than δ is paramount; it allows the pulse position to be defined directly from the carrier parameter β_m.

The randomization of β in the interval $[0,1]$ gives a random delay report δ in the interval $[0,(1-d)]$ and the resulting position of the switching signal varies randomly from the beginning ($\delta_{min}=0$) to the end of the switching period ($\delta_{max}=1-d$). Thus, the RPPM scheme requires a triangular carrier with a fixed period T and a randomized fall time report β.

The random carrier frequency modulation (RCFM) needs a carrier with a randomized period T between two values T_{min} and T_{max} and fixed fall time report β. The randomization limits T_{min} and T_{max} are fixed around a mean value $\overline{T}$. For the buck converter, a sawtooth with a randomized period T is usually used ($\beta=0$).

PWM Schemes	β	T
DPWM	fixed[a]	fixed
RPPM	randomized	fixed
RCFM	fixed[a]	randomized
RCFM-RPPM	randomized	randomized

a: $\beta = 0$

TABLE 1. Resulting RPWM schemes.

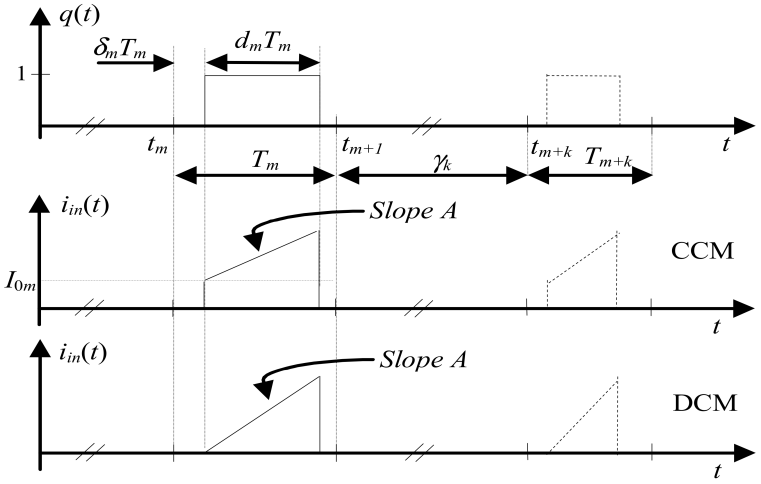

FIGURE 3. Switching signal and input current in CCM and DCM.

The proposed DRPWM combines the two previous schemes.

Related to the randomized parameters T and β, the resulting RPWM schemes are summarized in Table 1.

2.2. Continuous and discontinuous conduction mode

In the buck converter, the electronic switch (MOSFET or IGBT) chops both the input current and the output voltage at high switching frequencies, resulting in high (dv/dt) and (di/dt). This will cause a high EMI and will affect nearby electronic devices [3]. The switching signal q is approximated with a square wave and the input current i_{in} can be approximated with a triangular wave in CCM and DCM, as shown in Figure 3, [3, 8].

For a switching cycle T_m, in CCM and DCM, both the input current (i_{in}) and the inductor current (i_L) can be expressed as follows:

$$i_m(t) \begin{cases} A \times (t - t_m - \delta_m T_m) + I_{0m}, & \text{for: } \delta_m T_m \le t - t_m \le \delta_m T_m + dT_m \\ I_m - B \times (t - t_m - \delta_m T_m - d_{T_m}), & \text{for: } \delta_m T_m + dT_m \le t - t_m \le \delta_m T_m + dT_m + d_1 T_m \\ 0, & \text{elsewhere.} \end{cases} \tag{2}$$

And the general expression of Fourier transform $I_m(f)$ of the current $i_m(t)$ is:

$$\begin{aligned} I_m(f) = \frac{1}{(2\pi f)^2} \Big\{ & [A + B + j2\pi f d_m T_m (A - F)]\, e^{-j2\pi f d_m T_m} \\ & - [B - j2\pi f d_m T_m (F - BH)]\, e^{-j2\pi f (1+H) d_m T_m} + j2\pi f I_{0m} \left(e^{-j2\pi f d_m T_m} - 1 \right) - A \Big\} e^{-j2\pi f \delta_m T_m} e^{-j2\pi f t_m}, \end{aligned} \tag{3}$$

where:

t_m is the starting time of the m^{th} switching cycle,

T_m is the m^{th} switching cycle,

d is the m^{th} duty cycle,

δ_m is the m^{th}delay report: $\delta_m = \beta_m \times (1 - d)$,

I_{0m} is the initial value of the current pulse at: $t = t_m + \delta_m T_m$. Note that the value of I_{0m} is the only difference between the DCM and the CCM: For DCM, $I_{0m} = 0$ and for CCM, $I_{0m} > 0$,

I_m is the peak value of the current pulse at $t = t_m + \delta_m T_m + dT_m$, given by the relation: $I_m = FdT_m$,

Type of current	Input current (i_{in})	Inductor current (i_L)
A	$\frac{v_{in}-v_{out}}{L}$	$\frac{v_{in}-v_{out}}{L}$
B	0	$\frac{v_{out}}{L}$
F	0	$\frac{v_{in}-v_{out}}{L}$
H	$\frac{v_{in}-v_{out}}{v_{out}}$	$\frac{v_{in}-v_{out}}{v_{out}}$
v_{out}	$\frac{1}{2}\left(\sqrt{\left(\frac{K}{v_{in}}\right)^2+4K}-\frac{K}{v_{in}}\right)$	$K=\frac{(dv_{in})^2RT}{2L}$

TABLE 2. Values of A, B, F, H and v_{out} in the buck converter.

A and B are the slopes of the rising edge and the falling edge, respectively (Table 2),

F and H are constants (Table 2).

3. Spectral analysis of input current using power spectral density

The PSD allows for a rigorous spectral analysis of random signals; it can be expressed as follows [3, 10, 20]:

$$S(f)=\lim_{\tau\to\infty}\frac{1}{\tau}E\left\{|F[u_\tau(t)]|^2\right\}, \tag{4}$$

where:

$u_\tau(t)$: Considered signal during the time interval τ,

$F[u_\tau(t)]$: Fourier transform of $u_\tau(t)$,

$E\{.\}$: Statistical expectation.

3.1. Analytical expression of the PSD using wiener-khinchin theorem

For a random pulse signal $i(t)$, belonging to the class of Wide Sense Stationary (WSS) signals, expression (4) leads to the general expression (5), [3–5, 8–11]:

$$S(f)=\lim_{N\to\infty}\frac{1}{\overline{T}}E\left[\sum_{k=-N}^{N}I_m(f)I^*_{m+k}(f)\right], \tag{5}$$

where:

$\overline{T}$: Statistical mean of the switching period.

$I_m(f)$ and $I^*_{m+k}(f)$ are the Fourier transforms of the signal $i_m(t)$ during the switching period T_m and its conjugate during the switching period T_{m+k}, respectively.

After some mathematical transformations, the following expression can be set as [3–5, 8–11]:

$$S(f)=\frac{1}{\overline{T}}\left\{E_T\left[|I(f)|^2\right]+2Real\left(\frac{E_{T,\beta}\left[I(f)e^{j2\pi fT}\right]E_{T,\beta}\left[I^*(f)\right]}{1-E_T\left[e^{j2\pi fT}\right]}\right)\right\}, \tag{6}$$

where:

$E_T[\ ]$: Expectation related to the random variable T.

$E_{T,\beta}[\ ]$:Expectation value related to the variables T and β.

$Real(.)$: Real-part of the expression in brackets.

During the switching period T_m, Fourier transform $I_m(f)$ of the current $i_m(t)$, given by expression (2), is:

$$\begin{aligned}I(f)=&\frac{1}{(2\pi f)^2}\left\{[A+B+j2\pi fdT(A-F)]\,e^{-j2\pi fdT}\right.\\&\left.-[B-j2\pi fdT(F-BH)]\,e^{-j2\pi f(1+H)dT}+j2\pi fI_0\left(e^{-j2\pi fdT}-1\right)-A\right\}e^{-j2\pi f\beta\times(1-d)T},\end{aligned} \tag{7}$$

its conjugate form is:

$$I^*(f) = \frac{1}{(2\pi f)^2}\left\{[A+B-j2\pi fdT(A-F)]\,e^{j2\pi fdT} - [B+j2\pi fdT(F-BH)]\,e^{j2\pi f(1+H)dT} - j2\pi fI_0\left(e^{j2\pi fdT}-1\right) - A\right\} e^{j2\pi f\beta\times(1-d)T}. \tag{8}$$

Notes:

- Expressions (6), (7) and (8) apply for both the input current i_{in} and the output current i_L (inductor current) by using appropriate values of constants A, B, F and H, (Table 2).
- From expressions (6), (7) and (8), the simple schemes RCFM and RPPM are deduced as particular cases: for RCFM, the parameter β is constant ($\beta = 0$) and for RPPM, the period T is constant.

3.2. Welch approximation of the PSD

To validate the analytical expressions of the PSD, the analysis of the input current is also carried out using a numerical estimation of the PSD for a representative sample of the considered signal after the simulation of the buck converter [20]. This method is very satisfactory; it gives very good results as compared to the measurement and to analytical ones [8, 10, 11]. Welch's estimation method is implemented in the Signal Processing Toolbox of MATLAB by the Pwelch function:

$$PSD = pwelch(X, Window, Noverlap, NFFT, Fs),$$

where,

X: Discrete-time signal vector (sampled data),

$Window$: The window function applied to segments,

$Noverlap$: The number of overlapped samples,

$NFFT$: The number of discrete FFT samples used to calculate the estimated PSD,

Fs: The sampling frequency.

3.3. Randomness levels

T and β are the random parameters using the probability density function $p(T)$ and $p(\beta)$, respectively, the expected operator $E[I(f)]$ should be expressed as follows:

$$E[I(T,\beta,f)] = \iint_{T\beta} p(T,\beta)I(T,\beta,f)dTd\beta, \tag{9}$$

where $p(T,\beta)$ is the probability density function (pdf) used for the randomization of T and β.

In practice, any probability density function may be applied. In our applications, the uniform law is used, as it is the simplest to implement. The lower and upper limits of random parameters T and β are defined as follows:

- RCFM scheme: Related to the limits T_{min} and T_{max} and the statistical mean $\overline{T}$, a randomness level R_T is defined as follows: $R_T = \frac{T_{max}-T_{min}}{\overline{T}}$. Thus, T varies between $T_{min} = \overline{T}\left(1-\frac{R_T}{2}\right)$ and $T_{max} = \overline{T}\left(1+\frac{R_T}{2}\right)$. Theoretically, the maximum randomness level is obtained using $T_{min} = 0$ and $T_{max} = 2\overline{T}$, which gives: $R_T = 2$. In practice, R_T is fixed by practical considerations; generally it does not exceed 0.5.
- RPPM scheme: In general, for the buck converter, $\beta = 0$ for both the classical deterministic modulation and RCFM. For RPPM, β is randomized between $\beta_{min} = 0$ and $\beta_{max} \leq 1$. Thus, the randomness level R_β is then taken equal to $\beta_{max}, (R_\beta = \beta_{max} - \beta_{min})$ and β is randomized in the interval $[0, R_\beta]$ and $R_\beta \leq 1$.

Note: In general, for the buck converter: $\beta_{min} = 0$ and $\beta_{max} = 1$, [10].

3.4. PSD analysis of input current

The analysis of the input current (i_{in}) is performed using the PSD of random signals. To reinforce the validity of our results, the PSD is calculated analytically using the expression (6), then compared to that estimated using the Welch algorithm. Both CCM and DCM are considered with the following conditions:

- Input voltage: $v_{in} = 15$ volts.
- Load: ($R = 47\,\Omega$, $L = 1\,\text{mH}$, $C = 220\,\mu\text{F}$) for CCM.

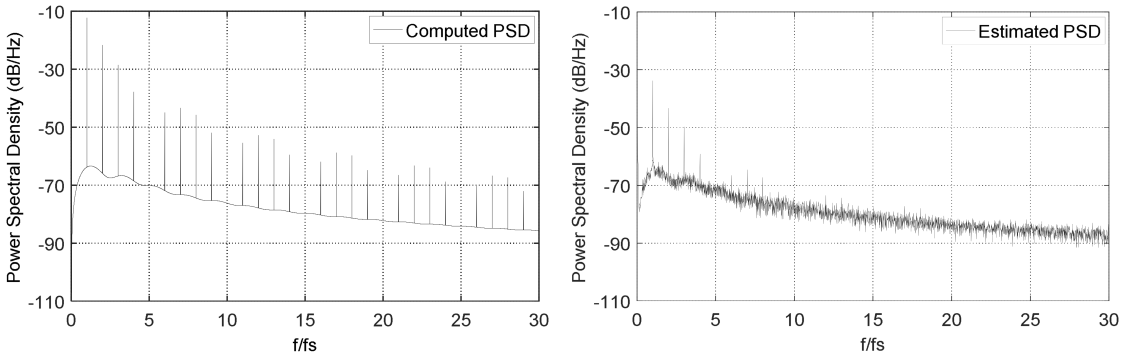

(A) . RPPM scheme.

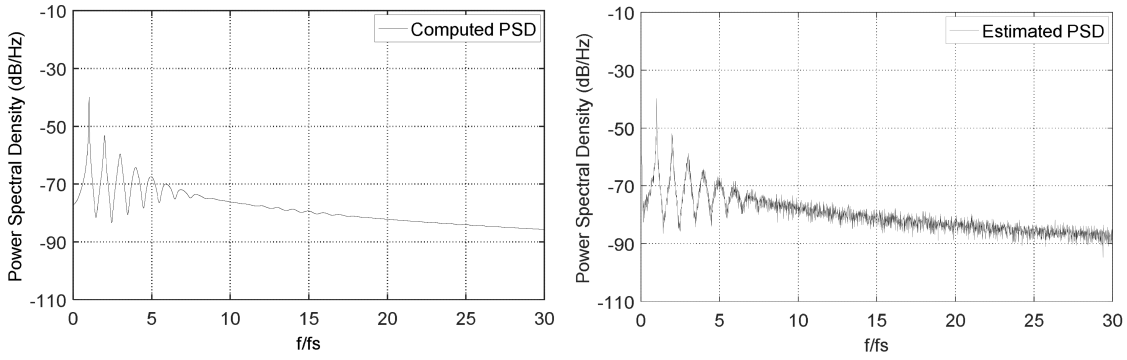

(B) . RCFM scheme.

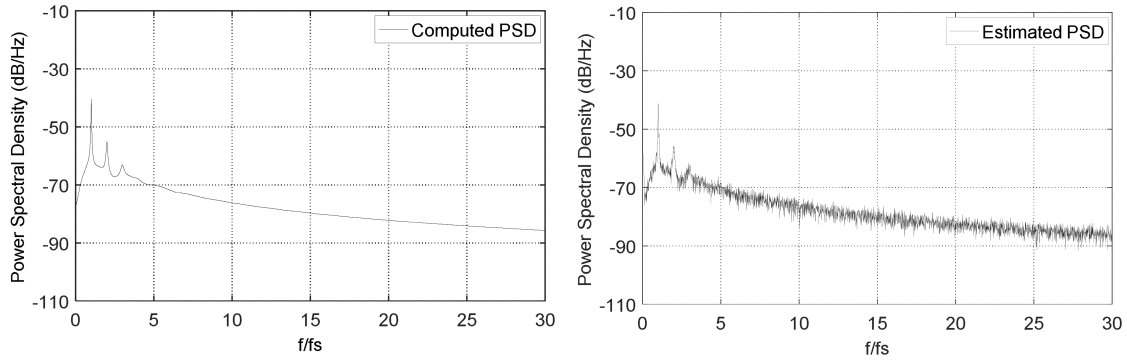

(C) . RCFM-RPPM scheme.

FIGURE 4. PSD of input current in DCM for (A) RPPM scheme, (B) RCFM scheme, (C) RCFM-RPPM scheme.

- Duty cycle: $d = 0.5$.
- Load: ($R = 47\,\Omega$, $L = 0.165\,\text{mH}$, $C = 220\,\mu\text{F}$) for DCM.
- Parameters of the carrier:

  (1.) RCFM scheme: the parameter β is fixed, ($\beta = 0$) and the period T is randomized in the interval $\left[\overline{T}\left(1-\frac{R_T}{2}\right), \overline{T}\left(1+\frac{R_T}{2}\right)\right], \overline{T} = (\frac{1}{f_s}), f_s = 20\,\text{kHz}$ and $R_T = 0.2$.

  (2.) RPPM scheme: T is fixed and β is randomized in the interval $[0, R_\beta]$, with $\beta_{min} = 0$ and $\beta_{max} = 0.4$, which gives $\delta_{min} = 0$ and $\delta_{max} = 0.2$.

  (3.) RCFM-RPPM scheme combines the two previous schemes (RCFM and RPPM) with the same parameters.

3.4.1. CASE OF DISCONTINUOUS CONDUCTION MODE

Figure (4a)–(4c) reveals perfect agreements between the computed PSDs using the proposed model (expression 6) and the estimated PSDs (Welch method) for RPPM, RCFM and RCFM-RPPM, respectively thereby validating our proposed model.

From Figure 4a, the RPPM scheme is not able to completely spread the PSD, which contains a continuous part (noise) and a discrete one (power harmonics), RCFM gives a completely spread PSD that considerably

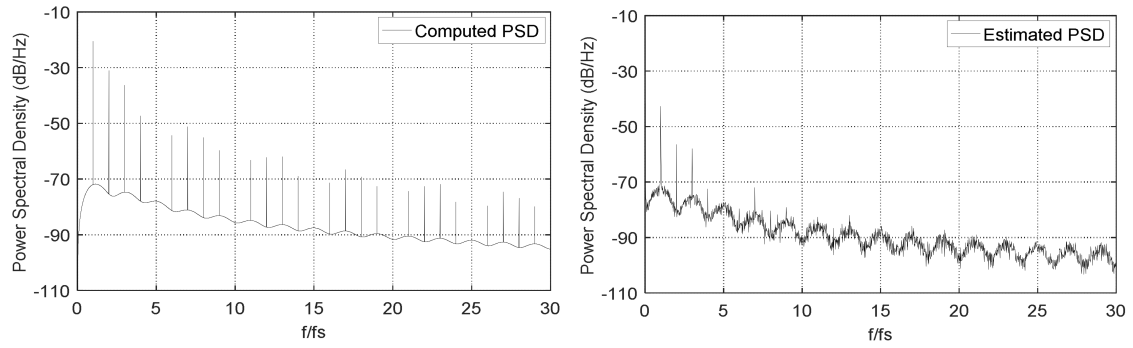

(A) . RPPM scheme.

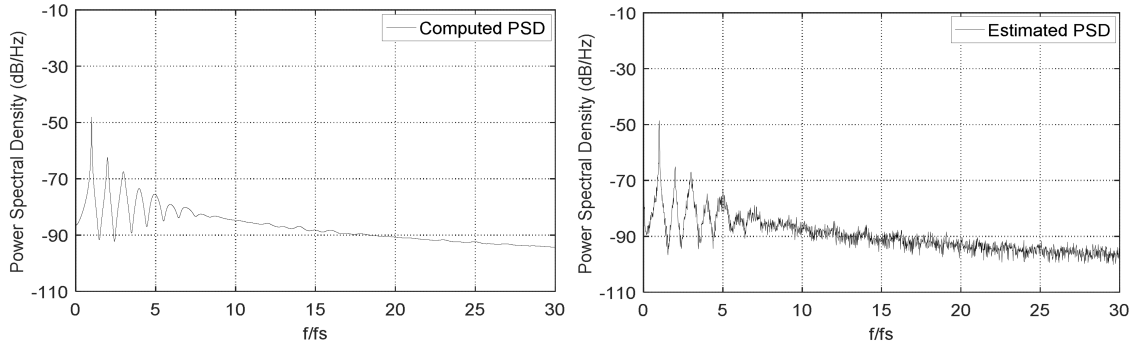

(B) . RCFM scheme.

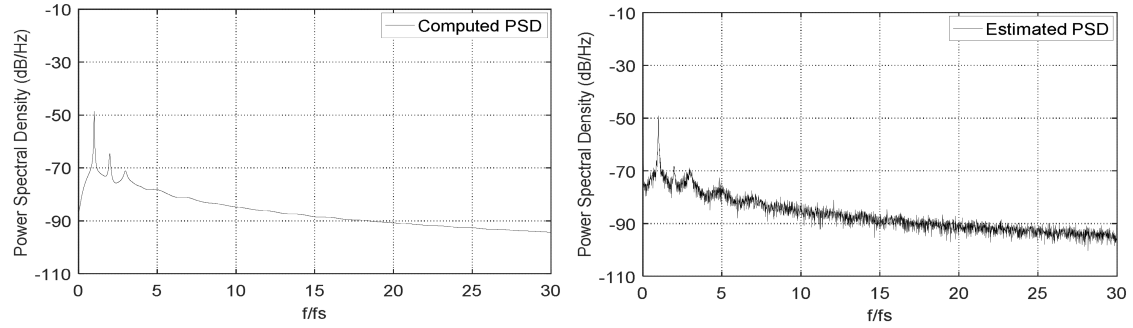

(C) . RCFM-RPPM scheme.

FIGURE 5. PSD of input current in CCM for (a) RPPM scheme, (b) RCFM scheme, (c) RCFM-RPPM scheme.

reduces the amplitude of the peaks as can be seen in Figure 4b, thus, the RCFM provides more EMC advantages than RPPM. Figure 4c clearly shows that the proposed DRPWM is the most effective in spreading the PSD and reducing its peaks; the PSD is more spread with only a meaningful peak at the switching frequency f_s; this advantage is expected because this scheme combines the properties of the two simple ones (RCFM and RPPM).

3.4.2. CASE OF CONTINUOUS CONDUCTION MODE

Figure 5a–5c compares computed and estimated PSDs for the three schemes (RPPM, RCFM and RCFM-RPPM), in CCM. A perfect agreement between the analytical model and the estimation is obtained for all schemes. In addition, the DRPWM scheme allows the most spread PSD, which is the purpose of the RPWM technique.

A comparison between Figure 4 (DCM) and Figure 5 (CCM) reveals similar shapes of the PSDs for each scheme with a lower amplitude for the CCM; this is predictable and will be discussed in the next section.

3.5. COMPARISON BETWEEN PSDS FOR CCM AND DCM

Figure 6 shows the PSD of the input current for the three schemes (RPPM, RCFM and RCFM-RPPM) and for both CCM and DCM. The PSD retains the same shape for the two modes (CCM and DCM). However, the CCM allows a significant reduction in amplitude as compared to the DCM. This is predictable because the CCM is obtained by increasing the inductance L, synonymous with reducing the current ripple (ΔI). Note that as the inductance L raises as smoothly as the input current waveform, as shown in Figure 3.

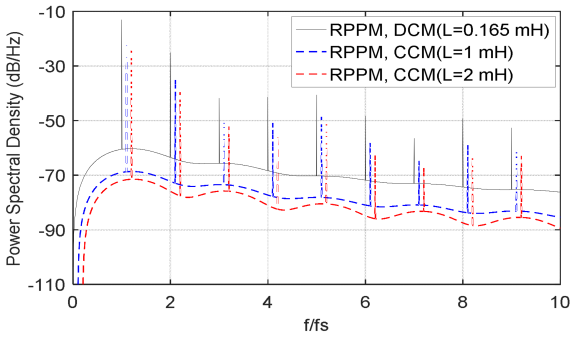

(A) . RPPM ($R\beta = 0.6$) (the peaks are intentionally shifted to see their amplitudes).

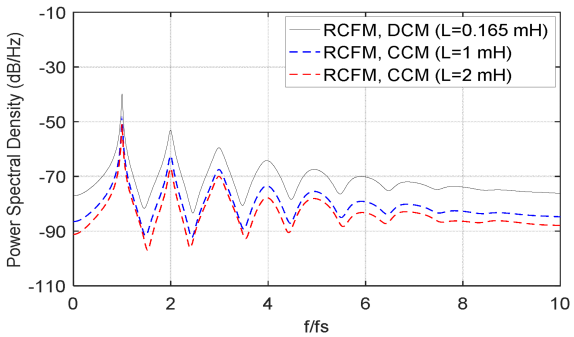

(B) . RCFM ($R_T = 0.2$).

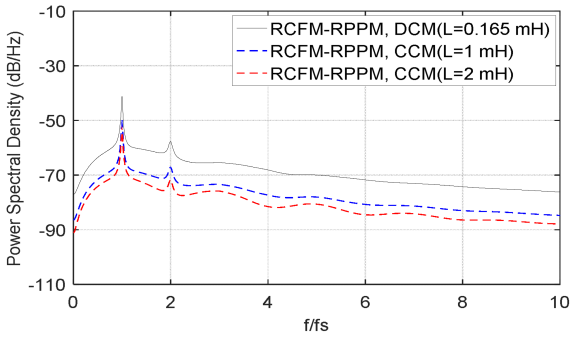

(C) . RCFM-RPPM ($R_T = 0.2$, $R\beta = 0.6$).

FIGURE 6. PSD of input current in DCM and CCM.

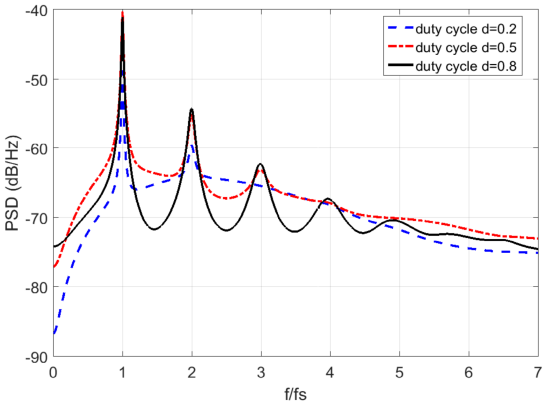

(A) . DCM.

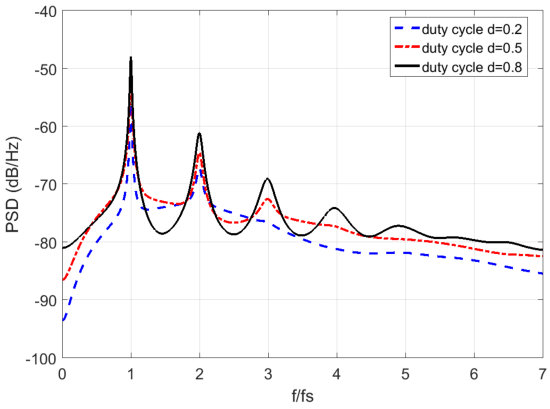

(B) . CCM.

FIGURE 7. PSD of input current for different duty cycles: (A) DCM ($L = 0.165\,\text{mH}$), (B) CCM ($L = 1\,\text{mH}$).

3.6. EFFECT OF DUTY CYCLE ON THE PSD FOR CCM AND DCM

Figure 7 shows the PSDs of the input current of the buck converter in DCM and CCM, respectively, with three values of the duty cycle d: ($d = 0.2, d = 0.5$ and $d = 0.8$). The PSDs are given for the RCFM-RPPM scheme, since it gives the best spread spectrum as compared to other schemes (RPPM and RCFM).

It is obvious that the low duty cycles ($d \leq 0.5$) allow a good spread of the PSD as compared to high duty cycles ($d \geq 0.5$) in both the DCM and the CCM. This is predictable because for low duty cycles, the switching signal duration is shorter than that for high duty cycles (Figure 3) thus the randomisation of the pulse position (RPPM) has a greater effect since it is achieved in the whole switching period.

4. ANALYSIS OF OUTPUT VOLTAGE RIPPLE

The ripple value of the inductor and capacitor is another converter design parameter and one of the main design factors, which must be considered during the converter design. In our case, we focused on the analysis of the

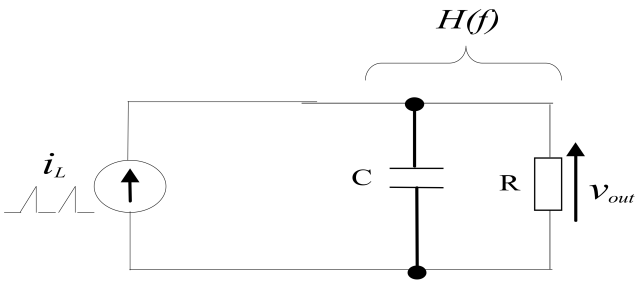

FIGURE 8. Equivalent circuit of the buck converter.

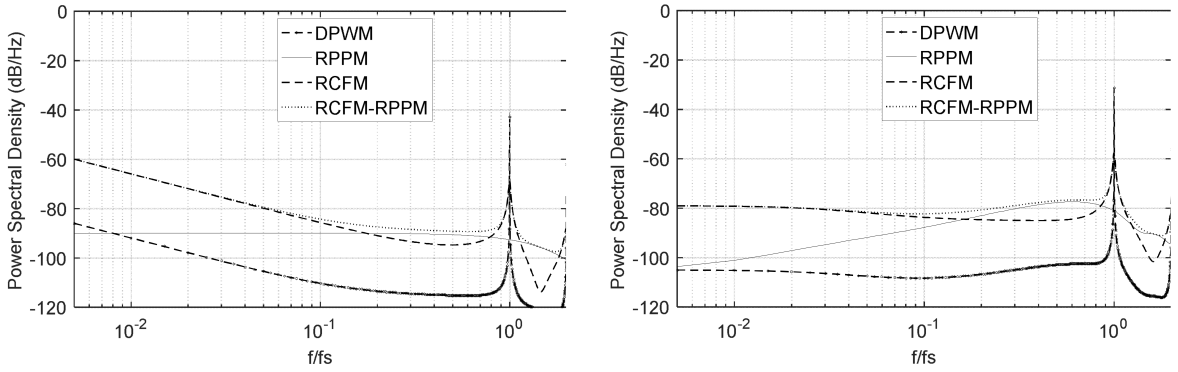

(A) . DCM. (B) . CCM.

FIGURE 9. Low-frequency characterizations of v_{out}.

low-frequency ripples introduced into the output voltage by the RPWM in CCM and DCM. Then, the values of the inductor are chosen based on the conduction mode: $L = 1\,\text{mH}$ for the CCM and $L = 0.165\,\text{mH}$ for the DCM. The capacitor is fixed for the two modes ($C = 220\,\mu\text{F}$).

Note that our aim is to study the effect of the RPWM on the output voltage regardless of the filter parameters, for this reason, the inductor and capacitor values are maintained fixed for each conduction mode.

4.1. PSD OF THE LOW-FREQUENCY OUTPUT RIPPLE

As shown in Figure 8, the buck converter can be considered as a low-pass filter fed by a current source (inductor current i_L), [3, 4].

The PSD $S_{n0}(f)$ of the voltage noise at the converter output is [3]:

$$S_{n0}(f) = S_{i_L}(f)|H(f)|^2, \qquad f \neq 0, \tag{10}$$

where:

$S_{i_L}(f)$: PSD of the inductor current given by expressions (6), (7) and (8) with the corresponding values of constants A, B, F and H, (Table 2),

$H(f)$: Transfer function of the (R-C) filter given by:

$$H(f) = \frac{V_{out}(f)}{I_L(f)} = \frac{R}{1 + j2\pi fCR}. \tag{11}$$

The low-frequency characterisations of the output voltage v_{out} within the pass-band of the filter in DCM and CCM are shown in Figure 9, where the DPWM scheme is taken as a benchmark. In DCM, the RPPM introduces the lowest PSD of the output voltage, while the RCFM-RPPM introduces the highest one as shown in Figure 9a. In CCM, the RCFM introduces the lowest PSD as shown in Figure 9b, while the RCFM-RPPM always introduces the highest one.

From the previous observations, we can say that although the RCFM-RPPM gives the most spread spectrum of the input current, it introduces the largest low-frequency PSD of the output voltage in both the DCM and the CCM.

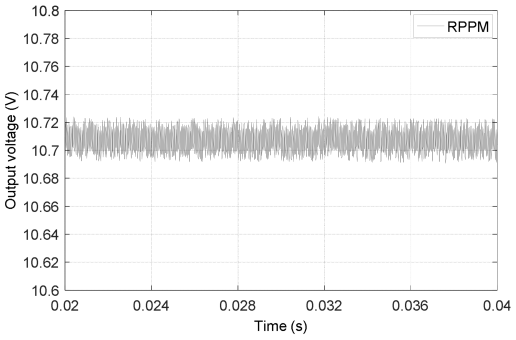

(A) . RPPM.

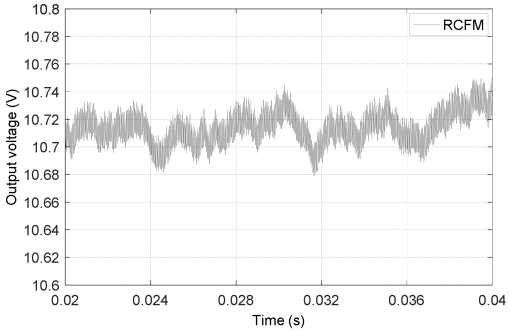

(B) . RCFM.

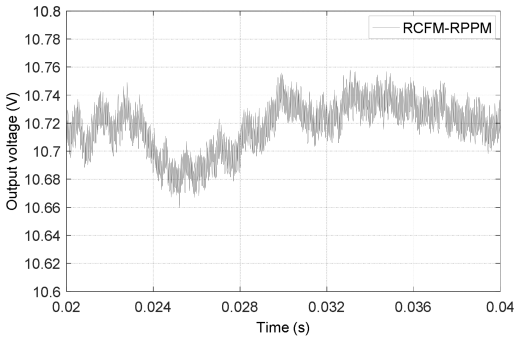

(C) . RCFM-RPPM.

FIGURE 10. Simulated output voltage ripple in DCM.

Duty cycle	Conduction mode	RPPM	ΔV	RCFM	ΔV	RCFM-RPPM	ΔV
0.2	CCM	12.08	0.16	12.04	0.08	12.07	0.13
	DCM	12.7	0.05	12.71	0.07	12.71	0.08
0.5	CCM	10.8	0.31	10.6	0.18	10.84	0.29
	DCM	10.72	0.03	10.76	0.08	10.75	0.09
0.8	CCM	6.12	0.035	6.012	0.016	6.125	0.035
	DCM	6.16	0.03	6.186	0.05	6.184	0.06

TABLE 3. Maximum peak voltage and peak-to-peak voltage ΔV.

Due to the buck converter output low pass LC filter characteristics, the low frequency ripples are considered as a significant problem, because they can easily corrupt the operation of electronic circuits [18]. The switching ripples are attenuated by the LC filter.

4.2. Analysis of the output ripple in DCM and CCM

Figures 10 and 11 show the simulated output voltage waveforms for the three schemes (RPPM, RCFM and RCFM-RPPM) in DCM and CCM, respectively.

From Figure 10 and Figure 11, in Table 3, we show the maximum peak voltage and peak-to-peak voltage for all RPWM schemes, in both the DCM and the CCM. The results are given for different values of the duty cycle d.

The results of Figure 10, Figure 11 and Table 3 show a perfect agreement with those of Figure 9. Indeed, in DCM, the RPPM scheme gives the lowest voltage ripple with a magnitude of 10.72 V as shown in Figure 10 and Table 3, while the RCFM-RPPM scheme gives the highest voltage ripple with a magnitude of 10.75 V, (Table 3). In CCM, it is the RCFM scheme that gives the lowest ripple voltage with a magnitude of 10.76 V as shown in Figure 10, while the RCFM-RPPM scheme still gives the highest ripple with a magnitude of 10.84 V, (Table 3), thus confirming the theoretical prediction of Figure 9. For low duty cycles ($d \leq 0.5$), the different schemes give the highest ripple as compared to high duty cycles ($d \geq 0.5$) for both conduction modes (Table 3).

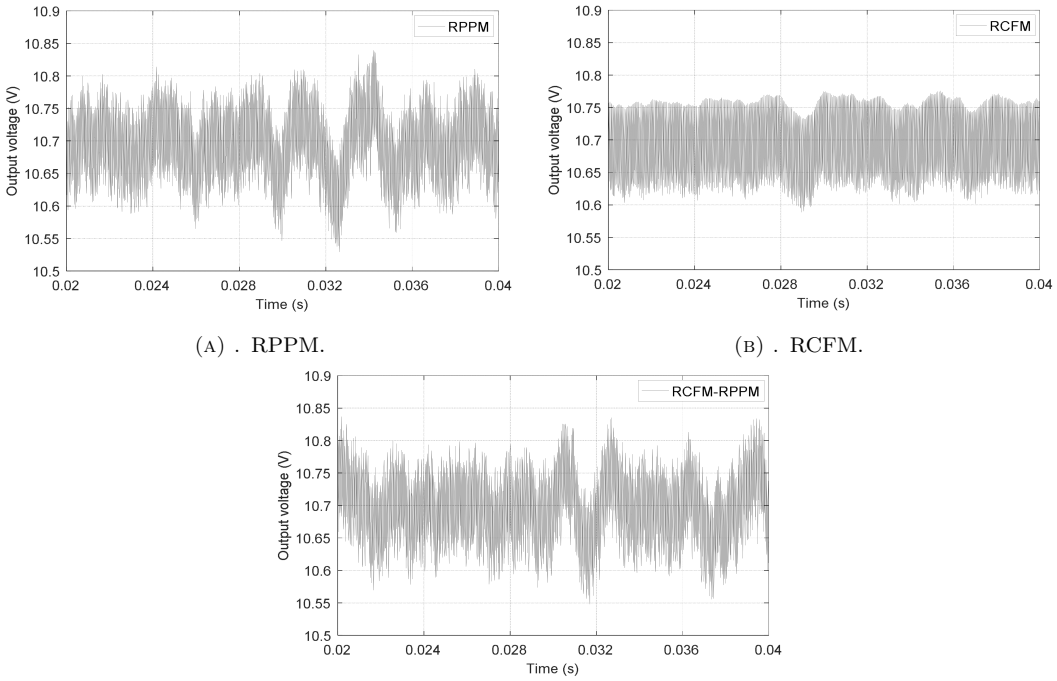

(A) . RPPM.

(B) . RCFM.

(C) . RCFM-RPPM.

FIGURE 11. Simulated output voltage ripple in CCM.

5. CONCLUSION

This paper gives an analysis of the effect of DRPWM on the input current and the output voltage ripple of a buck converter operating in CCM and DCM. For a rigorous analysis of the current and the voltage, we have proposed and validated a general mathematical model of the PSD in CCM and DCM. Overall, the CCM mode allows a significant reduction in the PSD amplitude of the input current as compared to the DCM mode. The RCFM-RPPM scheme realizes the most effective spreading of the PSD as compared to the simple schemes (RCFM and RPPM), particularly in CCM. However, this scheme introduces the highest low-frequency voltage ripple, especially in CCM and for low duty cycles, which must be taken into consideration. The RPPM and RCFM schemes give the lowest voltage ripple in DCM and CCM, respectively, which further decreases as the duty cycle "d" increases. Finally, simulation results confirm and validate the theoretical predictions.

REFERENCES

[1] M. Miloudi, A. Bendaoud, H. Miloudi. Common and differential modes of conducted electromagnetic interference in switching power converters. *Revue Roumaine des Sciences Techniques – Serie Électrotechnique et Énergetique* **62**(3):246–251, 2017.

[2] P. Lezynski. Random modulation in inverters with respect to electromagnetic compatibility and power quality. *IEEE Journal of Emerging and Selected Topics in Power Electronics* **6**(2):782–790, 2018. https://doi.org/10.1109/JESTPE.2017.2787599.

[3] K. K. Tse, H. Shu-Hung Chung, S. Y. R. Hui, H. C. So. Spectral characteristics of randomly switched PWM DC/DC converters operating in discontinuous conduction mode. *IEEE Transactions on Industrial Electronics* **47**(4):759–769, 2000. https://doi.org/10.1109/41.857956.

[4] Y. Shrivastava, S. Y. Hui, S. Sathiakumar, et al. Harmonic analysis of nondeterministic switching methods for DC-DC power converters. *IEEE Transactions on Circuits and Systems I: Fundamental Theory and Applications* **47**(6):868–884, 2000. https://doi.org/10.1109/81.852940.

[5] V. Adrian, J. S. Chang, B.-H. Gwee. A randomized wrapped-around pulse position modulation scheme for DC–DC converters. *IEEE Transactions on Circuits and Systems I: Regular Papers* **57**(9):2320–2333, 2010. https://doi.org/10.1109/TCSI.2010.2043997.

[6] H. Guo, Z. Li, B. Zhang. Characteristic analysis of switching voltage power spectra under the mode of random carrier-frequency modulation. *COMPEL – The International Journal for Computation and Mathematics in Electrical and Electronic Engineering* **29**(2):484–494, 2010. https://doi.org/10.1108/03321641011014940.

[7] E. N. Y. Ho, P. K. T. Mok. Design of PWM ramp signal in voltage-mode CCM random switching frequency buck converter for conductive EMI reduction. *IEEE Transactions on Circuits and Systems I: Regular Papers* **60**(2):505–515, 2013. https://doi.org/10.1109/TCSI.2012.2215796.

[8] A. Boudouda, N. Boudjerda, A. Bouzida, A. Aibeche. Dual randomized pulse width modulation technique for buck converter fed by photovoltaic source. *Revue Roumaine des Sciences Techniques – Serie Électrotechnique et Énergetique* **63**(3):289–294, 2018.

[9] K. El Khamlichi Drissi, P. C. K. Luk, B. Wang, J. Fontaine. A novel dual-randomization PWM scheme for power converters. In *IEEE 34th Annual Conference on Power Electronics Specialist, 2003. PESC '03.* 2003. https://doi.org/10.1109/PESC.2003.1218102.

[10] A. Boudouda, N. Boudjerda, K. El Khamlichi Drissi, K. Kerroum. Spread spectrum in full bridge DC-DC/DC-AC converter by optimized dual RPWM scheme. *The Mediterranean journal of electronics and communications* **10**(1):666–673, 2014.

[11] N. Boudjerda, A. Boudouda, M. Melit, et al. Spread spectrum in three-phase inverter by an optimised dual randomised PWM technique. *International Journal of Electronics* **101**(3):308–324, 2014. https://doi.org/10.1080/00207217.2013.780299.

[12] Y. Shrivastava, S. Y. R. Hui, S. Sathiakumar, et al. Effects of continuous noise in randomised switching DC-DC converters. *Electronics Letters* **33**(11):919–921, 1997. https://doi.org/10.1049/EL:19970655.

[13] K. Cui, V. Adrian, Y. Sun, et al. A low-harmonics low-noise randomized modulation scheme for multi-phase DC-DC converters. In *2017 15th IEEE International New Circuits and Systems Conference (NEWCAS)*. 2017. https://doi.org/10.1109/NEWCAS.2017.8010131.

[14] K. Cui, V. Adrian, B.-H. Gwee, J. S. Chang. A noise-shaped randomized modulation for switched-mode DC-DC converters. *IEEE Transactions on Circuits and Systems I: Regular Papers* **65**(1):394–405, 2018. https://doi.org/10.1109/TCSI.2017.2719700.

[15] V. Nguyen, H. Huynh, S. Kim, H. Song. Active EMI reduction using chaotic modulation in a buck converter with relaxed output LC filter. *Electronics (Basel)* **7**(10):254, 2018. https://doi.org/10.3390/electronics7100254.

[16] E. Babaei, H. M. Mahery. Mathematical modeling and analysis of transient and steady states of buck dc-dc converter in DCM. *COMPEL – The International Journal for Computation and Mathematics in Electrical and Electronic Engineering* **32**(1):337–363, 2013. https://doi.org/10.1108/03321641311293920.

[17] D. Stepins. Analysis of output voltage of switching frequency modulated DC-DC converter operating in discontinuous conduction mode. In *2010 IEEE International Symposium on Industrial Electronics*. 2010. https://doi.org/10.1109/ISIE.2010.5637199.

[18] D. Stepins, J. Jankovskis. Reduction of output voltage ripples in frequency modulated power converter. *Elektronika ir elektrotechnika* **119**(3), 2012. https://doi.org/10.5755/j01.eee.119.3.1361.

[19] A. Boudouda, A. Bouzida, F. Nafa. Spectral analysis of switch voltage for dual randomized PWM DC-DC converters operating in DCM. *International Journal of Electronics Letters* **10**(1):101–114, 2022. https://doi.org/10.1080/21681724.2020.1870717.

[20] P. Welch. The use of fast Fourier transform for the estimation of power spectra: A method based on time averaging over short, modified periodograms. *EEE Transactions on Audio and Electroacoustics* **15**(2):70–73, 1967. https://doi.org/10.1109/TAU.1967.1161901.

CYCLIC RESPONSE OF RC BEAM-COLUMN JOINTS STRENGTHENED WITH TRANSVERSE STEEL BARS AND WITH C-FRP DIAGONAL TIES

Emmanouil Golias[a,*], Emmanouil A. Vougioukas[b], Klaus Wittemann[c], George I. Kalogeropoulos[d], Chris Karayannis[a]

[a] *Democritus University of Thrace, School of Engineering, Civil Engineering Department, GR 67100 Xanthi, Greece*

[b] *National Technical University of Athens, School of Civil Engineering, Reinforced Concrete Laboratory, GR 15773 Athens, Greece*

[c] *Beratender Ingenieur, SLP Ingenieurbüro für Tragwerksplanung, Weinbrennerstr. 18, 76135 Karlsruhe, Germany*

[d] *Aristotle University of Thessaloniki, School of Engineering, Civil Engineering Department, Laboratory of Reinforced Concrete and Masonry Structures, GR 54124 Thessaloniki, Greece*

[*] corresponding author: egkolias@civil.duth.gr

Abstract. The use of additional bars, internally placed through drill holes, in external beam-column connections subjected to cyclic loading, as shear reinforcement is experimentally investigated.

The presented experimental work includes tests of full-scale specimens with different reinforcement arrangements in the joint area, they are as follows: (a) the JB0V control specimen with two (extra) vertical side bars without shear reinforcement in the joint area and, (b) the JB0R joint, same as in the case of the control specimen, without the extra vertical bars, but with four additional steel bars that were placed in holes, which were drilled through the concrete of the joint body for this purpose, (c) the JB0VFX joint, the damaged control specimen repaired and strengthened with C-FRP diagonal ties (rope connections) through the joint area. The effectiveness of these additional bars and ropes as a shear reinforcement on the overall seismic performance of the tested joint is examined.

A comparison between the test results of the examined specimens indicated that the applied retrofitting technique is appropriate for the enhancement of the overall hysteretic performance of the beam-column joints in terms of load carrying capacity, stiffness and hysteretic energy dissipation.

Keywords: R/C joints, repair and strengthening, CFRP ropes, cycling loading.

1. Introduction

Modern Codes' requirements for earthquake resistant structures are tighter than those a few decades ago. Several methods have been developed for upgrading the bearing capacity of existing concrete-framed buildings, the majority of which has been constructed according to elementary earthquake resistant provisions. Strengthening of existing structural members is usually necessary in most cases in order to reach modern demands in earthquake engineering, as reported by researchers, e.g., Cosenza et al. [1], and National structural codes and recommendations, e.g., EPANTYK [2].

Though several efficient methods are applied for the strengthening of existing linear members, there are many limitations for the upgrade of the capacity of existing nodes, mainly due to practical reasons. Nevertheless, increasing the capacity of linear members, without analogous provisions for the capacity of the nodes, attenuates the ability to improve the whole structure's capacity. As no specific rules had been established for shear reinforcement in the joint areas until about four decades ago, it was not rare that nodes were constructed with sparse, or even lack of stirrups.

The first structural attempts for strengthening of such existing nodes (with "poor" detailing), included jacketing, either with the use of steel plates, or shotcrete [3–7]. If a node had been lightly damaged, epoxy resin injections were used before jacketing [8]. Alternatively, adding steel collars have been proposed [9].

Introduction of the FRPs at the beginning of the new century led to the development of related techniques that have, gradually, substituted the older techniques that were labour intensive and increased the structural elements' dimensions [10]. Applications of externally applied FRPs have been studied for over 20 years by many researchers, due to their advantages [11]. An analytical review of state-of-the-art interventions to RC beam column joints with FRP has been also reported [12]. As the majority of the nodes are surrounded by 3 or 4 beams, abovementioned interventions require complex and expensive techniques for their application.

A novel technique has been proposed recently, so that both the complexity and the cost of nodes' restoration or/and strengthening can be reduced. In recent experimental techniques [13–17], external FRP flexural ropes have been used as an additional diagonal reinforcement to existing beam column joints. This type of reinforcement is encapsulated in U-shaped notches.

Focused on the use of flexural FRP ropes, the present paper deals with the performance of type "T" nodes, strengthened with CFRP bars, placed in their position through drilling, and subjected to cyclic loading. A direct comparison of results between an unstrengthened (initial) specimen, specimen strengthened in a conventional manner, and specimen strengthened through drilling, shows positive results for the examined node strengthening method (through drilling).

2. Design of specimens

The use of additional bars, internally placed through drill holes in external beam-column connections subjected to cyclic loading, as shear reinforcement is experimentally investigated. The presented experimental work includes tests of full-scale specimens with different reinforcement arrangements in the joint area.

The effectiveness of additional bars and ropes as shear reinforcement on the overall seismic performance of tested joints has been examined. To simulate an earthquake and the resulting loads, the unreinforced specimen JB0V was first subjected to cyclic loading on the test rig. Subsequently, the test specimen JB0R, reinforced with 2Ø10, $L = 25$ cm at the top and bottom, was subjected to identical cyclic loads on the test rig. The reinforcing bars were placed as shown in Figure 1. Afterwards, the specimen JB0V, pre-damaged by the first test, had been reinforced with C-FRP ropes connections in the nodal region and again subjected to the identical cyclic loads on the test rig, labelled as JB0VFX. The results were digitally acquired and recorded using the measurement technique described, in more detail, in section 4.1. The geometry of the test specimens was chosen based on frequently occurring buildings in frame-and-transom constructions (floor height ≈ 2.95 m, beam length = 0.5 × room width ≈ 2.0 m). Then, a simulated cyclic earthquake load was applied to the test specimens on the test rig in a deformation-controlled manner. In the first four steps, the deformation rate was 0.5 mm/s and then increased to 1 mm/s. The longitudinal reinforcement of the column consisted of 1Ø14 in each corner and 1Ø12 in the centre of each side. As a shear reinforcement of the column, Ø8/10 cm stirrups were arranged. The downstand beam was reinforced with 4Ø14 in the top and bottom layers and Ø8/10 cm stirrups. The column had a cross-section of $b/d = 250$ mm/350 mm and a total length of $L = 2.95$ m, the downstand beam had a cross-section of $b/h = 250$ mm/350 mm. The

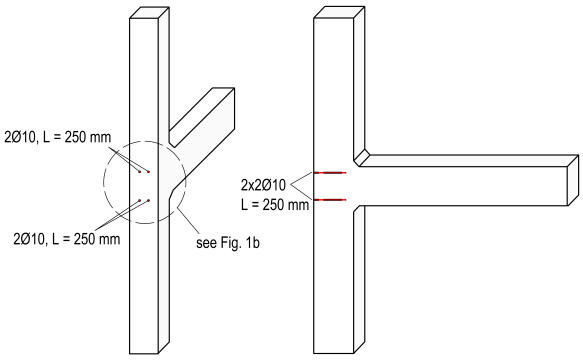

(A).

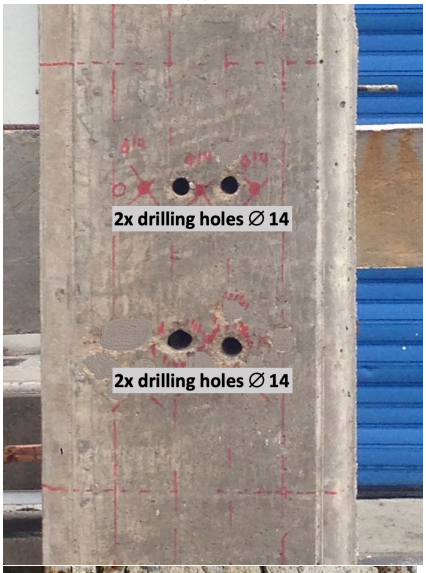

(B).

Figure 1. Reinforcement of additional bars for model JB0R.

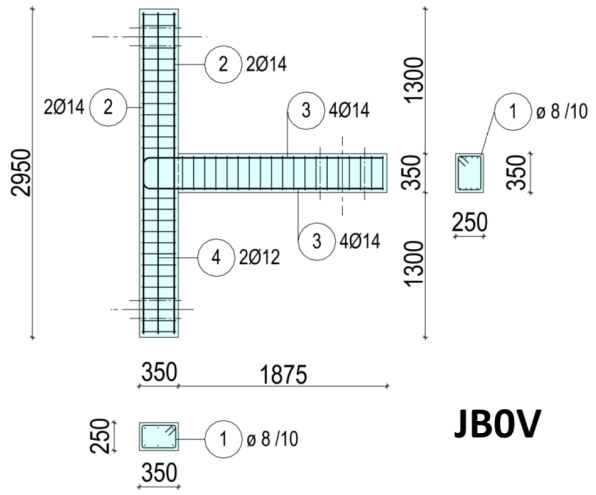

Figure 2. Geometry and reinforcement of initial model JB0V.

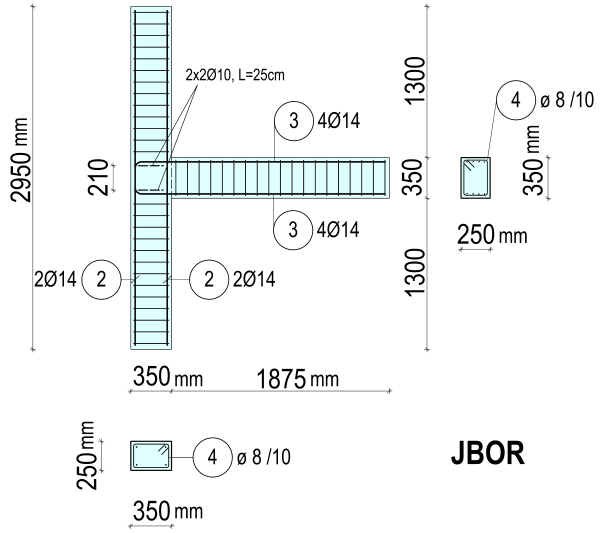

Figure 3. Geometry and reinforcement of initial model JB0R.

geometry, bending shape and location of the reinforcement are presented in Figure 2 and 3. The 28-day concrete compressive strength of the specimens was determined on cylindrical specimens of dimensions $D \times h = 150\,\text{mm} \times 300\,\text{mm}$ at $f_{cm} = 34\,\text{MPa}$. A total of 9 cylindrical specimens were tested to determine the concrete compressive strength from a total of 16 test specimens. The value $f_{cm} = 34\,\text{MPa}$ is the calculated average value of the compressive strength test. The steel grade of the reinforcing bars was B500S (B) bar steel with a yield strength of $f_{yk} = 500\,\text{MPa}$.

3. Strengthening techniques for frame nodes

Strengthening of the node of specimen JB0R has been performed prior to the tests. Holes Ø14 mm, L=250 mm were drilled at 0° into the test specimen JB0R to be reinforced (Figure 1a and 1b). The drill

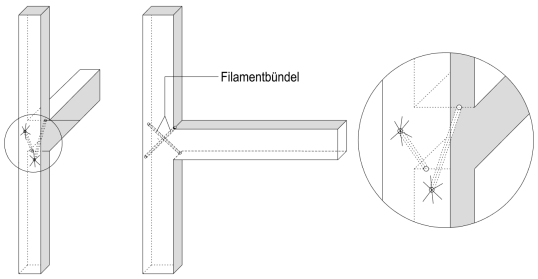

(a) . Strengthened specimen JB0VFX C-FRP rope.

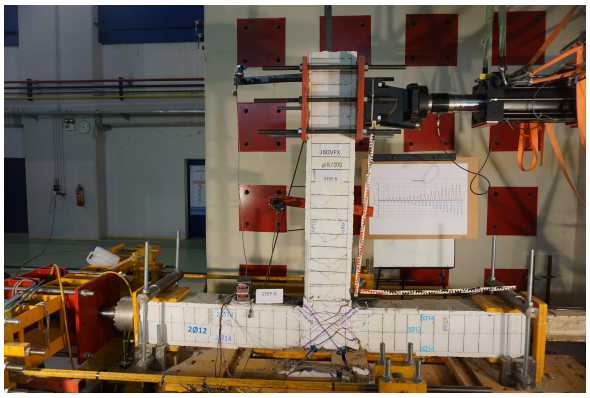

(b) . Reinforcement of additional bars for model JB0R.

Figure 4.

holes were cleaned with compressed air to remove drill dust and debris.

Sika Anchorfix-3+ was then injected into the boreholes and the Ø10 round steel reinforcement pre-impregnated with Sikadur-52 was inserted into the boreholes.

After cyclic loading of the test specimen JB0V, the damage was caused in the nodal area (Figure 4a). Loose concrete parts were first removed. Then, the damaged area was shuttered and grouted with Sika Monotop-34. During this process, C-FRP rope bundles, diagonally impregnated with Sikadur-52, were tightly installed and fixed to improve the shear force bearing capacity. The C-FRP ropes are high-strength plastics that act as ropes and can transfer high tensile forces. Details on these materials can be found in Table 1. The damaged specimen JB0V has been repaired and strengthened with C-FRP ropes crossing the node diagonally (Figure 4a and 4b). The first rope has been placed starting from the bottom back of the node and wound towards the upper face of the existing beam; the second rope started from the top back of the node and wound towards the upper face of the existing beam (Figure 4). The fixed specimen was labelled as JB0VFX. It was then subjected to the identical cyclic loads on the test rig again. The performance of the two test specimens is evaluated and compared.

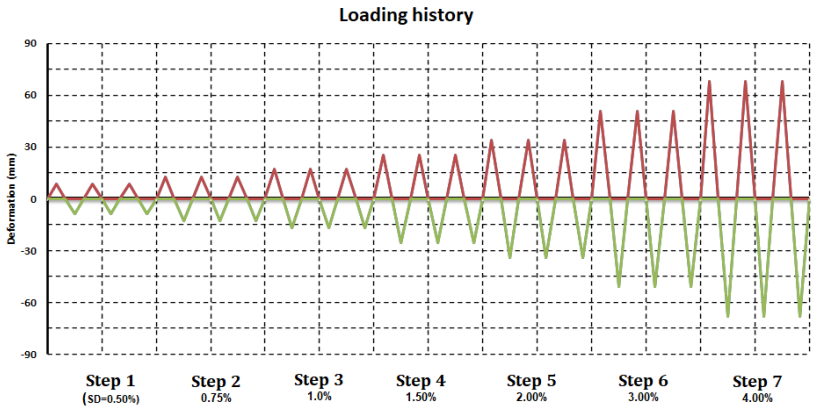

FIGURE 5. Loading sequence.

Material	E [Gpa]	f [MPa]	ε_{max} [%]
C-FRP	240	4000	1,6
Anchorfix-3+	n/a	114	>1,6
Sikadur-52	1,8	37	>1,6

TABLE 1. Properties of materials used for repair and strengthening.

The final anchoring of the rope ends is done in a star shape in milled slots. The Sika Anchorfix-3+ is then placed in the slots and the C-FRP ropes impregnated with Sikadur-52 has been casted. The properties of the materials used are given in Table 1.

4. Experimental program

4.1. Test setup and instrumentation

Properties of materials used are given in Table 1. The test rig and the measuring equipment used are shown in Figure 5. The test specimen was installed rotated by 90° so that the downstand beam pointed vertically upwards. The support was horizontal. By means of special support devices, free rotation of the frame node was made possible. This allows the position of the turning points to be moved to the centre of the supports, thus simulating an analogous frame construction. The support of the test specimen was constantly loaded with an axial normal force $\nu_c = N_c/A_c f_{cm} \approx 0.05$ during the entire test run. An axial normal force $\nu_c = N_c/A_c f_{cm} < 0.05$ would result in unrealistic nodal loading. In reality, such frame constructions are loaded with a related axial normal force $\nu_c = N_c/A_c f_{cm} \geq 0.05$, so that a conservative lower value of $\nu_c = 5$–$10\,\%$ is usually used as a basis for experiments. For loading the test specimens, a hydraulic piston was used, which was placed at a distance of 1.475 m from the side of the beam at the free end of the beam. The piston was equipped with a load cell screwed into its front part, while internally it was equipped with a linear differential displacement counter (LVDT). The piston was connected to a digital control unit to selectively apply a displacement or force to the piston under a precise software control. Thus, the force amplification command leads to the piston movement with parallel dense control (in short intervals) of the display of the force meter integrated in the piston. With the approach of the command, the program sends a signal for a small increase or decrease of the force until a predetermined accuracy is achieved in this step. Similarly, switching operations were also performed, which were recorded, checked and corrected with a displacement meter integrated in the piston. This digital control system was also used to record and store readings from external instruments, which could additionally act as experimental control instruments. The software used to perform the experiment was the M.T.S. Teststar software package. In addition to the piston used to apply the horizontal displacement, a second hydraulic piston was used, which was attached to the left end of the support. This was used to apply the support compression force, which remained constant throughout the experimental process ($N_c = 0.05 \times A_c \times f_{cm} = 122.5\,\text{kN}$).

Through the piston, the applied load was measured using a 0.025 kN precision load cell, while by using a linear 100 mm LVDT-A tensiometer, any spontaneous displacement of the test specimens was checked and taken into account in each load step. Additional cord displacement transducers SAA and SAE were attached to measure the displacements in this area and estimate the shear deformation. Figure 5 shows the described test setup.

4.2. Loading

During the test, the specimen was subjected to a full cyclic deformation. The piston for deforming the test specimen engaged at the free vertical end of the beam (Figure 6). The lever arm for generating the moment at the node was 1.475 m. The specimen was loaded in seven load steps with increasing applied deformation of ±8.5 mm, ±12.75 mm, ±17 mm, ±25.5 mm, ±34 mm, ±51 mm and ±68 mm (corresponding to storey drift (SD) from 0,50–4,00 %). Within each loading level, the deformation was applied with 3 repetitions, each in

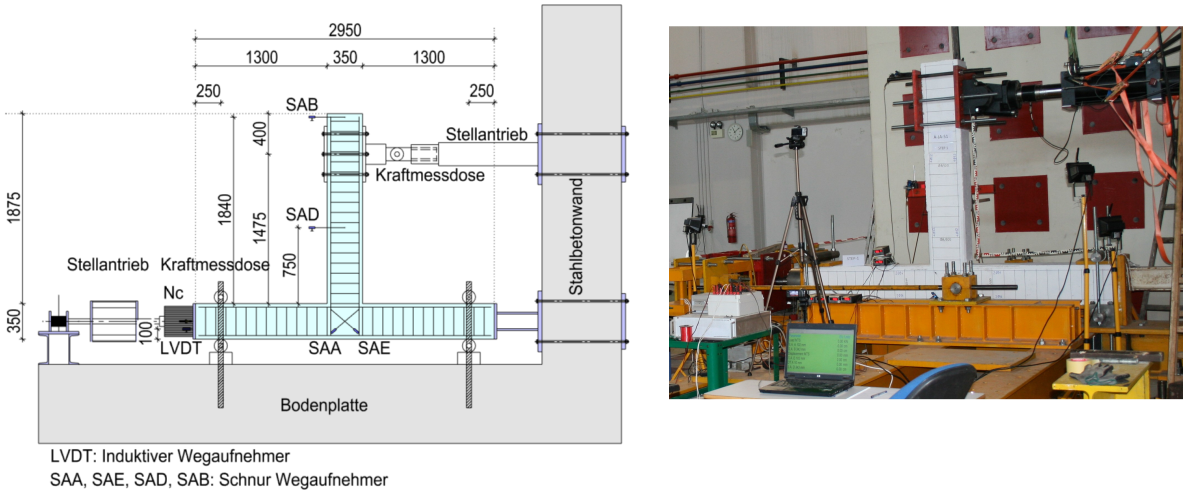

(A). (B).

Figure 6. Test setup and instrumentation.

positive and negative direction. The loading sequence can be seen in Figure 5. In large-scale tests on reinforced concrete components, it is of great importance to select the load intensity and load control in such a way that both the ultimate limit state/capacity of the test specimen and the expected actions due to earthquakes are adequately covered. In the case of simulated earthquake loads with deformations in the plastic range, the load-bearing capacity, component resistance, and action cannot be considered separately from each other, since they are strongly dependent on each other. The basic parameters for determining the capacity curve of a component are strength, stiffness, inelastic deformation capacity (ductility) and, in addition, cumulative damage capacity parameters such as energy dissipation.

All of these parameters are expected to deteriorate as the number of damage cycles and the amplitude/intensity of the cycles in the test increase. Any loading of the component beyond the elastic regime will cause a permanent damage to the component and, usually, a permanent plastic deformation. In the load sequence on which this study is based, the emphasis was deliberately placed on load levels with several load changes within each intensity level, since repeated load cycles cause a damage pattern such as is frequently found in moderate earthquake loading. In order to be able to draw meaningful conclusions from the damage patterns occurring in each case, 3 repetitions were selected for each load level, each with the same deflections within the same level. After 3 repetitions, the load was then increased by applying the next larger deformation, again in 3 cycles of equal deflection.

In severe earthquakes, the intensity and type of loads applied to individual building components do not follow a consistent pattern. With increasing deformations, the number of loading cycles outside the elastic range increases. At the same time, the vibration time of a building component increases. For structural components with a large initial stiffness, deformation states with stresses in the inelastic range occur very early. It is easy to see that the behaviour of a structure depends on a large number of variables. A single load sequence is, therefore, always a compromise or an approximation. The intensity of the load must be chosen so that it is conservative for most practical applications. In our experiment, this was achieved by a loading sequence of seven steps consisting of three cycles each (Figure 5).

A damage index was also included in the evaluation of the tests. The damage index introduced by Park and Ang (1985) was chosen in order to be able to compare the existing capacity (capacity for energy dissipation) of the existing nodal connection with reinforcement and the capacity of the same nodal connection without reinforcement.

4.3. Experimental results

In order to determine the effectiveness of the applied reinforcement method, the load-bearing capacity of the unreinforced specimen JB0V is compared with the load-bearing capacity of the reinforced specimens JB0R and JB0VFX. The hysteresis loops of the respective specimens are shown in Figure 7 by means of a force-displacement curves.

In the diagram, the dashed red lines represent the test results of the unreinforced specimen (JB0V), while the solid blue and green lines represent the results of the subsequently reinforced specimens JB0R and JB0VFX.

The comparison of the test results shows that the applied reinforcement method using 2Ø10 round steel reinforcement at the top and bottom increases the load capacity by only about 6 %. The reinforcement by C-FRP ropes shows a significant improvement. The

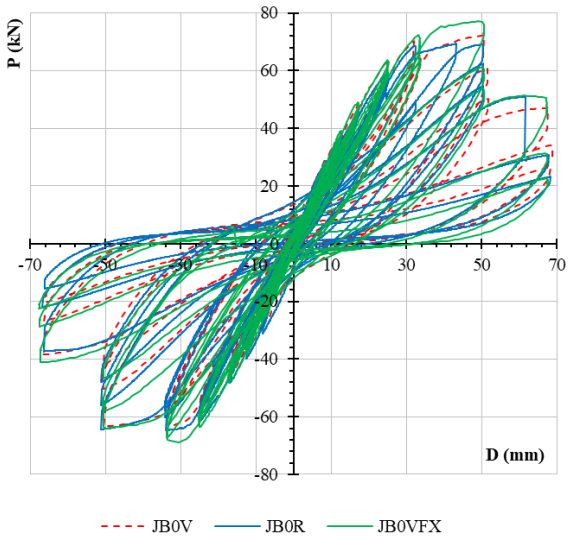

FIGURE 7. Force-displacement curves for all specimens.

damage patterns on the unreinforced specimen and the reinforced specimens after completion of the tests are compared in Figure 8. As can be seen, the damage pattern of both test specimens JB0V and JB0R is almost identical.

When reinforced with C-FRP ropes, the behaviour of the specimen JB0VFX is much more benign, the spalling of the concrete is greatly reduced, which is due to the fact that the rope reinforcement shows its effectiveness. This is also mainly due to the better anchorage of the C-FRP ropes adjacent to the highly stressed intersection. Thus, the overall damage pattern is significantly improved. The envelopes of the hysteresis loops for a full test run with 3 cyclic repetitions per loading level are shown in Figure 9a, 9b and 9c for all specimens, for all 3 cycles (seven steps per cycle).

In the diagrams, the test load (P) required for the selected deformation is plotted against the relative displacement (SD – story drift). For the sake of better representability, only values up to a load level 7 with SD = 4 % and a displacement of ± 68 mm are plotted. In addition, Figure 10 shows the change in stiffness regarding to load levels. The dashed red line corresponds to the unreinforced specimen JB0V, the solid blue line to the reinforced specimen JB0R and the solid green line to the reinforced specimen JB0VF.

5. Evaluation of results

5.1. Damage index

In the literature, several dimensionless evaluation methods are reported for assessing the damage of reinforced concrete elements after these elements have been subjected to loading outside the elastic regime. Most of these damage indices consider the damage of individual elements and are based on the plot of deformations and hysteresis curves with dissipated energy information. The damage index model of Park and

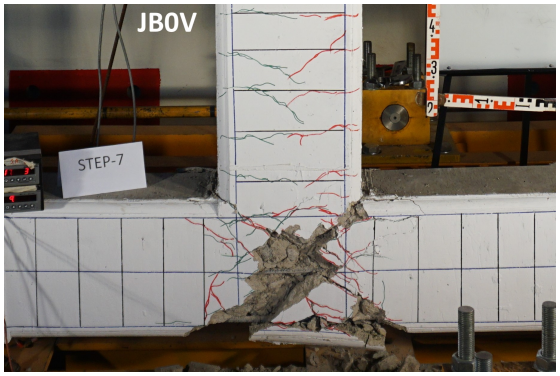

(A) . Final damage mode, specimen JB0V.

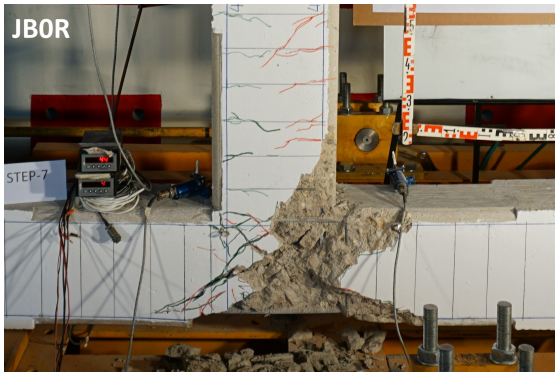

(B) . Final damage mode, specimen JB0R.

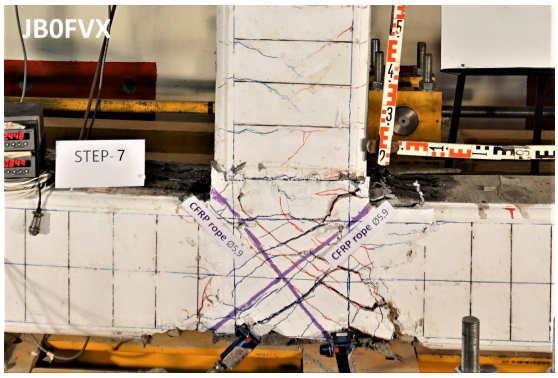

(C) . Final damage mode, specimen JB0VFX.

FIGURE 8.

Ang [18] has been widely applied in recent years, due to its simplicity and the fact that it has been calibrated with experimental data from different structures damaged during actual earthquakes.

The damage index is defined as a linear combination of the final displacement and the dissipated energy as:

$$D = \frac{\delta_M}{\delta_u} + \frac{\beta}{M_y \delta_u} \int dE \qquad (1)$$

where δ_M, represents the maximum deflection reached during seismic loading, δ_u is the maximum deformation capacity under static load, β is a model parameter, depending on the transverse and normal forces, the longitudinal reinforcement ratio and the reinforcement layout. M_y is the calculated yield strength and dE is the incremental dissipated hysteretic energy. In the

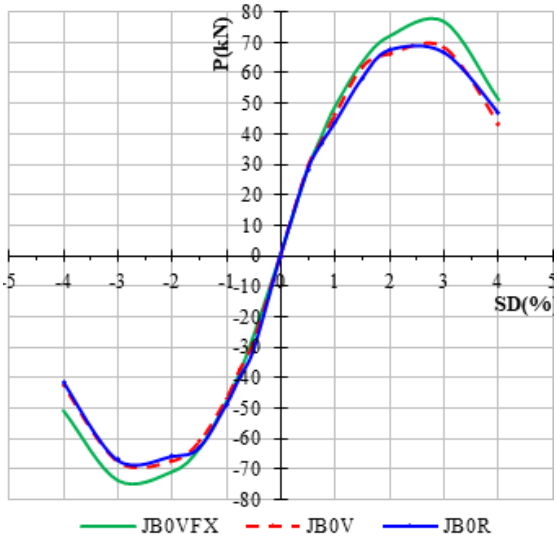

(a) . Envelope curves of maximum loads at 1st loading cycles.

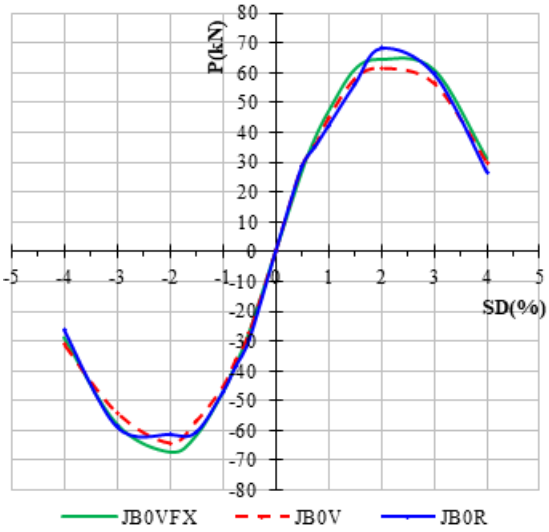

(b) . Envelopes of maximum loads at 2nd loading cycles.

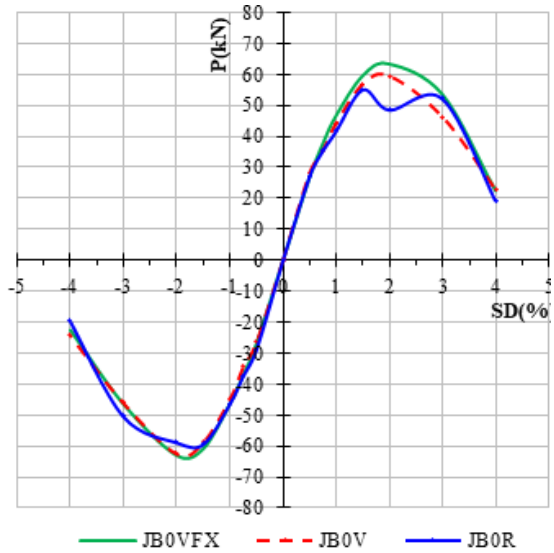

(c) . Envelopes of maximum loads at 3rd loading cycles.

Figure 9.

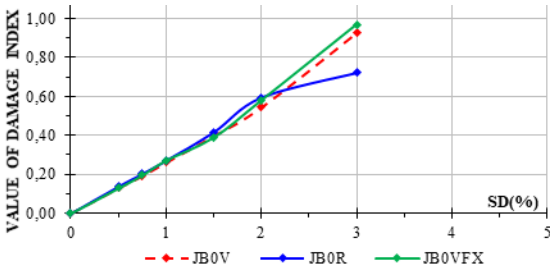

(a) . Damage index values for the 1st cycles of the loading steps.

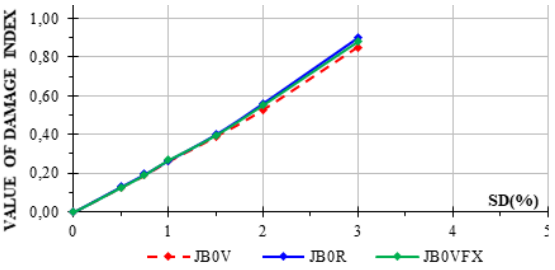

(b) . Damage index values for the 3rd cycles of the loading steps.

Figure 10.

present study, the described damage index model of Park and Ang (1985) is used to draw objective conclusions for the effectiveness of the described repair procedure for the column-transom node and to determine the degree of damage of the test specimens for each load step.

The values of δ_M, M_y, and dE of this model were obtained from the test results, while the value of δ_u was estimated using an empirical formula for calculating ultimate drift according to Eurocode 8 (EN 1998-1). Extensive tests have shown that for the quantitative estimation of the coefficient β, a value between 0.3 and 1.2 and a mean value of about 0.15 can be applied, as indicated by Cosenza et al. (1993). It should be noted that the value $\beta = 0.15$ correlates very well with the results of other damage models and that this value has, therefore, been adopted very frequently by other researchers. The stiffness degradation of the specimens is presented in Figure 11. The values of the damage indices thus calculated on the basis of the model described above are given for the three specimens tested in Figure 10a and 10b, for all specimens, after 1 and 3 loading cycles, respectively.

5.2. Equivalent viscous damping

In addition to the damage index, equivalent viscous damping is another good indicator of energy dissipation capacity per load cycle. The energy dissipation value determines the cyclic capacity of the specimen stressed to failure and defines the total energy that can be dissipated before the loss of system stability. The plastic deformations that occur after the specimen leaves the elastic region result in energy dissipation, which can be interpreted as additional damping. Figure 12 shows a general force-displacement diagram

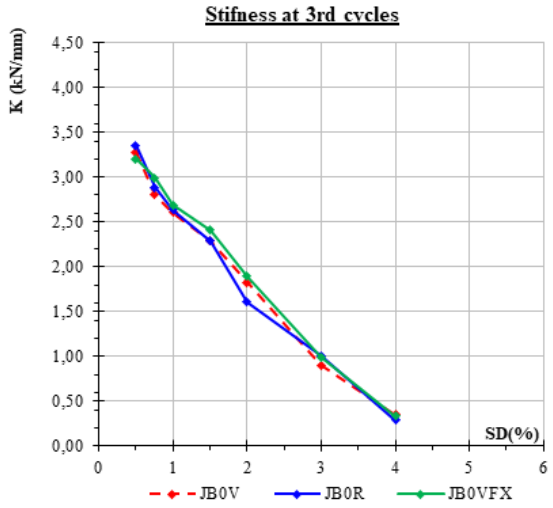

FIGURE 11. Stiffness degradation to load level.

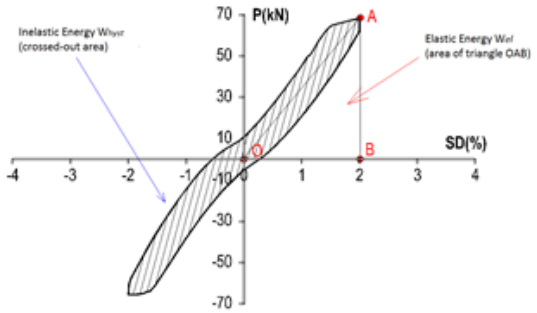

Hysteresis inelastic energy: $W_{hyst} = 1077,24\,\text{kNmm}$
Maximum elastic energy: $W_{el} = 1173,0\,\text{kNmm}$
Hysteresis damp. ratio: $\zeta_{eq} = \frac{1}{4}\pi \cdot \frac{W_{hyst}}{W_{el}} = 0.073$

FIGURE 12. Hysteresis loop of the 1st loading cycle of the 5th loading step of the specimen JB0R.

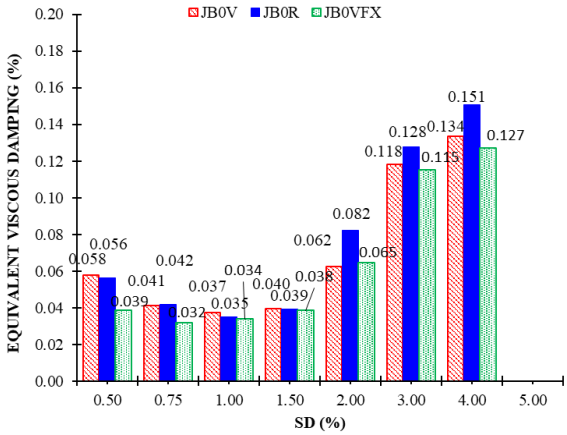

FIGURE 13. Equivalent viscous damping, per loading level, for all 3 tested specimens.

under cyclic loading. Depending on the node formation in the area of the column/beam, the curve can vary accordingly. The hatched (crossed-out) area exemplarily represents the inelastic energy (W_{hyst}) dissipated in the 1st loading interval of the 5th load level of specimen JB0R due to plastic deformations in the node. Obviously, the greater the ductility and thus the plastic deformation capacity of the materials, the greater is the integral of the hatched area, i.e., the energy enclosed by a hysteresis loop, and consequently the greater is the dissipated energy and thus the equivalent damping. The maximum elastic strain energy (W_{el}), which corresponds to the depicted degree of deformation, is equal to the area of the triangle OAB.

The additional dissipation-induced damping can be expressed in terms of viscous damping, for which the following equivalent hysteresis damping ratio is commonly used:

$$\zeta_{eq} = \frac{1}{4\pi} \cdot \frac{W_{hyst}}{W_{el}} \tag{2}$$

Based on the equivalent viscous damping ζ_{eq}, useful conclusions can be drawn about the efficiency of the investigated reinforcement measure with respect to the energy dissipation capability of the nodal formation.

The dissipated energy of the three tests is captured in terms of equivalent viscous damping (Figure 13). Viscous damping of unreinforced and reinforced specimens is compared. The representation includes the first load cycle of all load steps of an overall test (again up to SD = 4 %).

6. Conclusions

Comparing the abovementioned results, it can be stated that the energy dissipation capacity of the reinforced specimen (JB0R) is initially almost the same as that of the unreinforced specimen (JB0V) in the lower load levels. This can be easily explained by the fact that the bonded reinforcing bars have probably not yet been stressed into the plastic range, so the node with the reinforcement behaves similarly to the unreinforced one. Initially, the still low stress on the reinforcing bars does not cause a noticeable increase in dissipation (SD up to 1.50 %, Figure 13). With a further load increase, the damage increases, diagonal cracks form and the bonded reinforcing bars jump. This can be observed for load steps 5–8 (SD from 2–4 %), where the reinforced specimen shows a clear, though not too large, increase in energy dissipation capacity as compared to the unreinforced specimen.

Authors would have expected a more significant increase, but the fact that this did not occur is attributed to the cause that the glued-in bars are probably too short to be sufficiently anchored. If one looks at the crack formation and assumes a basic anchorage length of a Ø10 mm rebar of approx. 32 cm, only a few centimetres were anchored behind the crack flank. It is well known that cyclic loads lead to a very high stress on the anchorage areas anyway, since microcrack formation and the surrounding local tension fields in the anchorage area give rise to the possibility of premature slippage of the reinforcing bar.

For a future investigation, it is recommended to provide the reinforcement bars with at least an anchorage length l_b in the frame ledger. Also, to provide an additional end anchorage at the column, for example, by means of external, welded square anchor plates. The latter would also hinder spalling of the bottom concrete cover, which can be observed at the lower part of Figure 8c. Since gluing in straight reinforcing bars does not cause any major problems and can also be realized comparatively inexpensively, it is recommended that the node be penetrated with considerably more reinforcement, which must be anchored very carefully in accordance with the aforementioned recommendation.

References

[1] E. Cosenza, G. Manfredi, G. M. Verderame. Seismic assessment of gravity load designed R.C. frames: Critical issues in structural modelling. *Journal of Earthquake Engineering* **6**(sup001):101–122, 2002. https://doi.org/10.1080/13632460209350434.

[2] Structural recommendations (2006) EPANTYK, a National Greek program for the seismic assessment of existing buildings (in Greek), TEE; Athens, Greece, 2006. https://docplayer.gr/38084025-Synoptiki-paroysiasi-raseon-epantyk-ethniko-prograuua-antiseisuikis-enishysis-yfistauenon-kataskeyon.html.

[3] S. M. Alcocer. Rehabilitation of RC frame connections using jacketing. In *10th World Conference Earthquake Engineering*, pp. 5235–5240. 1993. https://www.iitk.ac.in/nicee/wcee/article/10_vol9_5235.pdf.

[4] R. S. Aboutaha, M. D. Engelhardt, J. O. Jirsa, M. E. Kreger. Retrofit of concrete columns with inadequate lap splices by the use of rectangular steel jackets. *Earthquake Spectra* **12**(4):693–714, 1996. https://doi.org/10.1193/1.1585906.

[5] A. Biddah, A. Ghobarah, T. S. Aziz. Upgrading of nonductile reinforced concrete frame connections. *Journal of Structural Engineering* **123**(8):1001–1010, 1997. https://doi.org/10.1061/(ASCE)0733-9445(1997)123:8(1001).

[6] A. Ghobarah, A. Biddah, M. Mahgoub. Rehabilitation of reinforced concrete columns using corrugated steel jacketing. *Journal of Earthquake Engineering* **1**(4):651–673, 1997. https://doi.org/10.1080/13632469708962382.

[7] A. G. Tsonos. Lateral load response of strengthened reinforced concrete beam-to-column joints. *ACI Structural Journal* **96**(1):46–56, 1999. https://doi.org/10.14359/595.

[8] C. G. Karayannis, C. E. Chalioris, K. K. Sideris. Effectiveness of RC beam-column connection repair using epoxy resin injections. *Journal of Earthquake Engineering* **2**(2):217–240, 1998. https://doi.org/10.1080/13632469809350320.

[9] A.-D. G. Tsonos. A new method for earthquake strengthening of old R/C structures without the use of conventional reinforcement. *Structural Engineering and Mechanics* **52**(2):391–403, 2014. https://doi.org/10.12989/SEM.2014.52.2.391.

[10] M. Engindeniz, L. F. Kahn, A.-H. Zureick. Repair and strengthening of reinforced concrete beam-column joints: State of the art. *ACI Structural Journal* **102**(2):187–197, 2005. https://doi.org/10.14359/14269.

[11] G. Kalogeropoulos, A.-D. Tsonos. Cyclic performance of RC columns with inadequate lap splices strengthened with CFRP jackets. *Fibers* **8**(6):39, 2020. https://doi.org/10.3390/fib8060039.

[12] D. A. Pohoryles, J. Melo, T. Rossetto, et al. Seismic retrofit schemes with FRP for deficient RC beam-column joints: State-of-the-art review. *Journal of Composites for Construction* **23**(4):03119001, 2019. https://doi.org/10.1061/(ASCE)CC.1943-5614.0000950.

[13] E. Golias, H. Lindenthal, F.-H. Schlüter, A. I. Karabinis. Ertüchtigung seismisch beschädigter Rahmenknoten aus Stahlbeton mittels FRP-Filamentbündelverbindungen. *Bautechnik* **97**(4):268–278, 2020. https://doi.org/10.1002/bate.201900085.

[14] E. Golias, A. G. Zapris, V. K. Kytinou, et al. Application of X-shaped CFRP ropes for structural upgrading of reinforced concrete beam-column joints under cyclic loading – Experimental study. *Fibers* **9**(7):42, 2021. https://doi.org/10.3390/fib9070042.

[15] C. G. Karayannis, E. Golias. Strengthening of deficient RC joints with diagonally placed external C-FRP ropes. *Earthquakes and Structures* **20**(1):123–132, 2021. https://doi.org/10.12989/eas.2021.20.1.123.

[16] C. G. Karayannis, E. Golias. Full-scale experimental testing of RC beam-column joints strengthened using CFRP ropes as external reinforcement. *Engineering Structures* **250**:113305, 2022. https://doi.org/10.1016/j.engstruct.2021.113305.

[17] E. Golias, A. G. Zapris, V. K. Kytinou, et al. Effectiveness of the novel rehabilitation method of seismically damaged RC joints using C-FRP ropes and comparison with widely applied method using C-FRP sheets – Experimental investigation. *Sustainability* **13**(11):6454, 2021. https://doi.org/10.3390/su13116454.

[18] Y.-J. Park, A. H.-S. Ang. Mechanistic seismic damage model for reinforced concrete. *Journal of Structural Engineering* **111**(4):722–739, 1985. https://doi.org/10.1061/(ASCE)0733-9445(1985)111:4(722).

ANALYSIS OF FACTORS AFFECTING THE EFFICIENCY OF *JATROPHA CURCAS* OIL AS AN ASPHALTENE STABILISER

Tomás Darío Marín Velásquez[a,*], Dany Day Josefina Arriojas Tocuyo[b]

[a] *Universidad de Oriente, Petroleum Engineering Department, Av. Universitaria, Maturín 6201, Monagas, Venezuela*

[b] *Petróleos de Venezuela, Data Analysis Management, Campo Rojo, Punta de Mata 6217, Monagas, Venezuela*

[*] corresponding author: tmarin@gmx.es

Abstract. The effect of temperature and applied dose on the efficiency of *Jatropha curcas* seed oil as an asphaltene stabiliser was studied. Two crude oil samples (light and medium) were used. *J. curcas* oil was subjected to heating at 100, 150 and 170 °C for 24 h with an unheated sample (25 °C) and applied at doses of 2, 4, 6, and 8 µL in 10 ml of sample. The asphaltene instability index (AII) was determined as the ratio between the amount in ml of n-heptane to flocculate the asphaltenes and the amount in ml of xylene to disperse the flocs. The experimental design was Taguchi factorial with a response surface for one response variable (AII) and two experimental factors (the applied dose and heating temperature). For light crude oil, the optimum conditions were 8 µL and T = 127 °C with an 85.3 % efficiency and for medium crude oil, 2 µL and T = 25 °C with a 94.3 % efficiency. The efficiency of *J. curcas* oil and the influence of the type of crude oil on the results obtained were demonstrated.

Keywords: Stability, asphaltenes, flocculation, dispersion, *Jatropha curcas*.

1. Introduction

Asphaltenes are a heavy fraction of petroleum that shows a capacity for self-association and aggregate formation, a phenomenon that can occur in any of the different stages of production and processing, due to variations in pressure, temperature, composition, and shear, among others [1]. Although the definition of asphaltenes has been the subject of discussion over the years, most researchers agree in defining them as the heavy organic components present in crude oil that are soluble in toluene and insoluble in heptane/pentane [2].

According to the colloidal theory, asphaltenes are surrounded by molecules of a similar structure, called resins, which interact with asphaltenes to improve their solubility in aliphatic media and stabilise in crude oil [3]. The aforementioned authors also consider that the asphaltenes-crude oil system is in a thermodynamically unstable state in many cases, which causes crude oils to be produced where the asphaltenes are unstable, that is when changes occur in the system conditions, they tend to separate from the liquid phase producing the phenomenon known as asphaltene precipitation. The stability of asphaltenes depends largely on the structure of the asphaltenes and their interaction with the rest of the oil components. However, the detailed molecular composition of asphaltenes remains unknown in many cases, which is because crude oil is made up of millions of different organic molecules and asphaltenes are the most complex of all [4].

Unstable asphaltenes form aggregates that precipitate and deposit in pipelines and process equipment, causing plugging and loss of productivity, which has generated a wide field of study and research on asphaltene stability and the mechanisms governing it [5–9]. The determination of stability not only leads to defining the tendency of crude oil to produce asphaltene precipitation but also lays the foundation for the application of methods to prevent the phenomenon [10]. The use of asphaltene stabilising chemicals is the most widely used method for the prevention of asphaltene precipitation due to its effectiveness and low cost [11].

The study of the efficiency of asphaltene stabilising chemical compounds is of vital importance for the oil industry, which has led to investigating chemical compounds, such as ethoxylated nonylphenol and hexadecyl-trimethylammonium bromide, which have shown positive performance [11], likewise, the use of solvents such as toluene as a stabiliser have been studied for its effect as an asphaltene solvent [12]. Alkylphenols have also been studied as asphaltene stabilisers, also demonstrating positive effects [13]. The use of aromatic polyisobutylene as an asphaltene stabiliser has also been reported, with equally positive effects [14].

The use of synthetic chemical compounds as asphaltene stabilisers generates expenses and environmental risks that have led to the search for alternatives, among which are vegetable oils, such as coconut oil, sweet almond oil, andiroba oil, and sandalwood oil, which have shown a certain degree of efficiency in asphaltene stabilisation [15]. Also, coconut oil was evaluated with positive results indicating that such oil can achieve efficiencies even higher than those of synthetic commercial products [16, 17]. Another vegetable oil that has been investigated is that of *Jatropha curcas* [18], with results showing that it can be applied

Property	crude oil A	crude oil B	Standard
API Gravity	30.8	25.5	ASTM D287
Viscosity [cP to 40 °C]	5.6	32.7	ASTM D2196
Asphaltenes [%]	1.5	6.7	ASTM D6560
Water and Sediment [%]	0.5	0.5	ASTM D4007
Viscosity-Gravity Constant (VGC)	0.878	0.854	ASTM D2501

Table 1. Properties of the crude oil samples.

as an asphaltene stabiliser. Similarly, oils, such as turnip, rosemary, sesame, chamomile, and olive oils, have been evaluated, which have shown asphaltene stabilising efficacy [19], and hazelnut and walnut oils, also with positive results as asphaltene stabilisers [20].

The objective of the present research was to determine the effect of *J. curcas* oil heating and the applied dosage on asphaltene stability in two crude oil samples, to achieve a better understanding of the parameters that may influence the performance of this vegetable oil as an asphaltene stabiliser, as an alternative for oil treatment.

2. Materials and methods

2.1. crude oil samples

Two crude oil samples, which were donated by personnel from the production management of *Petróleos de Venezuela (PDVSA)* and came from the producing fields of *El Furrial* and *Punta de Mata* in the north of the *Monagas* State, *Venezuela*, were used. The properties of the crude oil samples are detailed in Table 1.

2.2. *Jatropha curcas* oil

The seeds of *J. curcas* were collected in the town of El Furrial in Monagas State, Venezuela. Mature fruits were collected when the drupe capsule had a dark brown or black coloration. The seeds were transferred to the hydrocarbon processing laboratory of the Universidad de Oriente Monagas Nucleus, Venezuela, and the seeds were manually extracted, the shell was removed and dried in the sun for 4 days.

The seeds were crushed using a laboratory mixer and the oil was extracted by the solid-liquid extraction procedure, using a Soxhlet extraction equipment, with n-hexane as the extraction solvent. The extract was concentrated in a rotary evaporator and stored in a glass vial, according to the procedure established in previous research [18]. The extraction was performed at a ratio of 70 g of seeds per 250 ml of n-hexane and an extraction time of four hours. Several extractions were performed until 100 ml of oil was obtained. The oil was divided into four parts of 20 ml each, stored in glass bottles, and numbered consecutively from one to four. The oil one was not subjected to heating and was kept at laboratory temperature (25 °C), the other oils were subjected to heating in a laboratory oven at different temperatures for 24 hours, as shown in Table 2.

Oil sample	Heating temperature [°C]
1	25
2	100
3	150
4	170

Table 2. Heat treatment of *J. curcas* oil samples.

Temperatures were set at the researcher's discretion, taking into account previous research and the capacity of the laboratory equipment. Each heated oil sample was allowed to cool to laboratory temperature (25 °C) and then characterized by standardized density [21] and viscosity tests [22].

2.3. Asphaltenes Instability Index (AII) calculation

The Asphaltenes Instability Index (AII) was determined for the crude oil samples, defined for the research as the ratio between the amount in millilitres of n-heptane needed to obtain asphaltene aggregates visible under an optical microscope (asphaltene flocculation onset – FO) and the amount in millilitres of xylene needed to redissolve the asphaltene aggregates visible under an optical microscope or dispersion point (DP), according to Equation 1.

$$AII = \frac{DP}{FO}, \tag{1}$$

where

AII = Asphaltene instability index [ml],

FO = Flocculation Onset [ml],

DP = Dispersion point [ml].

The asphaltene instability index measures the amount of dispersant (in this case xylene) used to stabilise the asphaltenes in millilitres per millilitre of flocculants used to form the aggregates (n-heptane). The higher the AII value, the more unstable the asphaltenes are. The procedure performed to determine the original AII of the crude oil samples is shown in Figure 1.

Figure 2 shows examples of microphotographs of asphaltene aggregates obtained by the addition of n-heptane and dissolved asphaltenes upon the application of xylene.

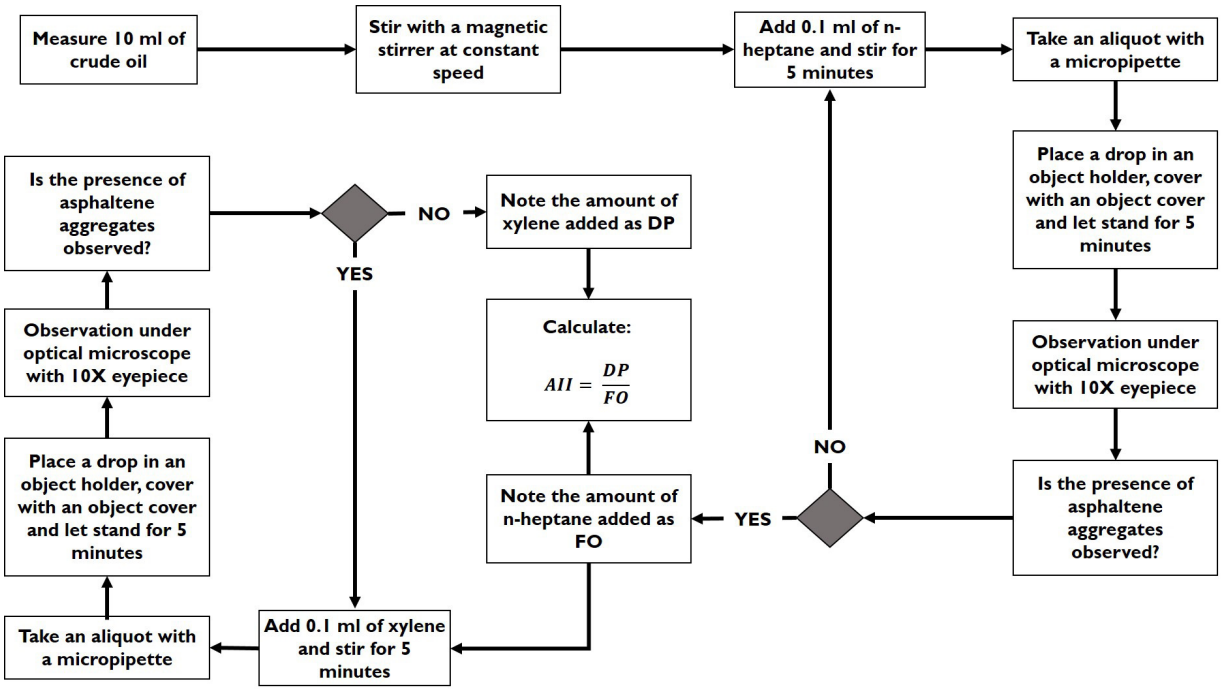

FIGURE 1. Flowchart of the procedure to obtain the AII.

FIGURE 2. Micro-photographs taken for an oil sample. A: Aggregates formed in the FO and B: Asphaltenes solubilized in the DP.

J. curcas oil samples were applied to each crude oil sample in doses of 2, 4, 6, and 8 µL in 10 ml and after mixing for 5 min with magnetic stirring, the AII was determined according to the procedure described in Figure 1. The efficiency of each oil sample at each dose applied was calculated by Equation 2.

$$\%Ef = \frac{AII_{original} - AII_{dosed}}{AII_{dosed}} \times 100, \qquad (2)$$

where

$\%Ef$ = Percentage efficiency of *J. curcas* oil,

$AII_{original}$ = Original instability index of Asphaltenes,

AII_{dosed} = Asphaltene instability index of crude oil dosed with J. curcas oil.

2.3.1. EXPERIMENTAL DESIGN

The experimental design evaluated was factorial, Taguchi type, with one response variable (AII) and two experimental factors (oil heating temperature and applied oil dose). The selected design has 16 runs, with one sample taken in each run. The model allowed estimating the effects of the 2 control factors on the response variable.

The result of the experimental analysis included Analysis of Variance (ANOVA), Pareto plot, main effects plot, response surface, and response optimization. Statistical analyses were performed with the statistical package Statgraphics Centurion XVII.

3. RESULTS AND DISCUSSION

According to the properties of the two crude oil samples shown in Table 1, it is observed that there are differences between the two. Especially in viscosity

Oil sample	Heating temperature [°C]	Density at 25 °C [g/ml]	Viscosity at 25 °C [cP]
1	25	0.917	34.47
2	100	0.919	75.14
3	150	0.922	94.13
4	170	0.910	117.61

Table 3. Shows the results of the density and viscosity properties measured for the *J. curcas* oil samples.

and percentage of asphaltenes. Crude oil B presents properties that characterise it as a heavier and denser fluid.

The VGC is a constant with which the composition of crude oil can be estimated according to the main hydrocarbon groups it contains. Crude oils with CGVs between 0.74 and 0.75 are considered paraffinic, with CGVs between 0.89 and 0.94 as naphthenic, and CGVs between 0.95 and 1.13 are typical of aromatic crudes. VGCs between 0.76 and 0.88 are typical for mixed composition crudes [23]. From the above, both samples are considered to be of a mixed base.

It is observed that the density remains almost constant, since its variations are low, which is corroborated by determining the variation coefficient (VC), whose value was 0.49 %. In contrast, viscosity did show a higher VC value of 38.98 %, which is indicative of a relationship between the oil heating temperature and viscosity.

To analyse the relationship between the two properties and the temperature to which the oil was subjected, a multivariate correlation test was performed, the results of which were that between the temperature and the density, the correlation coefficient $R = -0.1265$ and $p = 0.8394$ show that the relationship is low, negative [24] and not significant ($p > 0.05$) which corroborates the observation made in Table 3. On the contrary, the correlation coefficient between the viscosity and the temperature was $R = 0.9341$ and $p = 0.0201$, indicating a very strong and significant relationship ($p < 0.05$).

The effect of heating on oil viscosity can be accounted for by changes in composition that occur due to alterations in the fatty acid components of the oil due to the exposure to heat and oxygen, resulting in isomerization, polymerization, and oxidation reactions [25, 26]. In addition to the decomposition products mentioned above, heating of fats results in the formation of compounds of relatively high molecular weights [27], which will influence the increase in viscosity.

This behaviour was also reported when analysing the density and viscosity of coconut oil (*Cocos nucifera*) subjected to temperatures between 25 and 200 °C, also observing that the viscosity presented a coefficient of variation greater than 5 %, but without a significant correlation concerning temperature [17]. When comparing the average density of 0.917 g/ml with those reported by other investigations, it is observed that it is consistent with the values of 0.92 g/ml and 0.91 g/ml obtained in previous investigations [18, 28]. Another research reported a density of *J. curcas* oil of 0.938 g/ml, which differs from the one obtained in our work [29]. The differences or similarities in the properties of *J. curcas* oil may vary depending on both climatic and agronomic factors [30], so the results obtained are consistent with those of other investigations.

Run	Dose [µL]	Temperature [°C]	AII	%Ef
1	2	25	1.50	0
2	2	100	0.60	60.0
3	2	150	0.50	66.7
4	2	170	0.77	48.7
5	4	25	1.52	0
6	4	100	0.52	65.3
7	4	150	0.50	66.7
8	4	170	1.06	29.3
9	6	25	1.52	0
10	6	100	0.43	71.3
11	6	150	0.50	66.7
12	6	170	0.80	46.7
13	8	25	1.43	4.7
14	8	100	0.48	68.0
15	8	150	0.24	84.0
16	8	170	0.38	74.7

Table 4. Result to AII and efficiency for crude oil A with an original AII of 1.50.

3.1. Results for crude oil A sample

The data obtained after applying the experimental process with crude oil sample A are shown in Table 4.

The results indicate that the samples of *J. curcas* oil that were subjected to heating showed a promising asphaltene stabilising activity, since the efficiencies between 48.7 and 84.0 % were obtained, while the efficiency of the sample that was not subjected to heating, at a dose of 8 µL, was 4.7 %. On average, the efficiency obtained with a dose of 8 µL was the highest with 75.6 %, so it can be said that the efficiency depends on the dose applied, in addition to the heating temperature. The Taguchi model used was fitted to a quadratic trend, resulting in an ANOVA analysis (Table 5).

Source	Sum of squares	Df	Mean square	F-ratio	*p*-value
A: Dose	0.0479	1	0.0479	2.32	0.1585
B: Temperature	1.8223	1	1.8223	88.42	0.0000
AA	0.1024	1	0.1024	4.97	0.0499
AB	0.0571	1	0.0571	2.77	0.1271
BB	1.1729	1	1.1729	56.92	0.0000
Total error	0.2061	10	0.2061		
Total (corr.)	3.6891	15			

TABLE 5. ANOVA results for crude oil A sample.

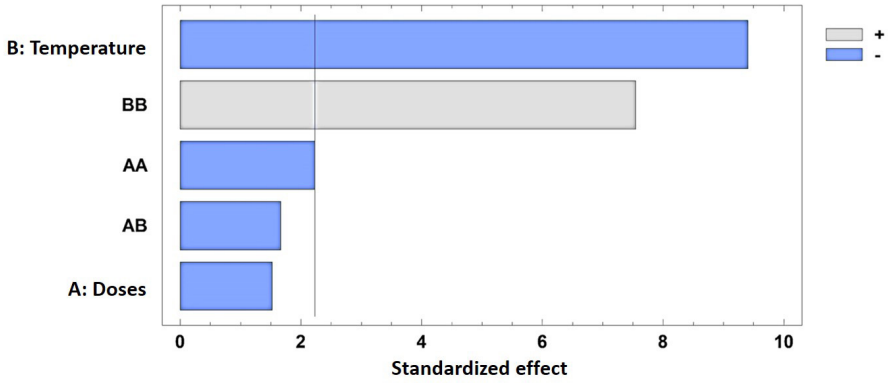

FIGURE 3. Standardized Pareto diagram for AII of crude oil sample A.

Table 5 shows that the factor that had a significant influence (p-value < 0.05) was the temperature at which the *J. curcas* oil was heated. Likewise, in the applied quadratic model, the quadratic interaction of dose (AA) and temperature (BB) also had a significant influence. On the contrary, the applied dose and the interaction between the dose and the temperature did not show a significant influence on IIA values (p-value > 0.05). This result agrees with those obtained by other authors [15, 17, 18]. It is observed that, although the efficiencies varied concerning the doses of oil applied, the differences were not statistically significant with a significance of 5 %, which contrasts with that reported in another research, where *J. curcas* oil was also applied to medium crude oil and the dose applied was significant [18], however, it is agreed that the best dose was that of 8 µL, even with the difference that in the cited research the oil was mixed with diesel oil and not pure as in the present research. For *C. nucifera* oil, it was also obtained that the 8 µL dose was the most efficient [16].

The standardized Pareto diagram (Figure 3) shows that the factor with the most important effect was temperature, followed by the quadratic factor of temperature. This is consistent with the results obtained in the analysis of variance. The effect of temperature is negative, which means that the AII for the crude oil sample varied inversely with temperature. The quadratic factor of temperature was the most important positive effect in the model.

The response optimization of the experimental design to find the dose and temperature values that generate the lowest AII value was performed using a response surface, whose model is shown in Figure 4. The optimal values were found to be a dose of 8 µL and a temperature of approximately 127 °C, with which a minimum AII value of 0.22 is obtained. These results indicate that the estimated maximum efficiency under the experimental conditions will be 85.3 %. This result is superior to that reported when applying *C. nucifera* oil to crude oil with the same API gravity (30.8), which showed a higher maximum efficiency as an asphaltene stabiliser, when heated up to 130 °C, of 78.6 % [17], indicating that *J. curcas* oil can be a more efficient alternative for asphaltene treatment in light crude samples as compared to *C. nucifera* oil.

The quadratic mathematical model used for the response surface presented a fit through the coefficient of determination R^2 of 0.944, which indicates that the model predicts the variability of AII by 94.4 %, representing a good approximation for an optimization.

It is demonstrated for crude oil sample A, that the factor that influences the efficiency of *J. curcas* oil as a stabiliser of asphaltenes is the temperature to which the oil sample is subjected, prior to its application. The effect of the heating temperature of *J. curcas* oil on asphaltenes is mainly due to the compositional change that the oil undergoes due to heating, as reported in previous research [25–27].

The formation of oxides from the fatty acids of *J. curcas* oil by heating can induce the creation of

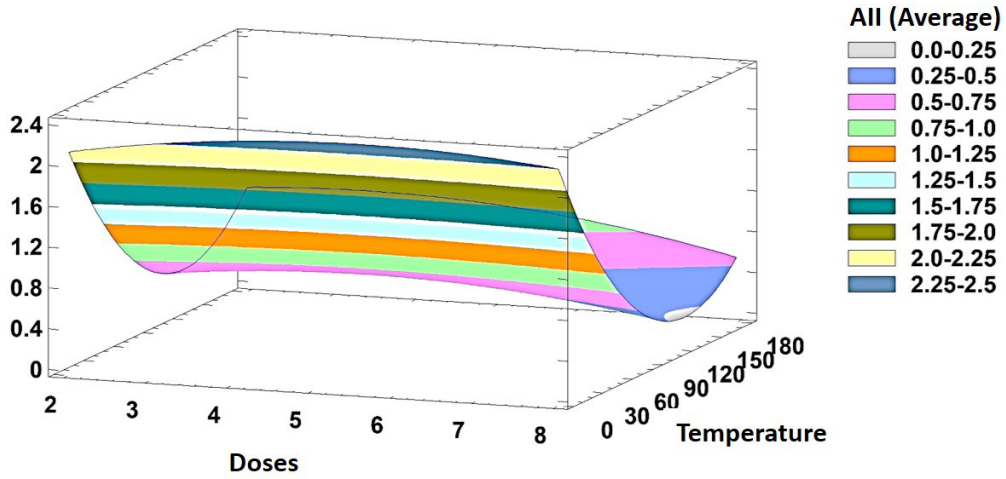

Figure 4. Estimated response surface for AII of crude oil sample A.

a surfactant layer that acts as a stabilising agent, so it is to be expected that the oil samples subjected to heating have had a higher efficiency. This indicates that the temperature to which the oil is subjected can create a more efficient surfactant system, since it has been demonstrated that the quality of the surfactant used is fundamental for achieving the stability of the asphaltenes in crude oil when a chemical treatment is applied, due to the fact that the interaction between the asphaltenes and the surfactant molecules is promoted [31].

3.2. Results for crude oil B sample

The data obtained after applying the experimental process with crude oil sample B are shown in Table 6. In the case of crude oil sample B, it was observed that the efficiencies obtained when applying *J. curcas* oil subjected to heating ranged from 17.1 to 89.3 %. The only dose at which a moderate efficiency values were obtained at all temperatures was 2 µL, which, on average, showed an efficiency of 46.9 %. At the 4 µL dose, efficiency was obtained at temperatures of 25, 100, and 170 °C, and at 150 °C, efficiency was not obtained. The higher doses (6 and 8 µL) only showed potential with the *J. curcas* oil samples heated to 170 °C. The Taguchi model used was fitted to a quadratic trend, resulting in an ANOVA analysis (Table 7).

As can be seen in Table 7, the effect of the factors on the AII of crude oil sample B differs from that obtained in crude oil sample A. In this case, the applied dose significantly influenced the AII values (p-value < 0.05) with a non-significant effect of temperature (p-value > 0.05). Looking at the interactions defined in the quadratic model only the interaction between the two factors (AB) is significant within the model (p-value < 0.05).

The influence of the dose applied coincides with that reported when applying *J. curcas* oil to a medium crude oil [18], which shows that the dose was significant even though the types of crude oil used in both investigations were different in composition.

Run	Dose [µL]	Temperature [°C]	AII	%Ef
1	2	25	0.36	74.3
2	2	100	1.16	17.1
3	2	150	1.10	21.4
4	2	170	0.35	75.0
5	4	25	0.37	73.6
6	4	100	0.88	37.1
7	4	150	1.83	0
8	4	170	0.96	31.4
9	6	25	1.91	0
10	6	100	1.54	0
11	6	150	1.78	0
12	6	170	0.74	47.1
13	8	25	1.95	0
14	8	100	1.71	0
15	8	150	1.40	0
16	8	170	0.15	89.3

Table 6. Result to AII and efficiency for crude oil B with an original AII of 1.40.

The analysis of the Pareto diagram shown in Figure 5 shows that the dose factor not only has the greatest influence on AII but also has a positive influence, while the interaction between the dose and the temperature is the factor with the greatest negative influence. It is also important to highlight that the other factors have a negative influence on the AII, although they were not significant, which may have an important effect on the behaviour of the graphical trend of the response surface method.

The optimization of the AII by response surface was determined considering a quadratic interaction model and the obtained graph can be seen in Figure 6.

Figure 6 shows that the lowest values of AII were obtained for the dose of 2 µL and at the lowest tem-

Source	Sum of squares	Df	Mean square	F-ratio	p.Value
A: Dose	1.4409	1	1.4409	7.10	0.0237
B: Temperature	0.2548	1	0.2548	1.26	0.2886
AA	0.1661	1	0.1661	0.82	0.3869
AB	1.4055	1	1.4055	6.93	0.0251
BB	0.8533	1	0.8533	4.21	0.0674
Total error	2.0290	10	0.2029		
Total (corr.)	5.5348	15			

TABLE 7. ANOVA results for crude oil A sample.

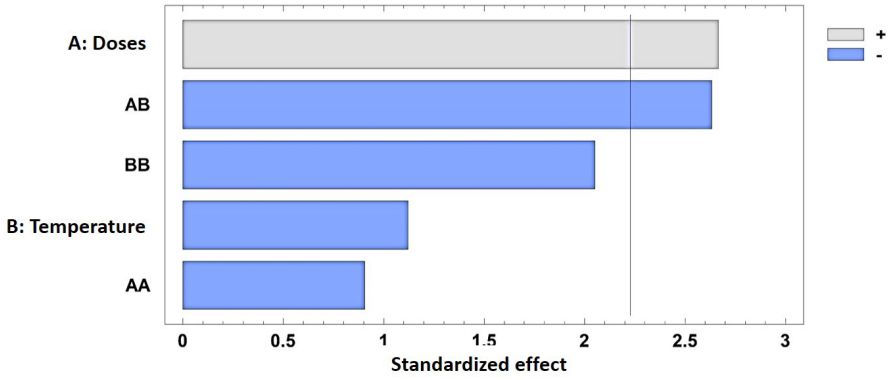

FIGURE 5. Standardized Pareto diagram for AII of crude oil sample B.

perature, which was evidenced when obtaining the dose and temperature that optimise AII, which were 2 µL and 25 °C where the response surface predicts a value of AII = 0.08, being the maximum predicted efficiency of 94.3 %. When comparing the estimated optimum efficiency with the maximum efficiency reported for a *J. curcas* oil heated at 150 °C applied to a medium crude oil sample of 28.8 °API, which was 88.33 % [18], it follows that for the crude oil sample of 25.5 °API, the oil was more efficient, although it should be taken into account that samples with different characteristics were used.

With the above, it is demonstrated that *J. curcas* oil is more efficient for the stabilisation of asphaltenes in the crude oil sample B and without being subjected to heating, as statistically obtained.

The quadratic mathematical model used for the response surface analysis, according to the coefficient of determination $R^2 = 0.633$, predicts, by 63.3 %, the optimal combination of the Dose and Heating Temperature values of *J. curcas* oil for crude oil sample B.

The results showed higher efficiency of *J. curcas* oil as compared to synthetic resins with which values of 55.56 % were obtained [32], however, as was also observed in other research, the stabilisation of asphaltenes does not depend only on the products used, but also on the characteristics of the oils where they are applied.

In the case of crude oil B, the stability behaviour is different from that observed in crude oil A. It is observed that the applied dose has a significant effect, in addition to its interaction with temperature. The lowest doses were those with the best performance, and amongst them, the 2 ml dose was shown to be efficient both for the oil sample not subjected to heating and for the one subjected to 170 °C. From the previous result, it can be said that for this particular crude oil, the composition of its asphaltenes seems to interact better with the oil in its original state (without being subjected to heating) and at lower doses, which was corroborated by the response surface, so the structural changes that the oil underwent when heated do not favour the stability of the asphaltenes in this sample.

The stability trend of asphaltenes, with respect to different chemicals, is, in most cases, not continuous, which is due to the fact that the interactions between asphaltenes and surfactants is dependent on the complexity of the former [33, 34].

According to what was obtained, it can be said that the characteristics of the crude oil and its composition can determine the optimum doses of asphaltene stabiliser product, as well as the most indicated product for its treatment. These results are consistent with those reported for the stability of two samples of medium crude oil after applying *C. nucifera* oil, where it was concluded that the results were dependent on the crude oil sample used [16].

According to previous research, it is accepted that composition influences the stability of asphaltenes in crude oil. Stable crude oil has higher values of the polar fraction, i.e., asphaltenes, resin, and aromatics. Therefore, when different crude oil samples are used in terms of their properties, different asphaltenes

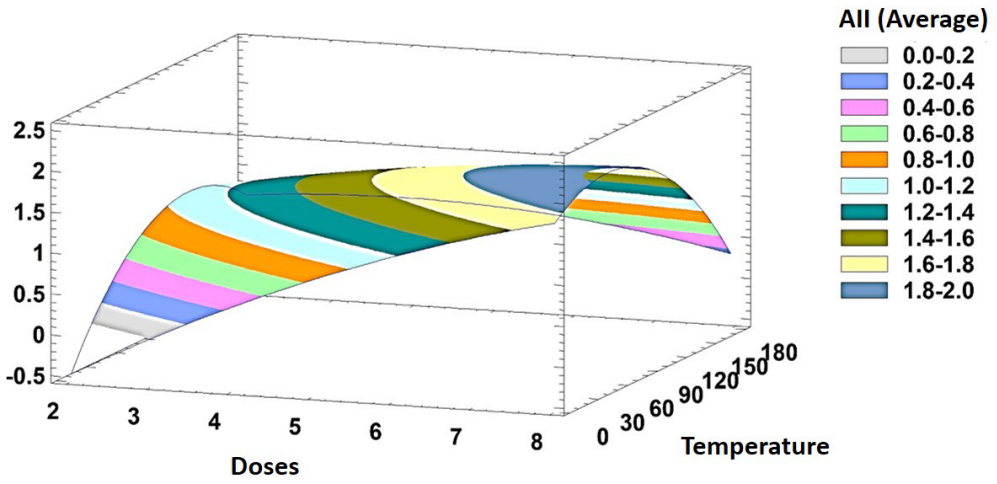

Figure 6. Estimated response surface for AII of crude oil sample B.

stability results and behaviour can be obtained [35], which justifies the differences observed in the present investigation when using two different crude oil samples.

One of the determining factors in the stability of asphaltenes that can influence the efficiency of the stabilising products is the presence of resins, which, in the crude oil, are considered a key factor as molecules that stabilise the colloidal particles of asphaltenes against aggregation, their mechanism of action being a combined repulsion/adhesion process [36, 37]. Likewise, other elements present in the crude oil composition, such as paraffin waxes, water, and organometallic compounds, act as destabilisers of asphaltenes, and also the presence of fine solids in the oil can stabilise asphaltenes [38, 39].

The use of *J. curcas* oil as an asphaltene stabiliser is shown to be feasible according to the results obtained, this is possibly due to its composition, formed by fatty acids, mostly linoleic acid [40, 41] which has been shown to have asphaltene-stabilising properties, as well as other acids such as palmitic acid, which is also present in the composition of the evaluated oil [15]. The polar nature of the fatty acid components of vegetable oils, such as that of *J. curcas*, give them surfactant properties, making them potential asphaltene stabilisers, which can be supported by the following factors: it is of utmost importance to find new substances with a higher solubility, because of the good results obtained with organic acids, taking into account that vegetable oils are mixtures rich in free or glyceride-forming organic acids, also vegetable oils are easy to obtain and cheaper than most of the polymeric dispersants used commercially Also, once the state of conservation of such substances is sufficient, their use could have positive social and economic consequences [19].

4. Conclusion

It is concluded that *J. curcas* oil is a viable alternative for the stabilisation of asphaltenes; however, its maximum efficiency depends on the dose applied, the temperature to which it is subjected in a heating process before its application, and the characteristics of the crude oil in which it is applied.

The compositional changes that occur in *J. curcas* oil when it is heated are a determining factor in its efficiency as a stabiliser of asphaltenes in crude oil, showing that when the oil is heated, a higher stabilisation efficiency is obtained.

The Taguchi factorial experimental design and response surface demonstrated that the optimum dosage and type of oil (based on heating temperature) to be applied to a particular crude oil can be obtained, which can also be applied to the selection of other products used for asphaltene stabilisation at the laboratory level.

References

[1] L. Ginçalves. *Precipitation of asphaltenes in petroleums induced by n-alkanes in the presence or absence of carbon dioxide (CO2) [in Portuguese]*. Ph.D. thesis, Universidade Estadual de Campinas, Brasil, 2015.

[2] H. Belhaj, H. A. Khalifeh, N. Al-Huraibi. Asphaltene stability in crude oil during production process. *Journal of Petroleum & Environmental Biotechnology* **4**(3):1000142, 2013. https://doi.org/10.4172/2157-7463.1000142.

[3] E. Buenrostro-González, C. Lira-Galeana, A. Gil-Villegas, J. Wu. Asphaltene precipitation in crude oils: Theory and experiments. *AIChE Journal* **50**(10):2552–2570, 2004. https://doi.org/10.1002/aic.10243.

[4] F. J. Martín-Martínez, E. H. Fini, M. J. Buehler. Molecular asphaltene models based on Clar sextet theory. *RSC Advances* **5**(1):753–759, 2015. https://doi.org/10.1039/c4ra05694a.

[5] A. Chamkalani. Correlations between SARA fractions, density, and RI to investigate the stability of asphaltene.

International Scholarly Research Notices **2012**:219276, 2012. https://doi.org/10.5402/2012/219276.

[6] A. Chamkalani, A. H. Mohammadi, A. Eslamimanesh, et al. Diagnosis of asphaltene stability in crude oil through "two parameters" SVM model. *Chemical Engineering Science* **81**:202–208, 2012. https://doi.org/10.1016/j.ces.2012.06.060.

[7] A. A. Gabrienko, V. Subramani, O. N. Martyanov, S. G. Kazarian. Correlation between asphaltene stability in n-heptane and crude oil composition revealed with *insitu* chemical imaging. *Adsorption Science & Technology* **32**(4):243–255, 2014. https://doi.org/10.1260/0263-6174.32.4.243.

[8] R. Guzmán, J. Ancheyta, F. Trejo, S. Rodríguez. Methods for determining asphaltene stability in crude oils. *Fuel* **188**:530–543, 2017. https://doi.org/10.1016/j.fuel.2016.10.012.

[9] S. Fakher, M. Ahdaya, M. Elturki, A. Imqam. An experimental investigation of asphaltene stability in heavy crude oil during carbon dioxide injection. *Journal of Petroleum Exploration and Production Technology* **10**:919–931, 2020. https://doi.org/10.1007/s13202-019-00782-7.

[10] M. Z. Hasanvand, M. Montazeri, M. Salehzadeh, et al. A literature review of asphaltene entity, precipitation, and deposition: introducing recent models of deposition in the well column. *Journal of Oil, Gas and Petrochemical Sciences* **1**(3):83–89, 2018. https://doi.org/10.30881/jogps.00016.

[11] R. G. Martins, L. S. Martins, R. G. Santos. Effects of short-chain n-alcohols on the properties of asphaltenes at toluene/air and toluene/water interfaces. *Colloids and Interfaces* **2**(2):13–22, 2018. https://doi.org/10.3390/colloids2020013.

[12] A. Natarajan, N. Kuznicki, D. Harbottle, et al. Understanding mechanisms of asphaltene adsorption from organic solvent on mica. *Langmuir* **30**(31):9370–9377, 2014. https://doi.org/10.1021/la500864h.

[13] L. Goual, M. Sedghi, X. Wang, Z. Zhu. Asphaltene aggregation and impact of alkylphenols. *Langmuir* **30**(19):5394–5403, 2014. https://doi.org/10.1021/la500615k.

[14] T. E. Chávez-Miyauchi, L. S. Zamudio-Rivera, V. Barba-López. Correction to aromatic polyisobutylene succinimides as viscosity reducers with asphaltene dispersion capability for heavy and extra-heavy crude oils. *Energy & Fuels* **30**(1):758, 2016. https://doi.org/10.1021/acs.energyfuels.5b02945.

[15] L. C. Rocha, M. Silva Ferreira, A. C. da Silva Ramos. Inhibition of asphaltene precipitation in Brazilian crude oils using new oil soluble amphiphiles. *Journal of Petroleum Science and Engineering* **51**(1-2):26–36, 2006. https://doi.org/10.1016/j.petrol.2005.11.006.

[16] Y. B. Bello, J. R. Manzano, T. D. Marín. Comparative analysis of the dispersing efficiency of asphaltenes of products based on coconut oil (*Cocusnucifera*) as active component and commercial dispersants applied to oil samples from the Furrial field, Monagas State Venezuela [in Spanish]. *Revista Tecnológica ESPOL – RTE* **28**(2):51–61, 2015.

[17] T. D. Marín. Coconut oil (*Cocosnucifera*) as an asphaltene stabilizer in a crude oil from Monagas State, Venezuela: effect of temperature [in Spanish]. *Ingeniería y Desarrollo* **37**(2):289–305, 2019. https://doi.org/10.14482/inde.37.2.1627.

[18] T. Marín, S. Marcano, M. Febres. Evaluation of *Jatrophacurcas* oil as an asphaltene dispersant additive in a crude oil from the Furrial field, Venezuela [in Spanish]. *Ingeniería* **20**(2):98–107, 2016.

[19] E. Mardani, B. Mokhtari, B. Soltani Soulgani. Comparison of the inhibitory capacity of vegetable oils, and their nonionic surfactants on Iran crude oil asphaltene precipitation using Quartz crystal microbalance. *Petroleum Science and Technology* **36**(11):744–749, 2018. https://doi.org/10.1080/10916466.2018.1445103.

[20] N. Mohamadshahi, A. R. Solaimany Nazar. Experimental evaluation of the inhibitors performance on the kinetics of asphaltene flocculation. *Journal of Dispersion Science and Technology* **34**(4):590–595, 2013. https://doi.org/10.1080/01932691.2012.681608.

[21] ASTM D1298. *Standard Test Method for Density, Relative Density, or API Gravity of Crude Petroleum and Liquid Petroleum Products by Hydrometer Method.* ASTM International, West Conshohocken, 2017. https://doi.org/10.1520/D1298-12BR17.

[22] ASTM D2196. *Standard Test Methods for Rheological Properties of Non-Newtonian Materials by Rotational Viscometer.* ASTM International, West Conshohocken, 2018. https://doi.org/10.1520/D2196-18E01.

[23] A. Bded, T. Hameed khlaif. Evaluation properties and PNA analysis for different types of lubricants oils. *Iraqi Journal of Chemical and Petroleum Engineering* **20**(3):15–21, 2019. https://doi.org/10.31699/IJCPE.2019.3.3.

[24] W. Hopkins. A new view of statistics, 2014. https://complementarytraining.net/wp-content/uploads/2013/10/Will-Hopkins-A-New-View-of-Statistics.pdf.

[25] L. Brühl. Fatty acid alterations in oils and fats during heating and frying. *European Journal of Lipid Science and Technology* **116**(6):707–715, 2014. https://doi.org/10.1002/ejlt.201300273.

[26] D. N. Raba, D. R. Chambre, D.-M. Copolovici, et al. The influence of high-temperature heating on composition and thermo-oxidative stability of the oil extracted from Arabica coffee beans. *PLoS ONE* **13**(7):e0200314, 2018. https://doi.org/10.1371/journal.pone.0200314.

[27] W. W. Nawar. Thermal degradation of lipids. A review. *Journal of Agricultural and Food Chemistry* **17**(1):18–21, 1969. https://doi.org/10.1021/jf60161a012.

[28] N. Araiza, L. Alcaraz-Meléndez, M. A. Angulo, et al. Physicochemical properties of Jatropha curcas seed oil from wild populations in Mexico [in Spanish]. *Revista de la Facultad de Ciencias Agrarias UNCUYO* **47**(1):127–137, 2015.

[29] S. A. García-Muentes, F. Lafargue-Pérez, B. Labrada-Vázquez, et al. Physicochemical properties of oil and biodiesel produced from Jatropha curcas L. in the province of Manabí, Ecuador [in Spanish]. *Revista Cubana de Química* **30**(1):142–158, 2018.

[30] A. K. M. Aminul Islam, Z. Yaakob, N. Anuar, et al. Physiochemical properties of *Jatrophacurcas* seed oil from different origins and candidate plus plants (CPPs). *Journal of the American Oil Chemists' Society* **89**(2):293–300, 2012. https://doi.org/10.1007/s11746-011-1908-7.

[31] M. Ahmadi, Z. Chen. Molecular interactions between asphaltene and surfactants in a hydrocarbon solvent: Application to asphaltene dispersion. *Symmetry* **12**(11):1767–1785, 2020. https://doi.org/10.3390/sym12111767.

[32] B. Gutiérrez. *Evaluation of the dispersant properties of modified (I) resins from hydrotreated blackberry crude oil on asphaltenes at laboratory level [in Spanish].* Master's thesis, Universidad de Carabobo, Valencia, Venezuela, 2017.

[33] Z. Rashid, C. D. Wilfredand, T. Murugesan. Effect of hydrophobic ionic liquids on petroleum asphaltene dispersion and determination using UV-visible spectroscopy. *AIP Conference Proceedings* **1891**(1):020118, 2017. https://doi.org/10.1063/1.5005451.

[34] Y. V. Larichev, A. V. Nartova, O. N. Martyanov. The influence of different organic solvents on the size and shape of asphaltene aggregates studied via small-angle X-ray scattering and scanning tunneling microscopy. *Adsorption Science & Technology* **34**(2-3):244–257, 2016. https://doi.org/10.1177/0263617415623440.

[35] S. Ashoori, M. Sharifi, M. Masoumi, M. M. Salehi. The relationship between SARA fractions and crude oil stability. *Egyptian Journal of Petroleum* **26**(1):209–213, 2017. https://doi.org/10.1016/j.ejpe.2016.04.002.

[36] J. C. Pereira, I. López, R. Salas, et al. Resins: The molecules responsible for the stability/instability phenomena of asphaltenes. *Energy & Fuels* **21**(3):1317–1321, 2007. https://doi.org/10.1021/ef0603333.

[37] C. García-James, F. Pino, T. Marín, U. Maharaj. Influence of resin/asphaltene ration on paraffin wax deposition in crude oils from barrackpore oilfield in Trinidad. In *SPETT 2012 Energy Conference and Exhibition*. Port-of-Spain, Trinidad, 2012. https://doi.org/10.2118/158106-MS.

[38] A. Prakoso, A. Punase, K. Klock, et al. Determination of the stability of asphaltenes through physicochemical characterization of asfaltenes. In *SPE Western Regional Meeting*. Anchorage, Alaska, USA, 2016. https://doi.org/10.2118/180422-ms.

[39] A. Prakoso, A. Punase, E. Rogel, et al. Effect of asphaltene characteristics on its solubility and overall stability. *Energy & Fuels* **32**(6):6482–6487, 2018. https://doi.org/10.1021/acs.energyfuels.8b00324.

[40] L. F. Campuzano-Duque, L. A. Ríos, F. Cardeño-López. Compositional characterization of the fruit of 15 varieties of *Jatrophacurcas* L. in the department of Tolima, Colombia [in Spanish]. *Corpoica Ciencia y Tecnología Agropecuaria* **17**(3):379–390, 2016. https://doi.org/10.21930/rcta.vol17_num3_art:514.

[41] P. Guevara-Fefer, N. Niño-García, Y. De-Jesús-Romero, G. Sánchez-Ramos. Jatropha sotoinunyezii and Jatropha curcas, species from Tamaulipas: a comparison from a bio-fuels perspective [in Spanish]. *CienciaUAT* **11**(1):91–100, 2016. https://doi.org/10.29059/cienciauat.v11i1.769.

A MINDLIN SHELL FINITE ELEMENT FOR STONE MASONRY BRIDGES WITH BACKFILL

Petr Řeřicha

Czech Technical University in Prague, Faculty of Civil Engineering, Thákurova 7, Prague, Czech Republic
correspondence: petr.rericha@fsv.cvut.cz

Abstract. Stone masonry bridges are difficult to analyse with commercial finite element (FE) packages for their specific heterogeneous composition. The stone arch is best modelled as a thick shell where there are predestined directions of tension failure, normal to the bed joints. A dedicated, very simple, Mindlin shell finite element is developed with five translational degrees of freedom per node. It features compatibility with linear isoparametric or constant strain elements for the backfill. Most bridges can be analysed with a sufficient accuracy assuming plain strain conditions. The element then simplifies to a Timoshenko beam element with three translational degrees of freedom per node. An application of the latter one to the bridge at Poniklá is presented.

Keywords: Masonry arches, no tension joints, thick shell elements, octave script.

1. Introduction

Masonry arch bridges still constitute a considerable part of the bridge stock of the transport infrastructure in Czechia. Many of them are valueable monuments of the technical expertise and craftsmenship of the past generations as well. Design standards for this sort of bridges do not exist worlwide, guides and manuals for load rating are provided instead, like [1] or [2]. They usually contain conservative approximate methods for a routine assessment and some guidance and recommendations for more complicated individual assessments based on advanced structural analysis methods.

A structural analysis of masonry arch bridges is specific in that the ultimate limit state forces and stresses cannot be solved for assuming homogeneous isotropic linear elastic material. In contrast to that, design standards for reinforced concrete and steel structures admit such solutions. EN 1996-1-1 codifies in clause 6.1.1(2) that plane sections remain plane and the tensile strength of masonry perpendicular to bed joints is zero in the ultimate limit state. The standard is not compulsory for bridges but its conditions should be perceived as the minimum for them. Cracks in the bed joints of the masonry arches affect the stress distribution in a way that does not admit a linear solution.

The simplest material model that can be accepted is the no-tension linear material where the no-tension condition applies to the normal stress in the planes parallel to the bed joints. This specific behaviour is difficult to simulate by material models available in general purpose program packages, [3]. Commercial packages do not include such material models. There were attempts to achieve the specific properties of the masonry arches with a trivial model of a heterogeneous material – individual meshing of voussoirs and joints by standard continuum finite elements with homogeneous material models. It is possible in academic works but not acceptable in design practice for demands on the labour, software and input data on materials properties. This experience testifies that *shell/beam elements using the rigid normals assumption (Timoshenko, Mindlin, Bernoulli-Navier and other assumptions) are indispensable for the solution of the masonry arch bridges.*

Several dedicated codes have been written around 1990 for the analysis of masonry arches based on the Castigliano principle, CTAP [4], [5], rigid block assumption RING , [6], mechanism based ARCHIE, [7] and others. All of them assume plane strain conditions. These models simulate very well the observed behaviour of masonry arches in situ and in large scale model tests. They have been applied worldwide in practice despite their common drawback that they underestimate the interaction of the barrel, backfill and pavement.

Two simple finite elements for thick shells are developed based on the Timoshenko/Mindlin kinematic assumptions, one for plane stress/plane strain conditions, the other for 3D shells. In order to facilitate a seamless interaction with the backfill continuum, only translational degrees of freedom (DOFs) are employed. The no-tension linear elastic constitutive equations are integrated in a closed form for the normal stress in planes parallel to the bed joints. The shape functions of the elements are 2D and 3D variants of the same concept. The simpler 2D variant is presented first with an application to a bridge, a triangle thick shell element follows.

2. The TT element, Timoshenko beam with translational DOFs

The displacement shape functions are sketched in Figure 1 for the axial displacement $u_{i,t}$ of node i, for the

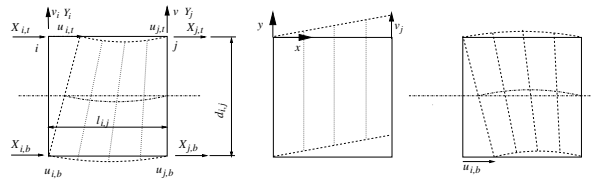

FIGURE 1. Shape functions, DOFs and conjugate nodal forces of the TT element

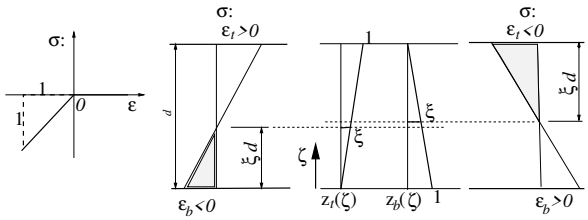

FIGURE 2. Stress/strain diagram, strain shape functions and normal stress diagrams of the TT element

lateral displacement v_j of node j and for the axial displacement $u_{i,b}$. Axial and lateral directions denote the element local x and y directions, indices t and b denote the top and bottom faces later also extrados and intrados of the arch. The local x axis goes from node i to node j. The deflection line is parabolic and symmetric. It's single free parameter is determined so that the shear strain energy is minimum for any imposed node displacements. Analogous shape functions are valid for all four axial DOFs $u_{i/j,t/b}$ and the same applies to the two lateral DOFs $v_{i/j}$.

The cross-sections remain straight but not normal to the deflected beam axis. In an isoparametric beam element (linear variation of the cross-section rotations and shear deformation, axial strain and lateral deflections along the beam axis), there would be no deflections for the $u_{i/j,t}$ DOFs. The element is known to lock for small depths of the beam owing to excessive work of the shear deformation. The present element features a constant shear deformation since the antisymmetric (with respect to the element centre) part of the cross-section rotations is assigned to a constant curvature of the deflection line. The element DOFs are ordered in the $\{u\}$ matrix,

$$\{u\} = \left\{ \begin{array}{c} \{u\}_i \\ \{u\}_j \end{array} \right\}, \quad \{u\}_n = \left\{ \begin{array}{c} u_{n,t} \\ v_n \\ u_{n,b} \end{array} \right\}, \quad n = i, j$$

Linear normal and constant shear element strains are specified by top and bottom face normal strains ε_t, ε_b and shear strain γ, ordered in the matrix of internal strains $\varepsilon = \{\varepsilon_t, \varepsilon_b, \gamma\}^T$. Shear strain γ and conjugate shear stress τ have *opposite signs than usual in elasticity*, $\gamma = -(\partial u_x/\partial y + \partial u_y/\partial x)/2$. The element geometric matrix $[B]$ reads:

$$[B] = \frac{1}{l} \left[\begin{array}{cccccc} -1 & 0 & 0 & 1 & 0 & 0 \\ 0 & 0 & -1 & 0 & 0 & 1 \\ l/2/d & -1 & -l/2/d & l/2/d & 1 & -l/2/d \end{array} \right]$$

Conjugate to node displacements $\{u\}$ are the nodal forces $\{X\}$, conjugate to $\{\varepsilon\}$ is the matrix of internal forces $\{S\}$. The nodal forces in terms of nodal displacements read

$$\{X\} = [B]^T\{S\}(\{\varepsilon\}) = [B]^T\{S\}([B]\{u\}) \quad (1)$$

Constitutive equations for the cross-section are developed separately for the bending, the first two members of $\{\varepsilon\}$ and $\{S\}_{int}$.

2.1. CONSTITUTIVE EQUATIONS FOR BENDING

No-tension linear elastic material is assumed, see the stress-strain diagram in Figure 2. The no-tension condition is applied to the normal stress in cross-sections and bed joints of the arch. Though simple, it makes possible the most frequent type of failure of the stone masonry arch bridges. The normal strain ε is determined by the top and bottom face strains ε_t, ε_b through the shape functions shown in the centre of Figure 2.

$$\varepsilon = z_t(\zeta)\varepsilon_t + z_b(\zeta)\varepsilon_b$$

Constitutive equations of the cross-sections are defined in terms of dimensionless functions $s_t()$ and $s_b()$ of dimensionless arguments:

$$s_t(\varepsilon_t, \varepsilon_b) = \int_0^1 z_t(\zeta) s(\varepsilon_t z_t(\zeta) + \varepsilon_{b,x} z_b(\zeta)) \mathrm{d}\zeta$$
$$s_b(\varepsilon_t, \varepsilon_b) = \int_0^1 z_b(\zeta) s(\varepsilon_t z_t(\zeta) + \varepsilon_b z_b(\zeta)) \mathrm{d}\zeta, \quad (2)$$

The cross-section forces are $S_{t/b} = Ebds_{t/b} = EAs_{t/b}$ (valid for both t and b subscripts, where E is the Young modulus, b the cross-section width, d the cross-section depth and A its area. Functions $s_{t/b}()$ and their derivatives with respect to ε_t, ε_b have to be developed separately for four possible strain states:

Algorithm start

When $\varepsilon_t > 0$ **and** $\varepsilon_b > 0$ then all internal forces are 0, the cross-section is totally disintegrated. All stresses and internal forces vanish in the element.

When $\varepsilon_t > 0$ **and** $\varepsilon_b < 0$,
then (see the left strain diagram in Figure 2):

$$\xi = \frac{\varepsilon_b}{\varepsilon_b - \varepsilon_t}$$

$$s_t = \varepsilon_b \xi^2/6, \quad s_b = (0.5 - \xi/6)\xi\varepsilon_b$$

$$\frac{\partial s_t}{\partial \varepsilon_t} = \xi^3/3, \quad \frac{\partial s_t}{\partial \varepsilon_b} = \left(1 - 2\xi\frac{\varepsilon_t}{\varepsilon_b}\right)\frac{\xi^2}{6}$$

$$\frac{\partial s_b}{\partial \varepsilon_t} = (0.5 - \xi/3)\xi^2, \quad \frac{\partial s_b}{\partial \varepsilon_b} = (0.5 - \frac{\xi}{6})\xi - (0.5 - \frac{\xi}{3})\xi^2\frac{\varepsilon_t}{\varepsilon_b}$$

When $\varepsilon_t < 0$ **and** $\varepsilon_b > 0$,
then (see the right strain diagram in Figure 2):

$$\xi = \frac{\varepsilon_t}{\varepsilon_t - \varepsilon_b}$$

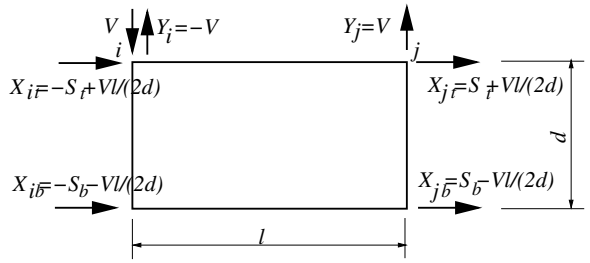

FIGURE 3. Element internal forces $\{S\}$ and nodal forces $\{X\}$

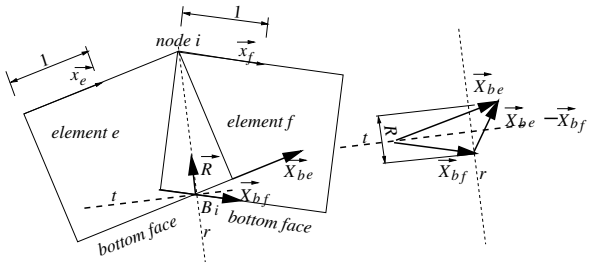

FIGURE 4. Equilibrium of node i

$$s_t = (0.5 - \frac{\xi}{6})\xi\varepsilon_t, \quad s_b = \varepsilon_t\xi^2/6$$

$$\frac{\partial s_t}{\partial \varepsilon_t} = (0.5-\frac{\xi}{6})\xi-(0.5-\frac{\xi}{3})\xi^2\frac{\varepsilon_b}{\varepsilon_t}, \quad \frac{\partial s_t}{\partial \varepsilon_b} = (0.5-\xi/3)\xi^2$$

$$\frac{\partial s_b}{\partial \varepsilon_t} = \left(1 - 2\xi\frac{\varepsilon_b}{\varepsilon_t}\right)\frac{\xi^2}{6}, \quad \frac{\partial s_b}{\partial \varepsilon_b} = \xi^3/3$$

When $\varepsilon_t < 0$ and $\varepsilon_b < 0$,
then the cross-section is linear elastic and dimensionless generalised forces are

$$s_{t/b} = (2\varepsilon_{t/b} + \varepsilon_{b/t})/6$$

The cross-section stiffness matrix:

$$\frac{\partial\{s_{bend}\}}{\partial\{\varepsilon_{bend}\}} = \frac{1}{6}\begin{bmatrix} 2 & 1 \\ 1 & 2 \end{bmatrix} \tag{3}$$

Algorithm end
The bending stiffness tangent matrix of the cross-section is denoted for a later reference

$$[D_{bend}] = \frac{\partial\{s_{bend}\}}{\partial\{\varepsilon_{bend}\}} = Ebd\begin{bmatrix} \frac{\partial s_t}{\partial \varepsilon_t} & \frac{\partial s_t}{\partial \varepsilon_b} \\ \frac{\partial s_b}{\partial \varepsilon_t} & \frac{\partial s_b}{\partial \varepsilon_b} \end{bmatrix} \tag{4}$$

2.2. Full cross-section stiffness matrix

The shear force V is computed from the shear deformation γ in the Timoshenko beam. Linear elastic behaviour

$$V = G_e bd\gamma$$

is assumed in the model, independent on the normal stress in the cross-sections. This assumption is mostly sufficient for cross-sections of the stone masonry arch bridges. The full cross-section stiffness matrix is then

$$[D_{cs}] = \begin{bmatrix} [D_{bend}] & \{0\} \\ \{0\}^T & G_e bd \end{bmatrix}$$

The matrix has to be adapted when more involved cross-section constitutive equations are necessary, for instance, shear failure of bed joints. The nodal forces $\{X\} = \{X_{i,t}, Y_i, X_{i,b}, X_{j,t}, Y_j, X_{j,b}\}^T$ of the element can be obtained in terms of the internal forces $\{S\}$ either by expansion of $[B]^T\{S\}$ or by the equilibrium conditions of the element in Figure 3: The dimensionless cross-section stiffness matrix for bending $[D_{bend}] = \partial\{S_{bend}/\partial\{\varepsilon_{bend}\}$ *is not symmetric* when the neutral axis lies inside the cross-section so that the element and structure matrices will not be symmetric, too. The element stiffness matrix is

$$[K]_{straight} = Ebdl[B]^T[D_{cs}][B]$$

It is ready for application in straight beams, but for arches and other curved beams, it must be modified.

2.3. Arch nodes equilibrium

The equilibrium of the nodal forces $\vec{X}_{ibe} = X_{ibe}\vec{x_e}$, $\vec{X}_{ibf} = X_{ibf}\vec{x_f}$ of the adjacent elements e and f at arch node i simplifies to $X_{ibe} + X_{ibf} = 0$ when the element's unit length direction vectors $\vec{x}_{l,e}$ and $\vec{x}_{l,f}$ coincide, see the Figure 4. The node index i is omitted for brevity as long as the the development concerns just a single node i. X_{be} and X_{bf} are the magnitudes of the respective forces with positive senses in element's direction vectors. These forces are stored in the third components of the element nodal forces matrices and in case of parallel elements, the equilibrium equation at a node is $\{X\}_e + \{X\}_f = \{0\}$, where indices $_e$ and $_f$ indicate the left and right element, respectively.

When the adjacent elements are not parallel, the resultants of the two forces add up to force $\vec{R}$. The force is decomposed into component R in the direction r and force T in the t direction. The component R can act anywhere on ray r since the arch is considered rigid in the transverse direction. It is thus added to forces acting at node i. Component T must vanish to keep the null moment with respect to joint i.

$$T = (X_{be}\vec{x_e} + X_{bf}\vec{x_f})\cdot\vec{t} =$$

$$= (X_{be}\vec{x_e} + X_{bf}\vec{x_f})\cdot(\vec{x_e} + \vec{x_f})/|\vec{x_e} + \vec{x_f}| = 0,$$

which implies

$$X_{be} + X_{bf} = 0,$$

provided the two elements are not normal to each other. Force R is

$$\begin{aligned} R &= (X_{be}\vec{x_e} - X_{bf}\vec{x_f})\cdot\vec{r} \\ &= (X_{be}\vec{x_e} - X_{bf}\vec{x_f})\cdot(\vec{x_e} - \vec{x_f})/|\vec{x_e} - \vec{x_f}| \\ &= (X_{be} - X_{bf})\sqrt{(1 - \vec{x_e}\cdot\vec{x_f})/2} \end{aligned}$$

and its vector

$$\vec{R} = R\vec{r} = 0.5(X_{be} - X_{bf})(\vec{x_e} - \vec{x_f})$$

The ray r of the force must connect points i and B_i, the intersection of the $\vec{X}_{be}$ and $\vec{X}_{bf}$ forces rays, otherwise node i would not be in equilibrium. Ray r is approximately radial to the arch. Vector

$$\vec{g} = 0.5(\vec{x_e} - \vec{x_f}) \tag{5}$$

is an important property of node i. The matrix expression for vector $\vec{R}$ is in terms of $\vec{g}$

$$\vec{R} = \{\vec{g}, -\vec{g}\} \left\{ \begin{array}{c} X_{be} \\ X_{bf} \end{array} \right\}$$

Recall that X_{be} denotes the third element of the nodal forces matrix of element e at node i and the analogue holds for X_{bf}. Conjugate displacements to X_{be} and X_{bf} are u_{be} and u_{bf}, conjugate to $\vec{R}$ is the displacement vector $\vec{u}$ of node i. The principle of virtual work thus implies

$$\left\{ \begin{array}{c} u_{be} \\ u_{bf} \end{array} \right\} = \left\{ \begin{array}{c} \vec{g} \\ -\vec{g} \end{array} \right\} \cdot \vec{u}$$

The same result can be obtained when the part of $\vec{u}$ in $\vec{r}$ direction, $(\vec{u}\cdot\vec{r})\vec{r}$, is projected on the $\vec{x_e}$ direction to obtain u_{be}:

$$u_{be} = (\vec{u}\cdot\vec{r})\vec{r}\cdot\vec{x_e} = \vec{g}\cdot\vec{u}.$$

Projection on $\vec{x_e}$ yields the same expression but for a negative sign at $\vec{g}$.

Expression for ε_b becomes

$$\begin{aligned} \varepsilon_b =& (u_{b,j} + \vec{g_j}\cdot\vec{u}_j - u_{b,i} + \vec{g_i}\cdot\vec{u}_i)/l_{i,j} \\ =& (u_{b,j} + \{g_j\}^T \left\{ \begin{array}{c} u_{t,j} \\ v_j \end{array} \right\} - u_{b,i} \\ & + \{g_i\}^T \left\{ \begin{array}{c} u_{t,i} \\ v_i \end{array} \right\})/l_{i,j} \end{aligned} \tag{6}$$

where indices i and j denote the nodes of the element with the element local x axis from i to j. In the wake of it, the geometric matrix is modified to

$$[B] = \frac{1}{l} \begin{bmatrix} -1 & 0 & 0 & 1 & 0 & 0 \\ g_{i,x} & g_{i,y} & -1 & g_{j,x} & g_{j,y} & 1 \\ \lambda & -1 & -\lambda & \lambda & 1 & -\lambda \end{bmatrix} \tag{7}$$

with $\lambda = l/d/2$ and subscripts x and y indicating components of the vectors $\vec{g}$ in the global coordinate system.

Different element lengths have to be used in the geometric Equation 7 and the volume integration implicit in 8. The top face nodes distance l is used in the former case, the reduced length $l_{red} = lR_{ax}/R_t = lr_{ratio}$ is used in the latter case. R_{ax} denotes the radius of the arch central axis, R_t is the radius of the top face curve. The element stiffness matrix for an arch element is

$$[K]_e = Ebdl_{red}[B]^T[D_{cs}][B] \tag{8}$$

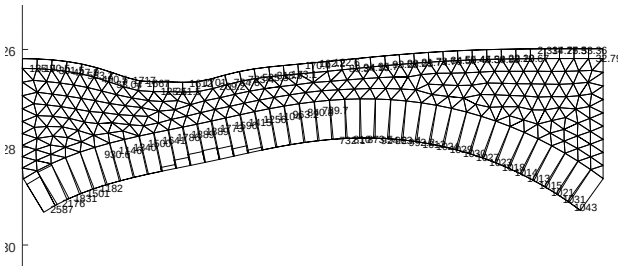

Figure 5. Bridge at Ponikla, compression stresses [kPa] and depths of the cracks in the bed joints

3. Application to an arch bridge

Exclusive translational DOFs facilitate the combination of the TT element with simple 2D continuum elements. A dedicated matlab/octave code has been written to utilize this combination for the analysis of masonry arch bridges. The code features the simplest possible way how the interaction of the masonry arch, backfill and pavement can be assessed parallel with the principal pattern of failure of the masonry arch. The arch and pavement are modelled by the TT elements, the backfill by the classic constant strain triangle (CST) elements. Meshing of the backfill provides the Persson and Strang mesh generator, [8]. The no-tension cross-section model defined in Section 2.1 supports the cracking of the arch bed joints, which is the dominant pattern of the masonry arch bridge failure. The code includes a simple, purely vector graphics output. It consists of 1150 octave command lines, not including the mesh generator.

An application to the sandstone arch bridge at Ponikla in north Bohemia illustrates the code output in Figure 5. The span of the arch is 11.4 m. Two principal quantities are shown in each arch element, the maximum compression normal stress value inserted at the arch face where it occurs and the depth of the cracks in the bed joint. The load case is the design dead load combined with the tandem axle live loads with twice the design intensity level, i.e., 360 kN per wheel in lane 1 according to EN 1991-2.

The TT element and the masonry arch FEM models based on it claim to be the simplest models available to assess the most frequent failure mode of the stone masonry arches and the interaction of the arch with backfill and pavement.

4. 3D Mindlin shell element TM

The 2D models are often not adequate for the solution of masonry arches whose widths are mostly comparable to spans which makes the transverse variation of stresses and displacements nonuniform. A 3D analogue to the 2D TT element is, therefore, derived. The Mindlin assumptions, [9], and the simplest triangular facet shape are adopted, see Figure 6. The element local coordinate system features z axis normal to the facet plane. There is always a preference direction in the facet plane, the direction closest to the normals

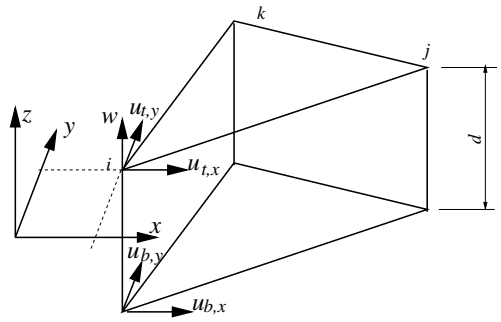

FIGURE 6. Geometry of the shell facet triangle element, the element local coordinate system and the DOFs at node i

to the bed joints planes of the masonry arch. It is assumed forthwith that the arch is a cylindric segment shell and the bed joints normals are tangents to the directrix of the cylinder so that their directions lie in a single plane. The global x axis is assumed to lie in that plane, too. In terms of the bridge nomenclature, the global x axis is in the direction of the arch span. *The element local x axis is chosen as the direction closest to the global x within the element plane. The no-tension condition is applied to the σ_x (local x) normal stress component* . Other options are possible and can be rather easily implemented in the code. It may be necessary in case of other than cylindric shells or more general failure modes and constitutive equations. Local y axis completes the element local right-handed cartesian coordinate system. All components are in this system up to Section 4.4, where two other systems are necessary.

Five translational DOFs per node are shown in Figure 6 for node i. They are ordered in matrix $\{u\}$ at each node, with node index omitted:

$$\{u\}^T = \{u_{t,x}, u_{t,y}, w, u_{b,x}, u_{b,y}\}$$

Deflection w and in-plane displacement vector $\vec{u}$ are approximated by linear independent functions of natural triangular coordinates ξ_i.

$$w = \sum_i w_i \xi_i, \quad \vec{u} = \sum_i \vec{u}_i \xi_i$$

In literature, a common term for this kind of approximation is isoparametric element, not to be confused with true isoparametric elements for 2D and 3D continua. Derivatives of ξ_i are constants in the element area,

$$\frac{\partial \xi_i}{\partial x} = \frac{b_i}{2A}, \quad \frac{\partial \xi_i}{\partial y} = \frac{a_i}{2A} \quad \text{or} \quad \frac{\partial \xi_i}{\partial \vec{x}} = -\vec{n}_i \frac{l_i}{2A},$$

where A is the element area (note that $l_i/2A$ is the slope of the ξ_i surface upon the element area) and

$$\vec{n}_i = -\frac{1}{l_i} \left\{ \begin{array}{c} b_i \\ a_i \end{array} \right\}.$$

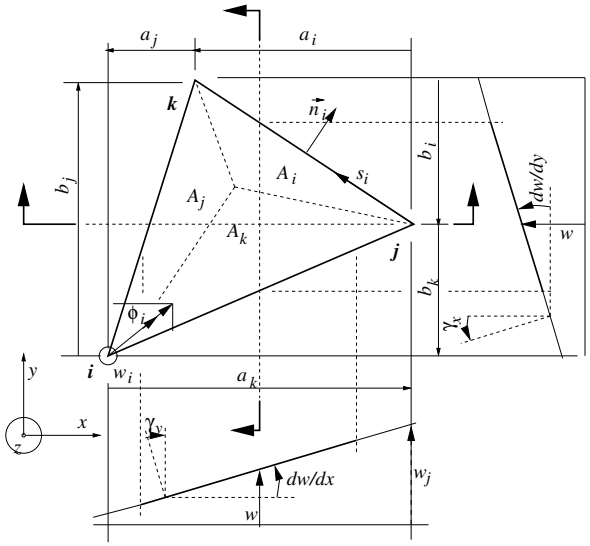

FIGURE 7. Triangular coordinates and shear deformation owing to deflection alone

Chain differentiation yields then

$$\gamma_{w,x} = -\frac{1}{2A} \sum_i w_i a_i, \quad \gamma_{w,y} = \frac{1}{2A} \sum_i w_i b_i \qquad (9)$$

The shear deformation $\vec{\gamma}_w$ owing to deflection alone is

$$\gamma_{w,x} = -\frac{\partial w}{\partial y}, \quad \gamma_{w,y} = \frac{\partial w}{\partial x}, \qquad (10)$$

note that *positive sense* is indicated in the figure for each of the four rotations and $\vec{\gamma}$ is the rotation of the normal to the element plane embedded in the material before deformation towards the normal to the element plane after deformation with standard sign convention of its components. In particular, the motion (rotation) shown in the section view right to left in Figure 7 goes from the inclined dashed line to the horizontal and γ_x is thus negative.

As in the TT element, the bending and shear deformation, are treated separately.

4.1. Bending and in-plane deformation

Pseudocurvatures define the bending deformation. They are the derivatives of rotations of the normals to the element plane. The rotations of the normals in their turn depend on the in-plane displacements $\vec{u}$ of the top and bottom faces of the element.

The element in-plane strains are specified in terms of the top and bottom faces (extrados and intrados) strain matrices $\{\varepsilon_t\}$ and $\{\varepsilon_b\}$ in analogy to the top and bottom uniaxial strains ε_t and ε_b in the Timoshenko 2D beam element. The element triangle geometry is defined in terms of distances $a_i = x_k - x_j$, $b_i = y_j - y_k$, where indices i, j, k are subjected to cyclic permutation and x_i, y_i specify node's i positions in the local system, see Figure 7. The geometric equations

of the CST triangle applied to the top face read

$$\{\varepsilon_t\} = \left\{ \begin{array}{c} \varepsilon_{t,x} \\ \varepsilon_{t,y} \\ 2\varepsilon_{t/b,xy} \end{array} \right\} = \frac{1}{2A} \sum_i \left[\begin{array}{cc} b_i & 0 \\ 0 & a_i \\ a_i & b_i \end{array} \right] \left\{ \begin{array}{c} u_{i,t,x} \\ u_{i,t,y} \end{array} \right\}, \quad (11)$$

substitute b for t subscript to get the bottom face strain matrix. The in-plane strains vary linearly across the element depth d,

$$\{\varepsilon\} = z_t\{\varepsilon_t\} + z_b\{\varepsilon_b\} \quad (12)$$

where $z_t = (d+z)/d = 1+\zeta$ and $z_b = -z/d = -\zeta$ are linear shape functions of the element in terms of the element local $0 > z > -d$ coordinate with $z = 0$ at the top face of the element or of the relative dimensionless $0 > \zeta > -1$ coordinate.

Plain stress conditions with $\sigma_{zz} = 0$ are assumed in the shell, then, the material stiffness matrix is

$$[D] = \frac{E}{1-\nu^2} \left[\begin{array}{ccc} 1 & \nu & 0 \\ & 1 & 0 \\ & & \frac{1-\nu}{2} \end{array} \right] \quad (13)$$

for a linear elastic isotropic material. When cracked bed joints occur in planes normal to element's x axis, the conditions become vague. Adjacent to the cracked joints an approximately uniaxial stress prevails. It is thus assumed forthwith that the material stiffness matrix in the cracked elements is

$$[D(\{\varepsilon\})] = E \left[\begin{array}{ccc} s(\varepsilon_x) & 0 & 0 \\ & 1 & 0 \\ & & \frac{1-\nu}{2} \end{array} \right] \quad (14)$$

where $s()$ is the normalized bilinear stress/strain diagram in the left sketch of Figure 2. It is obvious that the element local x axis must approximately coincide with the normals to the bed joints of the arch barrel.

The virtual work equation for cracked elements

$$\begin{aligned} \delta w &= \sum_i (\delta\{u_{i,t}\}^T\{g_{i,t}\} + \delta\{u_{i,b}\}^T\{g_{i,b}\}) \\ &= \int_V \delta\{\varepsilon\}^T[D(\{\varepsilon\})]\{\varepsilon\}\mathrm{d}V \\ &= E\int_V (\delta\varepsilon_x s(\varepsilon_x) + \delta\varepsilon_y\varepsilon_y + (1-\nu)\delta\varepsilon_{xy}\varepsilon_{xy}\mathrm{d}V \end{aligned} \quad (15)$$

delivers the expressions for the nodal forces $\{g_{i,t}\}$, $\{g_{i,b}\}$ when strains are expanded in terms of the virtual nodal displacements using Equation 11.

Functions $s_t(\varepsilon_{t,x}, \varepsilon_{b,x})$ and $s_b()$, see 2 in Section 2.1, return dimensionles top and bottom cross-section forces conjugate to top and bottom strains (input parameters) of a unit depth cross-section with $E = 1$ and no-tension stress-strain diagram. With the aid of the functions, the integrals in the virtual work expression can be expressed in a closed form:

$$\begin{aligned} \delta w = \frac{Ed}{2}&(\delta\varepsilon_{t,x}s_t + \delta\varepsilon_{b,x}s_b + \delta\varepsilon_{t,y}(\varepsilon_{t,y}/3 + \varepsilon_{b,y}/6) \\ &+ \delta\varepsilon_{b,y}(\varepsilon_{t,y}/6 + \varepsilon_{b,y}/3) + (\delta\varepsilon_{t,xy}(\varepsilon_{t,xy}/3 + \varepsilon_{b,xy}/6) \\ &+ \delta\varepsilon_{b,xy}(\varepsilon_{t,xy}/6 + \varepsilon_{b,xy}/3))(1-\nu)) \end{aligned} \quad (16)$$

Substitution by 11 and selection of individual nonzero virtual nodal displacements yields the expressions for the element nodal forces:

$$\begin{array}{rcl} g_{i,t,x} &=& \frac{Ed}{2}(b_i s_t + a_i(\varepsilon_{t,xy}/3 + \varepsilon_{b,xy}/6)(1-\nu)) \\ g_{i,t,y} &=& \frac{Ed}{2}(a_i(\varepsilon_{t,y}/3 + \varepsilon_{b,y}/6) + \\ & & b_i(\varepsilon_{t,xy}/3 + \varepsilon_{b,xy}/6)(1-\nu)) \\ g_{i,b,x} &=& \frac{Ed}{2}(b_i s_b + a_i(\varepsilon_{t,xy}/6 + \varepsilon_{b,xy}/3)(1-\nu)) \\ g_{i,b,y} &=& \frac{Ed}{2}(a_i(\varepsilon_{t,y}/6 + \varepsilon_{b,y}/3) + \\ & & b_i(\varepsilon_{t,xy}/6 + \varepsilon_{b,xy}/3)(1-\nu)) \end{array} \quad (17)$$

Derivatives of the nodal forces $g_{i,t/b,x/y}$ with respect to the DOFs can be written in terms of the $s_{t/b}$ functions, for instance

$$\begin{aligned} \frac{\partial g_{i,t,x}}{\partial u_{j,t,x}} &= \frac{\partial g_{i,t,x}}{\partial \varepsilon_{t,x}}\frac{\partial \varepsilon_{t,x}}{\partial u_{j,t,x}} + \frac{\partial g_{i,t,x}}{\partial \varepsilon_{t,xy}}\frac{\partial \varepsilon_{t,xy}}{\partial u_{j,t,x}} \\ &= \frac{Ed}{4A}(b_i b_j \frac{\partial s_t}{\partial \varepsilon_{t,x}} + a_i a_j \frac{1-\nu}{2}\frac{1}{3}) \end{aligned}$$

Functions s_t, s_b depend on x components of ε_t, ε_b only. The subscript x can thus be omitted in their derivatives. Formulas for the derivatives are in Section 2.1. When $\mu = \frac{1-\nu}{2}$ is introduced and common factor $\frac{Ed}{4A}$ is omitted for brevity, submatrices $[K_{bend,i,j}]$ of the element stiffness matrix associated with the in-plane DOFs

$$\{u_{plane}\}^T = \{u_{i,t,x}, u_{i,t,y}, u_{i,b,x}, u_{i,b,y}\}$$

are:

$$\begin{array}{ll} i,i: & \left[\begin{array}{cc} b_i b_j \frac{\partial s_t}{\partial \varepsilon_t} + a_i a_j \mu/3 & a_i b_j \mu/3 \\ a_j b_i \mu/3 & b_i b_j \mu/3 + a_i a_j/3 \end{array} \right] \\ i,j: & \left[\begin{array}{cc} b_i b_j \frac{\partial s_t}{\partial \varepsilon_b} + a_i a_j \mu/6 & a_i b_j \mu/6 \\ a_j b_i \mu/6 & b_i b_j \mu/6 + a_i a_j/6 \end{array} \right] \\ j,i: & \left[\begin{array}{cc} b_i b_j \frac{\partial s_b}{\partial \varepsilon_b} + a_i a_j \mu/6 & a_i b_j \mu/6 \\ a_j b_i \mu/6 & b_i b_j/6\mu + a_i a_j/6 \end{array} \right] \\ j,j: & \left[\begin{array}{cc} b_i b_j \frac{\partial s_b}{\partial \varepsilon_b} + a_i a_j \mu/3 & a_i b_j \mu/3 \\ a_j b_i \mu/3 & b_i b_j \mu/3 + a_i a_j/3 \end{array} \right] \end{array} \quad (18)$$

For a linear element (uncracked bed joints) $[K_{i,j}]^T = [K_{j,i}]$, which implies symmetry of the whole matrix $[K]$. For cracked bed joints $h_{t,b} \neq h_{b,t}$, the symmetry is lost.

4.2. Shear owing to the rotations of normals

The rotation of normals $\vec{\varphi}$ induces shear deformation, too. It would not induce any deflection in a consistent isoparametric element and then $\vec{\varphi}$ would simply be added to $\vec{\gamma}$ to obtain the total shear deformation. Such displacement pattern is known to imply locking in thin elements, like it does in the isoparametric variant of the TT element. In the TM element, $\vec{\varphi}$ induces a quadratic field of deflection w_φ, which must have zero values at all joints. The deflection should be compatible with the neighbouring elements along the boundaries. The antisymmetric part of the normal component of $\vec{\varphi}$ along an element's side is assigned to deflection, the symmetric part to shear deformation, in analogue, to the TT element. Perfect compatibility of deflections along boundaries with neighbouring elements is attained for elements lying in a plane. The implementation of the outlined displacement pattern is rather lengthy and it is skipped here. The resulting constant transverse shear owing to normals rotation is

$$\gamma_u = \sum_i [\psi_i](\{u_{i,t}\} - \{u_{i,b}\})$$
$$[\psi_i] = \left(\begin{bmatrix} 0 & -1/3 \\ 1/3 & 0 \end{bmatrix} - \frac{1}{12A} \begin{bmatrix} a_k^2 - a_j^2 & b_j a_j - b_k a_k \\ -b_k a_k + b_j a_j & b_j^2 - b_k^2 \end{bmatrix} \right) \frac{1}{d} \quad (19)$$

The full transverse shear of the TM element is then

$$\{\gamma\} = \sum_i \left([\psi_i], \frac{1}{2A} \begin{bmatrix} -a_i \\ b_i \end{bmatrix}, -[\psi_i] \right) \{u\}_i \quad (20)$$

where indices i, j, k are subject to cyclic replacement. Formula 20 is necessary with thin shells where shear locking can occur. Masonry arches and other burried shells are mostly thick shells. Matrices $[\psi_i]$ can be simplified by omitting the second summand in such applications. Experience with tests and applications testifies that keeping the second summand improves the element convergence.

4.3. TM flat slab element

Simple linear constitutive equations are assumed for the transverse shear,

$$V_x = G\gamma_x, \quad V_y = G\gamma_y. \quad (21)$$

V_x is the standard shear force in element local $y - z$ plane when looking along x axis and V_y is the standard shear force in element local $x - z$ plane when looking along y axis.

The contribution of the shear stiffness to the element stiffness matrix is written down in terms of the 5x5 submatrices associated with the two top vertex, one transverse and two bottom vertices translational DOFs of each node. Column matrices $[\varphi_i] = [-a_i, b_i]^T/2A$ and 2x2 symmetric matrices $\psi_{ij} = [\psi_i]^T[\psi_j]$ help to write down the shear contribution to the submatrices:

$$[K_{shear,i,j}] = GAd^2 \begin{bmatrix} [\psi_{ij}] & [\psi_i]^T[\varphi_j] & -[\psi_{ij}] \\ [\varphi_i]^T[\psi_j] & [\varphi_i]^T[\varphi_j] & -[\varphi_i]^T[\psi_j] \\ -[\psi_{ij}] & -[\psi_i^T[\varphi_j] & [\psi_{ij}] \end{bmatrix} \quad (22)$$

Complete 5×5 stiffness submatrices are the sums of the bending stiffness submatrices 18 extended by an empty third column and row inserted between the 2×2 subsubmatrices and submatrices 22:

$$[K_{i,j}] = [K_{bend,i,j}]_{extended} + [K_{shear,i,j}] \quad (23)$$

The whole element stiffness matrix is the size 15×15 composition of submatrices $[K_{i,j}]$, but the submatrices are assembled in the global stiffness matrix so that the whole matrix is never set up.

Cracking in the bed joints followed by development of virtual hinges in the arch have been considered the dominant failure pattern of masonry bridges since the early attempts [10], [11] to assess the load capacity. Other failure modes like shear sliding of the bed joints or transverse tension cracking of the arch require sophisticated material models and properties which are almost impossible to obtain in the design practice.

This stiffness matrix can be used for the solution of flat slabs loaded both in and out of plane but in shells, the bottom face DOFs $u_{b,x}$, $u_{b,y}$ require a special treatment since they are not simply shared by the elements attached to a node.

4.4. TM shell element

The DOFs at the bottom vertices of the elements connecting to a node do not lie in the same plane and are not independent of the DOFs at the top vertices. The equilibrium of the nodal forces at the top vertices is affected by the nodal forces at the bottom vertices. These two conjugate deficiencies must be removed.

The normal to the shell surface is needed for a consistent formulation of the TM element. The normal is rigid in the frame of the Timoshenko-Mindlin shell theory, which implies that the displacements of all points of the normal share the same lateral displacement component. The exact definition of the normal direction $\vec{n}$ would be through the shell surface mathematical definition. For practical applications of the TM element, it is sufficient to define the unit normal $\vec{n}_i$ at a node i as the normalized sum of the normals of all elements connecting to the node, each element normal length proportional to the sine of the angle of the two adjacent sides of the respective element. Position vectors of nodes are denoted $\vec{x}_i$ and nodes of the connecting elements i, j, k, ordered counterclockwise when viewed from the top side of the shell. The sum is

$$\vec{n}_{s,i} = \sum_e \vec{n}_e \sin(\alpha_e) =$$

$$\sum_e (\vec{x}_j - \vec{x}_i) \times (\vec{x}_k - \vec{x}_i)/(|(\vec{x}_j - \vec{x}_i)||(\vec{x}_k - \vec{x}_i)|)_e$$

$$\vec{n}_i = \vec{n}_{s,i}/|\vec{n}_{s,i}|$$

Vector $\vec{n}_i$'s positive direction is outwards from top surface of the shell. The vector also defines the tangential plane τ_i at node i, $\tau_i \perp \vec{n}_i$. The top vertices of the connecting elements share the displacement $\vec{r}_{t,i}$ of the top end of the rigid normal. The global components of vector $\vec{r}_{t,i}$ constitute the first three DOFs of the node i. The index of the node is omitted forthwith since a single node is considered.

The compatibility of displacements at the bottom facets of the connecting elements demands that the projections on the τ plane of the bottom vertices displacements of all connecting elements share the same displacement vector $\vec{r}_{b,\tau} \subset \tau$. A coordinate system is established in the τ plane such that axis 1 direction vector $\vec{n}_1$ lies in the intersection of the global coordinates plane $x-z$ and the τ plane, oriented as the global x axis. Axis 2 direction vector is $\vec{n}_2 = \vec{n} \times \vec{n}_1$ (vector product). The component expansion of vector $\vec{r}_{b,\tau}$ is defined this way. The two components in the τ plane define the two complementary DOFs of the node. Note that they are not the displacement components in the global coordinate system $x - y - z$ but in the local 'tangential' plane instead.

The transformation matrix from global to these tangential vector components is

$$[T]_\tau = \begin{bmatrix} \{n_1\}^T \\ \{n_2\}^T \\ \{n\}^T \end{bmatrix} \tag{24}$$

The whole bottom vertices displacement vector is

$$\vec{r}_b = \vec{r}_{b,\tau} + \vec{n}(\vec{n}\cdot\vec{r}_t) = \vec{r}_{b,\tau} + \vec{n} \otimes \vec{n}\vec{r}_t,$$

but just the two components of $\vec{r}_{b,\tau} \subset \tau$ constitute the two complementary DOFs of the node. The out-of-τ-plane component depends on the basic three DOFs $\vec{r}_t$ of the node. Several coordinate systems (all cartesian) are employed. The global one, common for all, the τ system, common for a node and the local e systems of individual elements. *The convention is adopted for component matrices that the matrix with components in the global system has no subscript τ, in the τ system, and subscripts e in the element systems.* Furthermore, the transformation matrix $[T]_e$ from the global to the element system has subscript e. The matrix form of the expression for the element DOFs is

$$\begin{Bmatrix} \{r_t\}_e \\ \{r_b\}_e \end{Bmatrix} = \begin{bmatrix} [T]_e & 0 \\ [T]_e\{n\}\{n\}^T & [T]_e[T]_\tau^T \end{bmatrix} \begin{Bmatrix} \{r_t\} \\ \{r_b\}_\tau \end{Bmatrix} \tag{25}$$

Recall that both the displacement component matrices $\{r_b\}_e$ and $\{r_b\}_\tau$ have zero third components so that the third column and row of the transformation matrix in 25 can be omitted.

The nodal forces conjugate to $\{r_t\}_e$ and $\{r_b\}_e$ are denoted $\{g_t\}_e$ and $\{g_b\}_e$. Rigid normals to the shell surface imply that the equilibrium equations of the top and bottom joints of a node are not independent. Just a single equilibrium equation can be written in the direction $\vec{n}$ and it is assigned to the top end of the rigid normal – the top joint of the node. The two remaining equations at the bottom joint of the node include components acting in the τ plane. Component decompositions of the element nodal forces in the coordinate axes tripod $\vec{n}_1$, $\vec{n}_2$, $\vec{n}$ – the node local τ system, are added in the matrix equilibrium equation of the bottom joint of the node:

$$\sum_e \{g_b\}_{\tau,e} = \sum_e [T]_\tau [T]_e^T \{g_b\}_e = \begin{Bmatrix} 0 \\ 0 \\ \{n\}\{n\}^T\{g_b\}_e \end{Bmatrix}$$

The sum includes all elements connecting at the node. The third (tranverse) components are added to forces acting at the top vertex of the node to obtain the final nodal forces of the element:

$$\begin{Bmatrix} \{g_t\} \\ \{g_b\}_\tau \end{Bmatrix} = \sum_e \begin{bmatrix} [T]_e^T & \{n\}\{n\}^T[T]_e^T \\ 0 & [T]_\tau[T]_e^T \end{bmatrix} \begin{Bmatrix} \{g_t\}_e \\ \{g_b\}_e \end{Bmatrix} \tag{26}$$

The transformation matrices of the nodal displacements and forces are transpose of each other, which testifies to their correctness.

Note that the last scalar equations in 25 and 26 can be omitted and so can be the last columns of the tranformation matrices. The transformation matrices are then 5×5 in size. They are specific for each node of an element since the $\{n\}$ and $[T]_\tau$ matrices are different at each node. For an easy reference, they are denoted $[T_i]$ for node i forthwith. The submatrices $[K_{i,j}]$ are transformed to the global coordinate system

$$[K_{i,j}]_g = [T_i]^T [K_{i,j}][T_j] \tag{27}$$

and assembled in the system matrix.

4.5. TM element code and test

The TM element has been implemented in a dedicated Matlab/Octave code including a simple graphic output. Just the shell reference surface is drawn to keep the view readable. The maximum compression stresses in the bed joints and the relative depth of the cracks are inserted in each element. These values are sufficient to decide on the arch load capacity in the context of the present model. The graphic output uses vector graphics so that pictures can be zoomed in with a stable resolution. The mesh generator [8] is used for the shell surface meshing. The code is entirely self-contained, no input data file and pre- or postprocessing is necessary. It contains just about 660 octave command lines, not including the mesh generator.

The pinched cylinder with rigid end diaphragms in Figure 8 is a popular benchmark to test shell elements. The shell is thin, $d/R = 0.01$ so that the test is a severe one for a thick shell element. The benchmark solution by double Fourier series with 80 terms in both directions was first presented in [12] based on

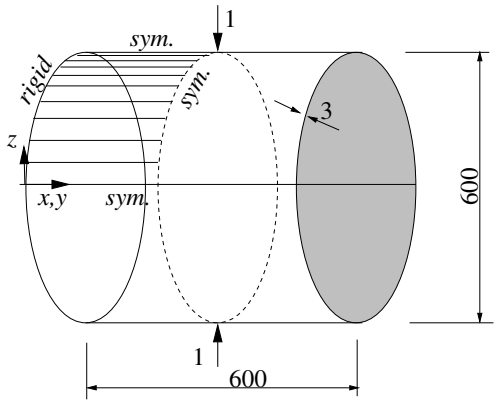

FIGURE 8. Benchmark shell

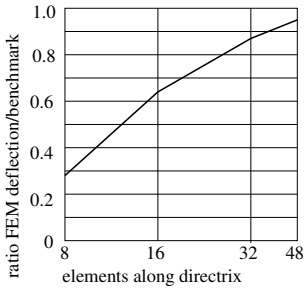

FIGURE 9. Convergence of the FEM deflections, ratio to the benchmark deflection

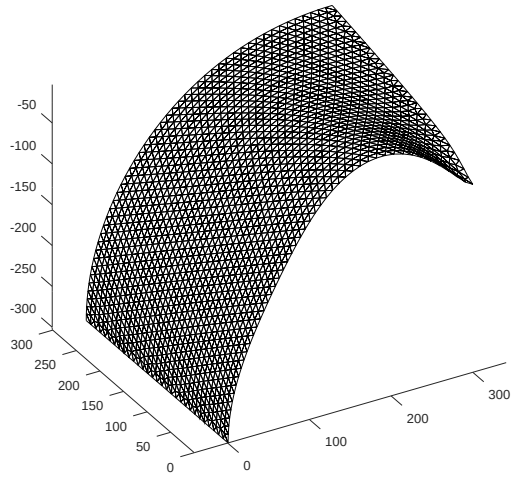

FIGURE 10. Deformed mesh, 48 elements along the directrix

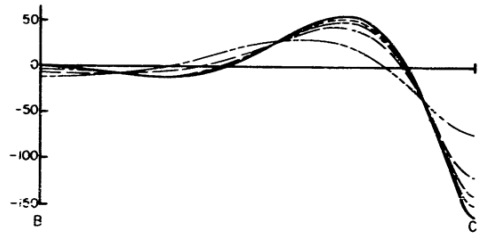

FIGURE 11. Radial component of deflection along the directrix, benchmark by the solid line, [12]

the work [13]. The Kirchhoff-Love kinematic assumptions are used in the benchmark so that a definite deflection is obtained. Differences can be expected between the present and benchmark solutions in the vicinity of the pin force, in particular for fine meshes. The Mindlin assumptions imply infinite deflection beneath the force in the continuum model, thus making the discretized models mesh dependent and inherently non-convergent. Owing to the three symmetry planes just shaded, 1/8 of the cylinder can be considered. Four mesh densities were considered with 8, 16, 32 and 48 elements along the directrix. The ratio of the loaded node deflection of the TM finite element solutions to the benchmark deflection $1.825 \cdot 10^{-5}$ is shown in Figure 9. In spite of the correction of the transverse shear strain in Equation 20, the residual shear locking still persisted and affected the results in this thin shell, in particular, for low densiiy meshes. In order to reduce it further, the material shear stiffness in the transverse direction (element local $x-z$ and $y-z$ planes) was selectively lowered eight times. This has a negligible effect on the overall response of the FEM model since the contribution of the transverse shear compliance to it is small. At the denser mesh side of the Figure 9, the curve already tends to adopt to the infinite deflection of the continuum Mindlin shell and break the Kirchhoff-Love benchmark limit. The deformed mesh is shown in Figure 10. The radial component of the deflection along the directrix from the benchmark solution [12] in Figure 11 compares well to the deformed mesh in Figure 10, note the shalow inward deflection in the lower part of the front directrix. The precision and convergence of the deflection beneath the pin force is, as expected, worse than for elements based on the Kirchhoff-Love assumptions.

A solution of the Ponikla bridge arch loaded by characteristic arch selfweight and standard LM1 tandem axle with wheel forces of 250 kN is provided for the illustration of the code output in Figure 12. Displacements are 2000 times scaled up. In comparison to the 2D solution of the same bridge arch in Section 3, the interaction and selfweight of the fill and pavement are not accounted for, the tandem axle load and mesh density are slightly different, too. The tandem axle position in the transverse direction is the extreme eccentric one within the bounds defined by the EN 1991-2. The differences between the loaded/unloaded sides of the arch barrel are 1261/405 kPa in extreme normal stresses in the bed joints and 0.41/0.25 in relative crack depths. The backfill and pavement stiffness and selfweight reduce the differences in the real bridge, but the example testifies that the 2D models need corrections. The 3D bridge model analogue to the one in Section 3 is currently being worked on.

The absence of rotational DOFs improves the convergence of the iterations. The no-tension, history independent material model admits a single load increment strategy. In the illustration example, the

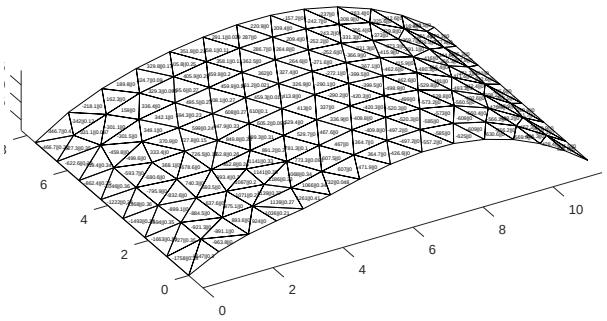

Figure 12. Bridge at Ponikla, 3D shell, compression stresses [kPa] and relative depths of the cracks in the bed joints

ratio 0.005 of the RMS norms of the imbalance and load was reached in 3 iterations.

5. Conclusions

The simplest finite elements for 2D and 3D thick shells have been developed for applications in masonry arch bridges limit load analysis. They feature seamless combination with 2D CST and 3D tetrahedron elements for the bridge's backfill. Exclusively translational DOFs are used, which improves the convergence of iterations. The no-tension condition is applied to the normal stress in the bed joints planes. The output minimum normal stresses and cracks depths in these planes can be used to assess the ultimate limit loads of a bridge. A sample analysis of an arch of the bridge at Poniklá testifies that this material law and shell elements develop a characteristic failure mode of the stone masonry arch bridges, the gradual creation of the virtual hinges.

Acknowledgements

The author was supported by the grant NAKI DG20P02OVV001, 'Tools for the preservation of historical values and functions of arch and vaulted bridges' provided by the Ministry of Culture of the Czech Republic.

References

[1] The Highways Agency, London. *Design manual for roads and bridges, vol. 3, Highway structures: inspection and maintenance, section 4, Assessment, Part 3, The assessment of highway bridges and structures*, 2001.

[2] Ministry of transport of the Czech Republic. *Zatížitelnost zděných klenbových mostů - Load rating of masonry arch bridges*, 2008.

[3] T. E. Ford, C. E. Augarde, S. S. Tuxford. Modelling masonry arch bridges using commercial finite element software. In *Proceeding of the 9th International Conference on Civil and Structural Engineering Computing*. Civil-Comp Press, Stirling, 2001.

[4] Mott-MacDonald, 20-26 Wellesley road, Croydon, CR9 2UL, UK. *CTAP manual for the assessment of masonry arch bridges*, 1990.

[5] R. Bridle, T. Hughes. An energy method for arch bridge analysis. *Proceedings of the Institution of Civil Engineers* **89**:375–385, 1990. https://doi.org/10.1680/iicep.1990.9397.

[6] M. Gilbert. RING: a 2D rigid block analysis program for masonry arch bridges. In *Proceedings of the 3^{rd} International Arch Bridges Conference*, pp. 459–464. 2001.

[7] W. Harvey. Application of the mechanism analysis to masonry arches. *Structural engineer* **66**:77–84, 1988.

[8] P.-O. Persson, G. Strang. Simple mesh generator in MATLAB. *SIAM Review* **46**(2):329–345. https://doi.org/10.1137/S0036144503429121.

[9] R. D. Mindlin. Influence of rotatory inertia and shear on flexural motions of isotropic, elastic plates. *ASME Journal of Applied Mechanics* **18**(1):31–38, 1951. https://doi.org/10.1115/1.4010217.

[10] A. Pipard, R. Ashby. An experimental study of a voussoir arch. *Proceedings of the Institution of Civil Engineers* **10**:383, 1938.

[11] A. J. S. Pippard. *The civil engineer in war*, vol. 1, chap. The Approximate Estimation of Safe Loads on Masonry Bridges., pp. 365–372. 1948. https://doi.org/10.1680/ciwv1.45170.0021.

[12] G. Lindberg, M. D. Olson, G. R. Cowper. New developments in the finite element analysis of shells, 1969. https://apps.dtic.mil/sti/pdfs/AD0707780.pdf.

[13] W. Flugge. *Stresses in shells*. Springer Verlag, 1962.

RESULTS OF RESEARCH ON BACKLASH COMPENSATION IN A POWER ELECTRIC DRIVE BY LOW-POWER ELECTRONIC DEVICE

Semen L. Samsonovich, Boris K. Fedotov, Nikolay B. Rozhnin, Roman V. Goryunov*

National Research University, Moscow Aviation Institute, Department 702, A-80, Volokolamskoye Av. 4, 125993 Moscow, Russia

* corresponding author: radiofizika01@mail.ru

Abstract. This article considers the feasibility of restoring and maintaining the kinematic accuracy of the support-rotary device drives by introducing a backlash compensation device into the control system. The power electromechanical drives of support-rotary device considered in this article contain two motors, the summation of the torques of which is carried out on a common output shaft. It is shown that the restoration of the required kinematic accuracy of the drives can be achieved by introducing one of two variants of an electronic device for backlash compensation into the control system. In the first variant, equal and opposite displacement signals are introduced into the control signals of the motors. The second variant introduces an electronic cross-connections backlash compensation scheme was into the control system. The study of the operation of the support-rotary device drive system with two backlash compensation devices carried out by a simulation method showed that the use of a cross-connection scheme is the most preferable and effective.

As a result of the research, it was shown that the introduction of an electronic backlash compensation device into the control system makes it possible to ensure the operability of the power electromechanical drives of a support-rotary device with initial kinematic accuracy.

Keywords: Backlash, backlash compensation device, multi-motor drive, tandem control.

1. Introduction

The long-time presence of a large-sized support-rotary device (SRD) in an open atmosphere leads, as a result of corrosion, to the appearance of additional gaps in the gearboxes, and this impairs the kinematic accuracy of electromechanical drives. It was found that after the 30 years of SRD being in the open air, the gears of the drive systems were corrosive, as a result of which the loss of the metal layer occurred, which in turn led to the appearance of backlash (gaps) and a decrease in the kinematic accuracy of the drive system [1]. The restoration of the kinematic accuracy of the electromechanical drive of a large-sized SRD after a long stay in an open atmosphere is of a great practical importance, and the way to restore it is an actual scientific task.

There are known ways to compensate for backlash in mechanical transmissions of electromechanical drives, described in [2–10], based on the following principles:

a) using mechanical spring devices to compensate for backlash [2];

b) frequency correction and system bandwidth degradation [4, 5];

c) the use of a backlash and elastic deformation sensor [5, 6];

d) converting signals from speed and torque sensors to determine the amount of backlash and elastic deformations [4, 7];

e) introducing a nonlinear corrective element "dead zone" into the error signal circuit [6].

Since the drive systems of SRD consist of two drives operating with the same load (Figure 1), it is possible to restore the kinematic accuracy by using special drive channels control circuits to compensate the backlash and improve the operation in dynamic tracking modes.

The greatest development in the multi-motor electric drive was made using two ways of backlash compensation. The first way of backlash compensation is similar to the operation of an "electromechanical spring", based on the creation of, opposite in sign, but equal in magnitude, torques that compensate for the gap, which is implemented by introducing constant displacements of a constant value into the control signals of the motors of the drive. Methods to implement this way are described in [11–17]. Another way is "tandem control", based on phase displacement of control signals for individual electric motors, depending on the calculated coordinates [18–24]. A feature of this way is the need to carry out a large amount of calculations and build a complex digital control system using microprocessors for its implementation.

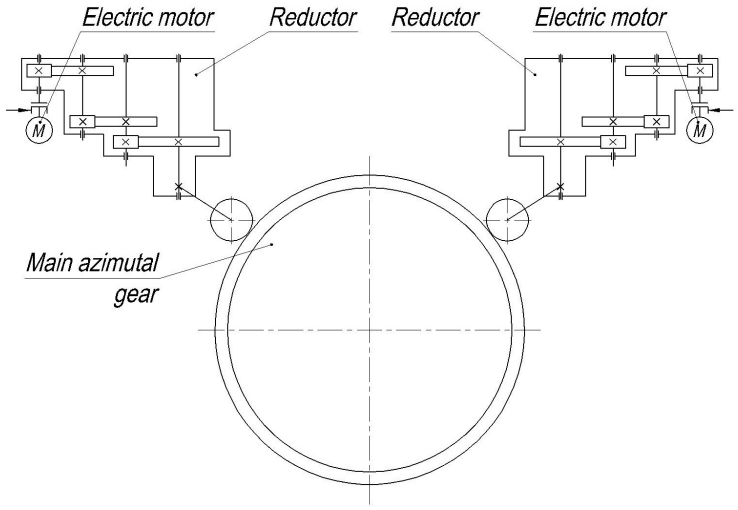

FIGURE 1. Kinematic diagram of support-rotary device drive.

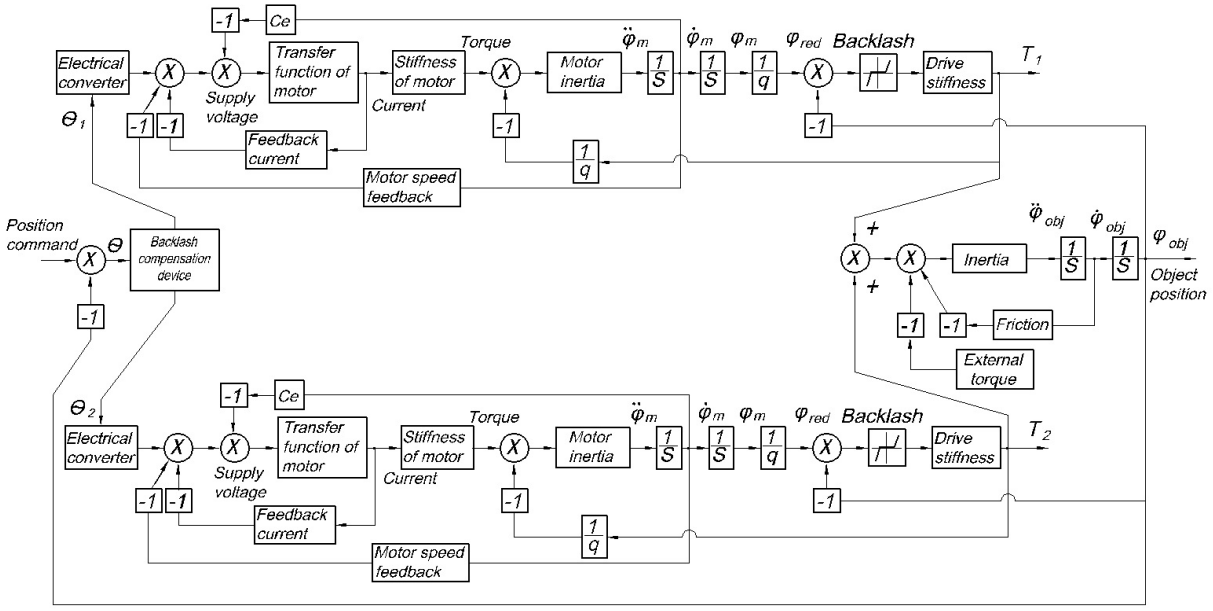

FIGURE 2. Block diagram of a system with non-linearity of backlash.

2. METHODS

The article discusses two ways to compensate for the backlash of a multi-motor electric drive gears, based on the transformation of a dynamic error signal: the well-known method of backlash compensating with the introduction of displacement signals (electromechanical spring) [11–17], and a newly developed method with a delay of the dynamic error signal [25]. Each of the methods is implemented by a special electronic device introduced into the dynamic error channel of the electro drive.

A comparison of the schemes was carried out by mathematical modelling. The simulation was carried out in the MatLab Simulink software environment, a mathematical model of the investigated drive system was compiled, consisting of two motors operating on a common load and the backlash model in the form of a dead zone coupled with transmission stiffness. The block diagram of the developed model is shown in Figure 2. The parameters of the SRD drives are considered using the example of the signal $\varphi(t) = A\sin(\omega t)$. The following parameter values are used in the model: electric motor armature voltage – 440 V; armature current – 115 A; rated power of the electric motor – 45 kW; rated speed – 750 rpm; the moment of inertia of the rotor – 2.575 kgm^2; gear ratio of the gearbox – 400; backlash of mechanical transmissions – 0.017 deg.

Initially, the operation of an idealized drive without any backlash was simulated, as a result, the reference characteristics of the drive with the guidance signal was obtained. Then backlash was introduced into the model and the results of its impact were considered. Then, one of the electronic devices for backlash compensation was introduced into the control system of the drives and the parameters were synthesized until

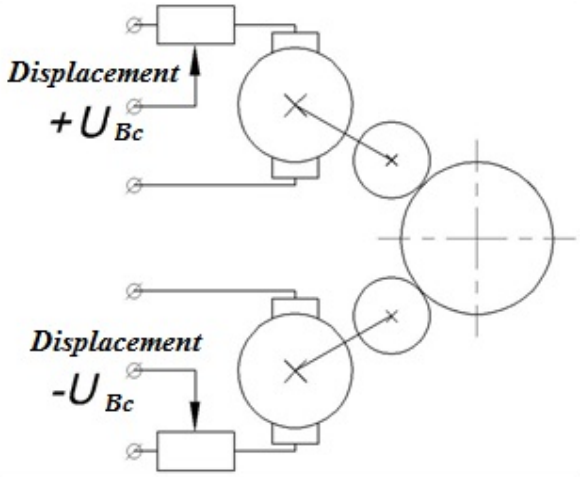

FIGURE 3. Backlash compensation with connecting additional supply voltages.

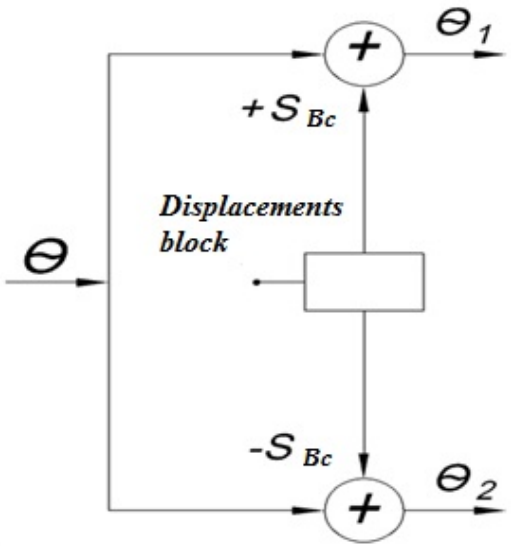

FIGURE 4. Backlash compensation device scheme on input of displacement signals.

the reference characteristics of the SRD drives corresponding to the idealized model without backlash was obtained.

3. Backlash compensation device with input of displacement signals

In the well-known scheme with an input of displacement control channels (electromechanical spring scheme), a certain constant displacement signal is supplied to each channel, equal in magnitude and different in sign. This creates an expansion of two gears relative to the common wheel. In the first known works [2], the thrust torques were created by additional supply voltages to the electric motors (Figure 3).

Later, to create thrust torques, instead of supplying voltages to the motors, an electronic device was used, which introduces displacements into the dynamic error signal (Figure 4), which is created by the preliminary displacement block [3]. This ensures opposite torques of the motors at zero value of the control signal, similar to the action of a spring.

The control signal θ in a system with the main position feedback is a dynamic error signal. When a control signal arrives, for example, a positive one, the signal value in the corresponding channel is added to the offset signal, and in the opposite channel, the offset signal is subtracted from the control signal. If the values of the control signals are lesser than the offset value, it creates a thrust torque to compensate for backlash in the system. When the value of the control signal exceeds the offset value, the signal in the second channel will change sign, and both motors will create torques in the same direction.

4. Backlash compensation device with cross connections

The disadvantage of the known method of backlash compensation, based on the introduction of displacement signals, is the low efficiency of the electric drive due to the high mutual loading of the electric motors. In the process of research, in order to compensate for the influence of backlash in gears, to ensure the summation of the dynamic capabilities of the channels in the steady-state motion mode, as well as to decrease the mutual torques and increase the efficiency, a control scheme for the drive channels with the introduction of cross-connections has been developed. The scheme implements a method for backlash compensation by introducing a delay into the dynamic error signal of one of the drive channels. The developed scheme of the backlash compensation device will be called a cross-connections scheme (Figure 5).

This scheme can be considered as a special type of tandem control, in which the phase shift is carried out not by calculating the coordinates of individual electric motors, but by converting the error signal by introducing a dynamic delay that depends on the value of backlash.

The backlash compensation device consists of two splitters, two switches, two aperiodic links with time constants T_1, T_2, a signal module extraction block, four multiplying blocks, and two summing blocks. The input of the backlash compensation device is branched with a splitter to three outputs. Two outputs are connected to corresponding switches. One output of the switch is connected to the first input of the summator through the first product block, and the second through the aperiodic link. The second product block forms a cross-connection line to the second input to the second summator. Switches are configured for positive and negative dynamic error signal. The outputs of the switches are signals (0, 1) and (-1, 0), respectively. After the switch, one of the branches includes a signal module extraction block, which is necessary to match the signs of signals at the outputs of the products blocks, the second inputs of the four product

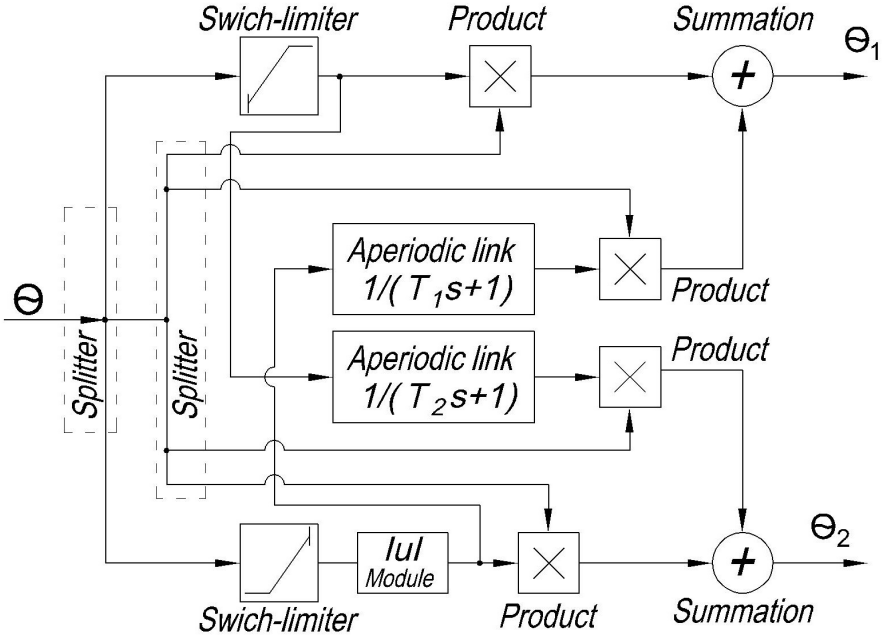

FIGURE 5. Scheme of backlash compensation device with cross-connections.

blocks are connected to the remaining outputs of the input signal splitter. The signals from the outputs of the summation blocks are the output signals of the backlash compensation device θ_1, θ_2.

The principle of operation of a cross-connections scheme is based on the phase shift of the signal in the second channel, the value of which is selected depending on the amount of backlash. For this purpose, aperiodic links with time constants T_1, T_2 are used. Initially, the values of the time constants are equal to $T_1 = T_2$, then the value – $T_{1,2}$ is selected depending on the individual parameters of a separate channel.

It is known that the backlash has the greatest influence in the tracking system when the direction of movement is changed; in that moment, there is a change in the working surfaces (sides) of the gear teeth, and for the time of this switching, the system appears to be open. Changing the direction of movement of the control object requires switching channels. Switches are used to prevent the backlash from opening when the direction of movement is changed. For this purpose, switching filters and cross-connections are used.

In the mode of steady motion, after the end of the transient processes, the signal in the second channel is close to the signal in the first channel, therefore, both channels operate in the same direction, in this mode of movement, the drive torques are summed up.

The backlash in mechanical transmissions causes amplitude limiting and phase displacement during the guidance signal processing. If the selected time constants T_1, T_2 provide a displacement in the second channel greater than the displacement produced by the action of the backlash, then in the electric drive consisting of two motors connected by a common mechanical transmission, there will be thrust torques for backlash compensation.

5. Experiment results

The study of the electric drive operation with a backlash was carried out by simulating in Simulink using the example of a harmonic guidance signal. The results of the operation of the drive under study with the known scheme of the backlash compensation device based on the introduction of displacement signals are shown in Figure 6. It follows from the graphs that the dynamics of the drive is close to the dynamics of an idealized model without any backlash. The smoothness of the change in the coordinates of the electric drive is ensured in the entire range of development (Figure 6a). Figure 6b shows significant thrust torques exceeding the required total torque.

A significant amount of energy is spent on mutual torques of the motors, which leads to a decrease in the efficiency of the electric drive, which does not exceed 30 % in the steady-state motion mode (Figure 6c).

The simulation results show that the use of a backlash compensation device with an input of displacement signals makes it possible to compensate for the effect of backlash caused by corrosion and ensure the required accuracy of operation. The operating parameters, in terms of processing the control signal, are as close as possible to the parameters of the drive without backlash, however, the high thrust torque leads to high energy costs and a decrease in efficiency.

The results of the operation of the drive with a cross-connection backlash compensation device when small values of T_1,$T_2 = 0.2$ s are selected (the displacement in the second channel is lower than the displacement produced by the backlash) and when a harmonic guidance signal arrives are shown in Figure 7. The simula-

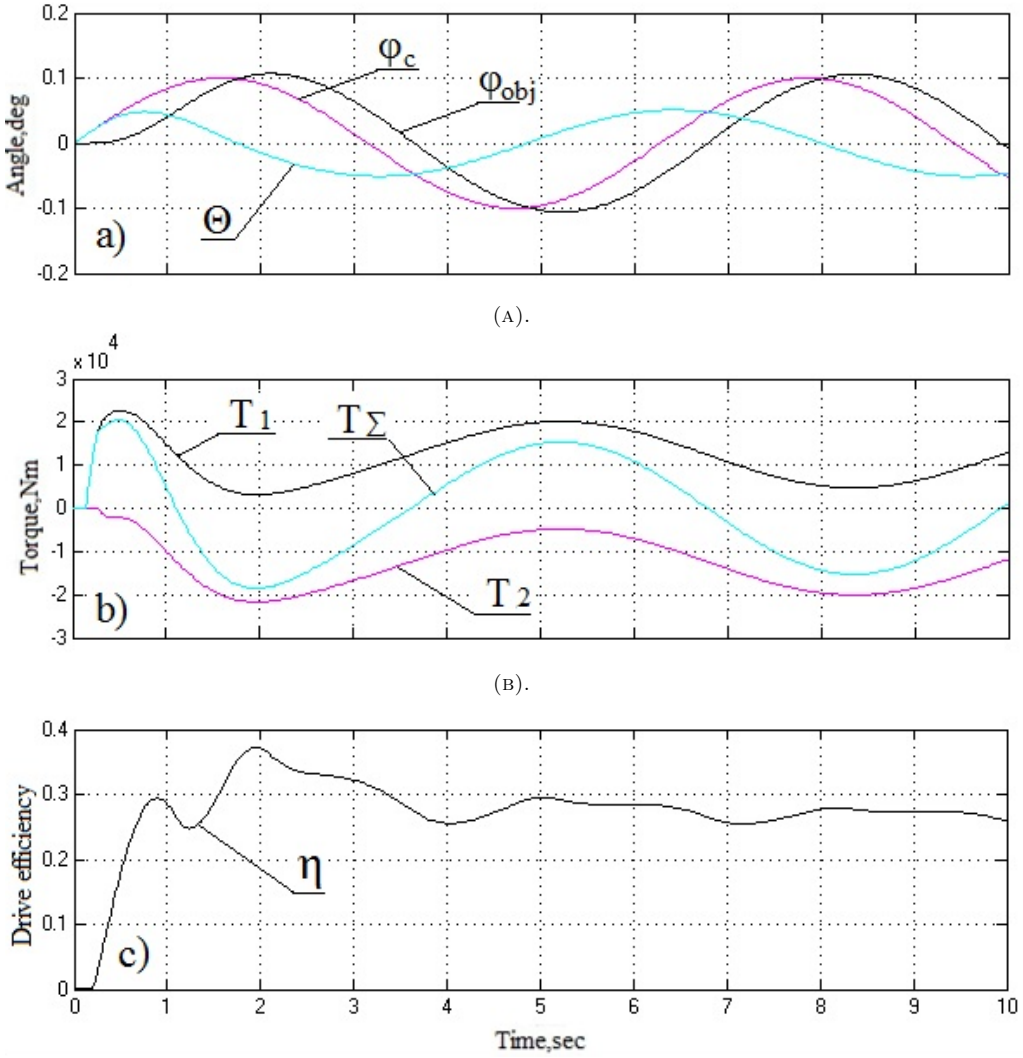

(A).

(B).

(C).

FIGURE 6. The operation of the drive with a backlash compensation device with input of displacement signals with harmonic guidance signal: a) guidance signal – φ_c, execution of the guidance signal by the drive – φ_{obj}, and dynamic system error signal θ; b) torques developed by motors and total drive torque; c) efficiency of the electric drive.

tion showed the drive execution to the guidance signal; when the sign of the dynamic error signal changes, a shift in the amplitudes of the torques of individual motors is observed (Figure 7b), which compensates for the backlash effect. A feature of the work is the absence of thrust torques. Figure 7c shows the change in the efficiency of the electric drive, which in the steady state motion mode, approaches 80 %.

Figure 8 shows the harmonic guidance signal processing by the drive when high values of the time constants T_1, $T_2 = 1.0$ s are selected. In Figure 8b, you can see that an increase in the time constants led to the appearance of thrust torques, which function in almost the entire operating range. Thus, when choosing high values of the time constants T_1, T_2, the backlash is compensated by creating thrust torques by an electric drive, similar to the action of the known device with the input of displacement signals. The disadvantage of this mode, as in the case of the known device, is the decrease in efficiency of the electric drive (Figure 8c), which in the mode of steady motion is in the range of 30–40 %.

The dependence of the efficiency of the electric drive on the selected values of the time constants T_1, T_2 is shown in Figure 9. The graph was obtained by simulating the processing of a harmonic guidance signal with an amplitude of 1^0 by an electric drive. The figure shows that an increase in the time constants T_1, T_2 leads to a decrease in efficiency, since thrust torques begin to appear in the system, which leads to energy losses.

By simulation, it was found that for the selected guidance signal and the amount of backlash, there is such a value of the time constant – T_1, $T_2 = 0.65$ s, at which the phase displacement in the second channel is close to the displacement produced by the backlash. Relative to this point, a combined graph of the dependence of the efficiency of the electric drive and

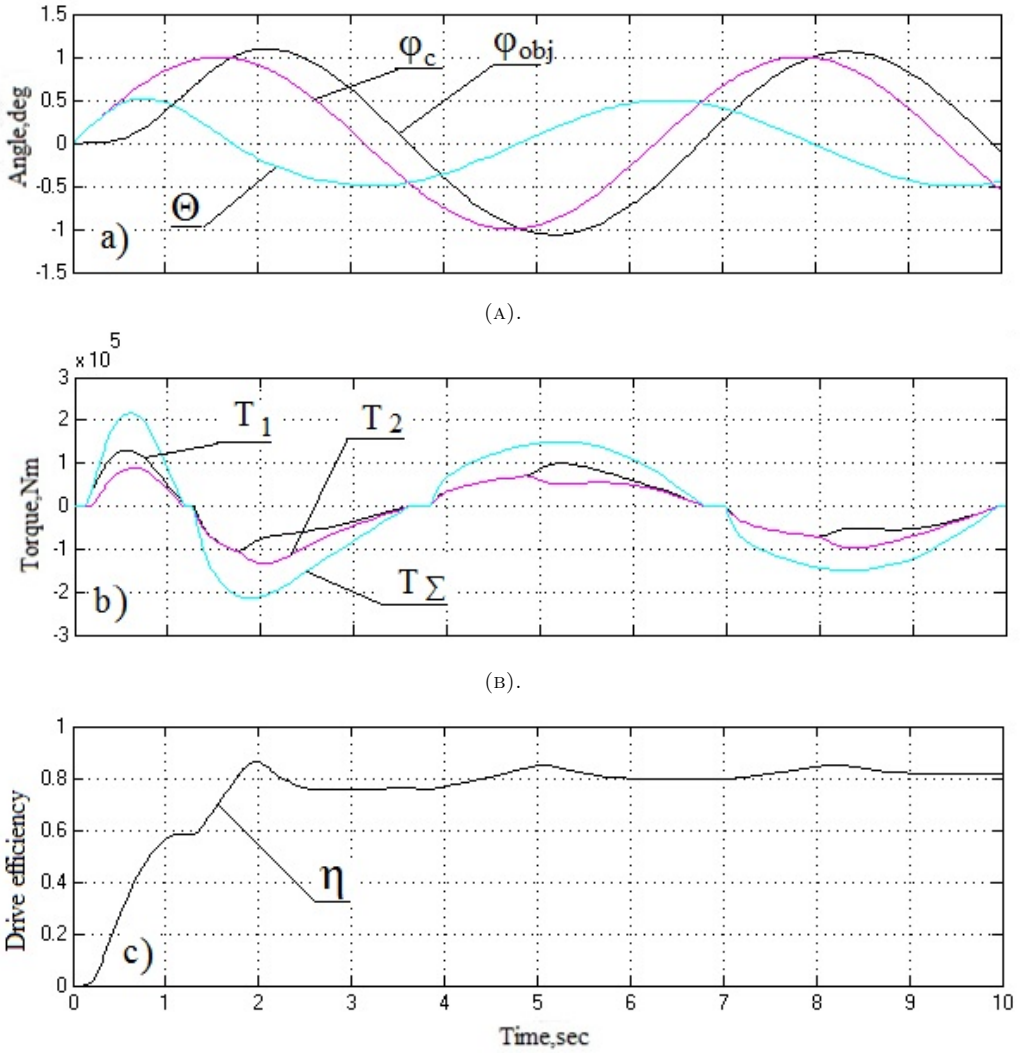

(a).

(b).

(c).

Figure 7. Operation of the drive with a cross-connection backlash compensation device with a harmonic guidance signal when small values of the time constants T_1, T_2 are selected: a) guidance signal – φ_c, execution of the guidance signal by the drive – φ_{obj}, and dynamic system error signal θ; b) the torques developed by the motors and total drive torque; c) the efficiency of the electric drive.

the torques of individual motors on the value T (Figure 10) is plotted. For convenience, this point will be called the transition point. When choosing values – T_1, T_2 to the left of the transition point, the electric drive will operate without thrust torques, to the right – there will be thrust torques in the system. An increase in the values of T_1, T_2 significantly to the right of the transition point will lead to a decrease in the participation of the second channel in joint work, up to the transformation of the drive into a single-channel drive with a passive load.

This graph is only valid for a specific backlash value and guidance signal parameters. When the values T_1, $T_2 = 0$ are selected, the drive will operate without displacements and the signals in the channels will be equal.

An increase in backlash will lead to a shift of the transition point to the right, a decrease in backlash – to the left. Specific values – T_1, T_2 depend on the speed parameters of electric motors and power amplifiers, therefore, the choice of values must be made individually, based on a combination of parameters.

When considering the operation of the cross-connections backlash compensation device, it was found that the electric drive can operate with the device in two modes of operation: with thrust torques and without thrust torques. The thrust torques mode (Figure 8) occurs when the control signal in the second channel (reversible) has a displacement greater than the displacement caused by the backlash.

Without thrust torques (Figure 7), the indicated displacement is lesser than the displacement produced by the backlash, and in this mode, the electric drive operates more efficiently. If the drive operates only with certain, previously known guidance signals, then it is possible to fine-tune the operating modes of the cross-connections backlash compensation device (with or without thrust torques). When the drive is operating

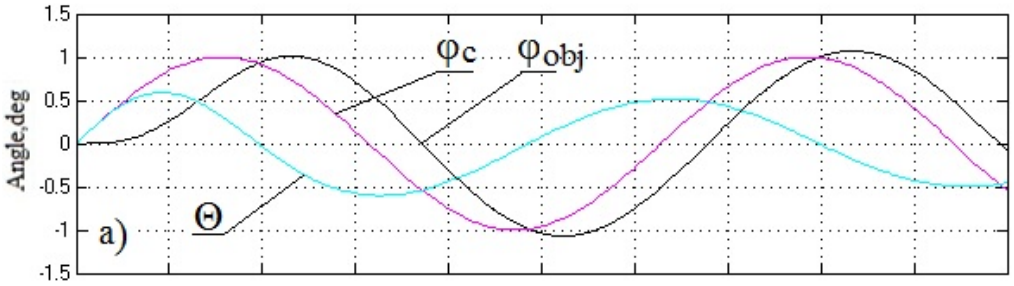

(A).

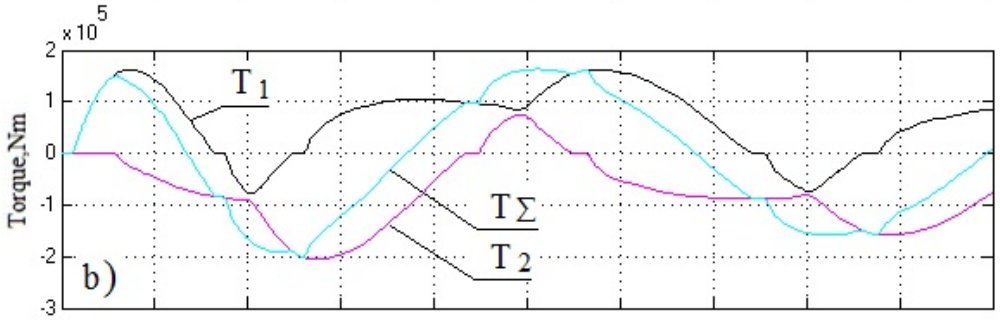

(B).

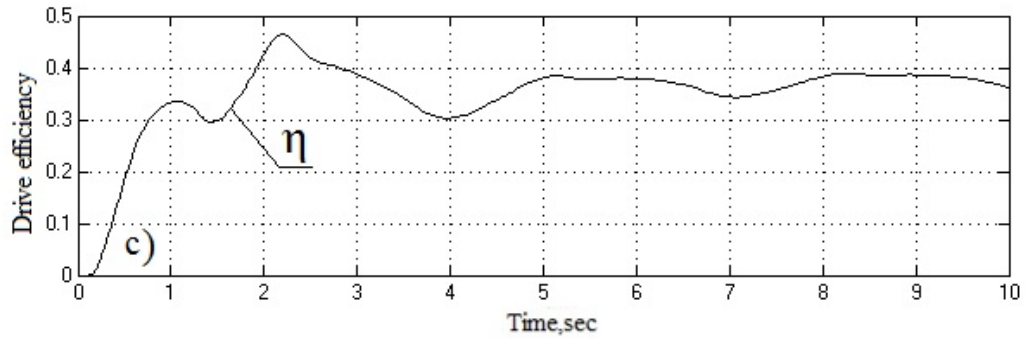

(C).

FIGURE 8. Operation of the drive with a cross-connection backlash compensation device with a harmonic guidance signal when large values of the time constants T_1, T_2 are selected: a) guidance signal – φ_c, execution of the guidance signal by the drive – φ_{obj}, and dynamic system error signal θ; b) the torques developed by the motors and total drive torque; c) the efficiency of the electric drive.

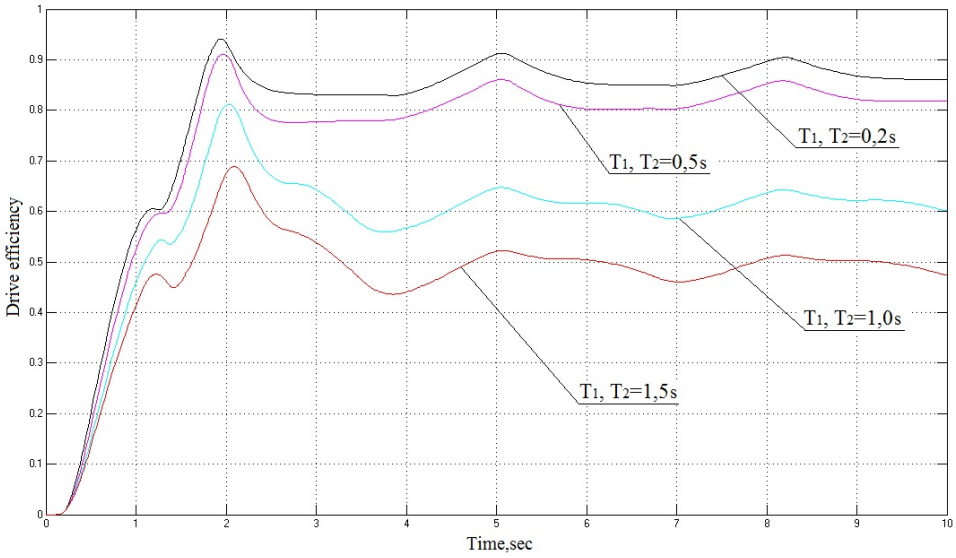

FIGURE 9. The dependence of the efficiency of the electric drive on the selected values of the time constants T_1, T_2.

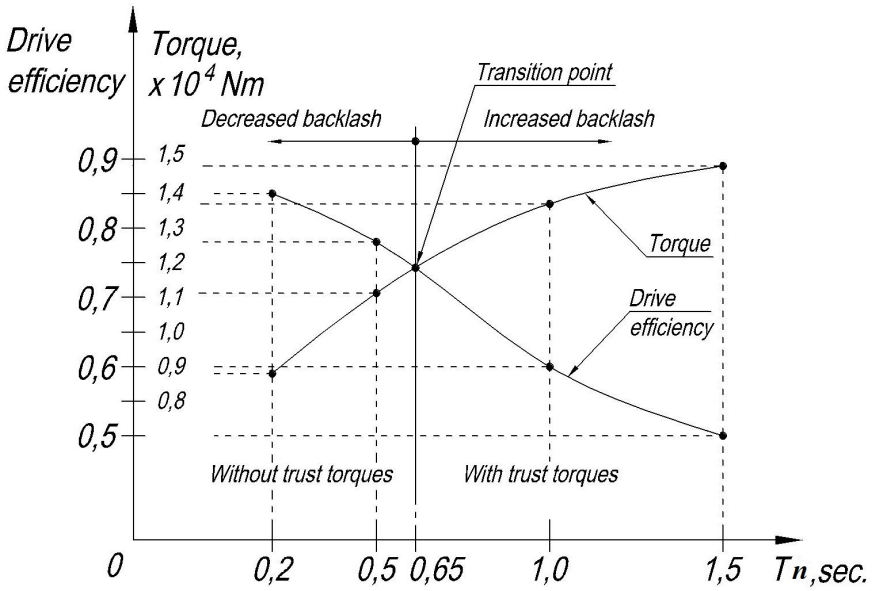

FIGURE 10. A combined graph of the dependence of the drive efficiency and the torques of individual motors on the value – T.

with arbitrary (random) guidance signals, a variable operation of the electric drive with backlash in gears in two modes is possible: with and without thrust torques.

6. Comparison results

The comparison of the schemes of the backlash compensation devices shows that the device based on the introduction of the displacement signal is the simplest to implement and gives an effect similar to the effect of a mechanical spring. The simulation results shown, when choosing the smallest value of the error signal displacements according to the condition of the absence of self-oscillations, one of the channels develops a torque that is almost twice the required one (Figure 6b), while excess energy is expended to create thrust torques. The effect of backlash compensation in the dynamics is achieved by significant energy losses for the mutual torques of the channels. The efficiency of a drive with a device with an input of displacement signals with a harmonic guidance signal does not exceed 40 %.

The cross-connection scheme shows that, when a small value of the time constant of the aperiodic block is selected due to the absence of self-oscillations in the steady-state mode of motion, the summation of the torques of individual motors is provided; the backlash is compensated by shifting the control signals in individual channels. The dynamics of the main movement is close to the dynamics of the ideal model without any backlash. The efficiency of the electric drive approaches 80 % when processing the harmonic guidance signal.

An increase in the time constants T_1, T_2 of the aperiodic links leads to a change of the operation of the electric drive. The thrust torques of the electric drive appear (Figure 8b), which increases the energy consumption and leads to a decrease in efficiency (Figure 8c), similar to the device with an input of displacement signals.

The use of a backlash compensation device for a drive containing two control channels will ensure the required kinematic accuracy of drive systems during the operation and will not require any additional effort to restore accuracy.

The simulation showed that the developed device for backlash compensation with cross-connections allows ensuring the accuracy of an electromechanical drive with backlash in mechanical transmissions, and compensating for the gap caused by prolonged idling periods so that when the dynamic error signal changes, it creates a shift in control signals in individual channels, providing a compensation for backlash, and in the mode of steady motion, it creates the summation of the torques of the channels.

When choosing large values of the time constants T_1, T_2 of a cross-connection device, the backlash is compensated by creating thrust torques, similar to a device with an input of displacement signals; in this case, the efficiency does not exceed 40 %. The choice of small values of the time constants T_1, T_2 of the aperiodic links of the backlash compensation device provides high-speed performance, an increase in the accuracy of operation (the value of the dynamic error is lower (Figure 7a)) and an increase in efficiency of up to 85 %.

An analysis of the operating parameters of a drive with various schemes for constructing backlash compensation devices testifies that it is advisable to use a circuit with cross-connections.

7. Conclusions

(1.) The conducted research on compensation of backlash in mechanical transmissions of a power electromechanical drive by introducing various devices for backlash compensation shows that the devices provide the required dynamic characteristics with different energy efficiency.

(2.) The proposed electronic device for backlash compensation allows, due to the transformation of the signal of the dynamic error of the system in low-power electrical control circuits, to create a shift of signals in each channel so that when the sign of the signal of the dynamic error changes, it compensates for the backlash, and when the motion is steady, the torques of the individual motors are summed up.

(3.) It is shown that the proposed cross-connection backlash compensation scheme provides a kinematic accuracy with increased efficiency, which is two times higher than the efficiency of the circuit with the input of displacement signals.

References

[1] S. L. Samsonovich, R. V. Goryunov. Research of the influence of atmospheric corrosion on the kinematic accuracy of the drive of a large-sized supporting and rotating device. *Handbook An engineering journal* (2):16–22, 2019. https://doi.org/10.14489/hb.2019.02.pp.016-022.

[2] P. V. Belyanskiy, B. G. Sergeev. *Control of terrestrial antennas and radio telescopes [in Russian]*. Sovet radio publishing house, Moscow, 1980.

[3] A. A. Kirillov, V. G. Stebletsov. *Bases of the electric drive of aircraft. Tutorial*. Biblio-Globus publishing house, Moscow, 2013. [2020-03-05], https://rucont.ru/efd/260901.

[4] M. Nordin, P.-O. Gutman. Controlling mechanical systems with backlash – a survey. *Automatica* **38**(10):1633–1649, 2002. https://doi.org/10.1016/S0005-1098(02)00047-X.

[5] R. M. R. Bruns, J. F. P. B. Diepstraten, X. G. P. Schuurbiers, J. A. G. Wouters. Motion control of systems with backlash, 2006. DCT rapporten; Vol. 2006.075 [2020-02-16], https://pure.tue.nl/ws/files/4295876/633392.pdf.

[6] B. K. Chemodanov. *Servo drives [in Russian]*. Bauman MSTU publishing house, Moscow, 1999. ISBN 5-7038-1383-2.

[7] L. Márton. Adaptive friction compensation in the presence of backlash. *Control engineering and applied informatics* **11**(1):3–9, 2009.

[8] R. R. Selmic, F. L. Lewis. Neural net backlash compensation with Hebbian tuning using dynamic inversion. *Automatica* **37**(8):1269–1277, 2001. https://doi.org/10.1016/S0005-1098(01)00066-8.

[9] G. Tao, F. L. Lewis. *Adaptive control of nonsmooth dynamic systems*. Springer-Verlag, London, 2001. ISBN 978-1-84996-869-0, https://doi.org/10.1007/978-1-4471-3687-3.

[10] S. Suraneni, I. N. Kar, O. V. Ramana Murthy, R. K. P. Bhatt. Adaptive stick-slip friction and backlash compensation using dynamic fuzzy logic system. *Applied Soft Computing* **6**(1):26–37, 2005. https://doi.org//10.1016/j.asoc.2004.10.005.

[11] V. V. Yavorsky. Backlash compensation device in a two-motor electric drive, 1980. Patent SU746399, Bull. No. 25.

[12] Y. Postnikov, et al. DC twin-motor driver, 1984. Patent SU1075360A, Bull. No. 7.

[13] Y. Oho, K. Iijima. Motor control device and motor control method, 2019. Patent US 2019/0079487 A1.

[14] T. Uchida, A. Ito, N. Furuya, T. Oshima. 3D14 positioning system based on twin motor cooperative control with gear backlash compensation. *The Proceedings of the Symposium on the Motion and Vibration Control* pp. 3D14–1–3D14–12, 2010. https://doi.org/10.1299/jsmemovic.2010._3D14-1_.

[15] W. Zhao, X. Ren. Adaptive robust control for four-motor driving servo system with uncertain nonlinearities. *Control Theory and Technology* **15**(1):45–57, 2017. https://doi.org/10.1007/s11768-017-5120-7.

[16] F. Xu, H. Wang. Clearance elimination method with two motors based on fuzzy control for turntable. In *Proceedings of the Seventh Asia International Symposium on Mechatronics*, pp. 702–710. Springer Singapore, Singapore, 2020. https://doi.org/10.1007/978-981-32-9437-0_72.

[17] M. Deng. *Operator-based nonlinear control systems: design and applications*. Wiley–IEEE Press, Piscataway, 2014. ISBN 978-1-118-13122-0.

[18] T. Uchida, A. Ito, T. Kitamura, N. Furuya. Positioning system with backlash compensation by twin motor cooperative control (Evaluation of rectilinear motion mechanism installed planetary gear speed reducer). *Transactions of the JSME (in Japanese)* **80**(814):DR0162, 2014. https://doi.org/10.1299/transjsme.2014dr0162.

[19] W. Gawronski, J. J. Beech-Brandt, H. G. Ahlstrom, E. Maneri. Torque-bias profile for improved tracking of the Deep Space Network antennas. *IEEE Antennas and Propagation Magazine* **42**(6):35–45, 2000. https://doi.org/10.1109/74.894180.

[20] Z. Haider, F. Habib, M. H. Mukhtar, K. Munawar. Design, control and implementation of 2-DOF motion tracking platform using drive-anti drive mechanism for compensation of backlash. In *2007 International Workshop on Robotic and Sensors Environments*. 2007. https://doi.org/10.1109/ROSE.2007.4373968.

[21] S. G. Robertz, L. Halt, S. Kelkar, et al. Precise robot motions using dual motor control. In *2010 IEEE International Conference on Robotics and Automation*. 2010. https://doi.org/10.1109/ROBOT.2010.5509384.

[22] Y. Toyozawa, K. Maeda, N. Sonoda. Tandem control method based on a digital servo mechanism, 1997. Patent US005646495A.

[23] S. Tararykin, et al. Method for controlling interconnected electric motors (variants), 2008. Patent RU2316886C1, Bull. No. 18.

[24] I. Polyushchenkov, et al. Method of the interconnected electric drives coordinates adjustment, 2018. Patent RU2655723C1, Bull. No. 16.

[25] S. L. Samsonovich, B. K. Fedotov, R. V. Goryunov. Method and device for selection of backlash in kinematic transmission of support-rotary device with two interconnected electric drives, 2020. Patent RU2726951C1, Bull. No. 20.

CFD MODELLING OF A SECONDARY SETTLING TANKS: GENERALIZATION BASED ON DATABASE RELATIONS

Ondřej Švanda*, Jaroslav Pollert

Czech Technical University in Prague, Faculty of Civil Engineering, Department of Sanitary and Ecological Engineering, Thákurova 2077/7, Prague 6, Czech Republic

* corresponding author: ondrej.svanda@cvut.cz

Abstract. The area of secondary settling tanks modelling using numerical methods has been quite extensively explored and researched by numerous authors and papers. These models utilize different approaches, from efforts to create a solely deterministic models to attempts to generalized or calibrated empirical models. Nevertheless, the processes are not easy to simulate due to the high complexity of the physics involving multiple phases, bio-chemical reactions and non-Newtonian fluids. Therefore, an additional effort should be focused on improving these models and to validate them against experimental measurements. This article is focused on creating a numerical model for settling tank optimization, which builds on the previous works and is then extended with newly obtained relations from vast experimental measuring using the database approach.

Keywords: CFD modelling, secondary settling tank, sludge database.

1. Introduction

The field of numerical solutions of the Secondary Settling Tanks (SST) has been under the scope of many researchers and over the years, numerous different models have been developed in order to describe the driving physics.

The comprehensive summary of early works in SST modelling was done by Ekama [1] and was later extended by Samstag [2]. Firstly, he mentions the historically first attempts to use CFD for sedimentation purposes done by McCorquodale and his student using the method of Roache [3] and Patankar [4]. Later, Zhou & McCorquodale [5] used a standard k-e turbulence model with the incorporation of solids transport and a settling model using double exponential equation of Takacs [6]. They concluded that the velocity pattern of the water-only flow is significantly different from the one containing solids.

A more advanced model was introduced by Griborio [7], who developed a model that included also flocculation and used the vorticity/stream function to model the fluid pressure correctly. The impact of flocculation in the centre-well design tank was studied in Griborio & McCorquodale [8], they stated that the influence of flocculation on the hydraulic performance is low. A recognizable author is De Clercq [9], who introduced a 2D model based on a commercial solver that took into account flocculation, solids transport, and density coupling with the Herschel Bulkley rheological model.

The possibilities of using a mixture model are well described in a PhD thesis by Burt [10], where the author tries to extensively validate and verify an extended drift flux model to be used in clarifier processes modelling. As a result, he points out that improved models are required for flocculent and discrete settling, since those cannot be captured by the standard Takács settling function.

The general problem is to incorporate all 5 regimes of sedimentation into one framework, which leads to the need for a generalized sedimentation model. In the recent years, there have been several attempts to do so, Morse, Sickza, & Nielsen [10] or Ramin, et al. [11] who introduced an extension of Tákacs' model for hindered settling to account for the compressive settling region. One of the most recent models is from Wimshurst & Burt [12], who modified the standard Tacacs' settling equation to account for lower velocity compression settling, but does not properly account for the floculant and discrete settling phase, as he points out in the paper. He also demonstrates a use of a response surface method to predict the behaviour under different conditions without the need to use a CFD model. This response surface is created by 64 CFD simulations of different conditions, but is not compared to any measured data to validate its accuracy outside the initial data.

The developed models differ by XD approach, the complexity of the physics taken into account and by the approach chosen. One type of the models is focused on discrete particle settling using different particle classes and modelling their kinematics, which does not capture the hindered phase correctly and seems not to be the correct path for a generalized sedimentation model for several reasons. The second type of models considers the sludge phase as monodisperse, which is beneficial for the hindered phase but struggles to correctly account for the flocculation and discrete particle sedimentation phase. But the recent research focuses on these models as they are continuously being improved. Nevertheless, what all these models share in common is that their performance

Properties recorded for every sample	External properties
Sampling – depth in the tank	SST inlet flow rate
Sampling – radial coordinate of the tank	SST outlet flow rate
Time and date	SST sludge removal flow rate
Temperature	SST inlet suspended solids concentration
Hindered sedimentation velocity	SST outlet suspended solids concentration
Viscosity	SST flocculant dosage
Sludge volume index	Weather (dry/rain)
Density	SST suspended solids concentration profile
Suspended solids concentration	
Flocs size distribution (small, medium, large)	
Microflocs	
Core consistency (compactness)	
Filament index	
Fragmentation	
Buoyancy	
Turbidity	

Table 1. Sludge sample properties and external properties recorded during experimental campaign.

decreases when used outside the sludge parameters they were calibrated on or require to obtain the sludge parameters for every settling tank they are trying to assess. Also, to this point, the CFD models are not validated against the real values in settling tanks during operation but rather against laboratory measured data, which is not optimal given the number of factors influencing the sedimentation.

This paper describes an attempt to create a generalized sedimentation model with a different approach from all previous works. It utilizes the Tacacs' sedimentation equation for the hindered settling, as it has been verified many times before, to provide good results for hindered settling phase, but modifies it by additional sub-models to account for the flocculation phase and floc breakups but more importantly, adds a modifying coefficient to the Tacacs' sedimentation curve to allow for an adjustment to different flow and sludge conditions as the sedimentation is influenced by numerous biological and chemical aspects that change the settleability of the sludge and cannot be described by a single parameter.

The novelty of this approach lies in the utilization of a big set of experimental data obtained over a long period of time. These data were put into a database in order to find relations between different influences, which allows to create a CFD model that can account for the sedimentation changes under different tank conditions. To be able to validate the model, a screening method for monitoring the suspended solids concentration distribution inside the settling tank was developed.

2. Materials and methods

The methodology consisted of several subsequent steps. First, the experimental data of the sludge properties of interest were gathered at the Central Waste Water Treatment Plant in Prague (CWWTP) from two different SSTs. Subsequently, the measured data were evaluated partly on-situ and partly in the lab for a more complex sampling. For each sample, a report including all measured and calculated properties was made. Due to an extensive amount of data gathered over a period of two years, a database framework was created to process that data and to find sludge sedimentation dependencies, which were then used as an input for the CFD model.

For the purposes of running the tests in-situ, a temporary field lab was built next to the SSTs. It houses two settling columns for sedimentation tests, viscosimeter, sludge pump and other accessories.

There were total of 9 data gathering campaigns from April to October 2017 from SST DN1 and then from April to September 2018 from tank DN3. Specific data for the need of the numerical model were also measured in 2019. A total of 136 complex samplings were conducted. The extent of data analysed for each sample is summarized in Table 1.

One of the main tests was the settling column test conducted at the site. Two three-meter-high cylindrical columns with a diameter of 0.3 m were used. The sludge from different locations in the SST was pumped into the columns up to the height of 2.8 m using a standard submerged sludge pump. The height of the interface between the water and the sludge was recorded each 5 minutes for the entire length of the test taking 1 or 2 hours. The outcome from this test was the hindered settling velocity (HSV) taken as the slope of the curve linear part (m/h). Later in the CTU lab, spectrophotometry was used to obtain the concentration of extracellular polymers (carbohydrates, proteins and humic substances). The suspended solids concentration was measured gravimetrically.

Rheological properties of the samples were measured using the rotary viscometer Rheometer RC20.

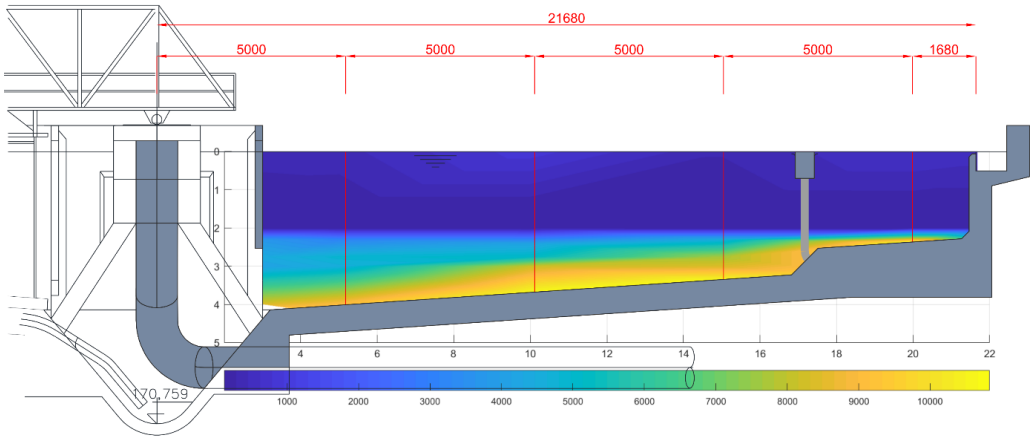

FIGURE 1. Distribution of suspended solids concentration in the SST (mg/l) – rainless flow.

The tests were conducted in a cylinder/cylinder setup suitable for non-Newtonian fluids. The strain rate range was chosen to be 0–1000 s^{-1} during the tests in 2017 and then changed to 3.5–500 s^{-1} during 2018. The overall time of the test was 300 s with the resolution of 50 values per test. The postprocessing of the data was done in Rheotec 3000, v2.0. The dynamic viscosity was calculated as:

$$\mu = \frac{\tau}{\frac{\partial u}{\partial y}}, \tag{1}$$

where μ is dynamic viscosity (Pa · s), τ is shear stress and $\frac{\partial u}{\partial y}$ is the strain rate.

The maximum strain rate in the SST obtained from a CFD simulation was around 20 s^{-1}, meaning that the resolution from the Rheometer RC20 was not sufficient for analysing the sludge in the SST as there was only 1 value between 0 and 20 s^{-1}. Changing the maximum test strain rate and/or sample resolution did not lead to usable results with the Rheometer RC20. Consequently, in 2019, a new viscometer Brookfield DV2TLV was obtained in order to measure the viscosity in the interested range of 0–20 s^{-1}.

The density of the sludge was measured using a 100 ml pycnometer. The weight of a dry pycnometer was recorded and then it was filled with the sample and closed. The redundant sample overflowed through a capillary and its weight was measured. The density was then calculated from the weight difference of a dry and full pycnometer. Also, the temperature of the sample was recorded using WTW Multi 3430 multimeter.

Sludge volume index (SVI) was determined as a specific volume of activated sludge after 30 minutes of settling in a 1 l container related to the suspended solid concentration.

$$\mathrm{SVI} = \frac{V_{30}}{X}, \tag{2}$$

where V_{30} is the settled sludge volume and X is the suspended solids concentration.

The concentration of suspended solids was measured gravimetrically according to Horáková et al. [13]. As a filter, Pragopor nitrocellulose 0.4 µm was used, pre-dried at 105 °C. The filtered volume was chosen based on the suspended solids concentration. It ranged between 5–20 ml for sludge samples, 50 ml for supernatant and 100 ml for the water outflow.

2.1. Sludge concentration profile

For the numerical model validation, it is important to capture the distribution and depth of the sludge blanket. For that purpose, an innovative approach was developed [14]. It is based on the suspended solids concentration measuring using the Cerlic Multitracker and then postprocessing the data in Matlab to visualize the concentrations in the SST.

The handheld multitracker consists of a probe connected to the device through a several-meter-long cable. As the probe is being submerged into the tank to the bottom, it continuously records the suspended solids concentration creating a vertical concentration profile.

This profile was measured at the SST at the radial distance of 3 meters from the tank's centre and then at each 2 m increment until the outer wall of the SST, with the last profile being taken at the radial distance of 21 m. These data were then assembled in Matlab to create a 2D concentration map (Figure 1). It vividly displays the position of the sludge blanket and provides more insight into the state of the sludge in the tank during different events such as rain flow. It serves as a main validation tool to compare the CFD model results with, as these distributions can be taken at any moment to validate different flow scenarios and conditions.

2.2. Sludge properties database

To consolidate the big amount of data obtained during the campaigns, a database system was developed. For that purpose, a commercial software Microsoft Access was used as a platform. Developing the database system was both beneficial and necessary from several aspects:

- ability to sort and show all properties and values from a certain sample,
- possibility to easily compare samples and to find relations between properties,
- ability to categorize and to create sludge groups based on the settling properties.

Each sample underwent several different tests. The settling column test and viscosity measuring was done in-situ, where microscopic test, sludge volume index, ECPs and densities were analysed in the CTU lab. On top of that, external parameters such as SST inlet and outlet flows and concentrations, flocculant dosage and weather information needed to be included as well. For that purpose, each sampling was given an ID through which all the tests can be connected together in the database. Choosing a certain sampling ID brings all the parameters associated with that sampling in a well-arranged matter. Plotting the properties from all samplings at once enabled to identify wrong data and error measurements and to exclude them from the database in order not to influence the relations.

Creating the database required an extensive amount of man hours and thus was developed with a cooperation of a small team who went through the input data a cleared them from any corrupted measurements, wrong readings and other misplaced data.

2.3. CFD model development

The framework on which the numerical model is built is the commercial CFD software Ansys Fluent. It is not the goal of this work to develop a new CFD code from scratch but to extend the ability of a widely used CFD code to simulate the specific behaviour of sludge in SSTs. That enables an easy deployment of the sludge settling model to any user with the Ansys Software package. The Ansys software package provides all the necessary tools for creating geometry, meshing, post-processing and already implements transient implicit solver, multi-phase models and common turbulence models.

The CFD sedimentation model is implemented through utilization of user defined functions (UDFs) to handle the flocculation, sedimentation and rheology of the sludge. This model can be easily adjusted through parameters to respect different sludge types and behaviour which extends its usage to be applied at any settling tank beyond the experimental one.

The developed numerical model consists of several sub-models, each handling different part of the sludge behaviour:

- flocculation sub-model handles the initial phase of the settling process, the flocculation and particle breakup,
- sedimentation sub-model is responsible for hindered zone and compress zone sedimentation,
- rheology sub-model is based on the non-Newtonian characteristics of the sludge.

2.3.1. Rheology

The purpose of the rheology sub-model is to find a relation between suspended solids concentration and strain rate. In the CFD model, both the strain rate and concentration are known so a viscosity can be calculated and assigned accordingly to each cell.

A total of 41 samples were analysed using the viscometer which outputs the relation between strain rate and shear stress. Using the well-known equation, the apparent viscosity was calculated:

$$\mu_m = \frac{\tau}{\dot{\gamma}}. \tag{3}$$

The data showed a good correlation with the Casson sludge type, that is described by the following equation:

$$\tau^{\frac{1}{2}} = \tau_0^{\frac{1}{2}} + \eta_\infty^{\frac{1}{2}} \cdot \dot{\gamma}^{\frac{1}{2}}, \tag{4}$$

where τ_0 is the Casson yield stress that needs to be overcome at zero shear rate and η_∞ is the Casson plastic viscosity. These parameters differ for each sample based on the solids' concentration, so we can obtain the function from a regression analysis of the data. The selected data to extract the dependency are the curves with $c = 4.9\,\mathrm{g/l}$ and $c = 13.5\,\mathrm{g/l}$ to capture both the low and high concentration profiles.

From the regression of the data the τ_0 parameter shows a linear dependency on the solids concentration that can be described as:

$$\tau_0 = 6.35 \cdot 10^{-2} \cdot c - 1.58 \cdot 10^{-1}. \tag{5}$$

Also, the η_∞ can be described using a linear function:

$$\eta_\infty = 7.51 \cdot 10^{-5} \cdot c + 1.85 \cdot 10^{-4}. \tag{6}$$

Eventually, we can create a viscosity function based on the solids concentration:

$$\begin{aligned}\tau^{1/2} = {} & (6.35 \cdot 10^{-2} \cdot c - 1.58 \cdot 10^{-1})^{1/2} \\ & + (7.51 \cdot 10^{-5} \cdot c + 1.85 \cdot 10^{-4})^{1/2} \cdot \dot{\gamma}^{1/2}.\end{aligned} \tag{7}$$

In the Figure 2, the aforementioned function is plotted against experimental data. One is constructed for $c = 4.9\,\mathrm{g/l}$ with $\tau_0 = 0.15$ and $\eta_\infty = 5.5 \cdot 10^{-4}$ to show low solids concentration region fitting and one for $c = 13.5\,\mathrm{g/l}$ with $\tau_0 = 0.7$ and $\eta_\infty = 1.2 \cdot 10^{-3}$ to show high solids concentration fitting. Only some of the sampling data are shown for better clarity.

2.3.2. Sedimentation

Overall, 108 samples were measured using the settling columns. However, 20 of the samples did not create a sludge-water interface and were therefore omitted from the data which is usually the reason for suspended solids concentration over $14\,\mathrm{g/l}$.

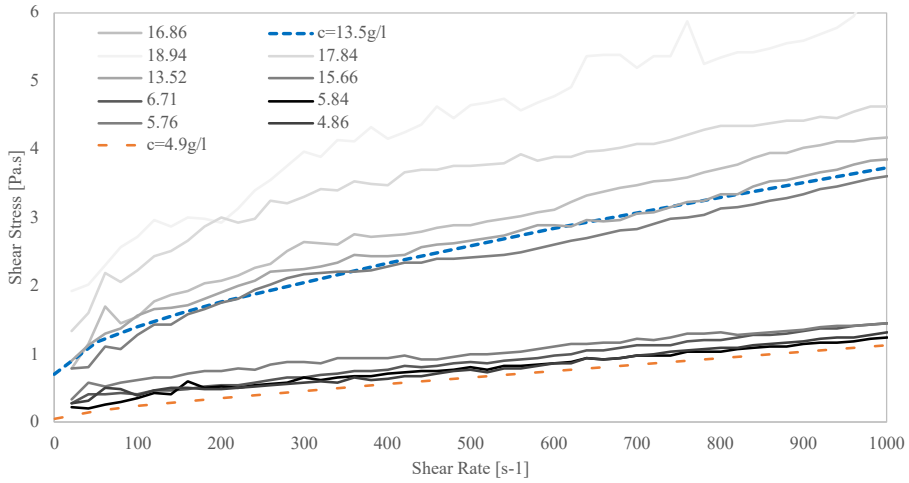

FIGURE 2. Fitted Casson sludge type rheology model.

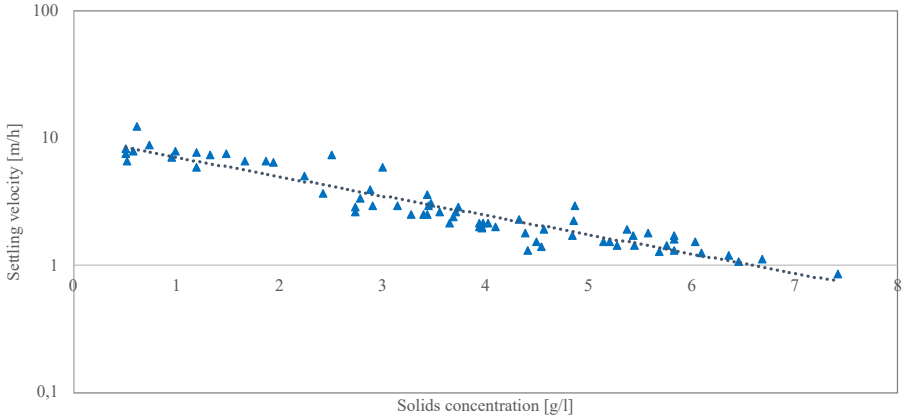

FIGURE 3. Dependency of settling velocity on solids concentration.

V_0 [m/h]	r_h [m^3/kg]	X_{min} [m/h]	r_p [m^3/kg]
10.08	0.35	0.008	3.5

TABLE 2. Obtained coefficients for the Takacs'-Vesilind settling curve.

The sedimentation sub-model origins from the well-known Takacs-Vesilind model:

$$V_s = V_0 e^{(-r_H \cdot (X - X_{min}))} - V_0 e^{(-r_p \cdot (X - X_{min}))}, \quad (8)$$

where V_0 is the maximum settling velocity, X_{min} is the minimum solids concentration at which settling occurs, r_H is a parameter describing the hindered zone and r_p is a parameter characterizing the low concentration settling. These parameters can be deducted from the batch column test data by linear regression same as the Vesilind parameters.

The settling velocity against suspended solids concentration was plotted on a natural log to linear scale. The gradient of the slope and the intercept of the curve are the V_0 and r_H coefficient respectively as shown in Figure 3.

From the regression the $V_0 = 10.08\,\mathrm{m/h}$ and $r_H = 0.35\,\mathrm{m^3/kg}$. The X_{min} parameter was measured by using decantation and resulted in $8 \cdot 10^{-3}\,\mathrm{m^3/kg}$. The last parameter r_p is generally considered to be a one order of magnitude larger than r_h, thus $r_p = 3.5\,\mathrm{m^3/kg}$. The summary of the coefficients is presented in Table 2.

It is apparent from the plot that the curve does not perfectly copy the shape of the source data. The settling velocity of the samples with low suspended solids concentration of $x < 2\,\mathrm{g/l}$ are undervalued where the velocity of the samples with higher concentration of $x > 3\,\mathrm{g/l}$ are slightly overvalued. The main reason for this is the fact, that the samples were taken over a long period of time (almost 2 years) and although they all come from a single WWTP, the properties of the sludge and especially the settleability may vary depending on the actual condition under which the samples were taken and thus creating a significant variance. This is very important to notice as this is actually the cumber stone of sludge settling models – they are fitted on very limited set of data representing usually only one flow condition.

It becomes apparent from the Figure 4, that a single averaged settling curve cannot enclose all the different sludge conditions and differentiate between well settling and badly settling sludge relatively to the suspended solids concentration.

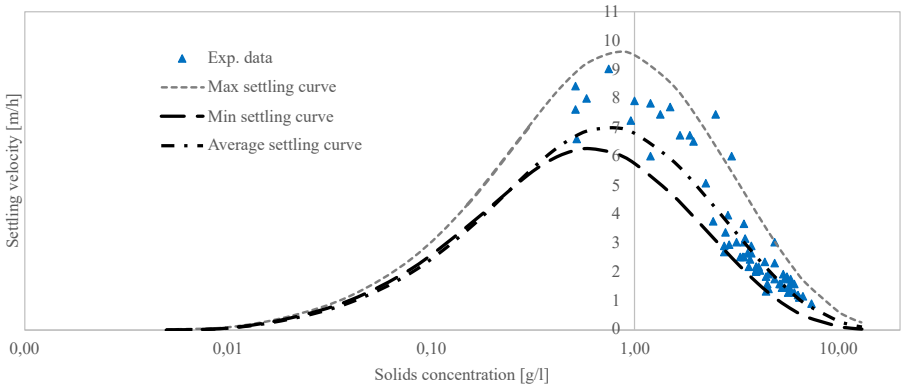

Figure 4. Envelope of the sludge settling curves.

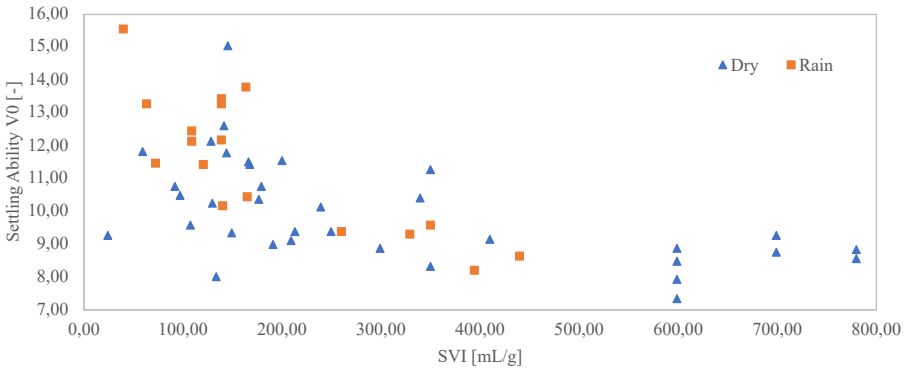

Figure 5. Relation between the sludge settling ability and SVI.

In order to be able to compensate the settling curves for different condition without the need to rerun the expensive batch settling measurement every time, an envelope is created to mark the maximum and minimum boundaries. That produces two new sets of settling curves as can be seen in Figure 4.

It is apparent from the range of min and max curves, that the settling velocity for the same sludge solids concentration may differ significantly. That corresponds to the fact, that there are other factors with a strong influence on the settleability of the sludge.

The settling curves are based on the ZSV which is considered to be a lumped parameter that inherently embeds sludge morphological, physical and chemical factors. Given the fact that a sludge property database was created during the campaigns, it is possible to try to find other relations between sludge settleability and other factors such as SVI, rain conditions, filament index, flocculant and coagulant dosage or retention time.

After investigation the relation between settleability and other factors, it turned out that from the gather data, there is no statistical dependency for rain, flocculant dosage, coagulant dosage and not enough data to asses the filament index. On the other hand, the SVI shows a logarithmic correlation of the data. Low SVI results in better settling performance and vice versa which corresponds to the general experience [15]. This correlation is valid for both dry and rain samples.

Now we can transform the Y-axis into a V_0 Correction Coefficient and add another parameter called r_H Correction Coefficient. These coefficients will serve as modifiers to the original Vesilind-Takacs exponential function to adjust the settling curve and we can rewrite the equation as follows:

$$V_s = 10.08 \cdot V_{0c} e^{(-0.35 \cdot r_{Hc} \cdot (X - 0.008))} - 10.08 \cdot V_{0c} e^{(-3.5 \cdot r_{Hc} \cdot (X - 0.008))}. \quad (9)$$

The dependency of the coefficients can be seen in Figure 6.

The ultimate benefit of this modified equation is that we can now construct a custom settling curve based only on a suspended solids concentration, flow rate and SVI for any sample. That means that the numerous samples laboratory batch settling tests required every time when we want to run a numerical model simulation can now be completely avoided. That significantly simplifies the preparation work to run a CFD simulation of the SST and more importantly, it expands the usage of CFD settling model outside the batch test specific WWTP.

The aforementioned models were converted into C language code and were implemented into the Ansys Fluent CFD solver using User Defined Functions. The simulation was run in 3D using $\frac{1}{4}$ of the tank and periodicity.

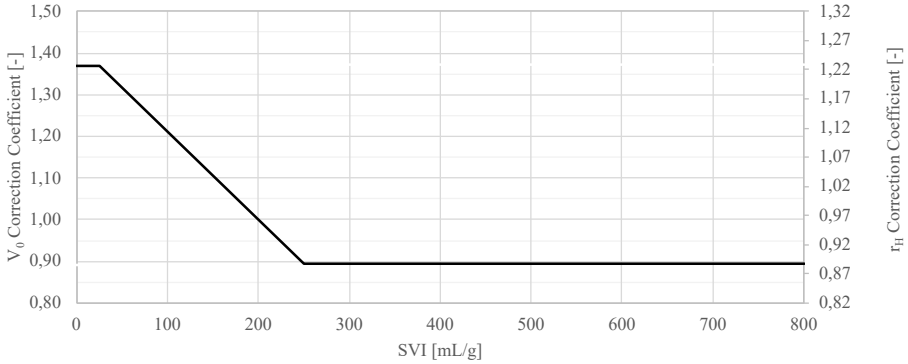

FIGURE 6. V_{0c} and r_{Hc} correction coefficient dependency on SVI.

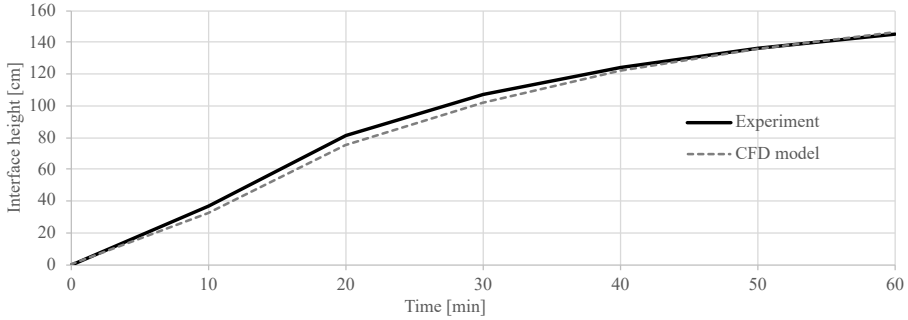

FIGURE 7. Results of sludge water interface evolution.

3. Results and discussion

First validation was done using the recorded batch settling column test where the water-sludge interface is of an interest. The column has a height of 3 m and diameter of 0.3 m. Initial suspended solids concentration was 5.7 g/l. As it can be seen from the Figure 7, the evolution of the interface is similar between CFD and experiment.

The 3D tank validation was done at settling tank DN3 located at the Prague WWTP within the old treatment plant. The radius of the tank is 21 m and depths are 5 m at the sludge removal pit and 2.1 m at the outer rim. The influent is a pipe located traditionally in the centre area. The inlet zone is bounded by 8 pillars supporting metal plates. The outlet area is located 17 m from the centre and consists of two circular weirs.

The geometry of the tank has a cylindrical periodicity and therefore only $\frac{1}{4}$ of the geometry was modelled. The inlet is considered to be a mass flow inlet and atmospheric pressure is setup at the outlet. Sludge removal is modelled as mass flow outlet. The side walls of the model are modelled as periodic to capture the symmetry. Top boundary that represents water-air interface is modelled as symmetry boundary condition – it ensures a non-zero velocity at the boundary.

For the tank DN3, a dry conditions scenario was simulated and compared to the experimental measurements. The flow rate 0.635 m^3/s represents the standard flow at the tank during normal conditions and was measured on 16th June 2016. The SVI at the tank inlet was 55 mL/g, which corresponds to the $V_{0c} = 1.31$ and $r_{Hc} = 1.18$.

The comparison of the suspended solids concentration between CFD and experiment can be seen on Figure 8. It is clear that the CFD model shows a good match with the experiment. Right after the inlet zone, there is a rising sludge eddy which is well-captured by the model. Also, the sludge blanket height matches the experiment.

Another validation was done on a tank DN1 which has a different inlet zone. The rain flow from 16th April 2018 was chosen and is represented by the 0.87 m^3/s flow rate and the concentration of suspended solids $c = 3.3$ g/l. The SVI was measured 270 mL/g which corresponds to the correction coefficients of $V_{0c} = 0.9$ and $r_{Hc} = 0.89$.

From the results of the rain event, the experiment shows an area of an increased blanket height after the inlet zone. The same phenomena can be seen from the CFD results, even though the peak is more apparent. Also, the overall sludge blanket height matches well between CFD and experimental data. The concentration of suspended solids is slightly over predicted by the model which might be caused by the fact, that during the rain events, the sludge properties vary quickly and the measured SVI at the moment might not have corresponded to the sludge SVI already in the tank because the retention time. That leads to the question of when to measure the SVI during the rain events to realistically capture the tank average and more effort should be put into this matter.

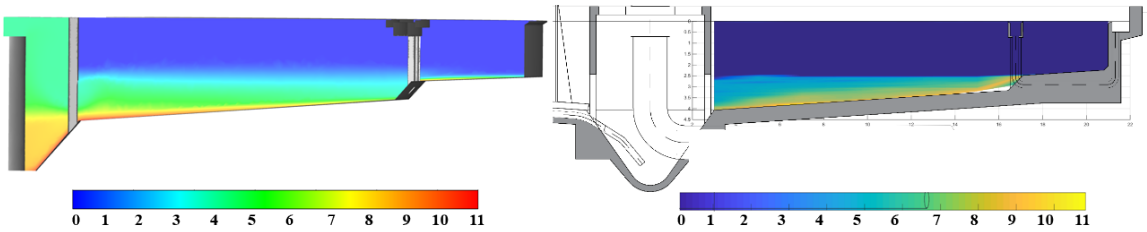

Figure 8. Comparison of the sludge blanket in DN3 between CFD model (left) and experiment (right).

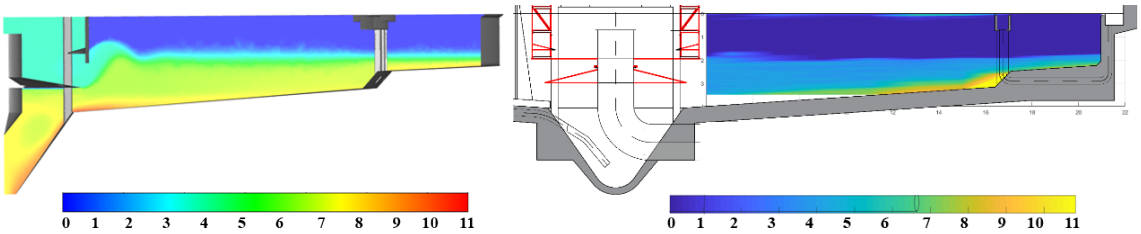

Figure 9. Comparison of the sludge blanket in DN1 between CFD model (left) and experiment (right).

The aim of this paper was an attempt to create a CFD model for secondary settling tanks which would be calibrated on a data obtained through a measuring campaign but also to try to generalize the model enough so it would be possible to use it on different tanks with different type of sludge. Based on a database data processing a new coefficient was used to extend the Takacs settling curve in order to compensate for better or worse settling sludges based on their SVI. That way it is possible to adjust the settling model based on an inlet flow rate, suspended solids concentration and SVI.

Further work should be aimed to test the model against different settling tanks and compare its performance. Also, additional work should be done to better the compression settling model which might lead to more accurate suspended solids distribution at the tank bottom.

Acknowledgements

The published results were achieved under the grant TAČR TE02000077 Smart Regions – Buildings and Settlements Information Modelling, Technology and Infrastructure for sustainable Development.

References

[1] G. A. Ekama. *Secondary settling tanks: theory, modelling, design and operation.* International Association on Water Quality, London, 1997.

[2] R. W. Samstag, J. J. Ducoste, A. Griborio, et al. CFD for wastewater treatment: An overview. *Water Science and Technology* **74**(3):549–563, 2016. https://doi.org/10.2166/wst.2016.249.

[3] P. Roache. *Computational Fluid Dynamics.* Hermosa Publishers, Albuquerque, USA, 1982.

[4] S. Patankar. *Numerical Heat Transfer and Fluid Flow.* Hemisphere Publishing Corporation, Taylor & Francis, New York, USA, 1980.

[5] S. Zhou, J. A. McCorquodale. Mathematical modelling of a circular clarifier. *Canadian Journal of Civil Engineering* **19**(3):365–374, 1992. https://doi.org/10.1139/192-044.

[6] I. Takács, G. Patry, D. Nolasco. A dynamic model of the clarification-thickening process. *Water Research* **25**(10):1263–1271, 1991. https://doi.org/10.1016/0043-1354(91)90066-Y.

[7] A. Griborio. *Secondary Clarifier Modeling: A Multi-process.* Ph.D. thesis, University of New Orleans, New Orleans, Louisiana, 2004.

[8] A. Griborio, J. Mccorquodale. Optimum design of your center well: Use of a CFD model to understand the balance between flocculation and improved hydrodynamics. *Proceedings of the Water Environment Federation* **2006**(13):263–280, 2006. https://doi.org/110.2175/193864706783710587.

[9] B. DeClerq. *Computational Fluid Dynamics of Settling.* Ph.D. thesis, Deparment of Applied Mathematics, Biometrics and Process Control of Ghent University, Ghent, Belgium, 2003.

[10] D. Morse, J. Sickza, K. Nielsen. Extending the McCoquodale model for 3D CFD of settling tanks. In *Water Environment Federation's Technical Exhibition and Conference (WEFTEC)*, pp. 3673–3690. Water Environment Federation, New Orleans, USA, 2016. https://doi.org/10.2175/193864716819707544.

[11] E. Ramin, D. S. Wágner, L. Yde, et al. A new settling velocity model to describe secondary sedimentation. *Water Research* **66**:447–458, 2014. https://doi.org/10.1016/j.watres.2014.08.034.

[12] A. Wimshurst, D. Burt, S. Jarvis. Enhanced process models for final settlement tanks. In *13th European Waste Water Management Conference.* Birmingham, 2019.

[13] M. Horáková, V. Janda, J. Koller, et al. *Analytika vody.* VŠCHT, Praha, 2nd edn., 2005.

[14] O. Švanda, J. Pollert, I. Johanidesová. Development of Screening Methods for Secondary Settling Tanks Monitoring and Optimization. In *New Trends in Urban Drainage Modelling*, pp. 242–245. Springer International Publishing, 2018. https://doi.org/10.1007/978-3-319-99867-1_40.

[15] B. Jin, B.-M. Wilén, P. Lant. A comprehensive insight into floc characteristics and their impact on compressibility and settleability of activated sludge. *Chemical Engineering Journal* **95**(1-3):221–234, 2003. https://doi.org/10.1016/S1385-8947(03)00108-6.

LOAD CARRYING CAPACITY OF MASONRY ARCH RAILWAY BRIDGES AT THE SERVICEABILITY LIMIT STATE

Marek Vokál*, Michal Drahorád

Czech Technical University in Prague, Faculty of Civil Engineering, Department of Concrete and Masonry Structures, Thákurova 7, 166 29 Prague, Czech Republic

* corresponding author: marek.vokal@fsv.cvut.cz

Abstract. This article focuses on masonry arch railway bridges. The main topic is the algorithm, which was developed for the purpose of a non-linear arch bridge analysis. The sensitivity analysis of the input parameters of the calculation was carried out. Subsequently, the study was carried out for the comparison of four calculation methods. For this comparison, a set of arch bridges were chosen. Two methods used commercial software, and the other two methods were developed. One of the developed algorithms uses a simple linear calculation. The second developed algorithm uses an iterative approach to handle material and geometrical non-linearity. The first commercial software method uses 2D non-linear models, the second method is a limit collapse analysis using the software LimitState:RING. These three methods were developed to handle the SLS (serviceability limit state) criteria, and their results were compared to the result of LCC at the ULS (ultimate LS) using LimitState:RING.

Keywords: Non-linearity, masonry, arch bridge, load carrying capacity.

1. Introduction

Masonry arch bridges are some of the oldest types of bridges in the world. Within the last century, these structures stopped being constructed. Therefore, the arch bridges, which are now still used as railway bridges, are from fifty to one hundred and fifty years old. For this reason, the tensile strength of the mortar should be considered to be at a zero level. On that account, the geometry of a thrust line of an arch is impacted. The linear calculation cannot handle the crack opening, which causes significant changes to the final thrust line.

The developed algorithm (hereinafter referred to as MVo) has two modes. In the first mode, just one linear calculation is completed, and the forces are verified directly after the first step. In the second one, the arch verification is done after the convergence of the steps of the non-linear analysis. The developed algorithm uses a beam model. This has two advantages: the algorithm is simplified and there is a lesser amount of computation time. The non-linear calculation means that the load carrying capacity, hereinafter referred to as LCC, is calculated iteratively for all load steps of the moveable load, which is time consuming even when using the beam model (for this article, around a hundred arch bridges were analysed using a usual computer, and the total computation time was around four hundred hours). The disadvantage is that the model parameters, such as the geometry of nodes and cross-section properties, must be completely renewed in every step of the calculation, therefore creating the algorithm of such a calculation was time-consuming for the programmer. The modelling of arch bridges using non-linear beam elements was proposed by [1] and used, for example, in [2].

The LCC is assessed according to [3] as a multiple of load model 71, which can pass the bridge safely (under conditions described in Section 5). This multiple is called Z_{LM71}.

The masonry can be modelled in several ways. For example, both the atomic model and detailed 3D model are simulating the masonry elements and mortar separately. The simplest method is to homogenize, in a suitable manner, the masonry in one material. This approach is referred to in [4], the main code of masonry structures, which is, according to [5], called "yield line theory" and is based on laboratory tests conducted on brick masonry walls subjected to lateral loads, showing that failure takes place along a well-defined pattern of lines. Other homogenization techniques are described in the paper [6], which addresses many different homogenization methods available in the literature, showing their advantages and disadvantages. The strategy employed in [7] is based on the well-established first-order homogenization schemes, e.g. [8].

The material non-linear behaviour of masonry is impacted mainly by the low or zero tensile strength of the masonry [9]. The tensile strength can be usually neglected, but, for example, in the article [10], the tensile strength is used and the increase of bearing capacity is shown. At the SLS (serviceability limit state), the crushing of masonry is not allowed, at the ULS, the crushing can occur and in RING (LimitState:RING – see [11] software), even plastic hinges and the sliding of blocks of the arch can occur, until the moveable mechanism of structure, and therefore collapse of the arch occurs. The geometric non-linearity is handled only in the created algorithm, MVo. The effect of geometric non-linearity cannot be

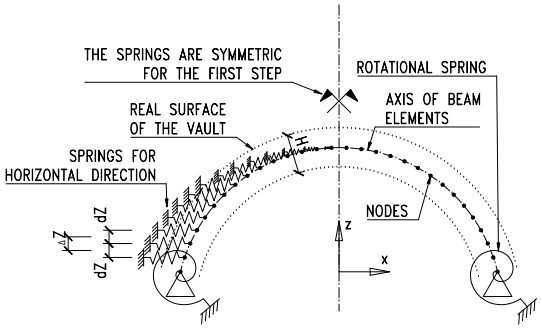

FIGURE 1. The model used in the first step of the calculation.

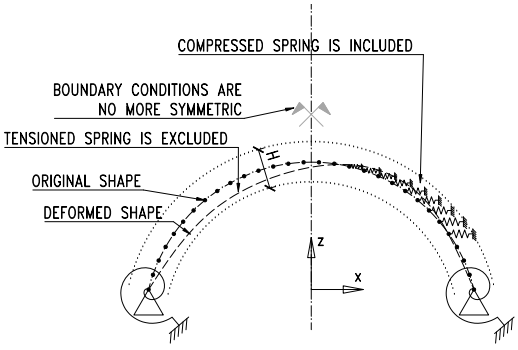

FIGURE 2. The model used in the second and every other step of the calculation.

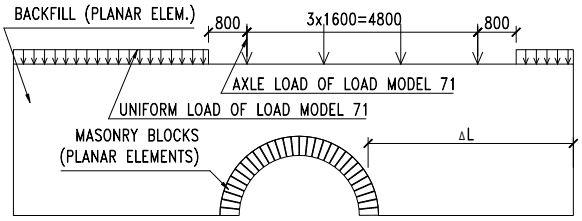

FIGURE 3. View of whole model.

neglected just for the case of arches of a large span and low ratio sagitta over the span of the arch. In this article, a sensitivity analysis of key input parameters is going to be performed using the MVo code. Afterwards, the results of four calculation methods will be compared:

- MVo code – modelling using beam elements,
  - ▷ Linear (SLS analysis),
  - ▷ Non-linear (SLS analysis),
- Scia – planar elements were used (SLS analysis),
- RING (ULS analysis).

2. The used method – MVo

The algorithm which was created using the MATLAB software can handle circular arch bridges or arch bridges given by the set of points representing arch axis and input of the desired degree of a polynomial, which will be used for finding a smooth geometry of the axis of the arch by the least square method. It is assumed that such a set of points can be obtained, for example, by geodetic measurements. In this article, the results of circular arch bridges will be presented. See the example of the Legion Bridge in the literature [12], for which the geometry was fitted by the least square method of the polynomial of 8th degree. The main property of the model is that it uses beam elements. From 128 to 256 elements are used. The axis of the original arch is considered for the first step of the calculation. Due to crack opening, the geometry changes. According to these geometry changes, the cross-section properties (area and moment of inertia) are changed correspondingly. The new geometry of every node of every step is "guessed" as a geometry of a thrust line of the previous step.

The springs representing the backfill behaviour act linearly for compression in the soil and the stiffness in the tension is considered to be zero. The fact that the stress in the soil is either tension or compression is assessed by the deformation from the live load. The spring acts only in a horizontal direction. The stiffness of the spring is calculated from E_{def}:

$$K_{spring} = E_{def}.\Delta Z.B/\Delta L, \qquad (1)$$

Where K_{spring} is the stiffness of the spring in the given node, E_{def} is the deformation modulus of the soil, ΔZ is one-half of the horizontal projection of distance between two adjacent nodes to the given node, B is the width of the vault, ΔL is the length of the substituted soil (the distance to each node), see Figure 3.

Assumptions of the calculation:

- The supports at the arch springing are considered infinitely stiff, no deformation is allowed, i.e., no uneven settlements of supports are considered.
- The Bernoulli-Navier hypothesis for beam elements is considered.
- Constant soil characteristics are considered for all points of the backfill.
- There is no inflection point in the geometry of the arch in the case of the polynomial shape.
- The new position of nodes must lie on a normal line of the curve of the original axis geometry.
- In the study of the sensitivity of input parameters, the arch is symmetric, the longitudinal slope of alignment of a railway is considered to be zero. The thickness of the arch is constant.

See the loading conditions in Figures 4 to 7. The structure is loaded by self-weight, the weight of the backfill, ballast, earth pressure, and live loads.

The live load dispersion (load distribution) is done in the same way as in LimitState:RING. The Boussinesq distribution is used, see the [11]. The load is distributed at angle ϕ_{Ball} in the ballast and ϕ_{Back} in the backfill. This distribution is displayed in Figures 6

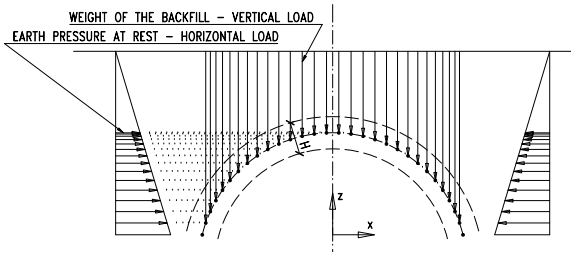

Figure 4. The load of the model by earth pressure and weight of the backfill.

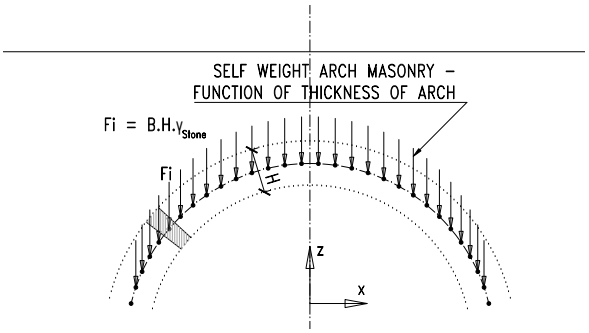

Figure 5. The load of the model by self-weight of masonry arch.

and 7 and it is denoted as "left and right dispersion lines". The figures are examples of a moveable load position. The "length of model" means the length of the load model 71. In the MVo code, the length is calculated as 4.8+0.8*2=6.4 m, because the concentrated axle forces are considered as distributed into the uniform load. The nodes, which are between the left and right dispersion lines, are loaded by the load model, the other ones are not loaded by the live load at the examined load position. The length of the blue vertical lines represents the value of force acting in the node.

The developed algorithm can be used for the calculation of LCC at the SLS limits or the ULS limits. In this article, only the SLS is handled. The collapse load can be calculated in other software. In this article, RING is used, see [11] and [13]. The used equations are described in [14], and [15]. The geometric non-linearity is handled by the second order analysis, the material non-linearity is handled by the crack opening and iterative changes of the cross-section. The smooth geometry is needed for all steps of a non-linear calculation. This is a typical property of the beam model. Even a small aberration from the smooth geometry causes the unreal values of internal forces – especially bending moment and shear force. In the algorithm, during tens of steps, the small aberration always occurred, which led to unreal results. There are two ways of handling this problem. The first is to use many (at least thousands) elements, the second way of handling this is to smooth all the new coordinates of nodes. The first way is very

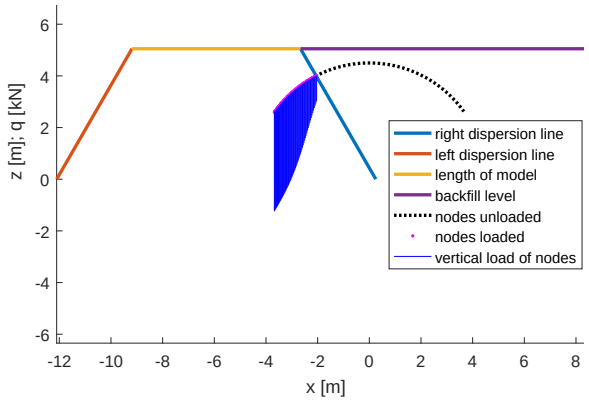

Figure 6. Example of dispersion of live load and values of nodal forces. q is a nodal load from the live load, $x$and z are coordinates of global coordinate system.

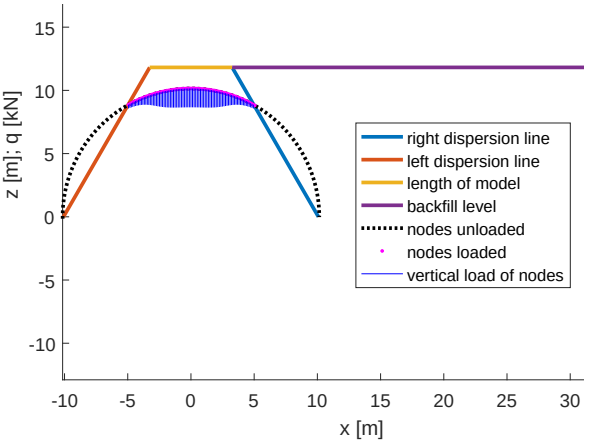

Figure 7. Example of dispersion of live load and values of nodal forces.

time-demanding. Therefore, smoothing was used. On the grounds of that, in circular arch bridges, the functions of bending moments are functions of sine and cosine functions, Fourier curve fitting was used. This curve fitting for the geometry of the new calculation step leads to the fastest calculation convergence. During the first few steps, the fitted data have some errors (as can be seen in the figure). The error is equal to the chosen precision ε, when the calculation converges. $eTh4Fit$ is e_{Th} before fitting, $fitted$ is after the curve fitting. In Figure 8, the fitting is done for an example of the third step of vault bridge calculation. In the next steps, the error is usually close to ε and the curves look identical.

The used parameters in the study using MVo code: $E_{def} = 40\,\text{MPa}$; $E_{masonry} = 1000 * f_k$; $\varepsilon = 10\text{e-}8\,\text{m}$; $\gamma_{Fill} = 18\,\text{kN/m}^3$ – weight of the backfill; $\phi = 30°$ – angle of internal friction – cohesionless soil is considered, earth pressure at rest is calculated as: $K_0 = 1 - sin(\phi)$; $\mu = 0.6$ – friction coefficient; $\gamma_{Stone} = 25\,\text{kN/m}^3$; $h_{Ballast} = 0.3\,\text{m}$ – height of the rail ballast (under the sleeper); $\gamma_{Bal} = 18\,\text{kN/m}^3$ – specific weight of ballast; $L_{Sleeper} = 2.4\,\text{m}$ – length of the sleeper in

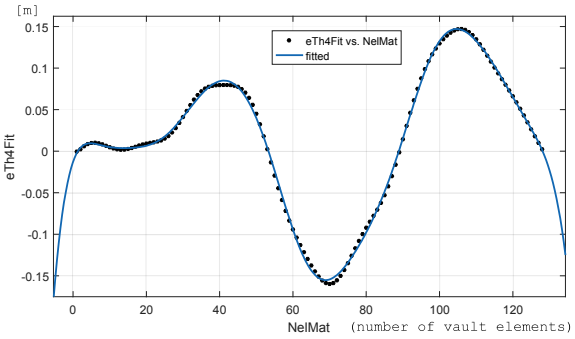

FIGURE 8. Curve fitting of geometry for the next step of the calculation.

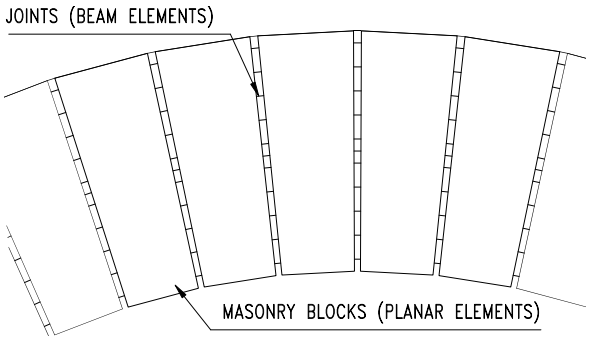

FIGURE 9. Blocks of masonry and beam elements representing the joints between the blocks.

the transverse direction; $\phi_{Ball} = 15°$ – disperse angle of live load through the ballast; $\phi_{Back} = 30°$ – disperse angle of live load through the backfill.

3. The control method taken from article [15] – Scia

The second group of used models is the group using 2D planar elements. The masonry blocks are represented by planar elements with a linear behaviour. The joints between the blocks are modelled by a set of beam elements that are "compression-only". The soil is modelled by elements with Young modulus equal to E_{def}, which allows us to also model the live load dispersion and all other effects of backfill, except for passive earth pressure. For the calculation of the SLS, these deformations are small, and passive earth pressure is not activated. As mentioned before, this analysis was done using the Scia commercial software [16].

For the details of this model, see [12], [15]. Scia parameters used in this article: E_{def}, $E_{masonry}$ are chosen the same as in MVo code, $\nu_{Mason} = 0.2$, $\nu_{backfill} = 0.333$; ν – Poisson's ratio.

4. The RING method

This program is designed for a collapse analysis – the ULS. Cracks can open up and parts of the cross-section can crush. The equations are built upon the theory of rigid bodies, where the vault is divided by the collapsed block. The number of such a collapsed block must be as big as to create a moveable

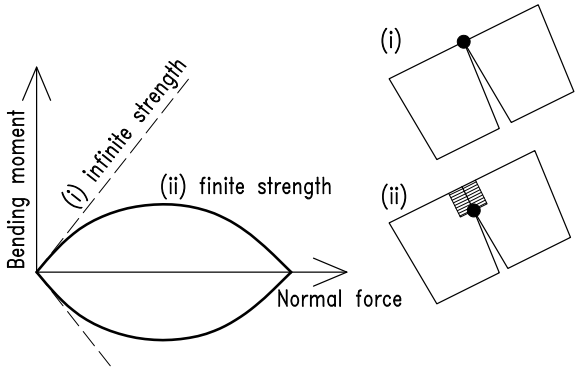

FIGURE 10. M-N diagram, compressed area.

mechanism. The resulting collapse mechanisms can be divided into the following cases: collapse by the crushing of masonry; collapse by the opening of cracks; collapse by shearing between the blocks. The method was described in [17] and [18], the modes of the vault collapse are also described in [19].

Figure 10 depicts the M-N diagram – the combinations of the acceptable moment and axial capacities of a structural member at the ULS.

The program RING gives two options for the analysis. The compressive force in the vault is transferred by the joints:

(i) Through an infinitely thin strip of stone at the edge of the vault (external when collapsing towards the inside of the arch, internal when deflecting outside the arch) if infinite strength of the masonry is assumed.

(ii) Through a rectangular strip that represents the stress at which the masonry is crushed.

For the case of infinitely stiff blocks, the curve of the M-N diagram is linear. The black dot is the point of rotation of blocks when creating a moveable mechanism.

5. The method of verification

The first main indicator of how the cross-section of height H is loaded is the position of the thrust line. The thrust line is a locus of points through which the resultant force goes. For each point of the vault, it can be (for the case of the beam model) calculated as $e_{Th} = M/N$, where M is the bending moment and N is the normal force acting on the cross-section – from the load in a given combination. The higher bending moment acting in the cross-section, the higher is e_{Th} and the lesser is the compressed area. For fulfilling the criteria of the SLS, e_{Th} must be lower than $H/3$ according to [20], for fulfilling the criteria of the ULS, e_{Th} must be lower than $H/2$. Eccentricity larger than $H/2$ means that the thrust line lies out of the cross-section, which leads to the collapse of the structure (if the tensile strength is neglected). This is illustrated by Figure 11:

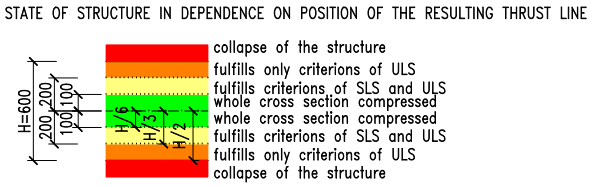

Figure 11. Verification of position of thrust line.

The method of obtaining the e_{Th} depends on the chosen model. For the case of 2D planar elements, the verification can be done by checking that the height of the compressed area is at maximum $0.5H$. For the case of the linear beam model, e_{Th} is obtained in a single step. For the case of the non-linear beam model, the e_{Th} varies for each step of the calculation and only the steps that fulfill the criterion of convergence (and equilibrium conditions as well as limit strain conditions) can be taken as a final value of e_{Th}. The second main indicator of the state of the vault is normal stress that is acting on the cross-section from the given load. In the SLS, the stress should be less or equal to $0.45f_k$. This criterion assures that, during the usual loading conditions, no point of the structures will crush. The crushing is permitted in the case of the ULS, a state of collapse of the structure.

6. Results of modelling – sensitivity analysis of input parameters

Figures 12 to 15 have resulted from modelling using the MVo non-linear analysis. This relates to the article [13]. In the cited article, the sensitivity of parameters is calculated according to the ULS criteria. In this article, the plots are calculated according to the SLS criteria. The investigated parameters are:

(1.) Deformation modulus of the soil E_{def},

(2.) Coefficient of friction μ,

(3.) Ratio H/L – arch thickness over span length (intrados),

(4.) Characteristic masonry strength f_k.

Nine masonry vault railway bridges of a circular shape were analysed in this article. The chosen spans were of 6, 12 and 20 m length, ratios of v/L (sagitta/span length) were chosen to be 0.1, 0.3 and 0.5. In the legend of the plot "06_0.6" means span 6 m, sagitta 0.6 m, which means a ratio of 0.1. The ratio p/L (depth of backfill at the top of the arch/span length) is 0.08333. The total depth of backfill is, therefore, 0.5 m for the span of 6 m, 1 m for the span of 12 m, and 1.666 m for the span of 20 m. The default value of the specific weight of masonry, specific weight of backfill, friction coefficient, angle of internal friction, and cohesion of the soil are the same as for the study. Characteristic compressive strength is 5 MPa. The thickness of the vault is considered to be 0.4 m

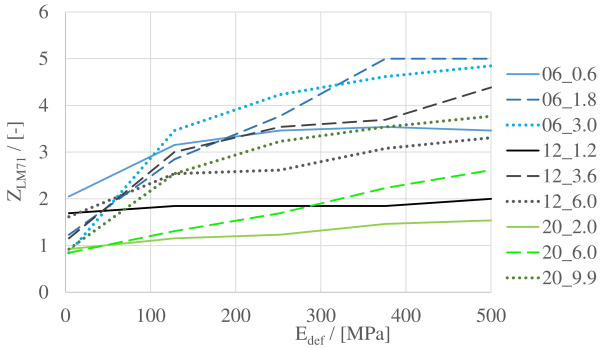

Figure 12. Load carrying capacity in dependence on E_{def}. For the legend, see Section 6.

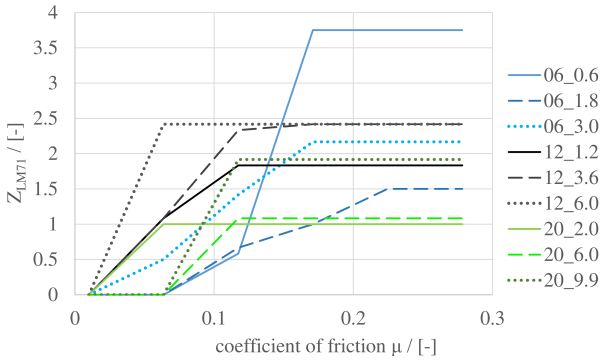

Figure 13. Load carrying capacity in dependence on the coefficient of friction. For the legend, see Section 6.

for the span of 6 m, 0.5 m for the span of 12 m, and 0.6 m for the span of 20 m.

6.1. Deformation modulus of the soil E_{def}

The chosen scope of E_{def} corresponds to the variation from the clay-sand to compacted gravel of an ideal grain size. It can be seen that the parameter is most sensitive for the case of arch bridges with a high ratio of v/L. The lower the ratio v/L, the lower is the sensitivity to E_{def}.

6.2. Coefficient of friction μ

The sensitivity analysis of the coefficient of friction between the blocks of masonry elements is done just for circular bridges. As it was shown in the article [13], the shear resistance depends mainly on the shape of the vault. The circular bridges usually have enough shear resistance. This fact is proven also by Figure 13, which shows the results of a calculation in the SLS. The ratio V/N – shear force over normal force – which should be less or equal to 0.4 due to [4] and which should be less or equal to 0.6 due to experimental data are for all the investigated arch bridges not higher than 0.225. Hence the LCC is not impacted by shear strength. However, for the lower values of the coefficient of friction, the sensitivity to change of this parameter is high.

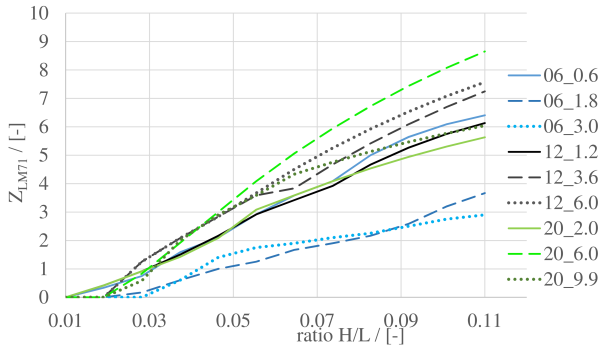

FIGURE 14. Load carrying capacity in dependence on ratio H/L, the thickness of the arch. For the legend, see Section 6.

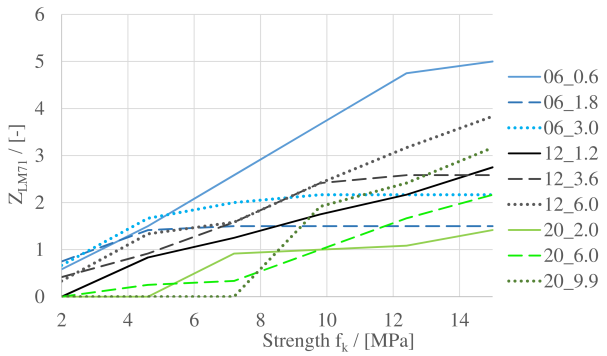

FIGURE 15. Load carrying capacity in dependence on the characteristic strength of masonry. For the legend, see Section 6.

6.3. The thickness of the arch

The thickness of the arch is the most sensitive parameter. That is why there should be put an effort in getting this parameter during the diagnostic survey. The thickness of the arch is sensitive both due to the maximal stress and the eccentricity of the load. The higher the thickness, the higher the range where the thrust line can occur. In the non-linear calculation, the crack opening, and therefore the possibility of finding the ideal geometry raises with increased thickness.

6.4. Characteristic strength of masonry

The characteristic strength of masonry is a parameter with similar sensitivity to the change in E_{def}. In the SLS, there is always some limit for which increasing the strength does not increase the LCC, because the maximal eccentricity is a decisive criterion. This can be seen from Figure 15, but mainly from the study and comparison of the three mentioned methods for handling the SLS criteria in Section 7.

7. The results of the study of the set of arch bridges – A comparison of the four forementioned methods

The LCC of bridge spans $L = 2.5, 5$ and 10 m was calculated, the characteristic strength of masonry was (1 for special cases) 2, 4, 6, 8, and 10 MPa, sagitta v was always considered to be $L/2$ and $L/4$. The depth of backfill p was always considered to be 0.5, 1, 1.5 m. Owing to the fact that Scia results were considered for a control reason, the LCC of the medial thickness (of total 3) was not calculated. The difference between the MVo code and the Scia model is that in Scia, the behaviour of the backfill is linear – in the horizontal direction as well as the vertical direction. Talking about the arches, where the height of the backfill is similar or even larger than the span of the arch, the results are significantly impacted by the soil behaviour. The problem becomes more influenced by the impact of soil and its modelling rather than the behaviour of the masonry arch. See the result of RING modelling in Figure 18, MVo non-linear code in Figure 19, the results of MVo linear code in Figure 20, the results of control Scia calculation in Figure 21 and a comparison of the RING method with the MVo code in Figure 22. For the purpose of clarity, the comparison of four forementioned method was added in two separate plots: 16 and 17.

8. Result discussion

It was confirmed that the results of the two models, which should have similar results, are, indeed, similar. The biggest difference is for the smallest arch of the span of 2.5 m. For this geometry, the calculations are impacted greatly by the behaviour of the backfill. The linear backfill behaviour helps the arch in both vertical and horizontal directions. For the arch with a high effect of backfill, special modelling should be done using special geotechnical software. It should be noted that the results of the control model – the Scia model – are imprecise due to the reading of the graphical results. Especially the verification of the maximal eccentricity is sensitive to interpretation of the height of the compressed area. Seeking the LCC iteratively is time-demanding when using the Scia software. Conversely, the MVo code is created for calculating the LCC and results are obtained simply, and straightforwardly. The verification is done with precise numbers.

c

The linear calculation must obviously give a lower LCC. In the non-linear calculation, the axis of the arch is "optimised", the geometry is updated to decrease the bending moments in the next step. The limits of changing the geometry are given by the arch extrados, intrados, and the SLS criteria. The resulting bending moments depend mainly on the crack opening. If the height of the cross-section decreases and is close to the limit – one-half of the cross-section height, then the moment of inertia decreases eight times. The bending moment in the next step decreases up to eight times. The optimization of the geometry is done for every load step, every position

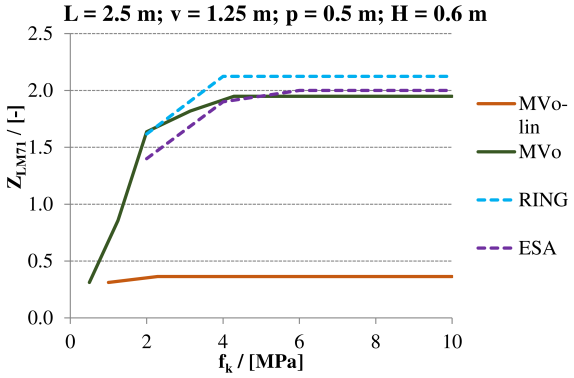

Figure 16. The comparison of all used methods for the example of $L = 2.5\,m, v = 1.25\,m, p = 0.5\,m$ and $H = 0.6\,m$.

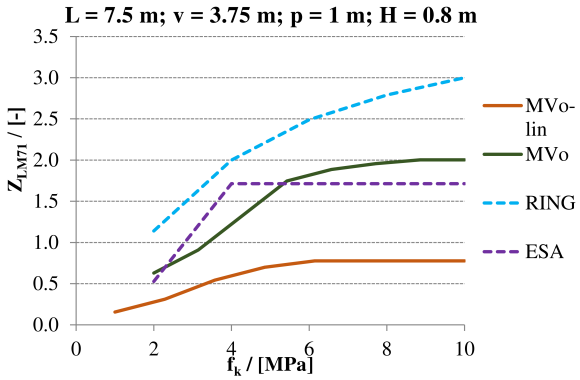

Figure 17. The comparison of all used methods fo example of $L = 7.5\,m, v = 3.75\,m, p = 1\,m$ and $H = 0.8\,m$.

of the live load, and so the non-linear calculation is much more time-demanding. The linear calculation of the MVo code with one position of a live load takes around 3 seconds. Around 20 positions were usually examined. The non-linear calculation including all iterations takes, therefore, around 40 minutes. The program Scia examines a similar calculation in 30 minutes, but the multiple of model 71 must be sought by the engineer (usually around 5 or more iterations) which takes around 2.5 hours. The non-linear calculation of Z_{LM71} of one arch bridge using the Scia software takes the engineer about 5 hours. The same calculation using the MVo code can take the engineer about 5 minutes. In the MVo code, all the input parameters can be changed easily, even the thickness of the arch or other geometry inputs. The iterative process of finding the multiple Z_{LM71} (including moving load) is implemented and the engineer gets the result directly. Finally, the advantage of the MVo code is that the geometric non-linearity of the structure and the non-linear behaviour of the backfill are included.

The authors tried to find the dependence of LCC using RING on LCC using the MVo code. Such an obvious dependence was not found. The curves of the LCC ratio Z_{RING}/Z_{MVo} are similar in shape, but the tendency to grow or decrease differs for every analysed arch. For most of the cases, the ratio is the lowest for the highest depths of the backfill. For the majority of the cases, the LCC is higher at the ULS, usually up to two times higher. A comparison of the sensitivity of input parameters due to the SLS (MVo) and the ULS (RING – see in the [15]) give very similar results when comparing the sensitivity to the change of E_{def} in the SLS and sensitivity to the change of angle of the internal friction in the ULS. The same applies to the coefficient of friction between the blocks of masonry, ratio H/L, and strength of masonry. Individual curves give a slightly different behaviour, but in general, the accordance of the compared plots was very good. In the RING result plots, there is no obvious breakpoint between the growing and constant segment, which can be seen in the SLS methods. The reason is that in the RING analysis, the criteria are different: low strength arches collapse by the crushing of the whole cross-section. The middle range of strengths is impacted by the crushing, and with growing strength, the crushed area decreases. When the strength is higher than usual masonry elements can have or is close to infinite, the criterion of the maximal eccentricity of the load is decisive and the constant segment of the plot occurs.

9. Conclusions

The comparison of sensitivity to change of the input parameters due to the SLS and the ULS gives very similar results. This comparison was done for key parameters, which were proven to be the most sensitive in the article [13]. The comparison of analysis using Scia software with 2D planar elements to the MVo results showed a good agreement except for small spans of the arch, where the behaviour of backfill affects the final LCC significantly. For this reason, a further study of the backfill behaviour with an advanced methods designed specifically for the soil behaviuor should be conducted. The comparison of analysis using the MVo non-linear method to the RING results showed no particular dependence. The LCC from the RING method is mostly higher than the LCC from the MVo method. The RING results are up to two times higher. The linear calculation gives very conservative results, LCC is usually two to three times lower than from the non-linear model. This is because of the fact that the non-linear model can change its geometry to minimize the bending moments and the only boundary conditions for the geometry of the arch are the extrados and intrados of the assessed arch. The effect of crack opening, which reduces the bending moment at the critical points of the arch, is also increasing the final LCC.

List of symbols

Z_{LM71} is the multiple of load model 71, which can pass the railway bridge safely,

Z_{RING} is resulting Z_{LM71} from the software LimitState:RING,

Z_{MVo} is resulting Z_{LM71} from the MVo code,

K_{spring} is the horizontal stiffness of the spring in the given node,

E_{def} is the deformation modulus of the soil,

$E_{masonry}$ is Young's modulus of masonry,

ΔZ is one-half of the horizontal projection of distance between two adjacent nodes to the given node,

B is the width of the vault,

H is the cross-section height,

L is the span length (intrados of the vault),

p is the depth of the backfill at the top of the arch,

v is the sagitta (rise) of the arch,

ΔL is the length of substituted soil (the distance to each node), see Figure 3,

ϕ_{Ball} is the angle of load distribution in the ballast,

ϕ_{Back} is the angle of load distribution in the backfill,

ϕ is the angle of internal friction of the soil,

K_o is the coefficient of earth pressure at rest,

q is the vertical nodal force from the live load,

ε is the chosen maximal error of resulting displacement, reaching this error terminates the iterative calculation,

$e_{Th} = M/N$ is the eccentricity of the load in a given combination. Maximal acceptable e_{Th} is displayed in Figure 11,

M is the bending moment acting on the cross-section – from the load in a given combination,

N is the normal force acting on the cross-section – from the load in a given combination,

V is the shear force acting on the cross-section – from the load in a given combination,

eTh_4Fit is the function of the eccentricity of the load before the curve fitting,

$fitted$ is the function of eccentricity of the load after the curve fitting,

γ_{Fill} is the specific weight of the backfill,

γ_{Stone} is the specific weight of the masonry,

γ_{Bal} is the specific weight of the ballast,

f_k is the characteristic masonry strength,

$\mu = 0.6$ is the friction coefficient (between the masonry blocks),

$h_{Ballast}$ is the height of the rail ballast (under the sleeper),

$L_{Sleeper}$ is the length of the sleeper (in the transverse direction of the bridge),

ν_{Mason} is the Poisson's ratio of the masonry,

$\nu_{backfill}$ is the Poisson's ratio of the backfill.

References

[1] S. De Santis, G. Felice. A fibre beam-based approach for the evaluation of the seismic capacity of masonry arches. *Earthquake Engineering and Structural Dynamics* **43**(11):112–120, 2014. https://doi.org/10.1002/eqe.2416.

[2] P. Zampieri, S. Perboni, C. Tetougueni, C. Pellegrino. Different approaches to assess the seismic capacity of masonry bridges by non-linear static analysis. *Frontiers in Built Environment* **6**:124–134, 2020. https://doi.org/10.3389/fbuil.2020.00047.

[3] SŽDC. *Systematic directive for determination of load carrying capacity of bridges*, 2015.

[4] D. Pume, K. Lorenz. EN 1996-1-1 – Design of masonry structures. Standard, ÚNMZ, 2007.

[5] G. Milani, P. Lourenco, A. Tralli. Homogenization approach for the limit analysis of out-of-plane loaded masonry walls. *Journal of Structural Engineering - ASCE* **132**(10), 2006. https://doi.org/10.1061/(ASCE)0733-9445(2006)132:10(1650).

[6] P. Lourenco, G. Milani, A. Tralli, A. Zucchini. Analysis of masonry structures: Review of and recent trends in homogenization techniques. *Canadian Journal of Civil Engineering* **34**(11):1443–1457, 2007. https://doi.org/10.1139/L07-097.

[7] J. Zeman, J. Novak, M. Sejnoha, J. Sejnoha. Pragmatic multi-scale and multi-physics analysis of Charles Bridge in Prague. *Engineering Structures* **30**(11):3365–3376, 2008. https://doi.org/10.1016/j.engstruct.2008.05.012.

[8] A. Anthoine. Derivation of the in-plane elastic characteristics of masonry through homogenization theory. *International Journal of Solids and Structures* **32**(2):137–163, 1995. https://doi.org/10.1016/0020-7683(94)00140-R.

[9] M. Drahorád. Load–bearing capacity of masonry arch bridges. In *International Conference Engineering Mechanics*, vol. 19, chap. 23, pp. 33–34. Institute of Thermomechanics of the Czech Academy of Sciences, v. v. i., 2013.

[10] G. Ramaglia, G. P. Lignola, A. Prota. Collapse analysis of slender masonry barrel vaults. *Engineering Structures* **117**:86–100, 2016. https://doi.org/10.1016/j.engstruct.2016.03.016.

[11] LimitState:RING Manual, 2020. https://www.limitstate.com/ring-documentation.

[12] M. Vokál, M. Drahorád. Legion Bridge in Prague - assessment of stone arches. *Transactions of the VŠB – Technical University of Ostrava, Civil Engineering Series* **19**(2):71–80, 2019. https://doi.org/10.35181/tces-2019-0023.

[13] M. Vokál, M. Drahorád. Sensitivity analysis of input parameters for load carrying capacity of masonry arch bridges. *Acta polytechnica* **60**(4):349–358, 2020. https://doi.org/10.14311/AP.2020.60.0349.

[14] M. Vokál, M. Drahorád. Non-linear analysis of slender masonry column subjected to biaxial bending. *Acta polytechnica* **61**(2):391–405, 2021. https://doi.org/10.14311/AP.2021.61.0391.

[15] M. Vokál, M. Drahorád. The load bearing capacity of railway masonry arch bridges. *Transactions of the VŠB – Technical University of Ostrava, Civil Engineering Series* **18**(2):66–72, 2019. https://doi.org/10.31490/tces-2018-0019.

[16] Scia engineer manual, 2020. https://www.scia.net/cs/support/downloads/scia-engineer-manuals.

[17] M. Gilbert, C. Melbourne. Rigid block analysis of masonry structures. *The structural engineer* **72**:356–361, 1994.

[18] M. Gilbert. RING: A 2D rigid-block analysis program for masonry arch bridges. In *ARCH01: 3rd International Arch Bridges Conference*, pp. 459–464. 2001.

[19] J. A. Ochsendorf. *Collapse of masonry structures*. University of Cambridge, 2002.

[20] V. Hrdoušek, M. Drahorád. ČSN P 73 6213 – Design of masonry road bridges. Standard, ÚNMZ, 2008.

A. Attachments

See the results of modelling in Figures 18 to 22, following each on a separate page.

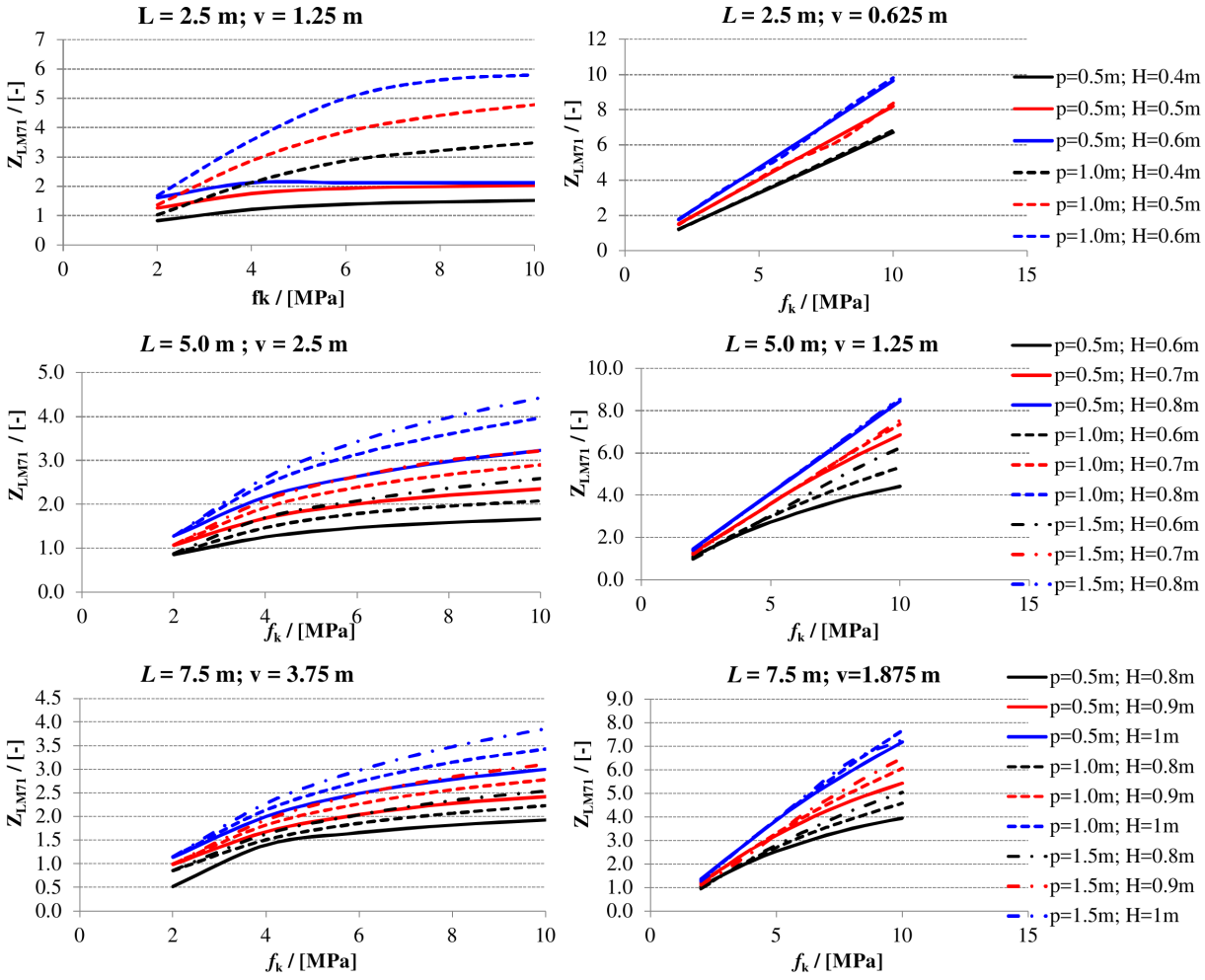

Figure 18. Results from the modelling using the RING software.

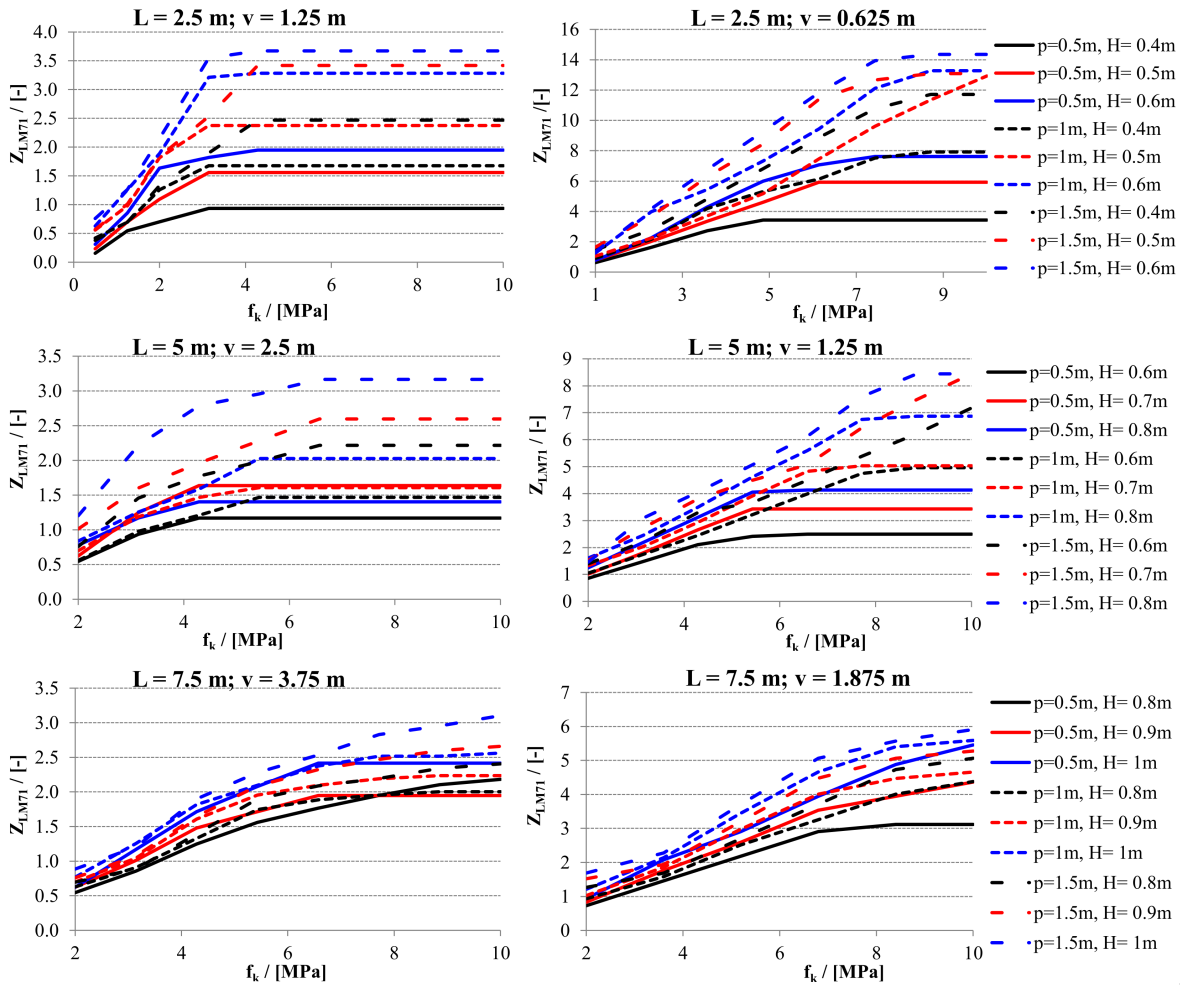

FIGURE 19. Results from the modelling using the MVo software – non-linear analysis.

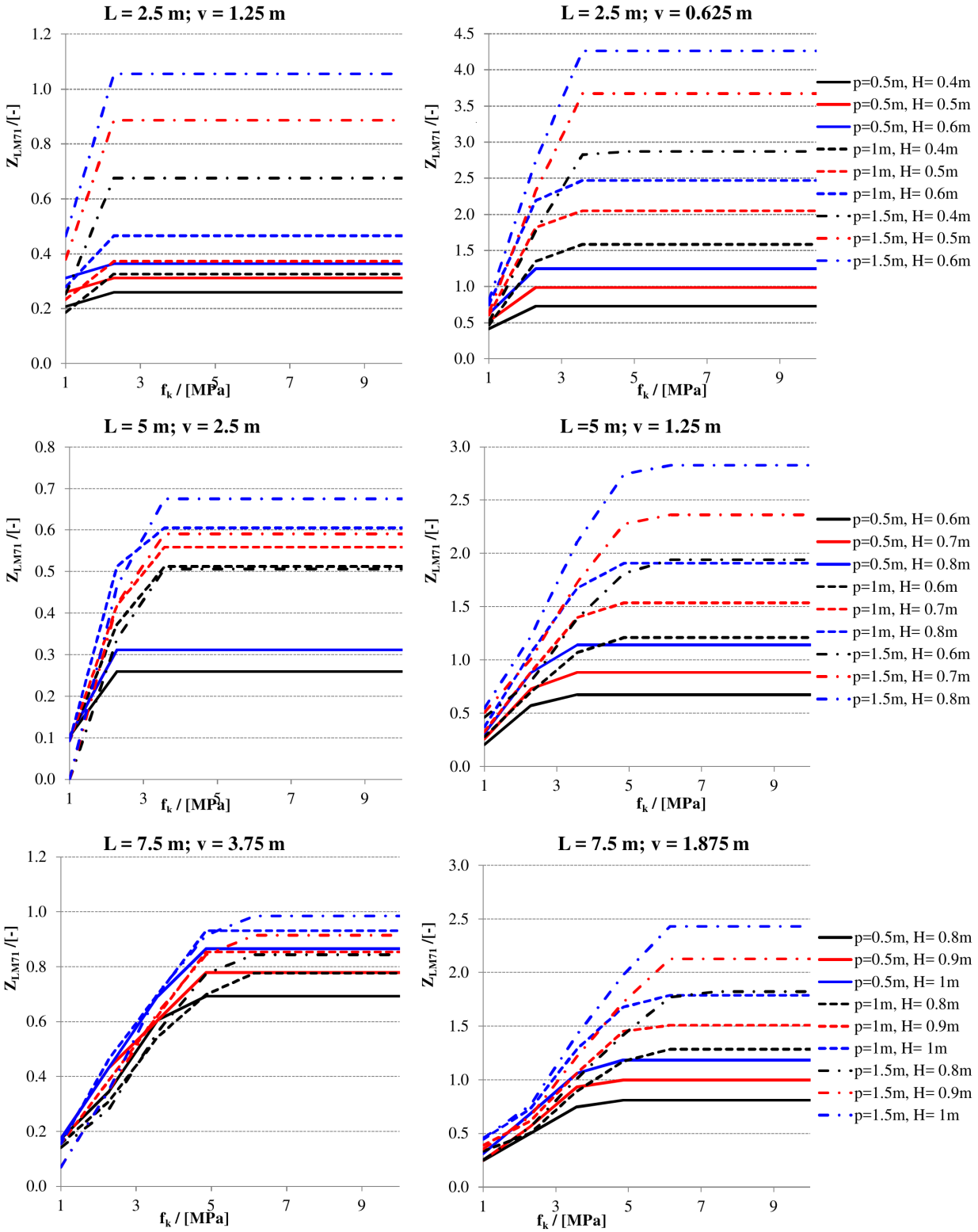

Figure 20. Results from the modelling using the MVo software – linear analysis

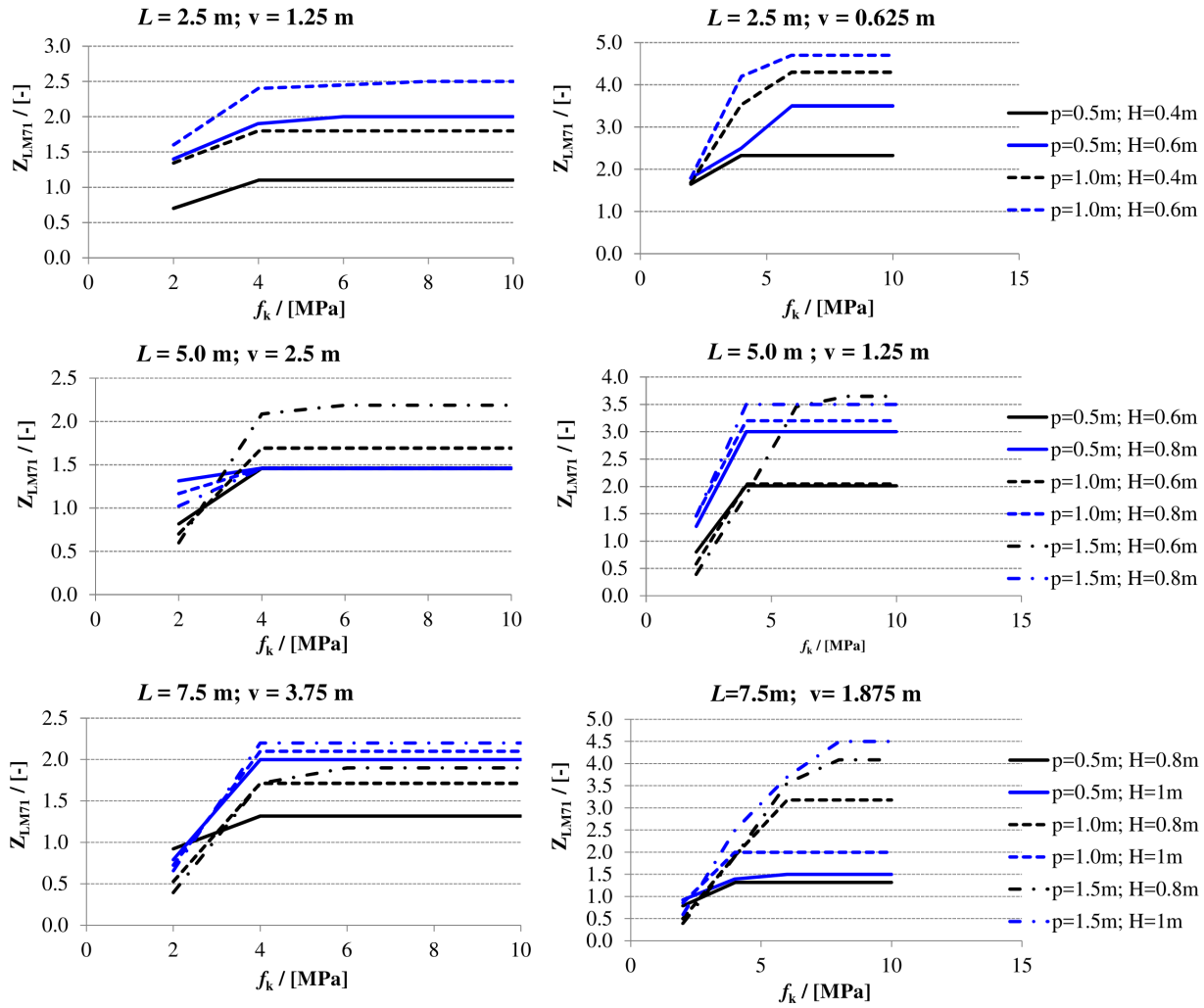

FIGURE 21. Results from the modelling using the Scia software – non-linear analysis.

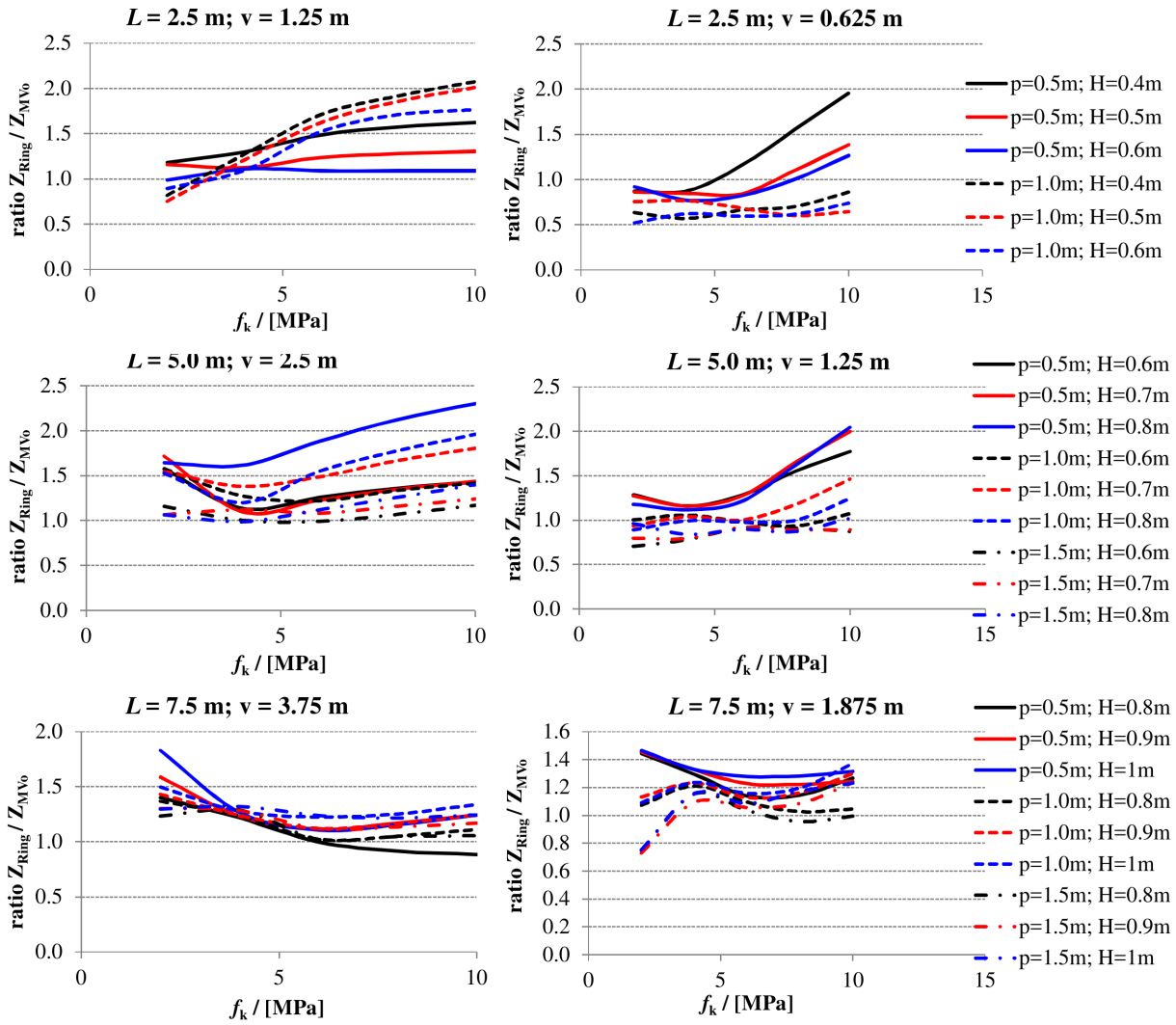

Figure 22. The ratio of $Z_{LM71,RING}/Z_{LM71,MVo}$ is simplified as Z_{RING}/Z_{MVo}.